Alma Mater Studiorum – Università di Bologna

DOTTORATO DI RICERCA IN

Chimica

Ciclo XXIX

Settore Concorsuale di afferenza: 03/C2

Settore Scientifico disciplinare: CHIM/04

Catalytic aqueous phase conversion of polyols to hydrogen and chemicals

Candidato: *Lombardi Erica*

Coordinatore Dottorato   **Relatore**

Prof. Aldo Roda   *Prof. Francesco Basile*

Esame finale anno 2017

"Ho imparato che tutti quanti

vogliono vivere sulla cima della montagna,

senza sapere che la vera felicità

risiede nella forza di risalire la scarpata."

Gabriel Garcia Marquez

Summary

Abstract

The present work is focused on the study of aqueous phase reforming reaction (APR), its mechanism and the relation within catalyst activity and metal/support properties. Several oxides and mixed oxides were studied, synthesized by traditional co-precipitation technique and microemulsion. The first focus was the upgrading of glycerol mainly towards the optimization of the system with different catalysts and the relation with the reaction mechanism. Heated ATR-IR technique was developed to perform in-situ reactions to elucidate the formation of reaction intermediates and confirm the mechanism hypothesis with different catalysts. In terms of catalytic performances interesting results were obtained with Pt/TiO_2 catalyst with the support prepared by water in oil microemulsion technique. Improved performances have been demonstrated in comparison with Pt over commercial TiO_2 support attributing the effect to the synergy between metal and support. Moreover it was studied and elucidated the effect of basic and acid sites in Pt-loaded Mg/Al supports. Similarly, the role of addition of redox metals as Ni and Fe in enhancing hydrogen production or liquid phase products was also determined. The interesting results obtained with glycerol allowed shifting towards a more complex polyol as glucose, studying the reactivity previously defined with degradation and isomerization reactions typical of this molecule. Beside the optimization of reaction parameters using Pt/TiO_2-m catalyst, the effect of the acid/base support features and the type of metal over products distribution was studied and the relation structure/reactivity based on catalyst characterization. The most interesting non noble metals tested have been used to synthesize bimetallic bulk catalyst with interesting properties even with respect to Pt reference metal.

Introduction

1. Biomass treatment

Part of this chapter was published in the book:

Basile, F.; Albonetti, S.; Cavani, F.; Lombardi, E.; Mafessanti, R. "*Biosyngas and Derived Products from Gasification and Aqueous Phase Reforming*" Chapter 4 from Cavani, F., Albonetti, S., Basile, F., Gandini, A. "*Chemicals and Fuels from Bio-Based Building Blocks*", Eds.; Wiley-VCH Verlag GmbH & Co. KGaA, 2016; pp 79–110. Rights and permissions retained (Appendix).

The production of second-generation fuels from biomass is entering a new stage focused on large projects and industrial initiatives. However, the uncertain scenario in terms of climate change commitment and burden share, fossil fuel price, and renewable legislation limits does not provide the best environment for a large-scale spread of new technologies. Furthermore, this innovation still requires a real breakthrough in order to lead to a clearly enhanced efficiency and sustainability. There are different approaches to drive the conversion of biomass bulk or its fraction into fuel:

- Fermentation process to bioethanol and biomethane,
- Production of oxygenated liquid compounds by several treatments (pyrolysis, liquefaction, triglyceride extraction) followed by hydrotreating to upgrade the bio-oil produced
- Gasification or aqueous phase reforming processes, which produces syngas and hydrocarbons or alcohols.

Gasification uses an oxidizing agent (air, steam, oxygen, or a combination of these) for the high-temperature transformation of a carbonaceous feedstock into a gaseous energy carrier consisting of permanent, non-condensable gases, mainly syngas. Subsequently, in a separate stage, the syngas obtained is transformed by Fischer-Tropsch reaction into

diesel or other syngas fuel such as methanol dimethyl ether or C_{2+} alcohols. In parallel, pyrolysis treatment works at high temperature in oxygen defect to obtain a higher quantity of oxygenated hydrocarbons in a liquid fraction that necessitates further upgrading for its use as fuel. On the other hand, the Aqueous Phase Reforming (APR) reaction is an alternative pathway to gasification for the transformation of biomass and its main components (sugars, polyols, and even proteins) into several products such as hydrogen, hydrocarbon, and oxygenated molecules, with the main products depending on the reaction conditions, process configuration, and catalysts.

1.1 Thermal processes

1.1.1 Gasification

Gasification technology was first known three centuries ago, when hot gases from coal and coke furnaces were used in boilers[1]. There are several examples of the gasification of biomass for the production of fuel at low pressure, and some of them even work at moderate pressure, while there is no experience in high-pressure systems using biomass in a full-chain Biomass-to-Liquid (BTL) process. Therefore, coal gasification is well established, while biomass gasification is still being developed: these two technologies, however, cannot be compared due to feedstock differences (e.g. char reactivity, composition, ash composition, moisture content, density and energy content).

The thermodynamics of biomass gasification leads to the formation of CO, CO_2, H_2, and H_2O in the gas phase, and their specific composition depends on the amount of oxygen, which also determines the overall autothermal temperature in the process. When using an equivalent ratio of 0.275, the equilibrium leads to:

$$CH_{1.4}O_{0.59} + 0.29O_2 \rightarrow 0.63H_2 + 0.07H_2O + 0.9CO + 0.10CO \qquad (Eq.1)$$

The first stage of gasification is pyrolysis of the biomass leading to a vapor, a solid, and a gas phase. The solid and vapor are then gasified by using steam and oxygen (Figure 1).
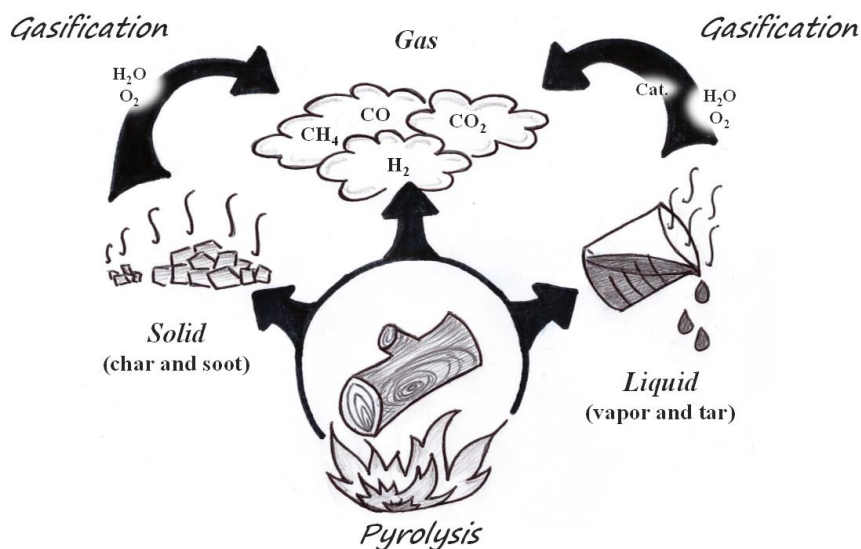
Figure 1: Representation of the biomass transformation during the gasification process.

Various gasifiers have been designed, but only those with direct and indirect (or double) fluidized bed and entrained flow configurations are being considered in applications that generate over $10MW_{th}$[2,3]. Fluid bed gasifiers are produced by a number of manufacturers in the range from 1 to $150MW_{th}$ for operations at atmospheric or high pressures, using air or oxygen as gasifying agent. This process produces a gas phase that contains several contaminants such as H_2S, NH_3 particulate, tars, alkali metals, fuel-bound nitrogen compounds, and an ash residue containing char. The gas composition and contamination level varies with the feedstock, reactor type, and operating parameters.

The main advantage of the gasification process is the transformation of the biomass as such, or after drying and mechanical pretreatments, into a gas mixture having cold gas efficiency (CGE), i.e. the higher heating value share of the biomass input that is contained in the cold gas, up to 80% (Figure 2). The energy of the process is stored in the chemical bond –i.e. H_2, CO, CH_4, light hydrocarbon, and tars– so the main disadvantage is the partial loss of the energy in the form of heat due to side reactions forming total oxidation species. What is more, the biomass gasification, if compared with other sources of fossil fuels (coke, heavy vacuum distillation residues, etc.), reaches the maximum level of higher heating value in the gas phase with an equivalent ratio with respect to the stoichiometry of total combustion of 0.25-0.33. This is due to

the presence of oxygen in the biomass feedstock, which leads to an autothermal temperature below 950°C in oxygen/steam gasification[4,5]. At this temperature the process is far from the equilibrium. Some reactions, such as water-gas shift, are considered closer to the equilibrium, while reactions such as hydrocarbon reforming and cracking or char gasification are far from the equilibrium, while methane light hydrocarbons and tars are still present. Moreover, the amount of tars present is rich in energy and needs to be subsequently transformed into syngas to obtain a high fuel yield[6].
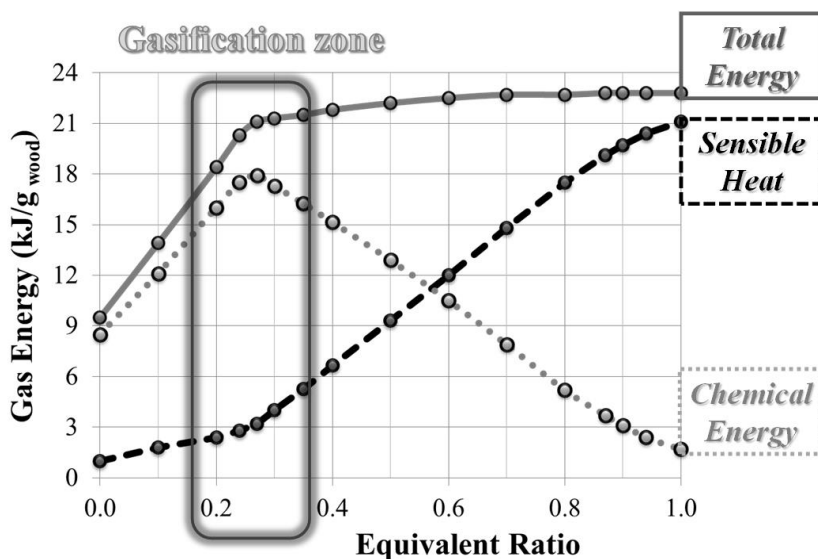
Figure 2: Total energy share of the gas products between sensible heat and chemical energy as function of the oxygen addition (Equivalent Ratio). Adapted from.[7]

From a scientific standpoint, the gasification process toward syngas can be run in oxygen/steam at about 850-950°C. The gas is then cleaned at low-to-medium temperature using a metallic candle filter at 400°C and desulfurized using ZnO, and then either upgraded by reforming methane, light hydrocarbons, and tars or separated for fuel production. Nevertheless, if the reforming is carried out after cooling, the process is not efficient in terms of energy required since, after cooling, it is necessary to raise the temperature up to 900°C and higher for the reforming process. Furthermore, it is not economically efficient, because the oxygen production plant either increases the cost or requires a larger plant size, with a consequent larger biomass land extension necessary to feed the plant.

Primary catalysts can be added directly to the biomass by dry mixing with the bed material or additives. These catalysts operate under the same conditions as the gasifier and are usually made of cheap material. The main purpose is to reduce tar content, but the method has little effect on the conversion of methane and C_{2-3} hydrocarbons into the product gas. Dolomite, with the general formula $MgCO_3 \cdot CaCO_3$, is a catalyst active in tar reduction inside a fluidized bed biomass gasification. An alternative material is olivine, a mineral containing magnesium iron silicate. Ni-based catalysts are very effective not only for hydrocarbon reforming, but also for decreasing the amount of nitrogenous compounds such as ammonia. In addition to dolomite and olivine, MgO has also been used in several gasifiers as bed material with enhanced properties. Another attempt in increasing tar cracking inside the reactor deals with the possibility of recycling the ashes produced after gasification, in the field of additives and fertilizers for biomass crops. Since the bed material cannot be separated from biomass residue after gasification, the elements present as tar cracking catalysts are limited to the harmless ones. Therefore, Fe and Cu-based materials, together with natural alkali oxides and salts, seem to be the best candidates for producing an active bed material, even though tar cracking and reforming activities must be improved[8].

1.1.2 Gas upgrading

The exit gas from the gasifier containing methane and light hydrocarbons must be upgraded to a clean syngas in order to produce fuels or other products. Today, the predominant commercial technology for syngas generation is Steam Reforming (SR), in which hydrocarbons and steam are catalytically converted into hydrogen and carbon monoxide in an endothermic reaction[9]. An alternative approach is partial oxidation (PO), the exothermic, non-catalytic reaction of hydrocarbon and oxygen to produce syngas mixtures, which have appreciably different compositions. In particular, SR produces a syngas having a much higher H_2/CO ratio. This, of course, represents a distinct advantage for SR in hydrogen production applications. Nevertheless, high-temperature SR is difficult to implement since it requires a source of external heat obtained by burning gaseous or liquid fuels, and this either decreases the overall efficiency or increases CO_2 emissions (if a fossil fuel is used). Autothermal reforming

(ATR) co-feeds oxygen and steam, and the oxidation reaction occurs in the burner at the entrance of the reactor and produces the heat required for the reforming, which takes place downstream in the same reactor.

$$CH_4 + H_2O \leftrightarrows CO + 3H_2 \qquad \Delta H^0{}_{298} = + 206 \text{ kJ/mol} \qquad \text{(Eq.2)}$$

$$CH_4 + 1/2O_2 \leftrightarrows CO + 2H_2 \qquad \Delta H^0{}_{298} = - 36 \text{ kJ/mol} \qquad \text{(Eq.3)}$$

The steam reforming reaction (Equation 2) is applied for the conversion of natural gas or light hydrocarbons into synthesis gas. Generally the gas undergoes desulfurization to avoid the poisoning of commonly used supported nickel catalysts in commercial plants[10,11], then it is heated through tubular reactors and the outlet products are rapidly cooled and can be sent to water-gas shift processes and separation/purification. The process requires considerable quantities of vapour to reduce the formation of carbonaceous residues; to enhance H_2/CO ratio vapour is also necessary for increasing the H_2 content. Catalytic partial oxidation process (Equation 3) works at higher temperature (1000-1050°C) compared to the steam reforming process and the outcome contains not only syngas but also combustion products as CO_2 and H_2O. For this reason the O_2/CH_4 ratio used in industrial plants is 0.7, instead of the stoichiometry 0.5[12]. By means of short contact time, CPO is capable of transforming hydrocarbon fractions, which cannot be used by the other cited catalytic technologies into synthesis gas but with high-energy consumptions and investment costs. Finally, autothermal reforming is a combination of partial oxidation and steam reforming (Equations 2 and 3) developed by Haldor Topsoe in the late 1950s. Typically, the process operates at high temperatures of about 1900°C resulting in a lower oxygen consumption with the addition of steam to eliminate carbon formation[13].

Industrial catalysts for those processes contain 15–25% wt. nickel oxide on a mineral carrier (α-Al_2O_3, alumina-silicates, calcium-aluminate, magnesia). Before starting the process, nickel oxide must be reduced to metallic nickel. This is preferably done with hydrogen, but is also possible with natural gas or even with the feed gas itself at a high temperature (above 600°C, depending on the reducing stream). The required properties of catalyst carriers are relatively high specific surface area, low-pressure drop, and high mechanical resistance at temperatures up to 1000°C.

Although the processes for the production of H_2 and/or syngas are well established[14], their feasibility applied to a gasification-generated gas depends on the activity and stability of the catalysts. The main problems of the reforming process are the deactivation and, especially, sulfur poisoning and coke formation, while some long-term effects of the alkali, passing through the hot gas filter, cannot be ruled out, especially on Ni sintering[15].

1.1.1 Pyrolysis

Pyrolysis is a thermal process in which the biomass is converted in absence of air into gas, liquid and solid fractions[16]. The solid and gas (mainly H_2, CO, CO_2, CH_4 and light hydrocarbons) fractions are smaller than gasification process and can be treated as previously reported. The liquid fraction, named bio-oil or pyro-oil, is composed by over 300 species of oxygenated hydrocarbons and water, thus it possess a low heating value, high viscosity and acidity together with chemical instability. Thus, while gas fraction is ready to be burned, the liquid one necessitates further upgrading to remove water and decrease oxygen content for fuel applications or chemical upgrading. The ratio within gas and liquid phases can be tuned by acting on temperature, heating rate, residence time and type of catalyst in the pyrolysis process. The increase in temperature, heating rate and residence time can, for example, give a higher gas yield[17]. For this reason, the process can be subdivided into slow, moderate and fast pyrolysis. Fast process necessitates rapid heating and short residence time to obtain the maximum yield of liquid products; slow one, called also conventional process, has as an output char and gas. Intermediate processes is also called moderate pyrolysis[18]. Fast pyrolysis is thus the most used process for biomass transformation not only for its yield in bio-oil (up to 70%) but also because it is a stable and low cost investment and can be applied to various biomass species (i.e. rice husk, mischantus, pinewood, cellulose and lignin). The economic feasibility of the process is also enhanced by the possibility of using solid bio-char in agriculture and bio-gas producers as fuel, or alternative heating technologies as microwave biomass heating[19]. Moreover, the process can be upgraded by additional steps as catalytic pyrolysis and co-pyrolysis with other polymers or additives[20]. The combination of the thermal process with a catalyst, also in this case,

gives the opportunity of tuning the reaction towards desired products and reduces the char formation. Besides it allows the reduction of working temperature lower than 750°C and it does not necessitates the use of a separate reactor. Nickel-containing catalysts are the most frequently used, usually incorporated onto supports with high thermal and mechanical stability for its use in fluidized bed reactors[21]. As gasification processes, olivine and dolomite supports are widely used.

On the other hand, the upgrading of bio-oil to transportation fuel is still a competitive task for the presence of oxygenated compounds as acids, alcohols, esters, ketones, sugars, phenols and derivatives from lignin degradation. The most applied upgrading methods can be divided into physical and chemical. Within the first family filtration with hot gas and emulsification can be accounted; while solvent addition, steam reforming, catalytic upgrade and hydrogen processing are chemical ones. Hydrogen processing, often subdivided into HDO, HDN and HDS processes, is the most effective method to remove heteroatoms (respectively oxygen, nitrogen and sulphur) with a hydrogenation reaction and the production of water, ammonia and sulphuric acid as by-products. Those methods can also be coupled to catalytic pyrolysis process itself[20].

1.2   *Chemical treatments*

Lignocellulosic raw materials are composed of hemicelluloses, cellulose and lignin (Figure 3): the first is a branched and amorphous heteropolymer constituted of C_5-C_6 sugars and uronic acids (C_5: xylose and arabinose, C_6: glucose, mannose, galactose, rhamnose, and fructose) easily de-polymerizable by dilute acid and bases or by enzymatic treatment. Its fraction is around 15-30% of total biomass weight and the total composition depends on the biomass type. Cellulose instead is a highly crystalline linear omopolymer constituted by D-glucose units linked by β(1-4) glycosydic bonds. It composes around 40-50% of biomass and can be deconstructed into glucose units by mineral acid treatment at high temperature, usually combining mechanical pre-treatment to favour chain rupture. Finally, lignin is the hardest part of biomass, making up 15-30%wt. as the constituent of cell walls and vascular systems. It is a branched amorphous polymer of cross-linked phenols with a composition varied depending on

the biomass type, and can be deconstructed only in hard conditions. Its building blocks are p-coumaryl, conyferyl and synapsyl alcohols[22]. Finally, other minor constituent of biomass structure are starch, as the energy storage of plants composed by $\alpha(1\text{-}4)$ glycosydic bonds and subdivided in linear amylase and branched amylopectin, mineral salts and water.
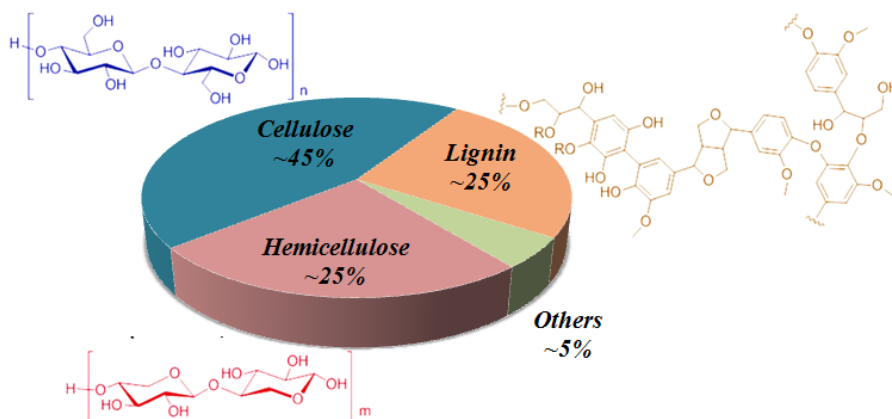
Figure 3: Composition of woody biomass. Adapted from[23].

Beside thermal treatments over whole biomass, a wide range of chemical treatments are possible on its constituents. The advantage of those latter is the higher efficiency; nevertheless, they require a complex step of separation of fractions and their depolymerisation into monosaccharides. Hemicellulose fraction is the easiest to be transformed into monomers[24], but for its homogeneous structure, cellulose is the most studied polymer[25,26]. Lignin instead has been recently studied because it contains the highest energy fraction of total biomass (around 40%)[22] and allows the obtainment of particular monomers, but it is the hardest to treat and to separate via chemical, thermal or microbiological processes[27].

The totality of possible biomass transformations can build up the biorefinery concept. In analogy with the petroleum refinery, it is defined as a facility that integrates biomass conversion processes and equipment to produce fuels, power, heat, and value-added chemicals valorising each fraction. Unlike the traditional refinery, the biorefinery presents several complications. At the beginning there is the need of turning a solid raw material into a processable liquid, i.e biocrude oil, by pyrolysis or hydrothermal

treatments. These liquids are, as explained in the previous chapter, a mixture of deconstructed biomass fractions with low heating value and expensive in term of separation into single monomers. Beside the complexity, it is not second that hemicellulose, cellulose and lignin fractions can vary significantly from feed to feed. More selective methods for the deconstruction of biomass are being developed. The mainly applied is solvothermal method, i.e. the treatment of biomass with solvents at elevated temperatures, aimed at the separation of carbohydrate fraction (cellulose and hemicellulose) from lignin. The treatment is similar to the pulping process in paper industry and is adaptable to various feed. Solvothermal process can be applied in water or organic media (called organosolve) and combined with catalyst or derivatization reagents, to obtain partially depolymerized chains easily separable. The use of catalyst allows to reduce the working temperature and to increase the selectivity of the process[28]. Other degradative methods can be enzymatic treatment or the coupling of the fraction separation with the hydrolysis reaction. By selecting the appropriate conditions it is thus possible to obtain directly monomers from the starting material[23]. Typically a pretreatment step removes hemicellulose and some lignin from the biomass. The separated hemicellulose and cellulose streams can then be upgraded to platform chemicals (as presented in Figure 4) by liquid phase catalyzed reactions to a variety of products. Lignin instead can be burned or upgraded to aromatic compounds or solvents[22]. The upgrade of hemicellulose and in particular cellulose streams, however, requires further treatments to improve its solubility, and in particular, its contact with heterogeneous catalyst. The most used pre-treatments are ball milling, steam explosion, chemical pretreatment (with ammonia, soda, etc.), and enzymatic degradation, not last the use of mineral acids, ionic liquids and supercritical water pretreatments. Some of those processes are expensive in terms of recovery of enzymes or reagents (in case of ionic liquids); others deal with problems of waste disposal (i.e. mineral acids and ionic liquids) or energy consumption (as ball milling, steam explosion and supercritical water working conditions). For these reasons, the most interesting studies in terms of eco-compatibility and energy savings are one-pot catalytic treatments in water to polyols. Nevertheless, the process presents still several problems in terms of mass transfer, number of reactions involved and clarification of the mechanism[29]. The main possible

processes are aqueous reforming (APR) for the cleavage of C-C bonds and the production of H_2, hydrogenolysis both to reduce heteroatoms content and chain length, hydrogenation of multiple bonds, oxidation and further hydrolysis. Useful catalysts are a combination of metals for hydrogenation/hydrogenolysis or oxidation processes (as Ru, Pd, Pt, Ni, Cu or Au) and acid support for hydrolysis (Al_2O_3, active carbon, mordenite, amberlyst, H-ZSM)[28]. Also bimetallic supported catalysts have been widely adopted because they can interact via geometric and electronic effects to improve stability and activity, but more interesting are synergistic and bi-functional metal couples that can create new reaction pathways[22].
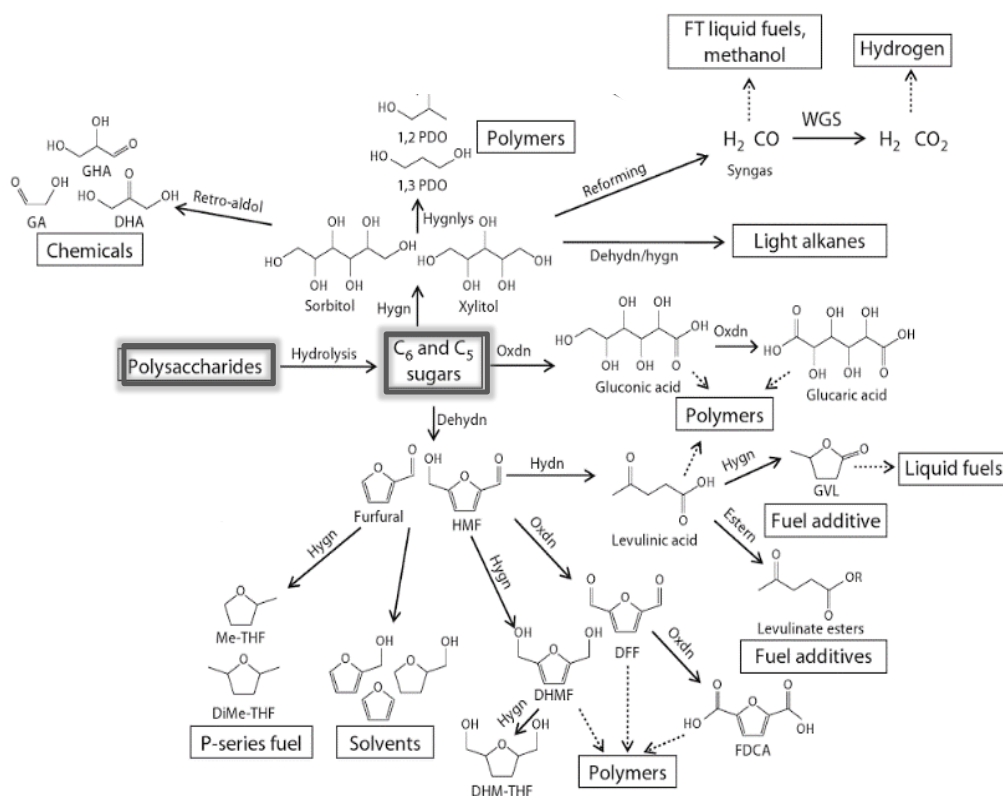
Figure 4: Complexity of chemical transformation in a biorefinery. Process involved hydrogenation (hygn), oxidation (oxdn), hydrogenolysis (hygnlys), esterification (estern), and dehydration (dehydn). Products: glycolaldehyde (GA), glyceraldehyde (GHA), dihydroxyacetone (DHA), 1,2-propanediol (PDO), hydroxymethylfurfural (HMF), diformilfuran (DFF), 2,5-furan dicarboxylic acid (FDCA), dihydroxymethylfuran (DHMF), dihydroxymethyltetrahydrofuran (DHM-THF), methyltetrahydrofuran (Me-THF), γ-valerolactone (GVL). Adapted from[30].

The most important building blocks obtainable from cellulose and hemicellulose are presented in Figure 5. One of the most used is lactic acid, it finds its application in the food, pharmaceutical and cosmetic industries, but can be used as intermediate to pyruvic acid, 1,2-propanediol and esters. One of the main industrial application is its use in polymer science for the production of polylactic acid (PLA). It can be obtained by fermentation from glucose or by triose reactions in presence of base and catalyst. Levulinic acid instead is obtained by acid catalyzed hydrothermal hydrolysis of cellulose together with stoichiometric amounts of formic acid and insoluble carbon deposits called humins. It is a starting material for the synthesis of other platform molecules as ethers, pyrrolydones, diols, cyclic lactones and overall γ-valerolactone as green solvent and fuel additive. 2,5-hydroxymethylfurfural (HMF) is produced, as levulinic acid during the hydrolysis treatment, but it requires milder conditions for its tendency to undergo irreversible formation of insoluble humins. It can be obtained via dehydration of glucose and fructose, the latter by an easier mechanism[31]. Furthermore, the catalysis/hydrolysis combination with organic solvents or ionic liquids can improve HMF yield. This building block can be transformed to reduction and oxidation reactions[32]. The most studied product is 2,5-furandicarboxylic acid (FDCA) as potential substitute of terephtalic acid in the production of PET and other polymers. Also 2,5-dihydroxymethylfuran (DHMF), as reduction product, is used in the preparation of polyesters.

Polyols as sorbitol, mannitol, xylitol, ethylene and propylene glycol are also important chemicals. The first two derive from hydrogenation of glucose, while xylitol comes from xylose. On the other hand, glycols are currently petroleum derived. Polyols find application in food and pharmaceutical industry but above all in the polymer sector. Within the biorefinery improvement, the valorization of polyols have obtained increasing interest, even if the production costs are not competitive with traditional petroleum-derived glycols[29]. Within polyols family, even if it does not derive in significant amount from C_6 sugars, glycerol has an important role as abundant byproduct of biodiesel industry. Currently its application in traditional chemistry or in mechanical and food industry is not enough to cover the excess of production by trans-esterification of fatty acids. This leaded to a cost drop that favored the coming out of

studies for glycerol transformation into building blocks or other molecules. Possible reactions are hydrogenolysis towards ethylene glycol, 1,2 and 1,3-propanediol, oxidation to glycolic and glyceric acid and aqueous phase reforming to hydrogen and CO_2.
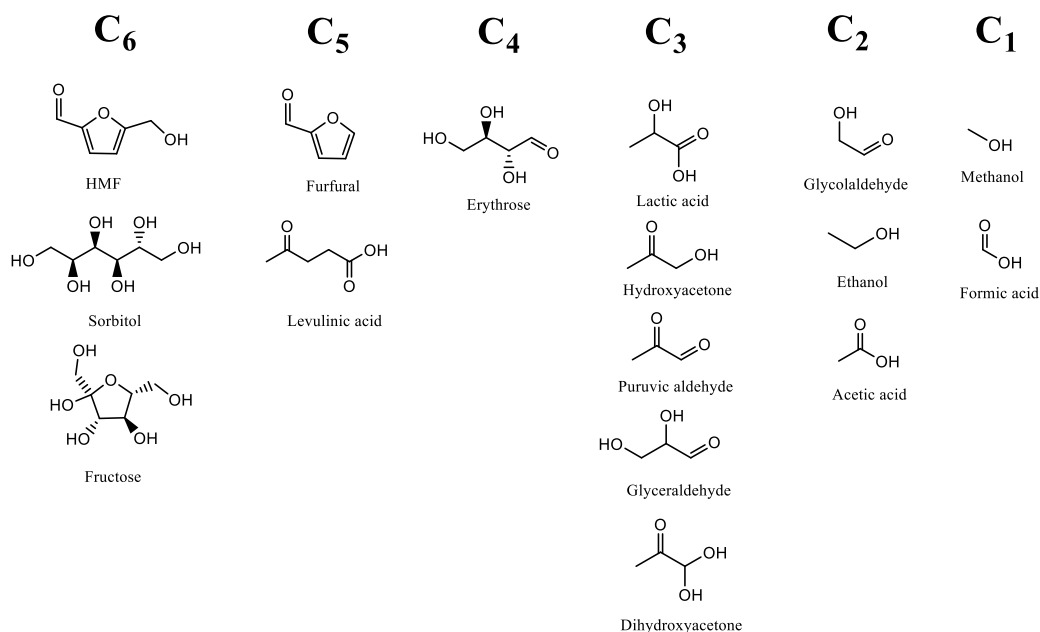
Figure 5: Main products and building blocks derived from cellulose transformation. Adapted from[28].

1.3   Aqueous Phase Reforming

Aqueous phase reforming has recently become of great interest in the production of green fuels and valuable bio-platform molecules, because it offers several advantages over other biomass transformation processes. In fact, sugars and polyols can react with water in the gas phase to generate reforming products, but significant energy is required for the vaporization of the feed and high temperature is required to obtain the complete conversion of the hydrocarbons formed during polyols decomposition. Thus, one of the main advantages of the APR process in the production of hydrogen and fuels is that the energy requirement is low, because the vaporization of the reaction feed is avoided, while the second advantage is related to the lower temperature, which minimizes

undesirable reactions such as thermal degradation and the formation of coke precursors. Moreover, the use of a water solution enhances the safety of the process and increases the economy thanks to the possibility to use hydrolyzed or wet biomass-derived products.

Further specific advantages are related to each configuration and the desired products; the process producing hydrogen leads to a mixture containing low amounts of CO, due to the possibility of coupling with Water Gas Shift (WGS) reaction in a single batch. Hydrogen is produced in a pressurized vessel reaching a partial pressure above 5atm and can be handled and purified with dense or porous membrane technologies. Furthermore, the overall reaction occurs in a single step, compared to the multistep reforming and WGS processes[33]. By acting on the reaction conditions and the type of catalyst, the process can be driven toward gas phase products for the production of fuel or liquid phase molecules such as acids, alcohols, glycols, and aldehydes for the polymer industry, cosmetics, and chemistry building blocks.

1.3.1 *Thermodynamic and kinetic considerations*

Equation 4 shows the generic steam reforming reaction for alkanes, while Equation 5 represents the APR and steam reforming process for carbohydrates with C:O=1. Moreover, during the reforming process, hydrogen yield can also be increased by WGS reaction, as indicated in Equation 6. This latter process is favored especially in APR conditions at low temperature and pressure. Figure 6 reports the $\Delta G°$ values for the steam reforming of low molecular weight alkanes (methane, ethane, propane and hexane) and examples of C_1-C_6 carbohydrates (methanol, ethylene glycol, glycerol and sorbitol), together with WGS reaction. As indicated, the reforming of alkanes becomes thermodynamically favorable only over 700K, in particular over 900K for methane, whereas for the reforming of carbohydrates the reaction is possible at considerably lower temperatures. Furthermore, the WGS reaction has no important role during the steam reforming of alkanes, due to the high reaction temperature, but it increases hydrogen production significantly in low-temperature reaction processes[33]. In the case of carbohydrates reforming temperatures, the reagent has low vapor pressure, especially for sugars. Thus, unlike in the steam reforming of alkanes, the reaction takes place in

the liquid phase and be carried out using water as solvent. As shown in Figure 6, the reforming reaction of sugars and polyols is thermodynamically feasible, but it is likely that the production of CO and H_2 is also the result of intermediate liquid phase dehydrogenation and decarbonylation reactions. Independently from the kinetic pathway followed, the overall reaction remains less energy-demanding than steam reforming for the production of hydrogen in a single reactor[33].

$$C_nH_{2n+2} + nH_2O \leftrightarrows nCO + (2n+1)H_2 \qquad \text{(Eq.4)}$$

$$C_nH_{2y}O_n \leftrightarrows nCO + yH_2 \qquad \text{(Eq.5)}[33]$$

$$H_2O + CO \leftrightarrows H_2 + CO_2 \qquad \Delta H^0{}_{298} = -41.2 \text{kJ/mol} \quad \text{(Eq.6)}$$

$$3H_2 + CO \leftrightarrows CH_4 + H_2O \qquad \Delta H^0{}_{298} = -206.1 \text{kJ/mol} \quad \text{(Eq.7)}$$

$$4H_2 + CO_2 \leftrightarrows CH_4 + 2H_2O \qquad \Delta H^0{}_{298} = -165.0 \text{kJ/mol} \quad \text{(Eq.8)}$$

$$nCO + (2n+1)H_2 \leftrightarrows C_nH_{2n+2} + nH_2O \qquad \text{(Eq.9)}$$

$$nCO + 2nH_2 \leftrightarrows C_nH_{2n} + nH_2O \qquad \text{(Eq.10)}[34]$$
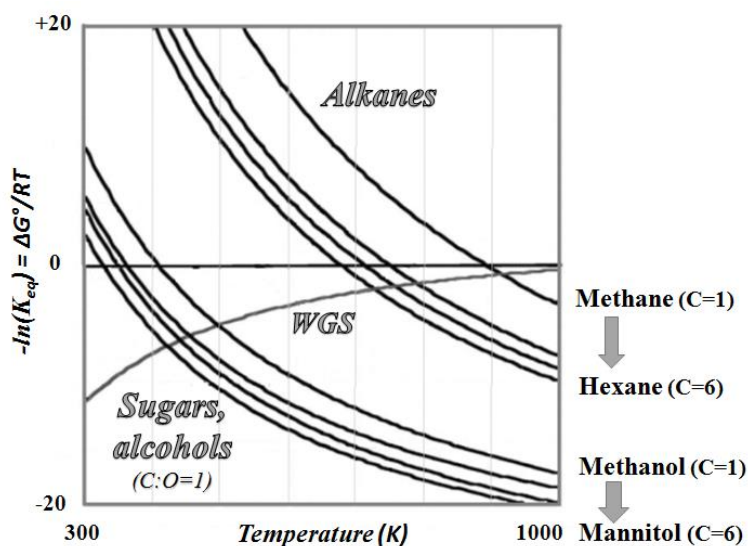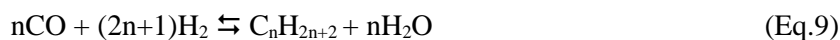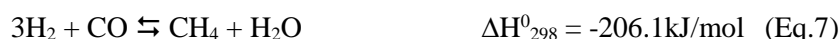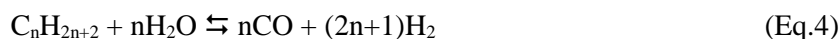
Figure 6: Gibbs free energy change with temperature for reforming reactions of alkanes and carbohydrates and WGS. Adapted from[33].

As for the equilibrium constants of side reactions, calculated by Van't Hoff equation in Figure 7, all the exothermic reactions are suppressed, showing that the conversion of CO at low temperatures is nearly complete, while the consumption of CO_2 via methanation (Eq.8) is more difficult[34]. In the range of temperatures considered for the APR process, the formation of alkanes via methanation and even the Fischer-Tropsch

reaction (Equations 9-10) are thus energetically more advantageous than reforming[33]. This means that the C-O bond breaking, followed by hydrogenation, is preferable to the C-C cleavage and Water Gas Shift. For this reason, to enhance the reforming reaction and the production of hydrogen, an appropriate catalyst can be used. Moreover, the catalyst serves to promote the WGS reaction to remove CO from the metal surface and avoid parallel reactions on to oxygenated molecules in water (Figure 8)[35,36].
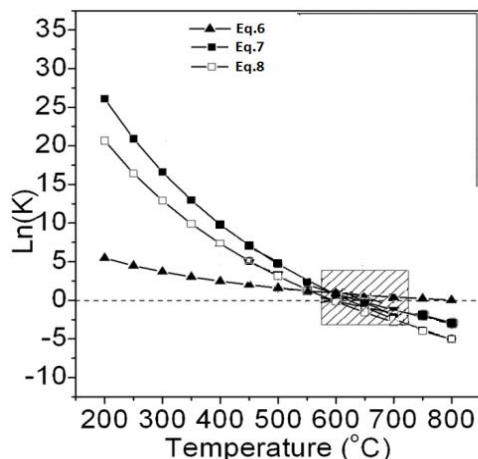
Figure 7: Equilibrium constants (K) of the first side possible reactions occurring in APR as a function of temperature. K is calculated by the Van't Hoff equation. Adapted from[34].
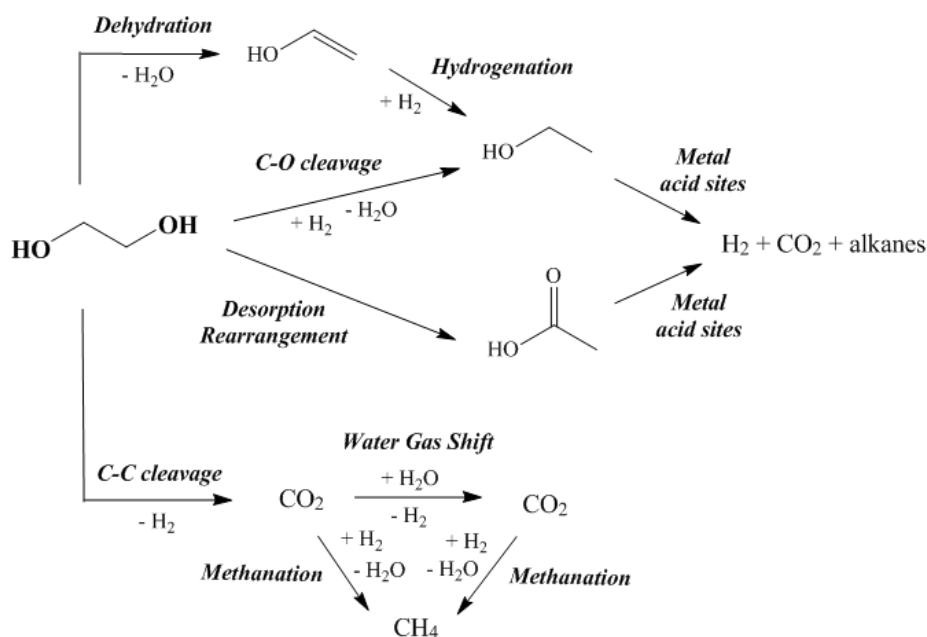
Figure 8: Parallel reactions in water for ethylene glycol. Adapted from[35,36].

1.3.2 Catalysts for APR reaction

Several metal-supported catalysts have been studied for the APR reaction, because the synergic effect between metal and acid/basic features of the support may promote different reactions. An analysis of the active phases to be used in the APR reaction may be conducted by comparing their activity toward C-C cleavage, WGS, and the production of alkanes. Primarily, the study of the hydrogenolysis reaction (C-C cleavage) has been evaluated on ethane using different metals[37]. The report scale of activity gives some indications on APR, even though the scale cannot be directly extended to the C-C cleavage of poly-alcohols:

$$Ru \approx Ni > Ir \approx Rh > Fe \approx Co > Pt \approx Pd > Cu$$

In addition, the metal should be active not only for C-C cleavage but also for WGS reaction, in order to allow the removal of CO adsorbed on the metal. In this regard, Grenoble et al.[38] reported the activity scale of metals over alumina support, which, nevertheless is depending on the oxidation state of the metal:

$$Cu > Co \approx Ru > Ni > Pt > Fe \approx Pd > Rh$$
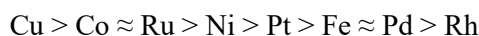
Lastly, the selected metal must not present high activity toward undesirable reactions such as methanation and Fischer-Tropsch, especially when hydrogen is the desired product of the reaction. A work by Vannice et al.[39] indicates the rate of methanation by different metals supported on silica:

$$Co \approx Fe > Ru > Ni > Rh > Ir \approx Pt > Pd$$
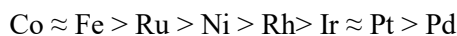
Thus, the most desired metals are the ones having the lowest methanation activity (i.e. Pt and Pd) but a good activity toward C-C cleavage and WGS reaction. Based on the same consideration, other interesting metal is Ni and due to its lower price, and its use in combination to Pt as bimetallic catalyst.

Several supports have also been tested for this type of reaction. Menezes et al.[40] reported an analysis on the basicity of the support at the same Pt loading. Within the oxides studied, MgO and ZrO_2 show the highest hydrogen production and low alkane yield (CH_4) due to the higher electron-donating nature of the metal and the basicity of the MgO support probably involved in the reaction mechanism. As reported by

Dumesic[41], the highest H_2 production rate from ethylene glycol was reached at 498K for Pt supported on TiO_2 and Pt black, followed by carbon, Al_2O_3, ZrO, and SiO_2-Al_2O_3. On the other hand, the production of alkanes and alkane precursors (acetaldehyde, ethanol, and acetic acid) is significant for Pt black and Pt supported on carbon, so these supports are not suitable for APR reaction if hydrogen is always the selected reaction product. Thus Pt/Al_2O_3 and, to a lesser extent, Pt/TiO_2 and Pt/ZrO are the most selective catalysts for this kind of reaction. Interesting results, comparable to Pt/Al_2O_3 catalyst, have also been reached with a Sn-modified Ni Raney catalyst at high Ni loading[42]. This low-cost catalyst has a good activity in the C-C cleavage of small polyols, while inhibiting the methanation reaction and producing higher yields compared to a not promoted Ni catalyst. The catalyst analysis demonstrate the sensitiveness of the reaction with respect to metal support and bimetallic systems, which needs further investigation and development.

1.3.3 Reaction conditions and feed

APR reaction is carried out in batch systems and in fixed-bed reactors. Closed-vessel reactors can be both batch and semi-batch systems, while fixed-bed reactors can be fed in co-current flow and in counter-current flow. The differences highlighted in the apparatus arise from the need to increase selectivity toward gas or liquid phase products. This is because maintaining the H_2 produced in the reaction in a close system can lead to secondary hydrogenation reactions in the liquid phase, thus leading to lower gas yields and a higher number of hydrogenation and hydro-deoxygenation products in the liquid phase. Instead, if a high H_2 yield is desired, there is the need for a sweep gas to permit the H_2 removal from the system, both in semi-batch reactors and in fixed-bed ones. Most of the works experiments in literature have been conducted on fixed-bed reactors because of their higher flexibility in studying reaction conditions.

Generally speaking, the reaction is carried out in a temperature range of 180-260°C because at lower temperatures the reaction is not promoted, while at higher temperatures the decomposition of sugars and polyols is dominating and the catalyst will be quickly poisoned by carbon formation. Pressure conditions are generally set in the 25-60bar range depending on the temperature of reaction, as to remain close to the

equilibrium pressure of water. In some cases, H_2 is added to provide the system with a reducing atmosphere, to drive the reaction toward the formation of alkanes. Batch reactors, conversely, work in autogenous pressure, which is the equilibrium pressure reached by water at a given temperature. The pressure at the end of the reaction is clearly incremented by the partial pressure of the gas generated in the reaction, unless a backpressure regulator is present in the plant.

The reagents used for the APR reaction are mainly sugars and polyols because they must originate from biomass, for the main purpose of the process, but they have also to be soluble in water. The most studied sugar is glucose, but xylitol and sorbitol have also been investigated. As for alcohols, methanol and ethanol are generally tested to analyze the effect of catalysts on primary alcoholic groups; a greater attention, however, is focused on ethylene glycol, propylene glycol, and glycerol. A study on H_2 production and alkane production has been performed by Dumesic[35,36] to compare different feeds in reaction at 225 and 265°C over 3% wt. Pt/Al_2O_3 catalyst (Figure 9). As expected, when increasing the feed complexity, the selectivity toward hydrogen decreases while alkane production increases, due to the presence of competitive reactions in the liquid phase when reagents with a higher functionality are used. Moreover, in the case of glucose, hydrogen yield decreases when increasing the feed concentration because, unlike with other polyols, in this case H_2 yield is not insensitive to the concentration of feed[43]. The sugar and polyol concentration in water is generally in the 1-10% wt. range.
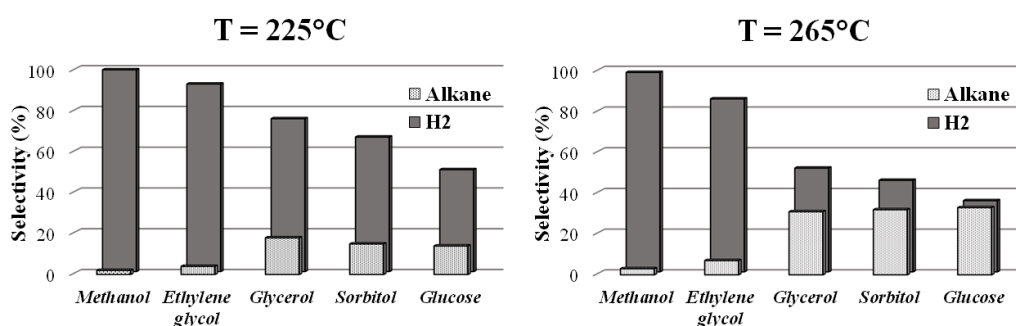

Figure 9: H_2 selectivity and alkane selectivity of diluted oxygenated hydrocarbon solutions (1% wt.) at 225 and 265°C. Adapted from[35,36].

Independently from reactivity issues, glucose and glycerol are certainly the most studied in the APR reaction. The first can be generated by hydrolysis and enzymatic

processes from polysaccharides deriving from second-generation biomass. Glycerol, on the other hand, is the main byproduct of the esterification process for producing biodiesel fuel, leading to a high availability of this feedstock on the market. As for glucose, the possibility of upgrading this molecule toward APR reaction is of high interest. Attempts have also been made to use crude glycerol in APR reactions[44], but the use of non-purified feed plays an important role in reducing hydrogen yields.

1.3.4 Mechanism of reaction

Since APR reaction can be applied to different feeds, the effect of product distribution can be significant. In all cases, gas phase products are H_2, CO (in low amounts), CO_2, methane and light alkanes (C_2-C_3), while liquid phase products may be alcohols, diols, aldehydes, acids and, in general, oxygenated compounds, and their distribution strongly depends on the type of feed used. In the liquid phase are possible, C-C cleavage, C-O cleavage, dehydrogenation, hydrogenation, hydrogenolysis –depending on the catalyst functionalities– and hydration and dehydrogenation, due to the presence of water. Furthermore, the presence of highly reactive compounds such as aldehydes and alcohols may generate tautomeric equilibria, aldol condensation reactions and, in some cases, polymerization and cyclization also.

The complexity of the above-mentioned reactions, therefore, can lead to different mechanisms with changes in the feed, but also to significant changes in selectivity by acting on both the acid/basic sites of the support and the type of active phase. An example is shown in Figure 10, adapted from the reviewing work of Lin et al.[18] on the mechanism of glycerol APR. Solid arrows represent reactions performed with Pt/Al$_2$O$_3$ 1-5%wt. at 225°C with glycerol feed concentration 10-30%wt. in water[45], while dashed arrows indicate the work of another group[46] dealing with Pt-Re/C 3%wt. catalyst at 225°C with a 10%wt. glycerol feed. Bold grey arrows represent the products that are generally accepted from glycerol, and it can be clearly seen how changing the catalyst in the same experimental conditions can affect the product composition. This can be explained by the effect of Re introduction in the active phase in changing the structure of the metal and on the role of the acid site (i.e. alumina).
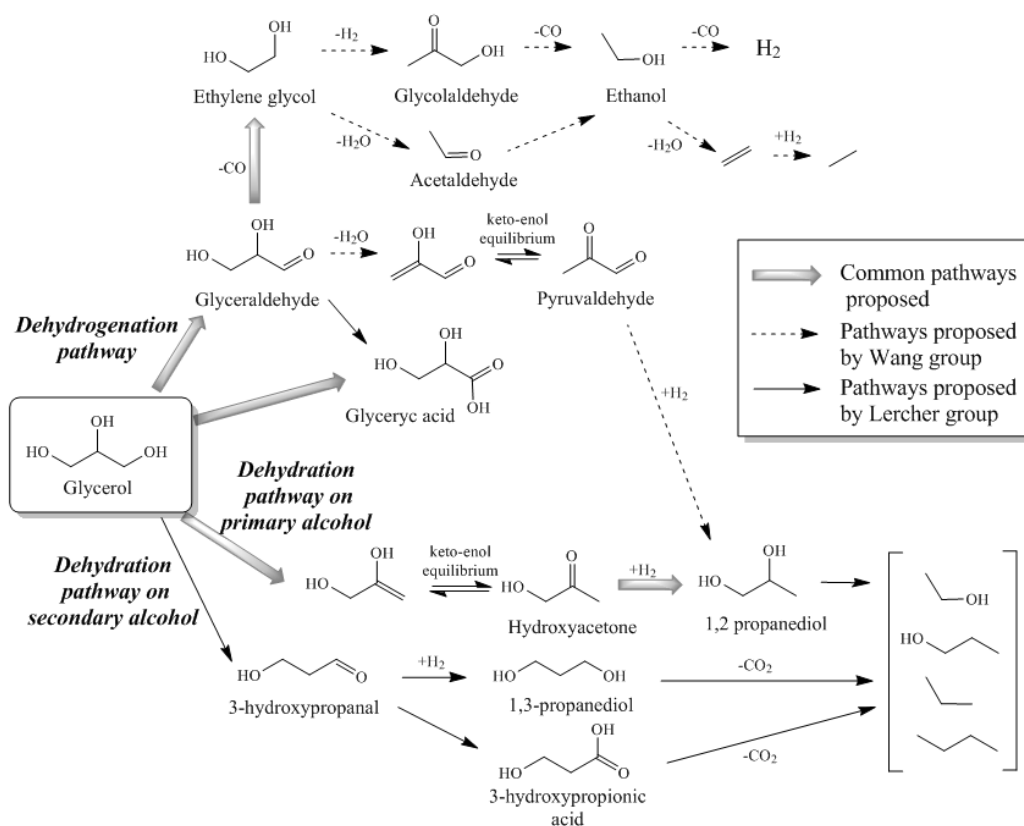
Figure 10: Proposed mechanism for the APR reaction of glycerol. Solid arrows pathways proposed by Lercher and co-workers[45], dashed arrows from Wang and co-workers[46]. Bold grey arrows represent commonly accepted reaction pathways from glycerol. Adapted from[18].

Another example of the mechanism is shown in Figure 11 but, unlike in the previous one, the reaction focuses on the production of alkanes over Pt/HZSM-5 and Ni/HZSM-5 1-4%wt. from xylitol[47]. Reactions were performed under H_2 atmosphere (2-4MPa) to inhibit the dehydrogenation pathway and in the 180-250°C range. Together with hydrogenation reactions on metal sites, C-O cleavage by dehydration on acid sites, and C-C cleavage by decarbonylation on metal sites, C-C coupling reactions on acid sites and isomerization and condensation processes due to the presence of highly functionalized molecules are also present.
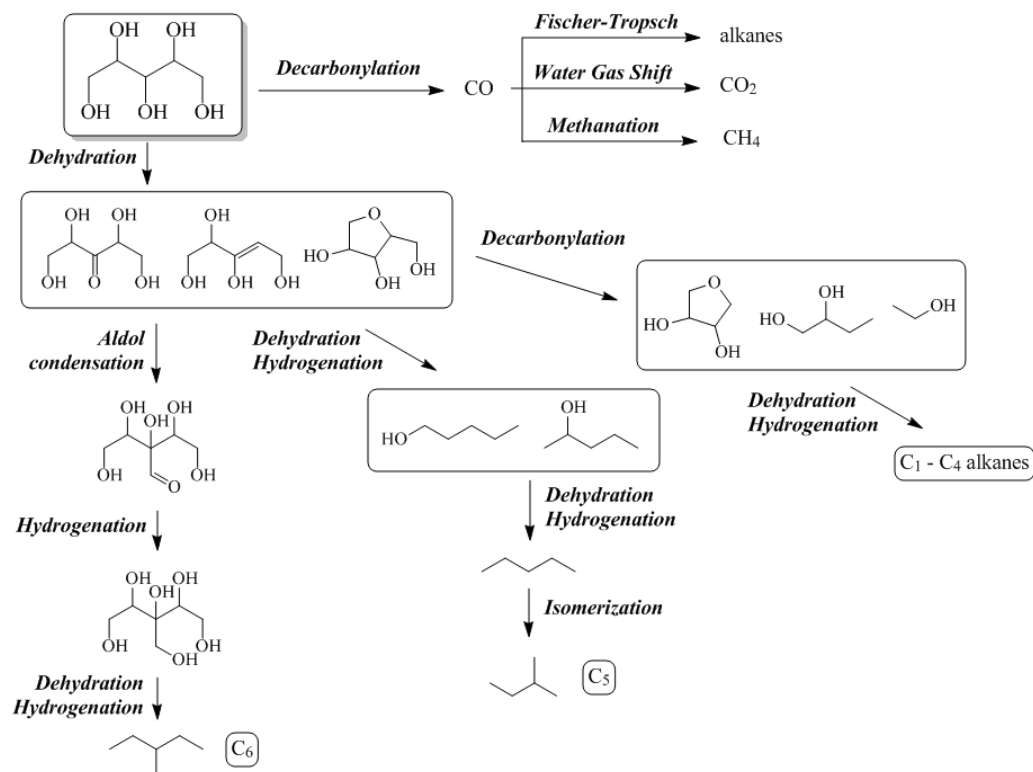
Figure 11: Proposed mechanism for the production of alkanes from xylitol over bifunctional metal-acid catalyst. Adapted from[47].

1.3.5 APR on biomass fractions

In addition to the study on polyols and monomeric sugars, the use of lignocellulosic fractions is also progressing for APR reaction., Erbatur et al.[48] report as study comparing the three fractions obtainable from different biomass (cellulose, hemicellulose, and lignin) after pretreatment in subcritical conditions before APR reaction. The comparison of the some hydrolysate feeds over commercial Pt/C shows that the lignin fraction does not produce hydrogen, but only CO_2 with small amounts of CH_4, while hemicellulose shows 27% H_2 and 10% CH_4 over the total gas produced. Conversely, the cellulose fraction shows the highest quantity of gases produced (48% more than hemicellulose over wheat straw and 28% for kenaf) but the relative percentage for hydrogen over the total gases is lower than with hemicellulose. Further comparison analyses were performed without a catalyst and showed no presence of hydrogen; CO_2 was mainly produced, with only a small amount of CO. In this case, the

differences in reactivity within the fractions of the type of biomass analyzed are explained by the crystallinity degree of the two supports. The hydrolytic pretreatment leads to a lower crystal index compared to the starting material (calculated as a ratio within the XRD crystal peak area and the amorphous one), so the fractions are more sensitive to degradation, producing a higher amount of gaseous products.

The effect of the crystalline fraction over APR reaction was analyzed more in depth by Tian et al. [49] By studying filter paper, degreased cotton, and microcrystalline cellulose, they correlated the decreasing crystalline index of those feeds with the decreasing H_2 selectivity in the same order, while the selectivity value was not correlated to the polymerization degree of the feed. The principal explanation for this behavior can be found in the absence –during APR reaction– of a strong acid catalyst that makes it possible to accelerate the hydrolysis step of the reaction, which is highly dependent on the crystallinity of the feed. Once produced by hydrolysis, the suggested intermediates, i.e. glucose, are then readily transformed into hydrogen over a Pt/C catalyst. To avoid the previous discussed limiting step, Lin et al.[50] proposed a combined hydrothermal-catalytic treatment to improve the hydrolysis step of the biomass by adding a mineral acid to the traditional aqueous phase reforming catalyst. The study reports that the amount of reducing sugar (glucose and other monomers) obtained by this combined treatment is higher than the amount of α-cellulose contained in each cellulosic feed tested, with the simultaneous production of hydrogen in a one-step process. This indicates that substrates such as cotton, sawdust, and pulp can be simultaneously hydrolyzed and reformed with good results as compared to α-cellulose.

In addition to the possibility of producing H_2 by APR of lignocellulosic fraction, one of the main drawbacks in the use of those feeds is the percentage of reagent transformed into gaseous products, compared with the amount of solid residues, i.e. water insoluble organics and char. Erbatur et al.[48] report (Figure 12) the percentage of carbon containing gaseous products (CO_2, CO, C_2H_4, CH_4) compared with the insoluble residue after reaction. As for hemicellulose, the gaseous carbon is dependent on the feed analyzed and may vary between 30 and 50%, but with a higher amount of ungasified products compared to other fractions. As for cellulose, gaseous carbon value is around 45%, while for lignin the carbon that goes to gas products is higher compared

to other fractions, thus indicating that the degradation toward CO_2 of this fraction is higher, while no H_2 is produced. Another study by Weckhuysen et al.[51] analyzed more in depth the lignin fraction, since it is more difficult to treat than other fractions due to solubility problems and sulfur content. They sustained the possibility of solubilizing the feed in APR reaction conditions in order to enhance the obtainment of gaseous products by combining the use of a Pt/Al_2O_3 catalyst with H_2SO_4 to enhance the hydrolysis step. H_2 yields up to 8% were obtained over different feeds with ethylene and methane as byproducts. As for the liquid phase, several aromatic monomers were identified. A more in-depth study was performed on the effect of this type of reaction on different model molecules, such as guaiacol and polyaromatics containing β-O-4 and 5-5' bonds, that are found to be susceptible of disruption, thus generating monomers and free methoxy groups susceptible to hydrolysis and consequently to be reformed into H_2. Unfortunately, re-condensation reactions can always lead to high molecular weight products causing a low gas yield of reaction.
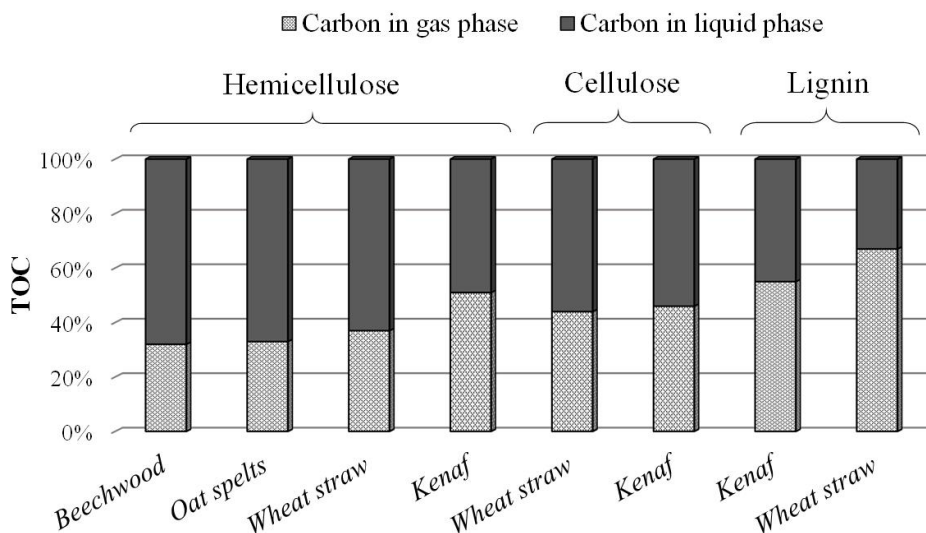
Figure 12: Comparison of TOC percentage of gaseous products and liquid products after APR reaction over different feeds[48].

In conclusion, the use of more complex feeds has not yet been studied in depth, mainly due to the complexity of the reaction mechanism, combined with the low reactivity of

the feed; however, some interesting results have been presented that indicate the possibility of H_2 production by APR reaction.

1.3.6 Pilot plants and patents

The first pilot plant developed for APR reaction belongs to Virent Energy Systems Inc., a partner of the University of Wisconsin, Madison[52]. The project started in 2005 with the aim of optimizing reactor, streams, and efficiency of the reaction to produce a 10kg H_2/day demonstration system within the DOE Hydrogen Program goals. The selected feedstock was glucose, hydrogenated to sorbitol in situ to produce a hydrogen-rich stream purified with pressure swing adsorption, as shown in Figure 13.
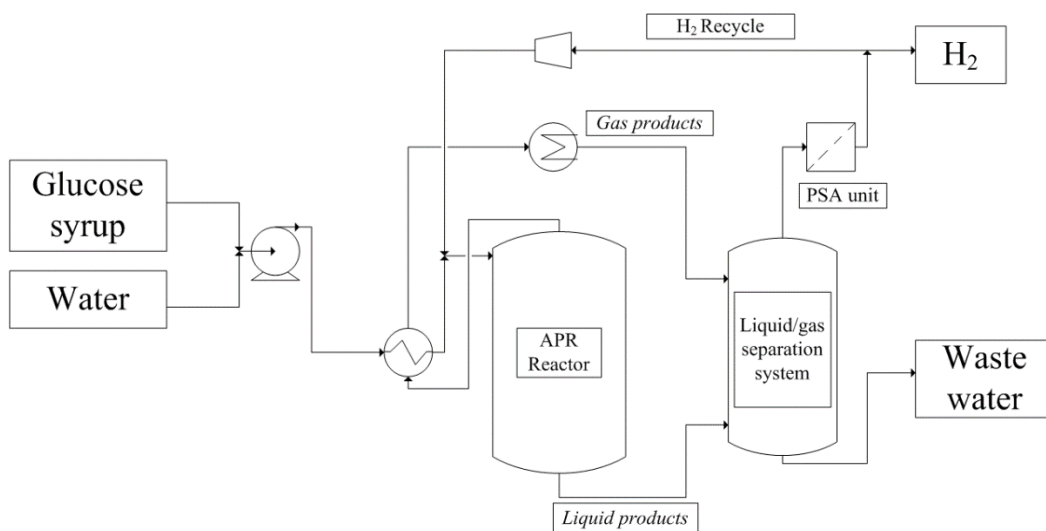
Figure 13: Schematic Virent APR pilot plant, adapted from[53].

In 2009, the catalyst was optimized to maintain hydrogen productivity and targets were achieved. In particular, the economic analysis showed that the sensitivity of hydrogen costs (including the cost of feedstock, processing and storage equipment, utilities, and maintenance) are strongly dependent on the cost of feedstock (Figure 14), followed by other raw material costs, capital costs, operation and maintenance[53]. The APR reaction has subsequently been developed by Virent in the BioForming® process, combining this technology with a modified conventional catalytic process (i.e. petrochemical process). This process can fit a wide range of water soluble C_5 and C_6 sugars, as well as

further products deriving from the degradation of biomass (polysaccharides, organic acids, furfural), and produces a mixture of chemical intermediates including alcohols, ketones, acids, furans, paraffins, and other oxygenated hydrocarbons. This mixture can further react over a ZSM-5 modified catalyst either via a traditional process to produce a high-octane gasoline blendstock named BioFormate™, or via hydrotreating[54].
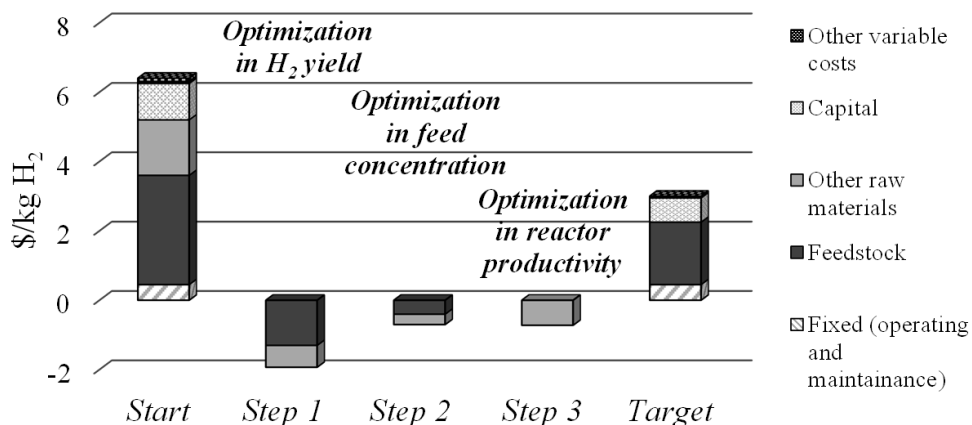
Figure 14: Cost breakdown for the Virent APR process adapted from[53].

Starting in 2005, another demonstration unit was developed by United Technologies Research Center (UTRC)[55] to study biomass slurry hydrolysis and reforming process for hydrogen production from woody biomass. One of the main differences from the Virent process is the use of slurry of ground biomass, directly hydrolyzed in the reactor with base (K_2CO_3) at high but subcritical pressure and the subsequent application of liquid reforming with a Pt or Ni catalyst. The aim is to deconstruct cellulose fibers with a base and separate H_2 continuously. Unfortunately, before the end of the project in 2009, only a fixed-bed Ni Raney demonstration plant had been developed, with a lower feed rate and a minor biomass concentration than the project objectives because of technical challenges.

There are not many patent submissions regarding the Aqueous Phase Reforming reaction, probably because the process is still being developed and so far high hydrogen yields have not been reached. In particular, patent literature can be subdivided between

works concerning the reforming process alone, and more complex projects that treat rough biomass through several steps, which also include an APR unit.

Monnier et al.[56,57] have developed a single liquid phase APR unit for the production of H_2 from oxygenated hydrocarbons (i.e. C_5 and C_6 sugars) in a stirred tank reactor with small metal particles dispersed on a solid support. The reaction is performed at low temperature (255-285°C), but high pressure, in order to maintain the condensed phase in the system. A sweep gas makes it possible to remove H_2 and CO_2 by a membrane separation system. Another single unit process has been patented by Cortright et al.:[58,59] it can be implemented for both liquid and gas phase reforming units, with the use of an alkali and a heterogeneous supported metal catalyst at low temperatures (below 400°C). The same author presented a work[60,61] on the reforming of biomass to produce polyols (i.e. propylene glycol, ethylene glycol) and other oxygenated compounds (ketones, aldehydes, carboxylic acids, and alcohols) with O:C ratio from 0.5:1 to 1.5:1. Differently from what is reported above, the reaction is developed in a two-step process: the first one generating H_2 and oxygenated hydrocarbons through APR, and the second one to react H_2 with oxygenated hydrocarbons. For both these steps, the bimetallic catalyst was supported on porous material and the process can be performed separately or in a single fixed-bed reactor loaded with a double catalytic bed. H_2 selectivity can be enhanced by the addition of an alkali solution to increase the pH to the 4-10 range for the first step and an acid solution for the second step in the 1-4 pH range.

As for the integration of the APR process in a biomass treatment plant, Chheda et al.[62,63] incorporated the reforming step in a more complex system to make it possible to pretreat rough biomass. The first step is a mild temperature treatment in water to induce the solubilization of carbohydrates; after a separation unit, the solid fraction is digested again thanks to a digestive solvent, to obtain a pulp containing cellulose, hemicellulose, and a fraction of soluble lignin. After the removal of nitrogen and sulfur compounds – which are poisonous for APR catalysts– the liquid stream and the pulp are reformed in a liquid phase at 200-280°C on a metal-supported catalyst. Lastly, the APR outflow (mainly made of oxygenated molecules) can be processed to fuel or, in part, re-directed to the plant as digestive solvent. Ma et al.[64] proposed the idea of pre-hydrolyzing the

lignocellulose biomass with water and maleic acid and subsequently treating it at first in a low-temperature reforming unit, and then in a high-temperature reforming unit. The first unit works at 160-210°C and 4-6.5MPa of H_2 with Ni/Al$_2$O$_3$-SiO$_2$ catalyst, the second unit at 210-270°C 2-5.6MPa of H_2 with Ni/HZSM-5. The advantage of the overall process is the production of an outlet stream with characteristics similar to those of bio-gasoline, with a cheap catalyst and the use of H_2 to avoid polymerization and coke formation on the catalyst. Furthermore, the use of maleic acid, instead of more traditional mineral acids, permits to avoid the separation step before the two-stage liquid reforming reaction.

1.3.7 Integration of the APR process in a biorefinery

Today, aqueous phase reactions of polyols are studied in industries to produce fuels and chemicals, thanks to the possibility of tuning this reaction to different products, as shown in Figure 15 [65].

Several pilot and demonstration units are currently in operation, for example for the production of chemicals such as isosorbide, glycols, and aromatics, or applications such as combined Aqueous Phase Dehydratation/Hydrogenation systems for the production of liquid fuels[66]. Furthermore, APR processes may be included in a biorefinery plant to auto-generate the necessary hydrogen supply (for HDT, HDO, pyrolysis reactions), which currently comes from fossil resources. On the other hand, the economic drawbacks of the application of APR sections into existing plants are primarily due to the difficulty of obtaining a high hydrogen yield with the use of crude feeds, and the need for a large number of steps involved in the biomass pretreatment. Moreover, the product stream necessitates costly purification steps before its application in subsequent units[65].

Nevertheless, the good results obtained and the possibility of applying the process to different feeds without significant changes in reactivity suggest that the APR process is a suitable alternative for the production of hydrogen and building blocks from renewable biomass.
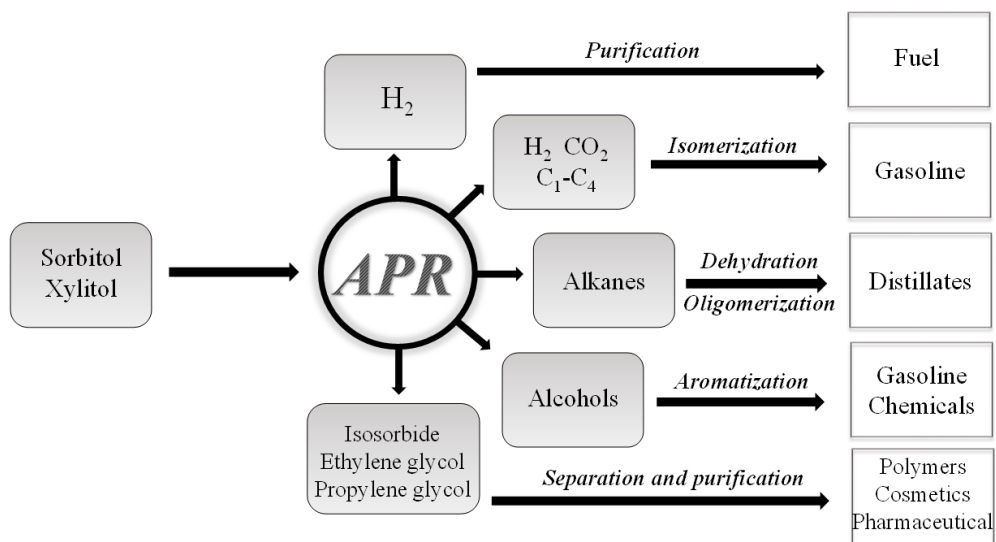
Figure 15: Industrial applications of Aqueous Phase Processes.

2. Synthesis of catalysts

A catalyst is defined as "a substance that increases the rate of a reaction without modifying the overall standard Gibbs energy change in the reaction"[67]. It is restored at the end of reaction and it does not influence the thermodynamic equilibrium composition. Catalytic reactions can be subdivided into homogeneous and heterogeneous. From a sustainability point of view, heterogeneous catalysis is better because the solid can be easily separated from reaction solution and recycled but suffers from mass transfer limitations compared to their homogeneous counterpart. A wide range of materials is used as catalyst, within them can be accounted traditional metal supported on oxides, zeolites, metal-organic frameworks, colloidal systems, single metal crystals and the research is still ongoing to find new and more active materials with tailored design and adapted dispersion of active sites. Solid catalysts can be subdivided into several families like metal, oxides, sulfides and carbons. They possess specific chemical properties, surface porosity, temperature and mechanical resistance, conductivity, bandgap, possibility of donating surface ions and each can be specific for a class of reactions.

2.1 Traditional methods

2.1.1 Classes of supports

The largest catalyst family is composed of mesoporous oxides: zeolites, clays, mixed oxides are the most important. They can also be called traditional catalysts because they cover a wide range of applications and their reactivity can be tuned to the desired properties.

Zeolites are the principal catalysts of petrochemistry industry. They can be defined as aluminosilicate constituted by SiO_4 and AlO_4 tetrahedron sharing a terminal oxygen in an infinite lattice. The difference in cation charge within Si^{4+} and Al^{3+} causes a total negative charge in the framework compensated by other anions. They are synthesized with the use of organic templating agents, subsequently removed by the system, and

this can arise the speciation into small, medium and large pore zeolites. The structure is highly tunable, not only by changing the dimension and counter-ion but also by substituting Si lattice atoms with other trivalent and tetravalent ions. These can influence the strength and number of Brönsted and Lewis sites. Another main property of those materials is the shape selectivity pioneered by Mobil group, which allows a specific selectivity for reactant, transition states and products due to the confined spaces in which reactions occur. Large studies are also devoted to the production of hierarchical zeolites with combination of micro- and mesopores. Presently more than 300 types of zeolites are existent, the most important for industrial applications are BES, FAU, MFI, MOR, SAPO-34[68].

Phosphates, in particular aluminum phosphates are another class of molecular sieves prepared by Union Carbide researcher from alumina, phosphoric acid and ammonium salts as organic templates. The structure is made up of AlO_2 and PO_2 tetrahedron in a 3D structure with cylindrical channels. If silicon is added to the structure, the SAPO molecular sieve structure is obtained. They have weak acid properties, good thermal stability and are mainly used in cracking reactions[68].

Metal organic-frameworks (MOFs) are quite recent materials constructed by reaction of organic and inorganic moieties (from arsenates, silicates, sulfates, phosphates and phosphonates plus amino complexes or branched carboxylic acids) linked by strong bonds. The variability of the ligands allows the formation of sophisticated enzyme-like materials and controlled metal type and distance[68].

Carbon based materials account single and multi-walled nanotubes, graphene, graphene oxide, nanofibers. They actually are a great challenge for catalysis both for their intrinsic features and for the possibility of embedding metals and molecules[68].

MCMs, SBAs, CMKs are sub-families of the mesoporous-silica materials founded by Mobil researchers. They are synthetized using surfactants and structure-directing agents (as co-polymers) with different 3D arrangement as honeycomb (MCM-41), cubic (MCM-48) and lamellar (MCM-50) and different intra-wall micropores. Each code is identifying a particular class of materials with different constituents. In addition, there

is again the possibility of incorporate heteroatoms with several techniques that work as active sites in reactions[68].

Last but not of less importance, layered double hydroxides or hydrotalcites are known for the possibility of embedding different anions in the structure interlayer, for their high surface area and uniform distribution of cations in a wide range of M^{3+}/M^{2+} ratio. They can combine basic and acid properties with the insertion of active metals in the structure. Moreover by calcination it is possible to obtain a random mixed oxide with high surface area and stability due to the collapse of the layered structure[69].

Beside these classes of tunable synthesis, simple oxides and hydroxides (as MgO, SiO_2, Al_2O_3, TiO_2, $CeO...$) are still widely used in heterogeneous catalysis. They are traditionally obtained by precipitation of inorganic metal salts or hydrolysis of organic precursors and applied for acid and basic catalysis or as support for monometallic and bimetallic clusters.

2.1.2 Support preparation techniques

The main synthetic methods for the above cited mesoporous oxides are reported in Figure 16 [70]. Zeolites, mesoporous silica materials, MOFs and phosphates are build up with the templating method, the second can be used for the synthesis of oxides with tailored properties and the last is related to carbon materials. Even if those methods are widely used in catalyst synthesis, the basic and most used technique for catalyst preparation remains precipitation. This is because with particular expedients it is the most tunable method both for the incorporation of metals, dopants and other cations but also for its simplicity. It occurs in three steps: supersaturation, nucleation and growth. The supersaturation region can be reached by an increase in concentration, by changes in temperature or pH. Nucleation and growth processes instead happen simultaneously. The ratio within those two infects the dimension and distribution of the final particles. Nucleation can happen spontaneously or can be initiated by seed materials (as external solid or vessel imperfections), while the growth process depends on temperature, pH and ripening. Depending on the velocity of the process, an amorphous or partially crystalline solid may be generated.

Another widely used technique for solid formation is gelation and flocculation. The starting solution in this case is colloidal, made of micelles of polycondensate material (generally an alkoxyde) separated by electrical charges. The initial reticulation of micelles gives a starting mixture called hydrogel. Subsequently the gelation process can last for different time depending on several parameters as concentration, temperature, ionic strength and pH. During this process is also possible to insert one or more species in the final gel. The transformation of the starting sol can also be obtained by drastic changes in pH or temperature that causes flocculation denser than hydrogels[71].

The obtained solutions, still in contact with their mother liquors are then generally hydrothermally treated at low temperature to achieve growth of crystals, increase in crystallinity and porosity. Successive steps are decantation, separation, washing drying and calcination.
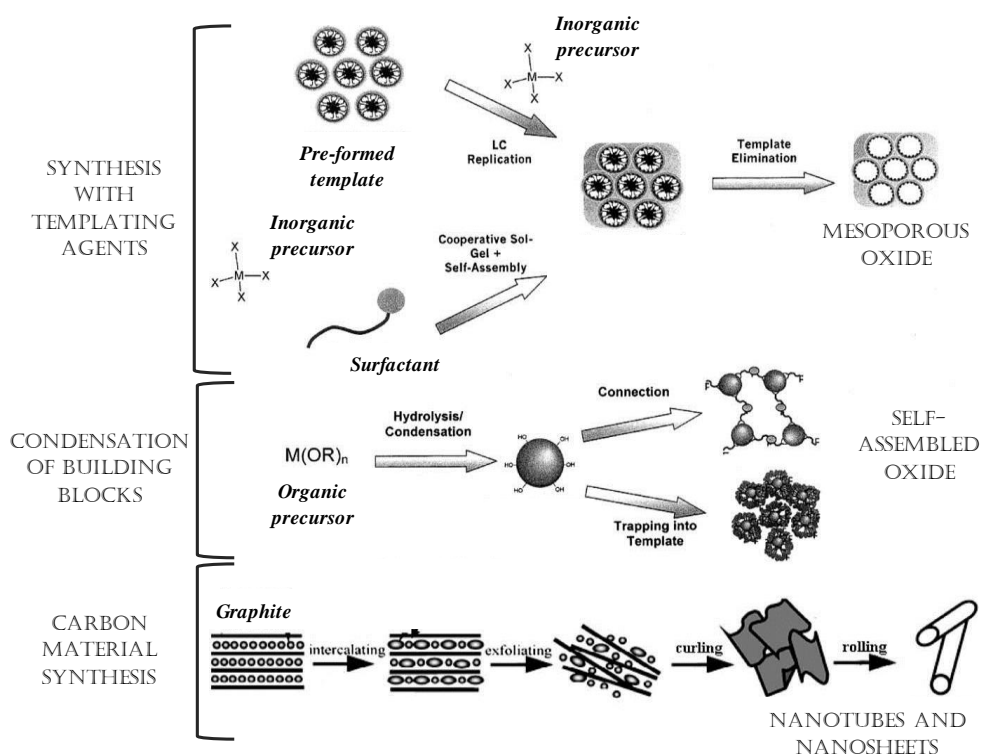

Figure 16: Schematic representation of synthesis of mesostructured materials. Adapted from[70].

2.2   *Microemulsion technique*

A microemulsion is defined as a dispersion made of water, oil, and surfactant(s) that is an isotropic and thermodynamically stable system with dispersed domain diameter varying approximately from 1 to 100 nm, usually 10 to 50 nm[67]. Differently from emulsion, the system is stable even without stirring and transparent to the light radiation because it does not present scattering phenomena due to the dimension of the micelles. The term was firstly introduced by Schulman et al. in 1949[72]. The first application for catalyst preparation goes back to Gault and Frieberg[73]. The idea was to improve the distribution and dimension of particles over a support compared to the traditional impregnation technique; moreover, it allows an improved control over bimetallic system composition. From the 1980s[74] microemulsion synthesis has become a more and more studied method for the synthesis of nanomaterials. This allows working in a selected environment, however in close contact within opposite polarity solution and permits an appropriate control using the micelles as nano-reactors for materials with specific properties.

2.2.1   *Components*

The two main components of microemulsions are the oil phase and the water one. There are several examples of oil phases used in literature, with a variety of chain length and branches. Generally, the only parameter considered for oil phase is the difference in length within the surfactant lipophilic chain and the oil chain. If the two molecules have comparable chains the solubility of the surfactant tail is better and this allows the formation of smaller particles[75]; oppositely if the two chains are significantly different there is a repulsion effect causing an enlargement of the micelles due to its lower number. As for aqueous phase, the describing parameter is the R_w factor, representing the water to surfactant molar ratio, which is also the indicator of stability of the micelles, thus the maximum quantity of internal water a surfactant can load inside droplets. Depending on the synthesis type, water can act as solvent for the metallic precursor, precipitating agent but also solvent for counter-ions of surfactant.

Despite the presence of water and oil, the system can not exist in absence of a surfactant layer which allows the formation of a flexible film. The elasticity of the film depends from not only external conditions and the type of surfactants, but also from the presence of additives as alcohols, electrolytes, block copolymers and polyelectrolites.

A review from Lòpez-Quintela et al.[76] analyzes the different types of surfactants used in microemulsion synthesis. The first classification must be done within anionic and ionic molecules. Within the first family the most used are:

- Sodium bis(2-ethylhexyl) sulfosuccinate ($C_{20}H_{38}NaO_7S^-Na^+$), commonly known as AOT, that allows the formation of a hydrophilic core compartmentalized by the polar heads and nonpolar hydrophobic alkyl tails.

- Cetyl trimethylammonium bromide ($C_{16}H_{33}(CH_3)_3N^+Br^-$, called CTAB or CTABr) which gives a very flexible film with high exchange dynamics and an improved solubilization capacity in aqueous salt solutions compared to AOT.

- Perfluoropolyethercarboxylic acid, PFPE, used in its converted ammonium salt with excess of NH_4OH with an average formula of $[CF_3O(CF_2CF(CF_3)O)_{\sim3}CF_2COO]^-[NH_4]^+$

- Sodium lauryl sulfate or sodium dodecyl sulfate ($CH_3(CH_2)_{11}OSO_3^-Na^+$) is the most widely used within anionic surfactants.

Nonionic surfactants instead are mainly used to prevent the dissolution of the counter-ion and its interaction with the forming particle, as happens mainly for Br and NH_4. Within this group the most used are:

- Triton X-100 [Polyoxyethylene(9)4-(1,1,3,3-tetramethylbutyl)phenyl ether] is widely used in the synthesis of metal oxides and nanoparticles of catalysis interest

- The family of Poly(oxyethylene)$_x$ nonylphenol ethers, called (NP-X): NP-5, NP-9 and NP-12 are also applied in the synthesis of nanoparticles for catalytic studies

- Brij30 or polyoxyethylene-4-lauryl ether [$H_3(CH_2)_{11}(CH_2CH_2O)_4OH)$] contains a short hydrocarbon chain

- Pentaoxyethylene-glycol-nonyl-phenyl ether or Igepal-CO520

Finally is worth naming other types of surfactants used for microemulsions not belonging to the previously named classes: PEG or polyethylene glycol, Span-Tween80 (a commercial mixture of sorbitol monooleate and polysorbate), polyoxoethylene-4-lauryl and 15-cethyl ethers, Epikuron-170 (a lechitin polymer) and S-1670 (a sucrose fatty acid ester).

2.2.2 Stability of microemulsions

The internal structure of a microemulsion is depending upon two main factors: temperature and ratio of its constituents. It thus can be present either in a nanosized droplet phase dispersed in a continuous one or as a bicontinuous system. Two type of microemulsion exist: water-in-oil (W/O or reverse microemulsion) systems and oil-in-water (O/W) depending on the ratio within the two phases. The surfactant acts on the dimension of the micelles, but also on its stability towards temperature, since those kinds of systems are existent only in a narrow range of temperature values. Outside those ranges a two phases system only exists[77].

A more complete classification of microemulsion systems is the Winsor one[78]. Triphasic systems are subdivided into four classes depending on the relative quantity within the components (Figure 17). Surfactant type, temperature and relative quantities determine the transition within the types:

- Type I: biphasic O/W microemulsion in equilibrium with a water excess phase. Surfactant rich water phase + monomers of surfactant in oil one.
- Type II: biphasic W/O microemulsion in equilibrium with an oil excess phase. Surfactant rich oil phase + surfactant poor water one.
- Type III: three phase system with surfactant rich middle phase + oil and water surfactant-poor phases.
- Type IV: single-phase system or microemulsion. It can be classified W/O, O/W or bicontinuous depending on the water/oil ratio.

Several parameters exist to quantify the range of existence of a microemulsion. The first is the above-cited R factor, which accounts the ratio of amphiphiles and solvents on the interfacial curvature. It compares the tendency of the surfactant to disperse in oil

or in aqueous phase (being thus R_o or R_w parameters). If one phase is favored, the interfacial region tends to curve. It can be extended to take into account the oil properties and interaction within surfactant[79]. The definition of a state at given temperature and surfactant is expressed by HLB factor of surfactant, i.e. hydrophilic-lipophilic balance. It expresses the ratio within hydrophilic and hydrophobic groups thus can also act as indicator with to the repartition of the surfactant within the two phases[80].
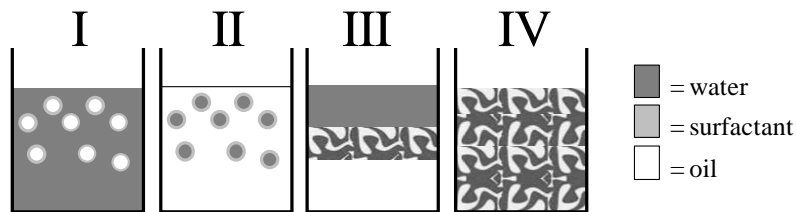
Figure 17: Schematic illustration of the four Winsor systems for microemulsion classification. Adapted from[80].
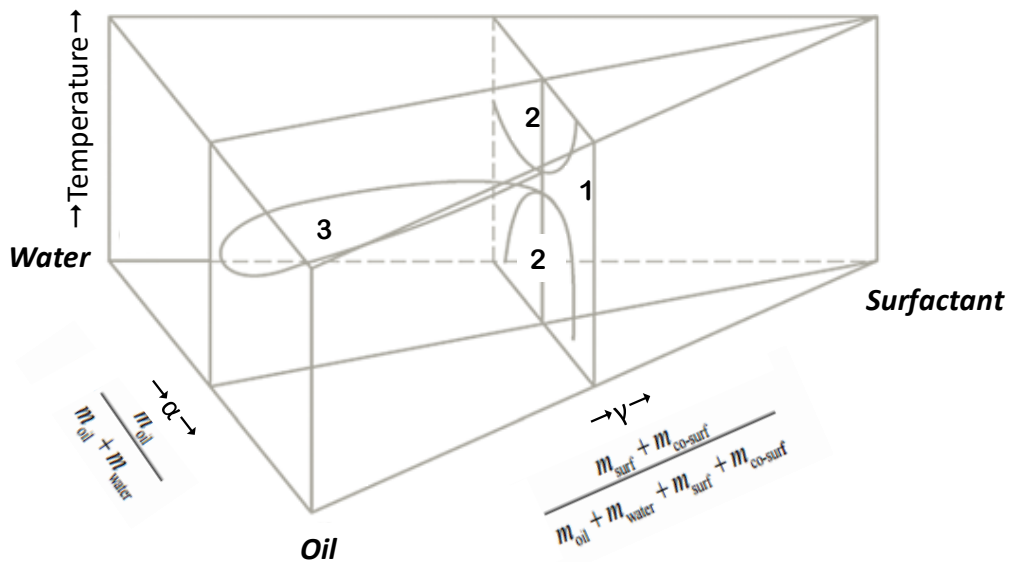
Figure 18: Gibbs phase diagram for ternary mixtures and temperature dependency and relative equations. Adapted from[80].

Figure 18 represents the temperature dependent phase diagram for a ternary mixture of oil, water and surfactant (nonionic). Each point in the diagram is defined by a combination of T, α and γ values. Relative equations are presented where m_x is the mass

of oil, water, surfactant and co-surfactant and the parameters α and γ are the ratio within the constituents. At constant α values the phase boundaries resemble the shape of a fish, due to changes in surfactant solubility with temperature that causes phase inversion (the nonionic switches from hydrophilic to hydrophobic). The number indicates the amount of phases that compose the system. Number 2 represents the existence of Winsor I and II types of O/W and W/O microemulsion. The area 3 indicates type III with the excess of surfactant equally soluble in both phases. Finally, the interception within 2 and 3 areas, named 1, shows the smallest amount of surfactant necessary to solubilize water and oil indicating the Winsor type IV[80,81].

Since the existence of a microemulsion depends on the ratio within constituent and temperature, those factors can also be used for separating the products of a microemulsion reaction from the other components. The challenge involves especially the surfactant, which is adsorbed onto the particle. The most used method is to destabilize the microemulsion by the addition of a third solvent, like THF for W/O microemulsions, which causes the precipitation of the solid. If the aim is depositing nanomaterials over a support, this action can be coupled with the presence of the support inside the solution to obtain direct deposition, only in case of particular support's properties[77]. Other applied methods are the increase or decrease in temperature or the change in pH. More particular can be the use of supercritical CO_2 during the synthesis as a solvent, than expanded to obtain a singular liquid phase and the precipitated solid[82]. Finally, other less used methods deal with the flame drying of the solid direct from microemulsion solution[83], filtration or ultrafiltration[84].

2.2.3 Parameters influencing solid dimension

There are several parameters influencing the solid dimension. The most obvious is the droplet dimension, depending on the ratio within water (or oil in O/W) and surfactant. An increase in this ratio at constant surfactant amount will cause an increase in micelles diameter. Surfactant concentration, with constant oil and water, will also increase the number of droplets causing a decrease in the size of the final particle. Finally the nature

of the precipitating agent and of the surfactant plays a role in the velocity of reaction and of interchange within the two phases[77].

It was believed in the past a "templating" effect of the nanodroplet over the forming solid[85], but, taking into account the Brownian motion, that assumption did not fit the dynamic nature of those systems. In fact, once two microemulsions make contact, there is the formation of a fused dimer (or encounter pair) with interchange of the internal solutions. This phenomenon happens with a constant k_{ex} depending not only from the temperature, but also from the film elasticity. Thus the interdroplet exchange of internal growing particles depends from the film flexibility, which favors the interchange[86]. This is one example to demonstrate that it is not always possible to apply bulk system principles over compartmentalized media, as microemulsions. It is thus necessary to apply simulation and experimental results to define the control of particle size. The main parameters can be summarized as:

- The reactant concentration acts on the particle size and polydispersity (in particular bimodality depends on rigid films)[87,88]
- The increase of one of the reactant decreases particle size until a plateau of dimension is reached[89,90]
- The raise in film flexibility allows an increase in particle size. This can be achieved by higher quantity of co-surfactant, modifying the chain length of oil or co-surfactant or acting over the droplet size[91,92]
- Even the increase in droplet size increases the particle; nevertheless, it does not follow a linear relation. That is because this parameter influences also the film flexibility and causes the superimposing of the two effects generating a bigger enlargement of the particles than what expected[91,93]

Another parameter that has to be taken into account in the particle growth is the adsorption of surfactant over the forming solid. This may explains why in several works[74,94,95] the particle size is almost independent from the above-listed parameters. The Gibbs energy for the formation of a surfactant capped particle changes with the radius, as reported in Figure 19. R_{crit} represents the minimum stable critical radius of the forming particle, but when the adsorption enthalpy is smaller, the final radius is

microemulsion-controlled (r_A). Oppositely, the effect of surfactant control can give the radius $r_B > r_{crit}$. The transition within microemulsion and surfactant control can explain the plateau observed with the increase in droplet size[86].
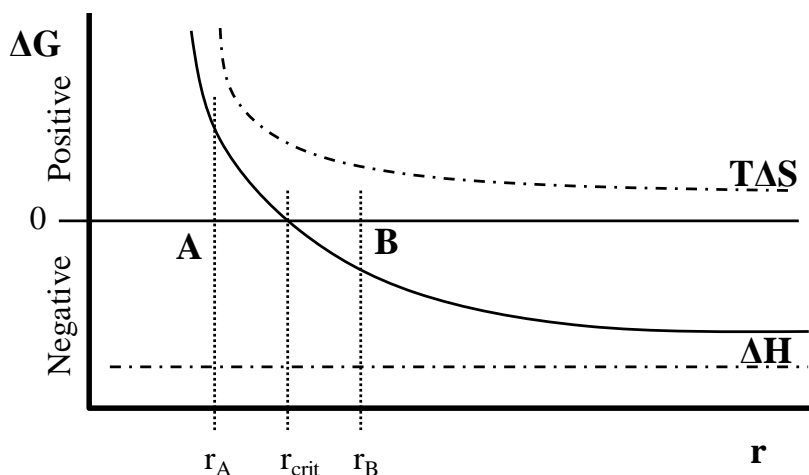
Figure 19: Dependence of the adsorption free energies on the particle radius for two microemulsions: A and B[86].

2.2.4 Applications

Together with the traditional application of microemulsion systems as cleaning agents, pharmaceutical and lubricants[96], several specific uses are being developed due to the peculiar features of those systems. In particular, their use as nanoreactors is applied in organic chemistry field to overcome reactant solubility problems, incompatibility within phases and to allow a compartmentalization and concentration of the reagents[97,98]. Moreover, the possibility of accumulation and orientation of bipolar molecules at the water-oil interface opens the possibility to regiospecificity of an organic microemulsion reaction[99]. Not least, the particular micro-heterogeneous nature of microemulsions causes strong differences in concentration of the reactants giving rise to local concentrations that can be significantly different compared to the bulk, thus allowing tuning of reaction rates. For the same reason, also the local properties of reaction media are different from bulk ones, causing a further modulation in reaction rates. In order to understand the reactivity in microemulsion systems is thus important

to know the concentration of the reagents and the corresponding reaction constants in the various pseudo-phases microenvironments. One possibility is building up a kinetic model applicable for O/W, bicontinuous systems and W/O microemulsions, which divides the system into oil, surfactant film and water region, treating them as separated phases and partitioning the reagents depending on their free energy of transfer within phases, as if it was an equilibrium system. The available models consider solvolytic reactions, ion-neutral molecule interactions, and interactions within two neutral molecules[76]. In addition, within organic chemistry field there is an interest in potential applications of microemulsion and drug delivery systems for particle sizes below 100nm, in particular for polymerization reactions[100]. Moreover, peculiar caved, core and multicore-shell system can be obtained by with this technique with specific absorption properties[101].

Nevertheless, the most important field of application is the synthesis of nanomaterials. There is a wide literature on this topic both for the preparation of metal nanoparticles and nanoxides[77,81,102–107]. These material can be embedded in matrixes to obtain innovative properties without changing the main features of the dispersant (i.e. self-cleaning TiO_2 surfaces, polymers and ceramics[86]) or used in catalysis. For the latter some examples can be the application of Pt, Pd and Rh particles in hydrogenation/dehydrogenation and cracking reactions[108–110], nano CeO_2-ZrO_2 for combustion[40,111,112], ZrO, TiO_2 and Al_2O_3 for methanol synthesis and hydrogen production[113,114], Pd-Ru and Pt-Ru deposited particles for electrolysis[115,116], CO and CO_2 hydrogenation[117–119] and photocatalysis[120,121]. Not only solid particles can be synthesized by microemulsion, but also the colloidal systems synthesized by microemulsion presents potential catalytic properties[122]. Moreover, synthesis inside the micelles is compatible with the use of a catalyst inside the system itself[123,124].

2.3 Metal deposition

A broad classification of catalysts depending on the preparation procedure is bulk catalyst or supports and impregnated catalysts. The first class comprises active substances catalytic on their own as zeolites, silica-aluminas, iron-molybdate, and

phosphates. Beside their work as bulk catalysts, some of them (i.e. aluminas, silica and oxides) can also be applied with the same preparation procedure as supports for the second class of impregnated catalysts. Oxidation, hydrogenation, dehydrogenation, dehydration catalysts are mostly part of this family. The deposition of the active phase is obtained by main techniques: precipitation, impregnation and immobilization. The first one is obtained by mixing a metal salt solution with the support in presence of a precipitating agent that can be an alkali in case the oxide form of the metal is desired or a reducing agent. Not only the precipitation of the solid is involved but also the overall process depends on the interactions of the metal particle with the surface OH groups. The process needs to be slow and controlled to obtain a small distribution of particles. Moreover, it can be named differently depending on the agent used for the transformation of the metal from the support to the final form: deposition-precipitation, deposition-reduction, or photo-deposition. Usually this technique is used for loadings above 10-20%. Impregnation instead is done by simple contact within the metal salt solution and the support. The two are made in contact for a certain period, the solid is then dried to remove the solvent and the metal fixed by calcination or reduction treatments. This process can be done in excess of liquid solution and called wet impregnation (WI) or with repeated applications of the amount of liquid contained by the pores, incipient wetness impregnation (IWI). The latter favors a better control on the dimension of metal particles and its positioning inside the pores. This technique does not require specific chemical interactions within the metal and the support[71,125,126].

Finally, immobilization technique accounts all the methods that are selective for peculiar metal-support interactions. It is used for example to support core-shell particles or metal cluster that electrostatically interact with the support surface groups[127], or applied for inorganic-organic clusters and supercritical fluids synthesis[128]. Preformed particles are stirred in solution in presence of the support and filtered after a certain time without drying of the solvent or addition of precipitating agent.

Aim of the work

Aqueous phase reforming reaction is obtaining more and more interest in industrial chemistry for the possibility of upgrading waste aqueous solutions of polyols or sugars that otherwise are dead ends of processes. The APR reaction moreover has low energy requirement together with an intrinsic safety with low CO production. It is a catalytic process with output tunable to hydrogen, alkanes or chemicals depending on the reaction conditions and catalyst.

Glycerol is a widely studied polyol in this process for the possibility of obtaining substantial H_2 yields or acids and glycols in liquid phase. Most of the studies in literature have been done with Pt on Al_2O_3, with strewn studies over different metals, in particular Ni, and less with other supports. Moreover, several mechanism pathways have been suggested for the obtained products, due to the impossibility of detecting aldehyde intermediates in batch or fixed bed reactors. In this perspective, the present work has the objective of providing an analysis, as complete as possible, over the effect of parameters and catalyst features in glycerol APR, correlating the synthesis and surface characterization with the reactivity results obtained. In addition, the possibility of in-situ analyses with ATR-IR technique offers the chance of a better comprehension of possible reaction intermediates and pathways.

Beyond this first part of the work, glycerol was selected as an interesting polyol to be upgraded due to its abundance in nature and the possibility of adapting APR process to the treatment of downstream aqueous effluents of paper and wood treatment industries. The practical application goes together with the challenges offered by this reagent in terms of thermal degradation and selectivity issues. Second aim will then be the application of the reactivity and catalyst knowledge obtained over glycerol in the upgrading via APR process of glucose.

Materials and methods

3. Catalyst preparation and characterization

3.1 Support synthesis

3.1.1 Chemicals

Chemicals for microemulsion preparation: Cyclohexane (99%, Sigma-Aldrich), n-heptane (99%, Sigma-Aldrich), 1-hexanol (98%, Sigma-Aldrich), tetramethylammonium hydroxide [TMAH] (98%, Alfa Aesar), Na_2CO_3 (98%, Alfa Aesar), NaOH pellets (98%, Alfa Aesar), double distilled water (MilliQ, Millipore), HNO_3 (68%, VWR)

Surfactants: Triton X-100 (Sigma-Aldrich), Marlophen NP5 (Sasol), CTABr (99%, Sigma-Aldrich), Sodium dodecyl sulphate (99% Sigma-Aldrich)

Metal precursors: Titanium(IV) butoxide [TBT] (97%, Sigma-Aldrich), Mg(NO3)2*6H2O (99%, Sigma-Aldrich), Ni(NO3)2*6H2O (99.9%, Alfa Aesar), Al(NO3)3*9H2O (98%, Sigma-Aldrich), Fe(NO3)3*9H2O (98%, Sigma-Aldrich), $Ru(NO)(NO_3)_x(OH)_y$ x+y=3 (1.5%v/w solution, Alfa Aesar), $Cu(NO_3)_2$*2,5H2O (98%, Alfa Aesar), $Co(NO_3)_2$*6H2O (98%, Alfa Aesar), Tetraammineplatinum(II) nitrate (99.99%, Alfa Aesar, Premion®) $Pt(NH_3)_4(NO_3)_2$

Commercial catalysts: TiO_2-comm (DT-51 CrystalACTIV™), TiO_2 P25 (Evonik Aeroxide®), Al_2O_3 (BASF, AL 3992 E 1/16)

Chemicals for HPLC calibration and APR reaction: Lactic acid (90%, Fluka), pyruvaldehyde (40%, Sigma-Aldrich), hydroxyacetone (95%, Alfa Aesar), pyruvic acid (98%, Alfa Aesar), sorbitol (99%, Sigma-Aldrich), xylitol (99%, Alfa Aesar), formic acid (98%, Fluka), ethylene glycol (99.5%, Fluka), propylene glycol (98% Sigma-Aldrich), glucose (Fluka), 1-propanol (98%, Sigma-Aldrich), ethanol (99.8%, Sigma-

Aldrich), acetone (99.8%, Sigma-Aldrich), fructose (99%, Alfa Aesar), levulinic acid (98%, Sigma-Aldrich), methanol (99.8%, Sigma-Aldrich), 5-HMF (99.9%, Avabiochem), glycerol (99.5% Alfa Aesar), mannose (99%, Alfa Aesar), glyceraldehyde (90%, Sigma-Aldrich).

3.1.2 Synthesis of TiO_2 by microemulsion (TiO_2-m)

TiO_2-m was synthesized by water-in oil microemulsion[120,129]. The organic components were cyclohexane as oil phase, Triton X-100 as surfactant and 1-hexanol as co-surfactant with weight ratios oil/surfactant=1.17 and co-surfactant/surfactant=0.46. A first microemulsion (A) was synthesized by adding slowly and under stirring 5M HNO_3 in double distilled water to the organic components with an R_w molar ratio (water/surfactant) of 42.6. The organic titanium precursor [TBT] was dissolved in a second solution of organics (hexanol, TX-100 and cyclohexane with the same amount as solution A) and stirred until a clear yellow solution was obtained (B). Then B was slowly added in the microemulsion A under vigorous stirring obtaining a light yellow transparent solution with a final R_w value of 21.3. The solution was stirred at RT for 1h to allow the slow hydrolysis of the precursor inside the micelles to form the oxide. Subsequently it was heated to reflux temperature (74°C) for 5h to complete the reaction and extract the solid from the micelles. Above 40°C, the microemulsion became opalescent due to temperature instability, after around 1h of heating some white deposit on the bottom showed the formation of TiO_2. The solid was than separated by centrifugation and washed 5 times with ethanol, dried at 120°C overnight and calcined at 400°C for 3h (ramp 2°C/min). The catalyst was compared with a commercial anatase support (TiO_2-comm).

3.1.3 Synthesis by co-precipitation

Co-precipitation and precipitation synthesis at constant pH were done following a method reported in literature by Cavani e al.[130] It consists in the preparation of three aqueous solutions. The first is a 2M solution of metal cations (Ni, Mg, Al and Fe nitrates) with the desired M^{2+}/M^{3+} ratio and atomic percentage within the cations. If only one metal is required, the total molarity remains 2. The second one is a 1M

Na_2CO_3 solution and the third a 3M NaOH solution. The amount of Na_2CO_3 solution is double the number of moles of the trivalent cation as to work in excess. Once completely dissolved the salts the Na_2CO_3 solution pH is adjusted to 10.5 with HNO_3.Then the first solution is slowly dropped in the second one using a separator funnel, the Na_2CO_3 solution is maintained under vigorous stirring and at constant temperature of 56°C. During the synthesis, the pH is monitored inside the second solution and kept constant at 10.5 value by manual additions of the third solution. The final solution is then aged for 1h, filtrated and washed with warm distilled water (around 1l for 5g of oxide) to remove the counter-ions and carbonate and base excess. The solid is dried at 70°C overnight and calcined at 650, 750 or 900°C for 5h (ramp 5°C/min). The solid is named after the metal constituents using the "/" sign if mixed oxide structure is obtained (i.e Mg/Al) or the correct spinel form. To differentiate within ratios the theoretical atomic percentage of one metal (generally Ni) is added as footer, not indicating the exact stoichiometric ratio of the oxide (i.e. $Ni_{40}Mg/Al$ where Ni atomic percentage is 40% of the total cations). The synthesis by precipitation and co-precipitation is named "p".

3.1.4 Synthesis of MgO by microemulsion (MgO-m)

MgO-m was synthesized adapting a different microemulsion method, reported for Ce/Zr mixed oxides[131]. Two identical microemulsion were prepared with R_w=14. Each contains as organic components: cyclohexane as oil phase, 1-hexanol as cosurfactant and Triton X-100 as surfactant with weight ratios oil/surfactant=3.05 and co-surfactant/surfactant=0.78. To the first microemulsion A was added a solution 1M of Mg nitrate precursor in double distilled water, while to the second (B) it was added a 2.2M aqueous solution of TMAH. The two microemulsions were stirred and A was slowly added into B obtaining a transparent solution. The final microemulsion is vigorously stirred for 1h at RT, than heated to 60°C for 2h. The solid obtained after cooling is separated from mother solution by centrifugation, washed with ethanol, dried at 120°C and calcined at 650°C for 3h (ramp 2°C/min)

3.1.5 *Synthesis of Mg/Al mixed oxides by microemulsion*

Microemulsion synthesis of Mg/Al resembles the co-precipitation technique but with microemulsions instead aqueous solutions. Cyclohexane was used as oil phase, 1-hexanol as co-surfactant and triton as surfactant, with some trials with NP5, sodium dodecylsulphate and CTABr. The weight ratio within the constituents were 0.85 for triton/cyclohexane and 0.39 for cyclohexane/hexanol. The R_w value was maintained at 21.3. A first cation microemulsion was formed mixing the organic phase with an aqueous one containing 2M solution of Mg and Al nitrates with 75/25 atomic ratio. Due to stability issues, the second microemulsion contained 0.15M of Na_2CO_3 (with double quantity of cyclohexane) and the third 0.5M of NaOH. The synthesis is performed as previously reported for co-precipitation method, by dropping the first microemulsion in the second one at constant temperature and pH maintained by the third microemulsion. The temperature was set at 30°C to avoid the rupture of the microemulsion system, than aged at 50°C for 1h, filtered still hot and washed with methanol. The solid, named Mg/Al-m was dried at 70°C and calcined at 750°C for 5h (ramp 5°C/min)

3.1.6 *Synthesis of ferrite-type supports*

Ferrite-type supports are spinel phases with iron as M^{3+} cation instead of Al and a typical crystalline structure $M^{2+}M_2^{3+}O_4$ with M^{2+}/M^{3+} ratio of 0.66. The synthesis is similar to co-precipitation method without the use of carbonate solution and the constant addition of base. 50ml of metal nitrate 1.5M solution, with the desired cation ratio is slowly dropped in 250ml of a NaOH 2M solution at the temperature of 45°C under vigorous stirring with a constant speed. The reaction temperature is constantly maintained at 45°C for all the time. After the addition, the suspensions is stirred for 2h at the constant temperature of 45°C adding NaOH 3M to maintain the pH above 13. The precipitates are separate by filtration and then washed with about 1.5l of distilled water at room temperature to remove sodium and nitrates ions. The washed samples, named "p", are dried at 120°C overnight and calcined at 600°C for 5h (5°C/min ramp).

3.1.7 Microemulsion synthesis of ferrites

Microemulsion ferrites synthesis is similar to Ce/Zr mixed oxides synthesis[131], with a cation containing microemulsion and a second one with the precipitating agent (base) to simulate the pH 13 working conditions of previous synthesis. The weight ratio within surfactant and 1-hexanol is 0.33 and co-surfactant/surfactant 0.79. Ni and Fe nitrates with a ratio 2:1 were dissolved in a 0.5M solution and added to the organic phase to obtain a transparent microemulsion. TMAH microemulsion instead contained an aqueous solution 1.5M. R_w value was 14.6 for both the solutions. The cation microemulsion was slowly dropped in the base one under vigorous stirring and let at RT for 7h. The solid named $NiFe_2O_4$-m was then filtered, washed with methanol, dried at 100°C and calcined at 600°C for 5h (5°C/min ramp).

3.2 Loading of the metal

The oxides were generally loaded with Pt 1-3% wt. by Incipient Wetness Impregnation of Tetraammineplatinum(II) nitrate. In specific cases, ruthenium nitrosyl nitrate or other nitrate salts were used. Bimetallic impregnations were done dissolving both the cations in the same aqueous solution to be impregnated. The solution was loaded on the sample avoiding the complete wetting of the solid, following cycles of loading and drying in oven at 100°C. Finally, the powder was dried at 120°C overnight, calcined at 350°C for 3h (ramp 2°C/min) and meshed 60-80. The metallic phase was obtained by reduction with H_2/N_2 flow (10%) at 350°C or 500°C for 3h. In case of reduction at 750°C the same H_2/N_2 ratio was maintained but the reduction was performed overnight. In blank tests with only the support, the catalyst was meshed and calcined at 350°C for reproducibility of post-treatments.

NiO loading was performed by University of Milan team following the method reported in literature[132,133].

3.3 Characterization

3.3.1 Microemulsion characterization

Microemulsion solutions were analyzed by Dinamic Light Scattering (DLS, Malvern ZetaSizer) with quartz cuvette. Hydrodynamic diameter reported includes the coordination sphere and the species adsorbed on the micelle surface as surfactants and cosurfactant.

UV-VIS tests were recorded in a Perkin Elmer Lambda 19 instrument equipped with quartz cuvette in the range 200-800nm. Several stirred emulsions were prepared (one for each analysis time) with TBT and acid water solution, in absence of surfactants. At the desired time aqueous and organic solution were withdrew and diluted ten times in water or cyclohexane. Reference cell was filled with the respective solvent for each analysis.

SEM/EDS analyses were performed by using an E-SEM Zeiss EVO 50 Series Instrument (Carl Zeiss, spa) equipped with an INCA Energy 350 EDS microanalysis system (Oxford Instruments Analytical). The accelerating voltage was 20kV and the spectra collection time 60s.

3.3.2 Oxide characterization

Powders were characterized by P-XRD in a Philips X'Pert X'Celerator, with Cu-kα radiation in the range 5-80°2θ with step of 0.1°2θ. Particle size determination was done by Scherrer calculation as follows over the 100% peak:

$$d = \frac{k \times \lambda_{Cu-k\alpha}}{\beta \times \cos\theta}$$

Where: d = mean size of crystallites, k = particle shape factor considered as spherical, λ = X-Ray wavelength, β = line broadening difference (FWHM) between the sample and Si standard, θ = Bragg angle. Rietveld approximate calculations were done by the semi-automatic method of X'Pert High Score Plus program.

Surface analyses were performed in an ASAP 2020 Micromeritics instrument using N_2 as probe gas and pretreating the sample under 30mmHg, prior at 150°C (ramp 2°C/min) for 30min and then for 60min at 250°C (ramp 10°C/min).

Temperature programmed desorption analysis were done in a Micromeritics Autochem II instrument equipped with TCD detector and mass analyzer (Cirrus II, MKS). In temperature programmed CO_2 analysis, the sample was first pretreated at 700°C for 45min (ramp 10°C/min), than cooled to 40°C in inert atmosphere. It was flushed for 2h with a CO_2/He 10% mixture (30 cm^3/min) at 40°C, than purged for 1h in helium. Finally desorption measurements were done up to 700°C with a ramp of 10°C/min and held for 20min. Temperature programmed NH_3 desorption analysis were done in with a similar procedure flushing for 1h at 100°C a NH_3/He 10% mixture (30 cm^3/min), than it was purged for 1h in helium. Finally desorption measurements were done up to 700°C with a ramp of 10°C/min and held for 30min.

Solid UV-VIS analyses were recorded in a Perkin Elmer Lambda 19 instrument equipped with integrating sphere in the range 280-800nm.

3.3.3 Catalyst characterization

Pt loaded catalysts were analyzed by high-resolution transmission electron microscopy (HR-TEM) using a TEM/STEM (FEI Tecnai F20), which a high-angle annular dark field (HAADF) imaging mode at 200kV and with an EDS PV9761N SUTW energy dispersive X-ray spectrometer (EDX) for X-ray microanalysis. The samples were suspended in ethanol and dispersed on a holey carbon film supported on copper grid. Selected area electron diffraction (SAED) measurements were done in situ and planar distances calculated with means of ImageJ program.

H_2 chemisorption analyses were done in the previous reported Micromeritics Autochem II instrument with TCD detector. The sample was first pretreated at 400°C for 10min in inert atmosphere, than pre-reduced at 400°C for 30min in 5% H_2/Ar (50cm^3/min), than held at 300°C in Ar for 30min and cooled to -40 or 50°C. After stabilization to the temperature, 5% H_2/Ar was pulsed 40times with 2min delay on the sample with a 1.13cm^3 calibrated loop. The same instrument was used for Temperature Programmed

Reduction measurements. The samples were pretreated at 150°C for 30min in He, cooled and reduced under H_2/He 5% flux up to 800°C with a 10°C/min ramp and held 30min.

4. Catalytic tests

4.1   APR tests and product analysis

Aqueous phase reforming (APR) tests were performed in a 300 ml stainless steel Parr autoclave reported in Figure 20, loaded with a 17.13% (or 5.71%) wt. solution of glycerol in water and 0.45g of catalyst to maintain a water/C molar ratio of 10 (or 30). The C/Pt molar ratio was 4000 or 12000, depending on the glycerol and Pt loadings. The system was purged under N_2 flow for some minutes to avoid the presence of oxygen in the gas phase, sealed with no added pressure, and heated to the desired temperature. The heating period was not considered in the reaction time and was around 50-60min depending on the desired temperature; heater controller slowed the heating speed approximately 20°C before the desired temperature. All the reactions were performed in the range of temperature 200-250°C at autogenous pressure for different time. Gas analyses were performed in an off-line Thermo Focus GC with a carbon molecular sieve column (CARBOSPHERE 80/100 6*1/8) and TCD detector. Liquid phase was analyzed in an Agilent HPLC over Rezex ROA Organic Acid column (0,0025M H_2SO_4 eluent, oven temperature 30°C or 60°C and 0.6ml/min flux) with DAD and RID detector.
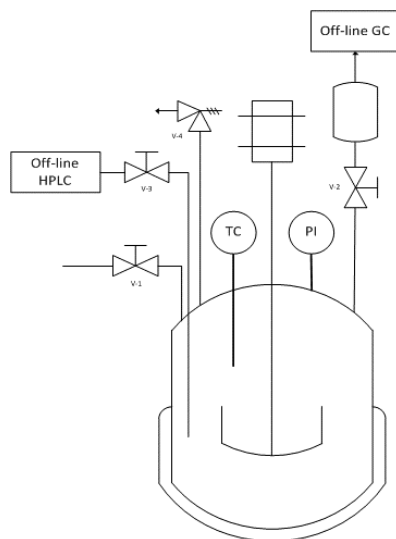
Figure 20: Scheme of autoclave batch system.

Gas products yields were calculated as a mean of five GC injections, over the total amount of reagent utilized. Stoichiometry factor (SF) was calculated considering the transformation of a glycerol molecule into the selected product B:

$$Y_B = \frac{n_{B\,injected}}{n_{injected\,tot}} \times \frac{P_{system} \times V_{system}}{0.08314 \times T(K)} \times \frac{100}{n_{0\,gly}} \times SF$$

SF= 1/4 for H_2; 1/3 for CO, CO_2, CH_4; 2/3 for C_2H_4, C_2H_6; 1 for C_3H_8

Liquid phase yields were calculated over the total amount of reagent utilized. Stoichiometry factor was calculated, as above, considering the ratio of the transformation of a glycerol molecule into the selected carbon-containing product B:

$$Y_B = n_B \times V(L)_{liquid\,phase} \times \frac{100}{n_{0\,gly}} \times SF$$
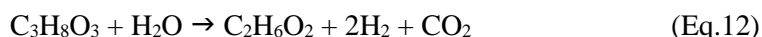
SF= 2/3 for C_2 (ethanol and ethylene glycol); 1 for C_3 products (lactic acid, 1,2-propanediol, hydroxyacetone, propionic acid, acetone and 1-propanol). Lower yields products were identified but not calibrated.

Selectivity values were calculated for both gas and liquid phase products from yield and conversion values as:

$$S_B = \frac{Y_B}{X_{gly}}$$

4.1.1 Lump sum and productivity calculations

Lump sum approximation was done analyzing the H_2, H_2O and CO_2 molecules exchanged in the direct reaction from glycerol to the desired product. For example the production of 1,2-propanediol and ethylene glycol from glycerol can be written as:

$$C_3H_8O_3 + H_2 \rightarrow C_3H_8O_2 + H_2O \qquad\qquad \text{(Eq.11)}$$

$$C_3H_8O_3 + H_2O \rightarrow C_2H_6O_2 + 2H_2 + CO_2 \qquad\qquad \text{(Eq.12)}$$

The product selectivity were then summed considering their stoichiometry factor (SF) depending on the class of reaction involved: dehydration, dehydrogenation, hydrogen-consuming reactions and decarboxylation (intended as CO_2 production due to WGS reaction). Each product can be accounted in more than one classes, as reported in Equations 11 and 12: 1,2-propanediol has SF=1 for hydrogenation and dehydration, while ethylene glycol has SF=1 for decarboxylation and SF=2 for dehydrogenation. The hydration reaction was not considered because the whole system is in water environment. The list of products accounted for glycerol reaction and their multiplying factor is reported in Table 1. Table 2 represents the classes of reaction and the products accounted for glucose tests in which are included isomerization reactions and C-C cleavage ones as direct reaction from glucose. In this case, yield values were summed since conversion was near to 100% for several reactions. Fractional values are due to the subdivision of the SF of the selected product with the reagent one to leave the reagent with "1" SF value.

Other parameters calculated are hydrogen productivity, carbon balance and yield sum. Yield sum indicates the amount of products detected only by summing all the carbon containing molecules, carbon balance instead accounts also the residual amount of reagent unconverted, together with carbon-containing products. Finally, H_2 productivity is calculated as follows:

$$p(H_2) = \frac{n_{H_2}(mmol)}{t(h)}$$

Table 1: Sum of product selectivity in the lump sum method for each class of reaction for glycerol tests. SF= stoichiometry factor

Dehydration		Decarboxylation		Dehydrogenation		Hydrogen consumed		Total hydrogen produced	
Product	*SF*	*Product*	*SF*	*Product*	*SF*	*Product*	*SF*	*Product*	*SF*
Hydroxyacetone	1	Ethanol	1	Lactic acid	1	1,2-propanediol	1	1,2-propanediol	1
1,2-propanediol	1	Ethylene glycol	1	Ethanol	1	Propanol	2	Propanol	2
Propanol	2			Ethylene glycol	2	Acetone	1	Acetone	1
Acetone	2					CH_4	5/3	CH_4	5/3
Propionic acid	1							H_2	
CH_4	1								

Table 2: Sum of product yields in the lump sum method for each class of reaction for glucose tests. SF= stoichiometry factor

Isomerization	Dehydration		Hydrogenation		Dehydrogenation		C-C cleavage	
	Product	*SF*	*Product*	*SF*	*Product*	*SF*	*Product*	*SF*
Fructose	Levulinic acid	2.4	Sorbitol	1	Formic acid	6	Lactic acid	2
	Propionic acid	2	Levulinic acid	1.2	CO_2	12	Acetic acid	3
	Ethanol	3	Propionic acid	2			Levulinic acid	1.2
	HMF	3	Ethanol	6			Propionic acid	2
	Hydroxyacetone	2	Glycerol	2			Methanol	6
	1,2-propanediol	2	Hydroxyacetone	2			Ethanol	3
	CH_4	6	Ethylene glycol	3			Glycerol	2
			1,2-propanediol	4			Formic acid	6
			Methanol	6			Hydroxyacetone	2
			CH_4	12			Ethylene glycol	3
			C_{4-5}	0.3			1,2-propanediol	2
							C_{4-5}	1.3
							CO_2	6
							CH_4	6

4.2 Products identification

Products identification was done by injection in HPLC taking the retention time as indicative for each product in different conditions. Analysis tests were also performed changing the acidity of the eluent, the flux and column temperature. Moreover, some identification tests for glucose reactivity were done with double Rezex ROA Organic acid column with oven temperature 80°C and 0.5ml/min flux and with Agilent Hi-Plex Pb column at 80°C using water 0.6ml/min.

Unknown products were analysed by electrospray ionization mass spectroscopy (ESI-MS) and gas chromatography equipped with mass analyser (GC-MS). The first was a Waters micromass ZQ 4000 instrument; the aqueous product solution was diluted in methanol and injected without further derivatization. Positive ions conditions were 3.57 KV for the probe and 20V for the cone, while for negative ions the probe voltage was 2.5KV and 30V for the cone with a 20μL/min flux. The GC-MS used was a Agilent Technologies 6890 GC coupled with a mass spectrometer Agilent Technologies 5973 with a non-polar column (5% Phenyl - 95% methyl siloxane, 30m x 250μm x 1.05μm). Helium was used as carrier gas at a flow rate equal to 1ml/min; the injector was maintained at a temperature of 250°C in the split mode (50:1); total flow was 23.9ml/min. The volume of solution injected was 0.5μL and the standard temperature program was isothermal step at 50°C for 5min, ramp 20°C/min until 280°C, and a final isothermal step for 5min.

Leaching tests were done by XRF technique in a Panalytical AXIOS Advanced instrument equipped with an Rh tube 4kW, 60kV RX tube. Liquid samples are analyzed in a PE 27mm cell with a 6μm Mylar (PET) window or 4μm Prolene (PP) window for acid solutions.

4.3 ATR-IR setup and tests

ATR-IR tests were performed in a Bruker Tensor II instrument equipped with a Specac Gateway™ cell with interchangeable crystals. Three 7 x 1cm ZnSe 45° angle crystals

were equipped with the cell: a flat plate for solid analysis and two trough ones for liquid samples, one of which combined with a high stability temperature controller (Specac 4000 series). The system was generally used in the heating setup, as presented in Figure 21. The IR beam is reflected six times on the crystal and through the evanescent wave is partially adsorbed by the solution and finally collimated to the DTGS detector. Catalyst powder are dispersed in methanol by sonication and dropped over the crystal uniformly; the alcohol is then removed by mild heating. Background spectrum acquisition is done after catalyst deposition for intermediates analyses or with bare crystal to see eventual adsorption of the catalyst. Pure glycerol, 1%wt. glycerol solution or solution of other reagents is placed over the catalyst and the overall is covered with an aluminium bar pressed over the plate to reduce evaporation. Analyses were performed in isothermal conditions and controlled ramp. In the first, the system is rapidly heated to the desired temperature and 1spectrum/min is analysed for a maximum 100min; the latter consist in a slow ramp (5°C/min) with a spectrum each min and stopped when the solution starts to vaporize. Spectra acquisition and analyses were done by OPUS 7.0 software in the range 400-700cm^{-1} with an average of 16scans for each spectrum. Data analysis is performed subtracting from each spectrum the first of the series in case of isotherm analysis or subtracting a blank test with catalyst and water or only solution acquired at the same temperature for ramp analysis. Peak assignation is done by comparison with IR databases.
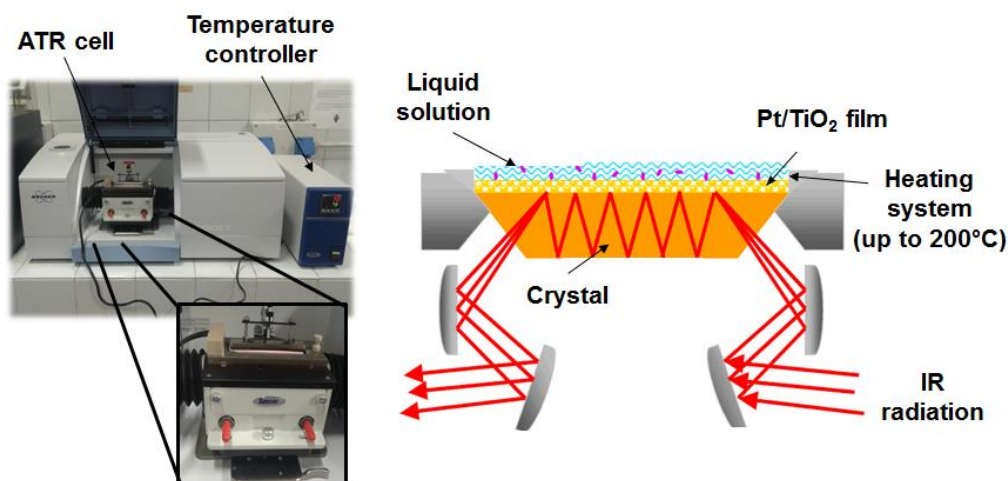

Figure 21: ATR-IR instrument setup.

Results and discussion

5. Conversion of glycerol

5.1 Pt/TiO$_2$ prepared by microemulsion

Within the variety of Pt supported catalysts, TiO$_2$ is reported as the oxide with the highest hydrogen production rate for ethylene glycol at 498K followed by Pt-black, carbon, Al$_2$O$_3$ and ZrO$_2$. In parallel, the production of alkanes and their precursors from ethylene glycol (acetaldehyde, ethanol, and acetic acid), is not negligible, but lower than Pt-black and carbon, combined with a considerable ratio of WGS[41]. For these reasons, Pt/TiO$_2$ can be selected as an interesting catalyst for the optimization of liquid or gas phase products by acting on the reaction conditions. Moreover, TiO$_2$ surface characteristics can change with the preparation method, therefore the possibility of enhancing its properties by a water in oil microemulsion synthetic technique. Microemulsion-synthesized TiO$_2$ finds its main catalytic application in the photo-degradation of organic pollutants in water[129,134–136] due to the possibility of controlling crystal phase and its bandgap. On the other hand, TiO$_2$ is widely applied in heterogeneous catalysis and photo catalysis usually in complex arrangements as nano-rods and core-shell particles[137,138]. In this field, the use of microemulsion technique is a not common application in APR heterogeneous catalysis.

5.1.1   Analysis and optimization of microemulsion preparation

Several microemulsion-mediated synthesis are reported in literature with the use of TiCl$_4$[134,135,139], titanium isopropoxyde[140], and titanium butoxyde[134,136,141–144] as precursors, and a variety of surfactants and oil phases. Within the possible precursors, titanium butoxyde (TBT) was selected because it presents a hydrolysis rate higher than titanium isopropoxyde and it is safer compared to TiCl$_4$. Results on TBT hydrolysis

show two separated phases if TBT is added to acid water, while instantaneous bulk gel formation occurs in neutral and basic solutions. A study carried out on the effect of acid concentration on TiO_2 precipitation demonstrated that 5M HNO_3 was able to avoid the formation of bulk solid for several days, while decreasing the acid concentration up to 0.5M increased the hydrolysis rate and the formation of gel was suddenly observed. The experiment carried out using a 5M solution of HNO_3 in microemulsion showed the formation of the first precipitate after few hours of mixing at RT. The reason of the enhanced reactivity can be twofold: the double phase environment favors the solubility of precursor and byproduct (1-butanol) in organic phase, and increases the organic-water interface where the TBT and hydrates of TBT are supposed to react[129]. Therefore, with the selected precursor, the synthesis of TiO_2 is estimated to happen as reported in Figure 22, suggesting water as nucleophile, due to the low amount of OH groups in acid environment.
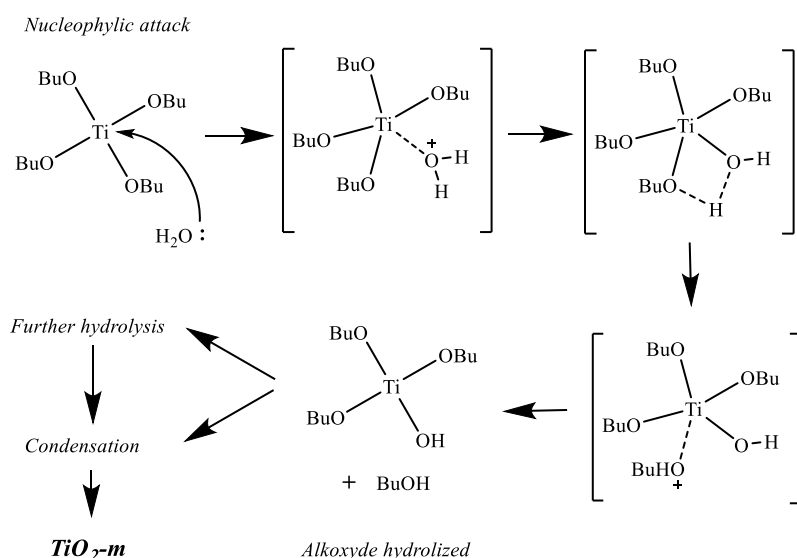

Figure 22: Scheme of hydrolysis mechanism of TBT in water environment. Adapted from[129].

TBT is supposed to enter in contact with the micelle thanks to the flexibility of the triton/hexanol layer, facilitated by collision within droplets. Once in contact with acid water the alkoxyde is hydrolyzed and the reaction is driven by the removal of 1-butanol from the micelle by its higher solubility in organic phase. As represented in Figure 22, two pathways are possible: multiple hydrolysis on the same precursor molecule and the

possibility of formation of Ti-O-Ti dimers or chains, by condensation reactions within mono- and bi-hydrolyzed molecules. The rates of the two reactions depend on the ratio between multiple-hydrolysis and the condensation step. Since the microemulsion system shows a DLS peak at 6nm at the beginning of the reaction, the active interface within organic and aqueous phases is increased by a factor 10^6 for this microemulsion system compared to a biphasic system. It thus favors the possibility for TBT, which is soluble in organic phase, to react faster with H_2O. It can moreover be speculated that the condensation step may be faster than the hydrolysis rate, because the latter is inhibited by the presence of acid environment while the first one is slightly affected. This may lead to a higher nucleation rate and the formation of an ordered structure since the early stages of reaction, as confirmed by XRD (Figure 23).
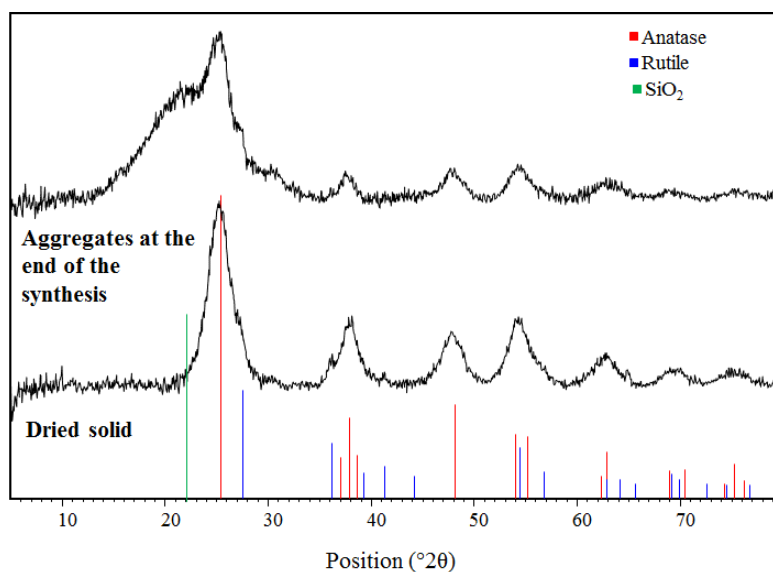

Figure 23: P-XRD analysis of the agglomerates obtained after the synthesis deposited on a silica glass and of the dried solid.

Once the TBT is partially hydrolyzed and the condensation starts, it is supposed to remain at the interface of the micelle, until further hydrolysis happens for the final formation of the solid. An attempt to verify the given hypothesis was done by following the amount of 1-butanol released by the reaction. Several attempts were done using UV-VIS, IR, HPLC, GC-MS and did not give appreciable results. That was because the

presence of a stable microemulsion makes impossible the separation within organic and aqueous phase without altering the system composition.

A study on the formation of TiO_2 agglomerates during the microemulsion reaction was performed on a room temperature stirred microemulsion analyzed by DLS and ex situ SEM microscopy. SEM images permit to detect particle size, even though they cannot be directly correlated to the dimension of the micelle. In fact, as reported in literature[129,145], the radius of the forming oxide depends both upon the R_w factor (water to surfactant ratio) and on the water to oil ratio by modifying the interchanges within the phases[145] and preventing the aggregation of the particle[139]. DLS permits to study the hydrodynamic diameter of the micelle and the enlargement due to TiO_2 formation directly in solution. In parallel, sample drops were dried for SEM analysis overnight at 120°C allowing the removal of the most volatile compounds (water, cyclohexane and hexanol). This permitted the study of bigger agglomerates of solid starting from 0.2µm; smaller particles were not detectable due to sensitiveness. At the beginning of the reaction, DLS showed micelles with a mean diameter of 6nm, and SEM detected no particles, in accordance with the aim of microemulsion synthesis to avoid rapid hydrolysis of the precursor. After 1h of stirring, DLS detected mainly the presence of micelles with a 6nm diameter and a small amount of signal corresponding to larger species around 4-5µm. SEM images (Figure 24 and Figure 25) showed some particles with a maximum near the detection limit of 0.2-0.3µm. Both the measurements underline that after 1h of stirring some aggregates are present in the solution. Nevertheless, the difference in dimension detected within the two instruments can be attributable to the presence of surfactant and organic layer around the particles in liquid scattering measurements and to the size reduction after solvent and water evaporation in SEM samples. Up to 5h of reaction, no significant changes were detected in the distribution of the micelles. At this time, DLS did not give any significant result due to the opalescence of the solution, caused by the presence of small TiO_2 agglomerates. SEM analyses at 24h showed particles with a broadening of the maximum and the shift of the mean diameter to 0.5µm probably due to agglomeration and crystallization of the amorphous hydrates of TiO_2. Finally, after 48h particle distribution appeared as multimodal with the presence of bigger particles in the range 0.8-1.8µm, probably due

to the partial change of TiO_2 from anatase to rutile crystals, as reported for room temperature synthesis[120].

During SEM measurements, EDS analyses were performed after 24h to detect the percentage of Ti in different parts of the sample (Figure 26). An indication of the type of Ti species forming the particles can be carried out by analysis the O/Ti ratio after subtracting the O contained in the surfactant remained on the particle (evaluated by the C/O ratio). An O/Ti ratio around 3 has been observed by focusing the beam on a particle, giving a value coherent with partially condensed species with an intermediate value between O/Ti ratio of 2 (in TiO_2) and 4 (for TBT or completely hydrolyzed precursor). The same analysis was performed in two areas of the sample with apparent no particles present. In these cases, Ti is still present even if, due to the large amount of C and O, its presence can not be attributed to any species.
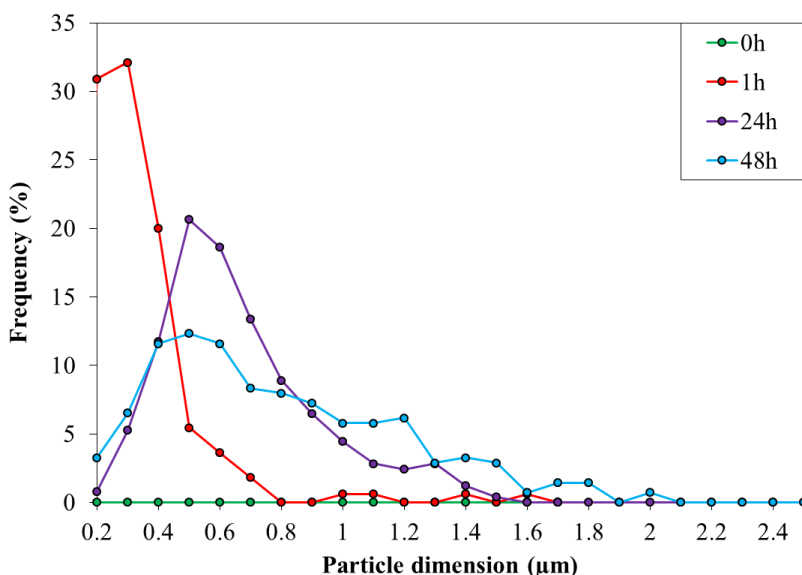

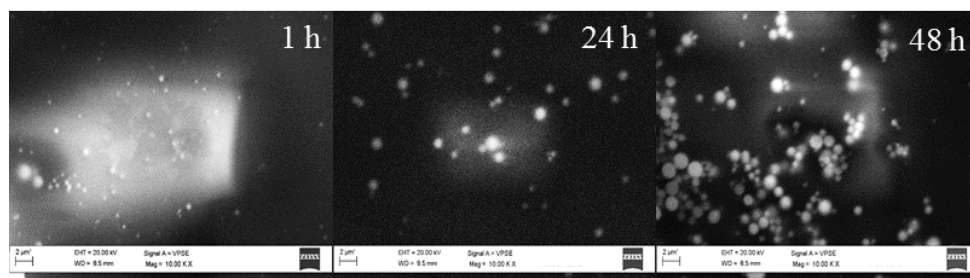*Figure 24: SEM analysis of TiO$_2$ particle dimension over time.*

Figure 25: SEM images of the microemulsion synthesis after 1, 24 and 48h of stirring RT. Samples dried at 120°C for the removal of the most volatile compounds.
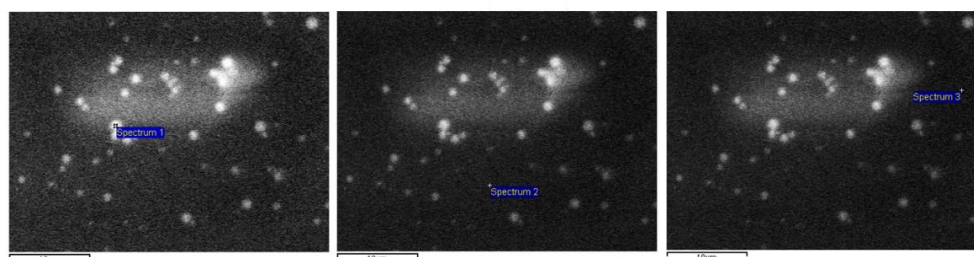

Figure 26: SEM images with localization of the EDS spectra for the analysis of composition of the mixture.
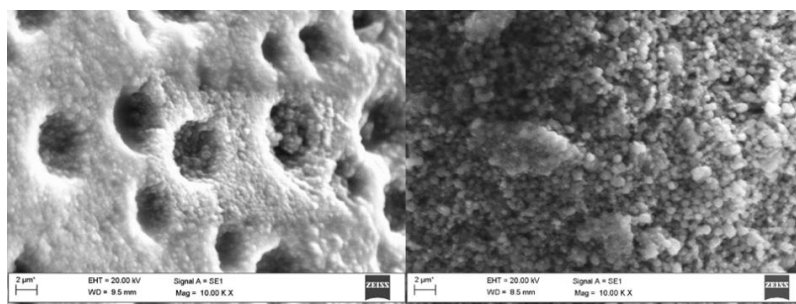

Figure 27: SEM images of the sponge-like solid deposited on the bottom of the flask soon after the synthesis.

The observation on the microemulsion stability and precipitate evolution allows the possibility of modifying the synthesis reported in literature for anatase in microemulsion[120,144,146] acting on the reaction time, temperature and addition of the reagents. The first parameter studied was the addition order of the reagents to be able to work with isotropic and well-dispersed solutions. The addition order was changed from the literature synthesis[120] to obtain a more stable microemulsion, as reported in Figure 29. The total amount of organic phase was subdivided into a water-containing microemulsion (A) and a homogeneous solution containing organics and TBT (B). The

slow addition of B into A permitted to maintain the overall system in acid pH avoiding uncontrolled hydrolysis reactions, and favored the transparency of the overall microemulsion after few minutes. The stability of the system was confirmed by the absence of visible solid after stirring for several hours at room temperature. Previously reported data showed the formation of titania aggregates starts after 1h, thus it was selected this time before the increase of temperature. The heating leads to the disappearance of the microemulsion but contemporarily increases the formation rate of solid which otherwise requires more than 4 days[120]. Furthermore, instead of autoclave heating, milder conditions have been used simply by heating the solution at reflux (temperature around 74°C). The breakage of the microemulsion[129] leads to the formation of sponge-like solid detected by SEM (Figure 27), due to the formation in temperature of a stirred emulsion[145]. Moreover, XRD analysis performed on the solid before the drying step (Figure 23) showed already the formation of low crystalline anatase phase supporting the hypothesis that after high nucleation, slow condensation controls the synthesis also during the reflux treatment.

Other trials were done with GC-MS and IR, but they did not give appreciable results. In the first case, it was because TBT molecule was degraded due to injection temperature before the elution and in the second because with IR spectroscopy was not possible to discriminate within the OH signals of butanol with the one deriving from TBT precursor. UV-Vis spectroscopy was performed stirring several emulsions, in absence of surfactant and co-surfactant, for different time. This gave the formation of a biphasic cyclohexane/water system, maintained in close contact by vigorous stirring. The aim was to simulate the interface of droplets and study the dissolution of reagents in the two phases. Both the organic and water solutions were analyzed using water or cyclohexane as reference. The organic one did not give reasonable results, while for aqueous one data are reported in Figure 28 together with two reference solutions of nitric acid and butanol in water. Butanol in water shows a negative peak at 263nm, while nitric acid solution a positive one at 265nm[147]. The reaction trend starts at t=0 with no peaks, than a peak centered at 260nm increases up to 3h, gradually decreasing and slightly shifting to higher wavelength up to 5 and 7h and becoming similar to butanol peak at 24h. A possible explanation is that the two signals (butanol and HNO_3) are both present in the

samples but with different ratios. At 1h, the signal is zero because butanol is produced in significant quantity due to the starting of the hydrolysis reaction. Probably up to 3h, the signal increases because also condensation reaction starts within the mono-hydrolyzed TBT molecules, giving a lower amount of butanol produced, while nitric acid is still present. From 5 to 24h it is possible that small titania particles are formed and have left the micelle giving space for more butanol production up to water saturation. Besides, part of the acid can be consumed by coupling with free OH groups and diminishing its concentration. Nevertheless, nor the test timing is linkable with a microemulsion reaction due to system differences, but also the hypothesis done cannot be confirmed by other techniques.
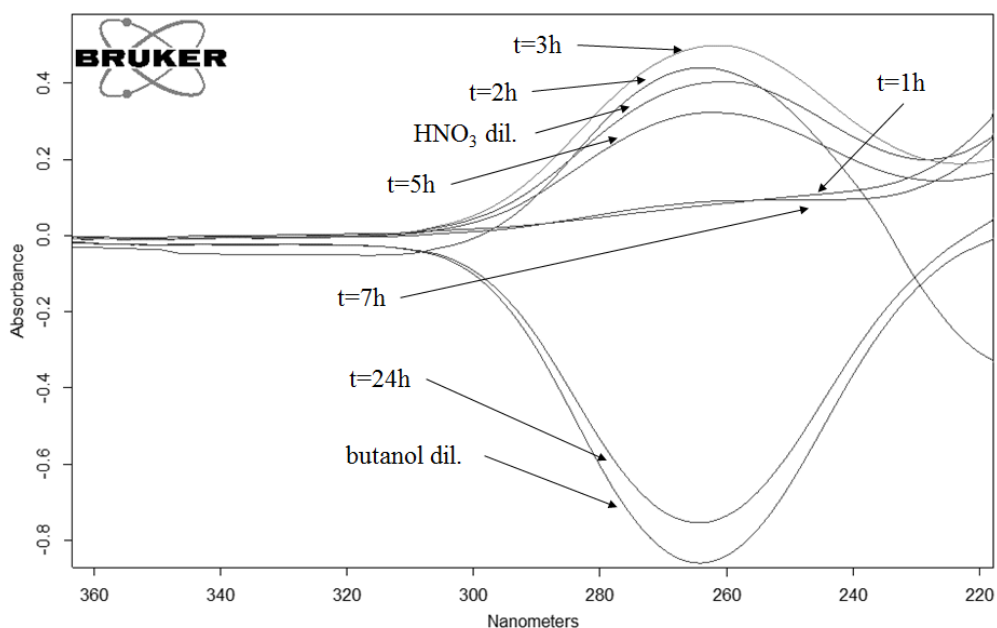

Figure 28: UV-VIS analysis of aqueous solutions in a test in absence of surfactant.

Some other synthetic parameters were modified in Table 3, analyzing the effect over TiO$_2$ features after the synthesis (crystallinity, surface area and rutile fraction). As first, the synthesis was carried out in absence of surfactant in sample A. The biphasic system was stirred to maintain the contact within an aqueous acid and organic phase containing the precursor at RT for 1h, and then heated at reflux temperature. Scherrer equation defines small particles dimension probably due to the immiscibility of the two phases,

and a rutile fraction of 64%. The absence of surfactant gives thus a not homogeneous system, together with a small yield in solid, due to the low interface surface that slows down hydrolysis rate. Samples B and C, represent the synthesis reported in the reference articles[120,129]. The first gives, as reported[129], over 90% of rutile with small surface area. This type of synthesis was not further analyzed because anatase phase is preferred in heterogeneous catalysis mainly for its higher surface area[137,148]. Sample C was obtained by hydrothermal treatment in autoclave[120] while the one reported as sample D is the optimized synthesis indicated in this work by reflux heating (Figure 29). Respect to sample C, the synthesis shows a higher rutile fraction (up to 7%) but smaller particle size and a slightly higher surface area derived by the less severe reflux treatment compared to hydrothermal. These data underlines that using reflux heating instead of hydrothermal conditions permit the obtainment of mainly anatase phase with good results in terms of particle dimension and surface area.
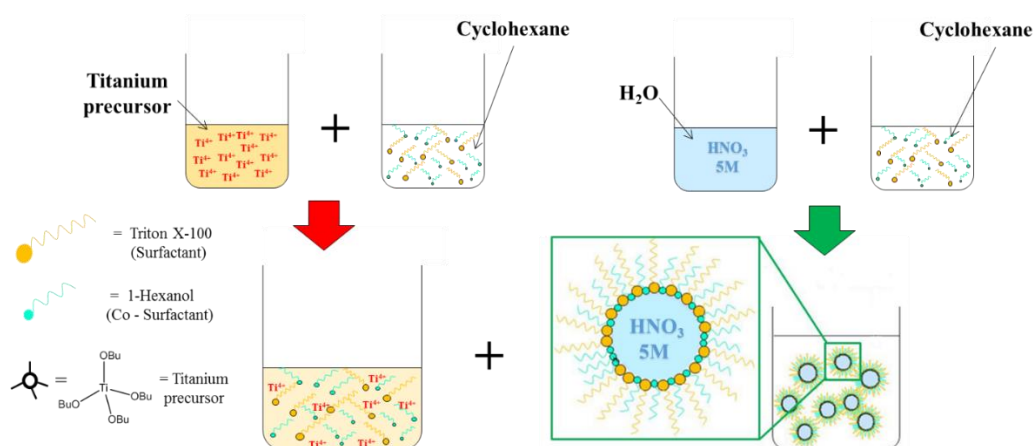

Figure 29: Schematization of the microemulsion preparation procedure.

Table 3: Characterization data for TiO₂ samples synthesized with method variation. Fr=weight fraction of rutile phase calculated by Rietveld over XRD analysis. Particle dimension are calculated by Scherrer equation. RT=room temperature

*value comparable with reference article 256m²/g after 13h of heat treatment reported in the reference article

	Surfactant + co-surfactant	Time of stirring RT	Heating type	Heating time (h)	Fr (%)	Particle dimension anatase (nm)	S_{BET} (m²/g)
Sample A	NO	1 h	Reflux	5	64	5	199
Sample B	✓	5 days	-	-	91	9	123
Sample C	✓	1 h	Autoclave (120°C)	4	1	5	249*
Sample D	✓	1 h	Reflux	5	7	4	319

5.1.2   *Characterization of TiO₂ and Pt/TiO₂*

TiO₂ synthesized by microemulsion technique (TiO₂-m) was calcined at 400°C, characterized and compared with a commercial high-surface area TiO₂ anatase (named TiO₂-comm). The sample prepared by microemulsion shows higher surface area and smaller pores with monomodal distribution, as reported in Table 4. Moreover, the hysteresis loop presented in Figure 31 is linkable to progressive size and shape pores[149,150], as reported in literature for similar microemulsion-synthesized titanium oxides[151], while the commercial sample with porosity attributable to slit-shaped channels. P-XRD analyses showed that 7% of the microemulsion solid synthesized was in rutile phase, while no other crystalline phases were detected in the commercial (Figure 30). The crystalline domain dimension, calculated by Scherrer equation, is reported in Table 4 and it is notably smaller for microemulsion sample, as peculiar for this kind of synthesis. This was also confirmed by TEM analyses that showing small crystallites for TiO₂-m sample and bigger aggregates for the commercial (Figure 32). The same analysis reports a similar distribution of the Pt particles centered at 1nm for the 1% wt. loading and 1.5nm for the 3%, TiO₂-m but with the simultaneous presence of bigger Pt aggregates up to 15nm for the commercial support. The analysis of acid

sites over the two titania samples was performed by ammonia temperature programmed desorption. The total NH_3 uptake (Table 4) is higher for the microemulsion sample compared to the commercial. The desorption curves, reported in Figure 33 are centered in the range 150-650°C showing for both the supports a convolution of Lewis acid sites[152] of different strength. At temperatures above 450°C, it was detected the release of water and CO_2 for both the sample by mass analysis, confirming also the higher NH_3 adsorption per unit of sample for the microemulsion support.
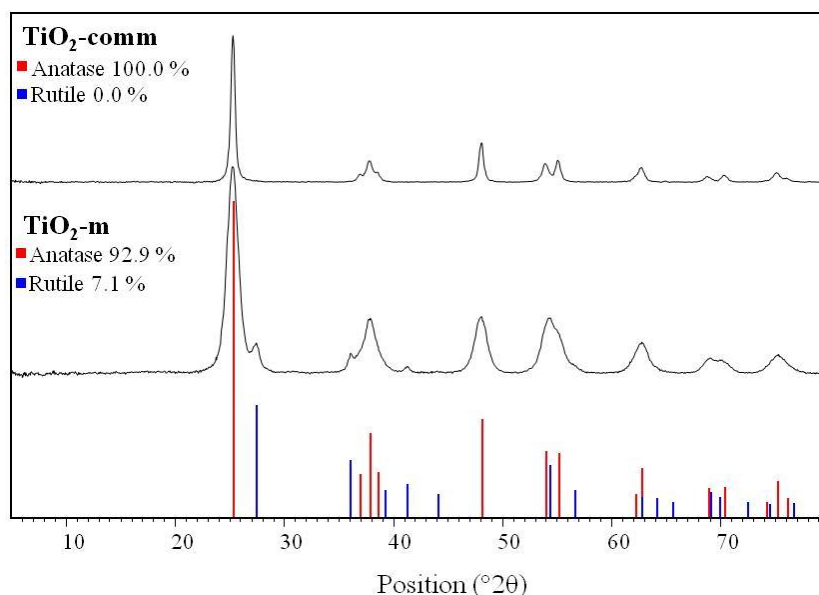

Figure 30: XRD analyses of he prepared sample and commercial, with anatase and rutile fractions calculated by Rietveld approximation. Reference patterns by database are reported with blue (rutile) and red lines (anatase).
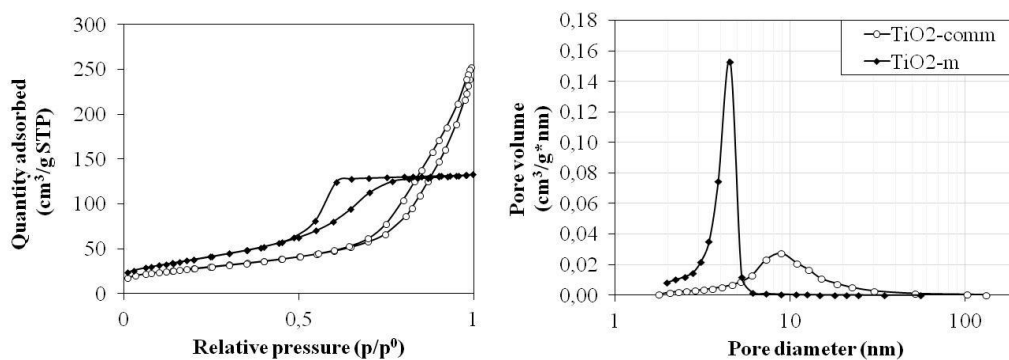

Figure 31: Adsorption/desorption isotherms and pore distribution of the TiO₂ samples.

Table 4: Characterization of TiO₂-m compared to a commercial sample. Particle size is calculated by Scherrer equation, surface characterization done by porosimetry and ammonia uptake by TPD analysis.

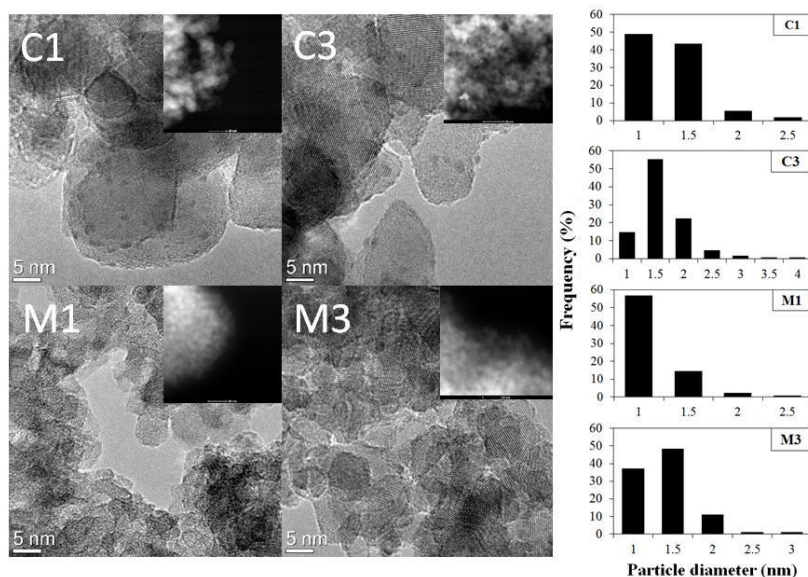|	Crystal phase	Particle size (nm)	S_{BET} (m²/g)	V_{pore} (cm³/g)	Pore average diameter (nm)	NH₃ uptake (cm³/g STP)
TiO₂-comm	anatase	24	90	0.32	14.6	9.2
TiO₂-m	anatase	8	152	0.15	5.9	13.3

Figure 32: TEM images of Pt/TiO₂ (C=commercial, M=microemulsion; the number represents the metal loading of Pt) and Pt particles distribution.
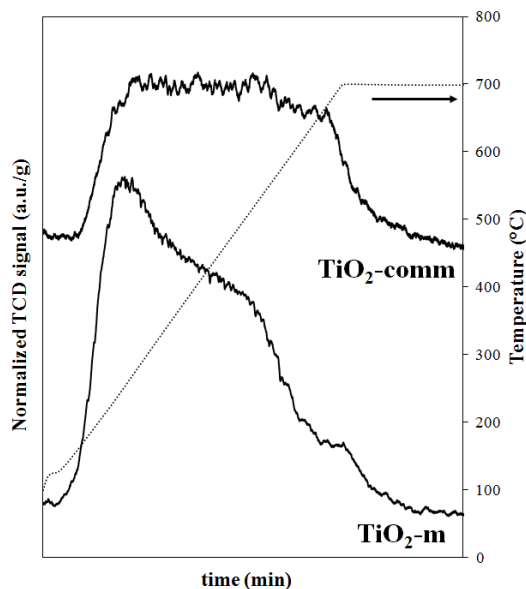
Figure 33: Temperature programmed desorption analysis of NH₃.

TiO_2 is a well-known support in literature for the strong metal support-interactions with noble metals as Pt and Pd that causes the partial reduction of TiO_2 to TiO_{2-x} (x<2)[153–159]. TPR and H_2 pulse chemisorption analyses evidenced a different interaction within the Pt particles and the support for the commercial and microemulsion. The reduction of the catalyst showed two peaks, the first one below 200°C for the reduction of PtO and a second one above 350°C due to the transformation of neighboring Ti^{4+} ions into Ti^{3+} (Figure 34)[153–159]. Nevertheless, a negative peak is present around 250°C for both the samples more evidenced for the microemulsion support, attributed by mass analysis to the production of water by the reduction process[156]. The different area of this peak suggests a more effective reduction and hydrogen consumption for the TiO_2-m support but prevents a quantitative analysis of the consumed hydrogen. The stronger interaction within Pt and TiO_2-m was proved by H_2 chemisorption analyses performed at 50°C and -40°C to minimize the spillover effect (Figure 35). Table 5 shows that in both the conditions, the microemulsion catalyst absorbs more hydrogen quantity giving an active metal surface area of $3.7m^2/g$ even at low temperature with a Pt dispersion of 50% compared to the $0.2m^2/g$ and 2% of the commercial support. This can be possibly explained by the better reducibility of smaller TiO_2 particles compared to the commercial[160], with a possible effect of coverage of Pt particle by TiO_2 crystallites

(named strong metal-support interactions). The higher reducibility of Pt/TiO$_2$-m may also justify the higher water production in TPR measurements. Another parameter evidenced by chemisorption analyses is the spillover effect of the two supports at different temperatures. The microemulsion sample maintains almost halves its adsorption at low temperature but not lowering significantly the active metal surface area. Oppositely, the commercial support reduces its adsorption of more than thirty times, evidencing not only the drastic reduction of spillover effect but also a possible diminution of reducibility bigger Pt agglomerates. The average dimension of Pt crystallites at high temperature confirms TEM data, a part from the low temperature commercial sample, probably due to the presence of bigger aggregates with not complete reduction. This demonstrates both the better dispersion of Pt over the microemulsion support and the improved interaction within the noble metal and the reducible support even at low temperature.

Of lower relevance in terms of heterogeneous catalysis, but interesting for future photocatalytic applications, Figure 36 repots the UV-VIS bandgap of the two supports in presence and absence of Pt. It can be noted the shift towards visible wavelength of the microemulsion support, favoring its use with solar simulator systems even in absence of dopants and linked to the difference in particle size within the two titania. The difference is maintained in presence of Pt but with lower reflectance values due to the color of the system.
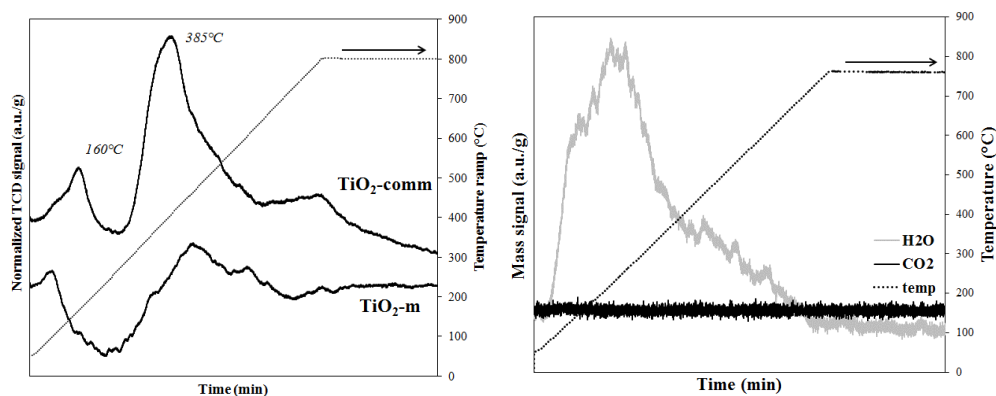

Figure 34: Temperature programmed reduction of the Pt loaded supports on the left and mass analysis of the reduction of Pt/TiO$_2$-m support on the right.
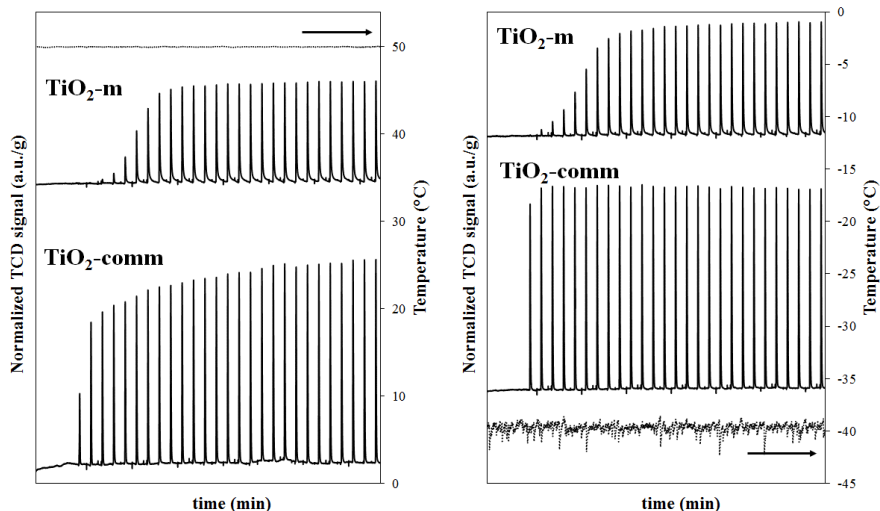
Figure 35: Pulse chemisorption analysis of Pt/TiO₂, analysis performed at 50°C on the left and -40°C on the right.

Table 5: H₂ Chemisorption analyses at different temperature for 3% Pt loaded supports.

	Analysis temperature (°C)	Quantity adsorbed (cm³/g STP)	Active metal SA (m²/g)	Metal spherical crystallites (nm)	Metal dispersion (%)
Pt/TiO₂-m	50	2.34	5.02	1.70	67.80
Pt/TiO₂-comm	50	1.85	3.97	2.15	53.60
Pt/TiO₂-m	-40	1.74	3.73	2.29	50.39
Pt/TiO₂-comm	-40	0.07	0.15	55.62	2.07

Figure 36: Kubelka-munk functions (right) and bandgap energies (left) of supports and Pt supported catalysts.

5.1.3   *Preliminary tests*

Preliminary APR tests were done analyzing first of all 1%wt. catalysts at different temperature. As reported in Figure 37, conversion was close to 10% at 200°C, increases slightly at 225°C and shows a sign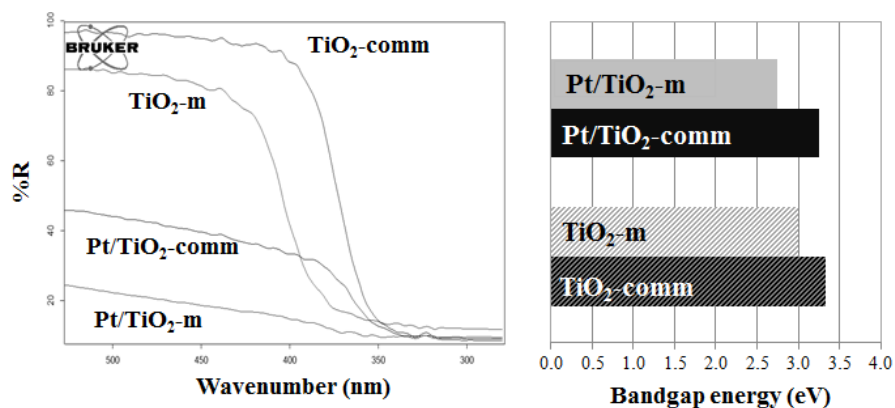ificant increase up to 55% at 250°C. Nevertheless, gas and liquid yield were very low even at the highest temperature. It was additionally found that at the end of the reaction Pt was in its reduced state, due to the adsorption of H_2 from the reaction environment. A comparison within the reactivity at different temperature and unreduced and reduced catalyst is given within Figure 37 and Figure 38. Conversion values are similar but yields in gas and liquid products are significantly different. In particular, H_2 yield is increased from 2 to 4% while CO_2 up to 6%. In liquid phase, 1,2-propanediol is favored and also C_2 products as ethylene glycol and propylene. From the reported data, it seems likely part of the hydrogen is consumed in catalyst reduction at the beginning of the reaction, slightly reducing activity in liquid phase reactions. Thus, following tests were performed with pre-reduced catalyst to avoid time and hydrogen losses during reaction. These preliminary tests allow choosing the conditions for the reaction studies: in particular, the tests at 250°C were used to verify the reactivity at the highest conversion conditions, while reactions at 225°C were used to enhance selectivity in primary liquid products and study the reaction mechanism.

A first study on the time of reaction was done at 250°C with Pt/TiO_2-m for 1.5, 3 and 4.5h (Figure 39). CO_2 and CH_4 are constant from 3 to 4.5h, also H_2 with all the reaction time. In the liquid phase, hydroxyacetone yield decreases by increasing the reaction time together with 1,2-propanediol, which is the main product after 3h. On the other hand, 1-propanol at 4.5h becomes the most abundant. Lactic acid instead remains more or less constant. The trend indicates that apparently lactic acid, 1,2-propanediol and hydroxyacetone are formed in the first stages of reaction, while secondary products appear to be ethanol, ethylene glycol, propionic acid and 1-propanol. The increase in conversion should go in parallel with an increase in H_2 yield by dehydrogenation pathway (through glyceraldehyde intermediate[45]). However, H_2 selectivity appears as

constant with reaction time because hydrogen-consuming secondary reactions take place, i.e. 1,2-propanediol and 1-propanol production.
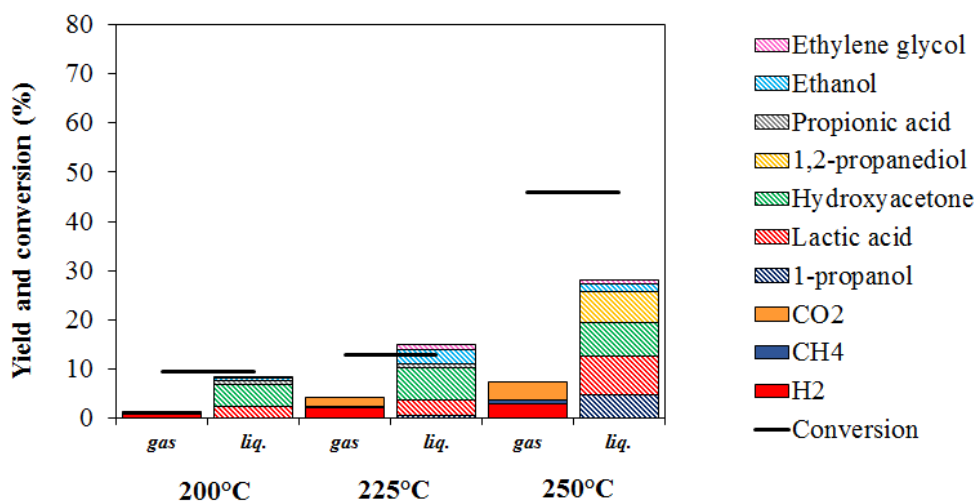

Figure 37: Gas and liquid yield and conversion for Pt/TiO$_2$-m 1%wt not reduced. Reactions performed for 3h; glycerol loading 17% wt.
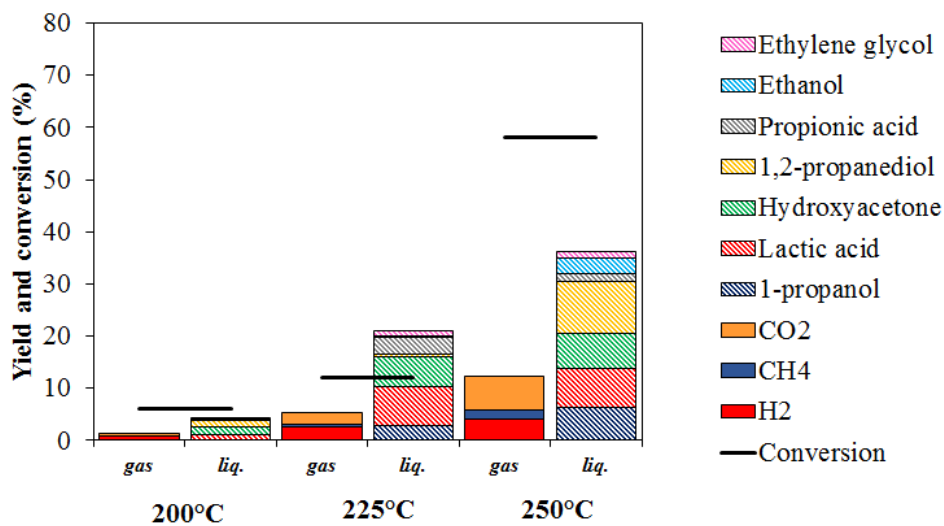

Figure 38: Gas and liquid yield and conversion for Pt/TiO$_2$-m 1%wt reduced. Reactions performed for 3h; glycerol loading 17% wt.
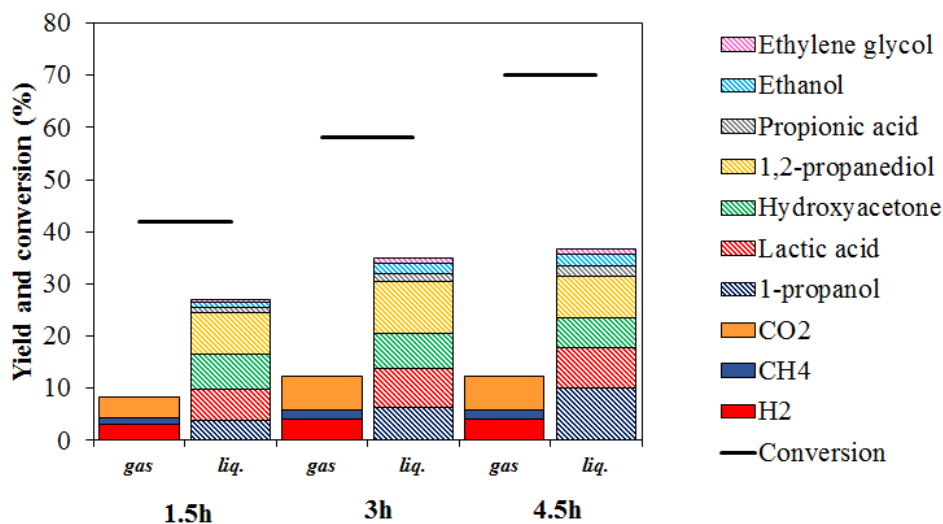
Figure 39: Gas and liquid yield and conversion for Pt/TiO$_2$-m 1%wt reduced. Reactions performed at 250°C; glycerol loading 17% wt.

5.1.4 **Effect of metal loading**

Metal loadings of 1 and 3%wt. were studied, in line with the literature data with a Pt content usually within 1 and 5%wt. [35,47,161,162]. To better compare the activity of the catalysts at different conversion values, selectivity data are presented. Reactions performed at 250°C for 3h indicate an increase in conversion from 58 to 72%. H$_2$ and CO$_2$ selectivity increase slightly while CH$_4$ remains close to the same value (Figure 40). Liquid phase selectivity instead are significantly changed: hydroxyacetone selectivity is lowered from 12% to 6% and 1,2-propanediol raises proportionally suggesting that it could be a secondary product deriving from hydroxyacetone. Also 1-propanol is enhanced because it may be produced by a consecutive reaction from 1,2-propanediol. In addition, lactic acid selectivity is lower for higher conversion values in agreement with the hypothesis of primary product.

Nevertheless, the selectivity sums of dehydrogenation pathway products[45,46] (lactic acid, ethanol, ethylene glycol and propionic acid) and dehydration pathway products (hydroxyacetone, 1,2-propanediol and 1-propanol) remain approximately constant for the two loadings. This could mean that increasing the metal loading does not change the selectivity of the catalyst in the activation of glycerol but only increases the reaction

rate and selectivity in consecutive products. This is confirmed also by the conversion, which increases in parallel with the loading. Nevertheless, H_2 selectivity is not enhanced of a large extent from 7 to 10%. The main explanation of this behavior is that, while increasing the rate of hydrogen production, also its consumption in parallel reactions is favored. The demonstration of this assumption can be done by considering the selectivity sum of products deriving from hydrogen-consuming reactions, (1,2-propanediol, 1-propanol, acetone and CH_4) normalized by their stoichiometry factor. The results are that selectivity in hydrogen-consuming products accounts for 44% for the 1%wt. loading and 53% for the 3%wt. By summing then the obtained values with H_2 selectivity detected at the end of reaction is possible to deduce that the total H_2 produced and consumed during the reaction is higher for the 3%wt. catalyst compared to the 1%wt. The major activity of the 3%wt. loading is due to the higher number of particles and sites available on the surface[44] because the increase in loading causes a small rise their dimension, as detected previously by TEM measurements.
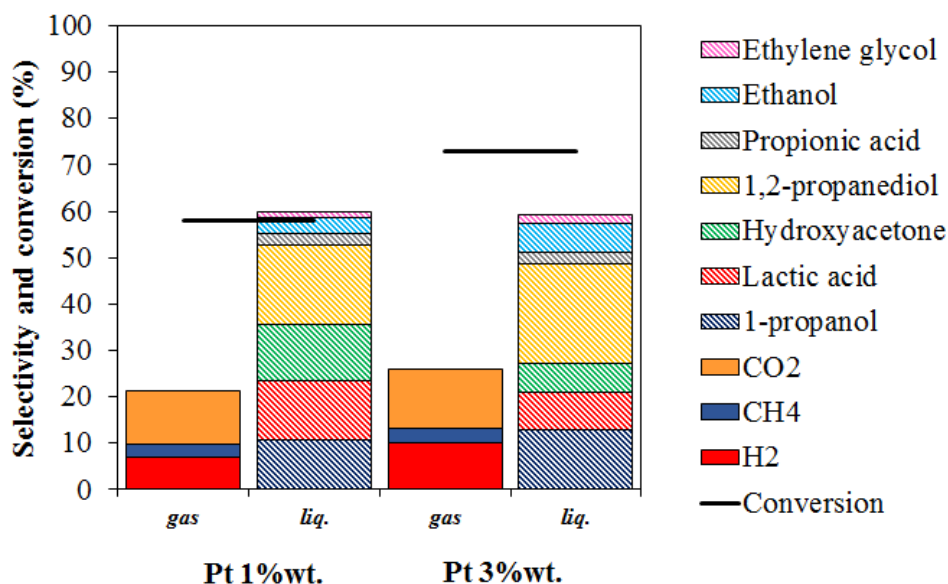

Figure 40: Gas and liquid selectivity and conversion for Pt/TiO$_2$-m 1 and 3% wt. Reactions performed at 250°C for 3h; glycerol loading 17% wt.

In conclusion, it is demonstrated that the reaction is sympathetic with the variation of the quantity of metal and its presence is necessary to drive the reaction to higher yield

in products because conversions lower than 12% were obtained with TiO_2 tests in absence of metal.

5.1.5   *Study of the mechanism of reaction*

The analysis of the selectivity trend over time gives a good indication over primary and secondary products in liquid phase. Reactions were performed with 3%wt. catalyst supported on microemulsion TiO_2 lowering both temperature at 225°C and glycerol quantity to 6%wt. to better analyze reaction trends (Figure 41). Time zero was considered as the moment in which the system reaches the reaction temperature and rapidly cooled. H_2 selectivity is higher at low reaction time, while decreases with time due to the consumption in liquid phase. Hydroxyacetone and lactic acid are formed since the early stages of reaction as primary stable products in the reaction environment. In particular, the decrease in lactic acid concentration is linkable to propionic acid growth as its secondary product; similarly for hydroxyacetone and 1,2-propanediol. Lactic acid is a common reaction product for hydrogenolysis of glycerol from glyceraldehyde intermediate in presence of an homogeneous and heterogeneous bases[163–165]; lactic acid and other acids are reported being produced from glycerol by rearrangement mechanism even in acid environment obtained for the presence of TiO_2 (pH=3-4 after reaction)[45,166]. Moreover, Lewis acid sites are known as responsible for the transformation of C_3 into lactic acid and its lactate salt, depending on the presence of an alcohol in the reaction mixture[167–170]. Ethylene glycol does not appear to be correlated with the other products but may be related to CO_2 production by loss of carbon from glycerol and acting as intermediate product for ethanol. Lastly, 1-propanol and propane show a trend different from the previously reported with a slow and constant increase with time, suggesting a behavior of tertiary products. In gas phase, CO_2 production cannot be completely accounted by C_2 production because several processes are involved in its production as decarbonylation, decarboxylation, water gas shift and in part reforming. Analogously, CH_4 selectivity can be the result of C-C cleavage to C_2, combined with a surface recombination with adsorbed hydrogen. In literature it is reported being produced by several mechanisms: together with ethanol over Ru catalysts from degradation of 1,2-propanediol in presence of an hydrogen-rich

environment[171,172], by prior cleavage of C-O bond and sequent C-C[173], by reforming of methanol or ethanol[46,174] or by CO or CO_2 methanation[45]. Since CH_4 selectivity in the present reaction appears constant with time, it may be formed by a complex reaction mechanism from primary and consecutive products. Likely it comes from the cleavage process through alcohol intermediate; from methanol it is not detected since in this conditions is completely reformed; from glycerol to ethylene glycol transformation which shows the same trend, or by 1,2-propanediol to ethanol.

Tests with intermediates of reaction were performed to confirm the hypothesis based on the time of reaction (Table 6, tests A, B, C). To simulate the reaction environment the reactions were performed under H_2 pressure. Reported data confirm lactic acid as precursor for propionic acid, hydroxyacetone is the intermediate mainly to 1,2-propanediol and ethanol giving also 5% of acetone, while ethylene glycol gives only ethanol as liquid product. CO_2 yield is linked for tests A and B with the production of ethanol by decarbonylation reaction. As for ethylene glycol the high CO_2 yield can be due to possible direct reforming reaction, since the amount of H_2 detected at the end of reaction was higher compared to the beginning. CH_4 production instead is higher for hydroxyacetone, confirming the possible degradation of 1,2-propanediol to methane and ethanol.
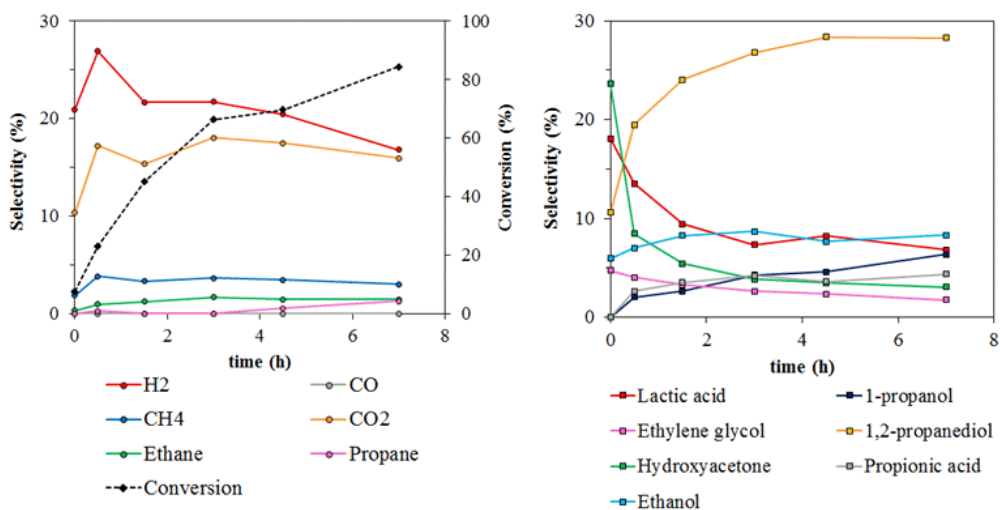

Figure 41: Liquid and gas phase products trend. Reactions performed at 225°C over Pt/TiO$_2$-m 3% wt. catalyst; glycerol loading 6%.

Table 6: Results of reactivity tests with intermediates. Reactions performed at 225°C for 3h over Pt/TiO$_2$-m 3% wt; amount of reagent 1.5g in 50ml water, 0.45g of catalyst. P (H$_2$) refers to the initial gas pressure loaded in the reactor before heating at the reaction temperature.

	reagent	Gas phase yield and pressure			Liquid phase yields					
		P (H$_2$) bar	CO$_2$	CH$_4$	lactic acid	1-propanol	1,2-propanediol	hydroxyacetone	propionic acid	ethanol
A	lactic acid	3	2	1	-	0	2	0	22	2
B	hydroxyacetone	3	11	4	1	4	31	-	2	9
C	ethylene glycol	3	11	1	0	0	0	0	0	11
D	pyruvaldehyde	-	5	1	72	0	9	8	8	4
E	pyruvaldehyde	3	5	1	56	0	23	5	6	0

Thanks to experimental data and linking with literature reported mechanisms over glycerol and ethylene glycol both for APR[18,45,46] and hydrogenolysis reactions[44,136], it was possible to draw the reaction scheme in Figure 42. No aldehydes were detected in the reaction environment probably due to their high reactivity. The main transformation pathways over glycerol are dehydrogenation or dehydration pathway. The first is supposed to pass through glyceraldehyde intermediate, as reported in several literature articles[45]; the H$_2$ produced can further undergo hydrogenation reactions. The main products detected in this pathway are lactic acid and propionic acid, with the possible production of ethanol. In parallel, dehydration on the primary alcoholic group of glycerol can give 1,2-propanediol and 1-propanol through keto-enol equilibrium. On the other hand, dehydration over the secondary alcoholic group of glycerol to 1,3-propanediol was not observed, probably due to steric hindrance of the absorption and lower statistical probability.
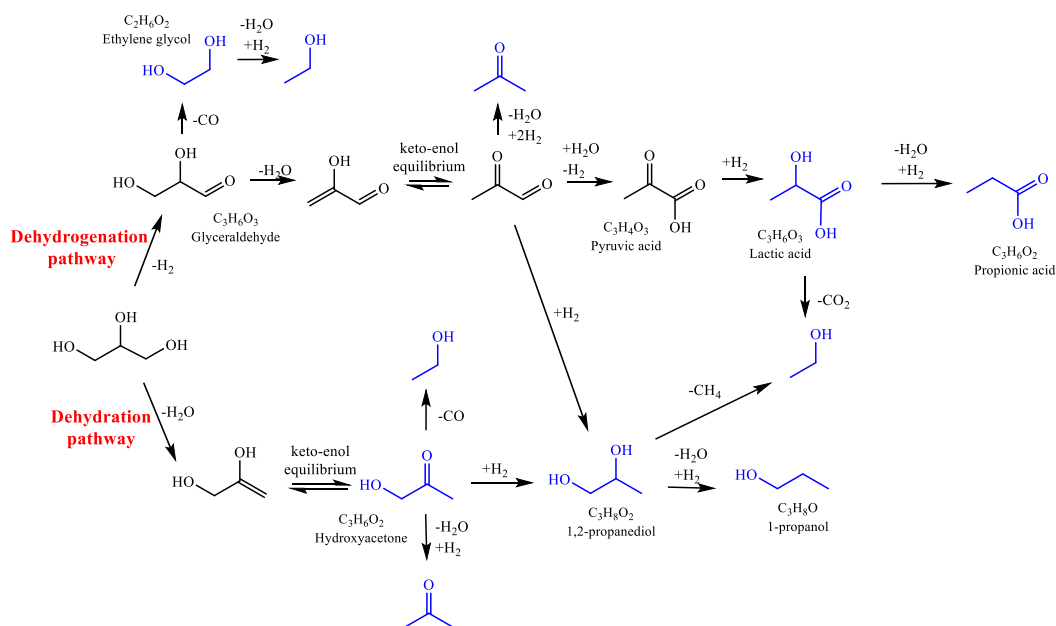
Figure 42: Hypothesis on the mechanism of glycerol conversion. Blue products have been detected, black ones are supposed by literature data.

The complexity of this mechanism is enhanced by the possibility of interchange within the two pathways, as demonstrated in entries D and E in Table 6. Reactions performed over pyruvaldehyde, a supposed intermediate of dehydrogenation pathway, gave different results in presence or absence of H_2 pressure. In particular, in the first test, dehydrogenation pathway was favoured with the production of lactic acid mainly, while in presence of hydrogen 1,2-propanediol yield was significant, even remaining lower than lactic acid formation. Thus, depending on the amount of hydrogen produced by the reaction, the two pathways can be interconnected, as reported also in literature[170].

5.1.6   *Comparison within Pt over TiO₂-m and TiO₂-comm*

The catalyst supported on titanium oxide synthesized by microemulsion technique was compared with a commercial high surface area support impregnated with the same 3%wt. loading of Pt. All the reported selectivity values for the comparison within the supports normalized to the carbon balance, due to differences in carbon loss within the reaction. Since the sum of selectivity is calculated taking into account the stoichiometry from glycerol to the selected carbon-containing product, the total value can exceed

100% due to the presence of H_2, which is independent from carbon-containing molecules.

A first test was performed comparing the two catalysts at the same conditions (225°C, 3h) and it is reported in Figure 43. The difference in conversion is significant: for the microemulsion support, glycerol conversion reaches 66% with a 27% H_2 and a 33% 1,2-propanediol selectivity. In comparison, the commercial sample is 4 times less active and presents major selectivity in primary products as lactic acid and hydroxyacetone with very low amount of hydrogenated products. A further comparison of the support activities without Pt confirmed the microemulsion support as more active, even at conversions lower than 8%. In addition, even if the support activity is very low compared to Pt loaded, the presence of some amount of products it is an indication that the support itself can participate to the reaction and enhance Pt activity. A more specific evidence of the improved support activity is the sum of dehydration products (hydroxyacetone, 1,2-propanediol and propanol) that is known to be possible over TiO_2 surface by the presence of acid sites[152,175], which is higher for Pt/TiO_2-m sample.
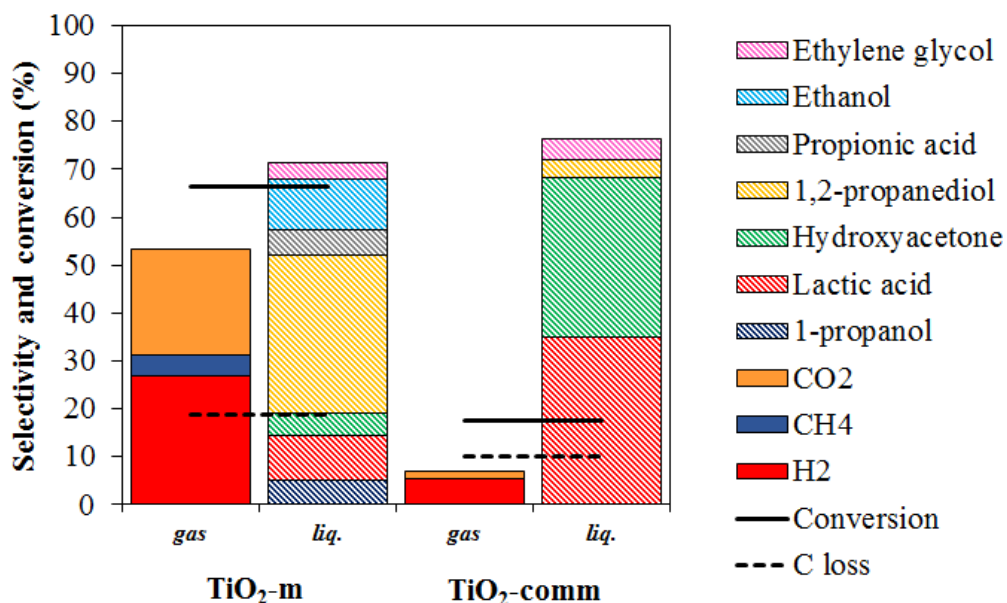

Figure 43: Comparison within 3% wt. metal loading TiO₂-m and comm. Reaction performed at 225°C for 3h; glycerol loading 6%.

To confirm further the improved activity of the Pt/TiO$_2$-m catalyst, two tests with similar conversion data and different reaction conditions were compared. In the first parallel, microemulsion Pt/TiO$_2$ test was performed at 225°C for 3h, while for the commercial at 250°C. Figure 44 clearly reports an enhanced rate of reaction for the microemulsion support with a higher selectivity in gas phase, in particular decarbonylation and decarboxylation reactions, and secondary liquid phase products compared to the commercial. Inasmuch different temperatures can influence the rate of reaction, another comparison was performed at 225°C and lower glycerol feed for both the samples but with different reaction time (Figure 45). A conversion around 8% was obtained for 0h of reaction for the microemulsion support, while 12% value after 1.5h for the commercial. In this case, the primary products are prevalent for the Pt/TiO$_2$-m, with 27% selectivity in H$_2$ and 14% in CO$_2$ but with significant yield even in secondary as 1,2-propanediol and ethanol. As for the commercial, it shows scarce gas product generation and mainly hydroxyacetone and lactic acid in liquid phase, with small selectivity in other secondary products. The reported comparisons can thus be a confirm of the higher activity in APR of the microemulsion synthesized support in different reaction conditions, since it presents always higher hydrogen selectivity and not negligible presence of secondary and tertiary products in liquid phase.

Figure 44: Comparison of tests with the same conversion value. Metal loading 3%, time of reaction 3h, glycerol feed 17%. Pt/TiO$_2$-m test performed at 225°C, Pt/TiO$_2$-comm at 250°C.
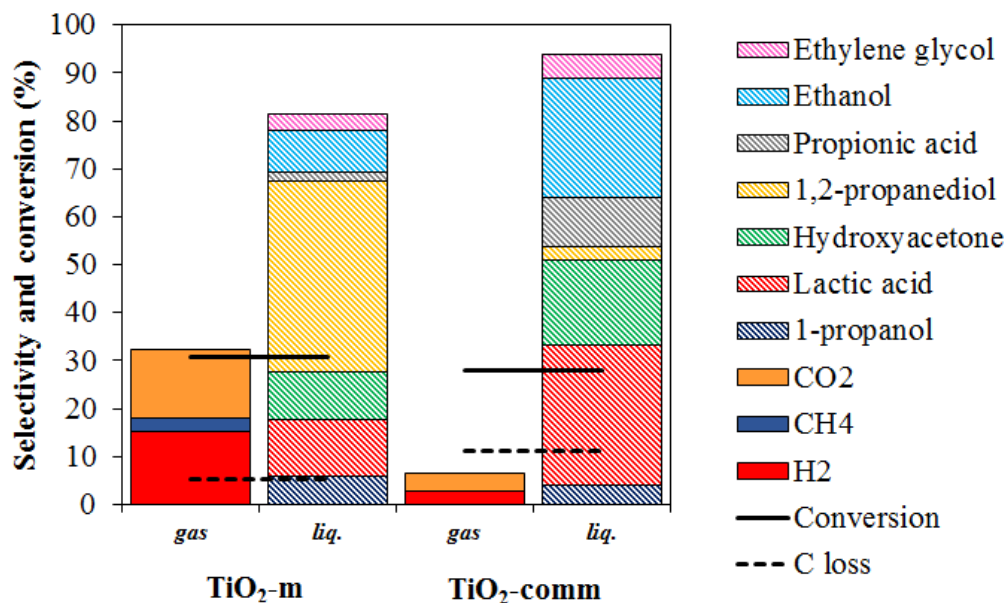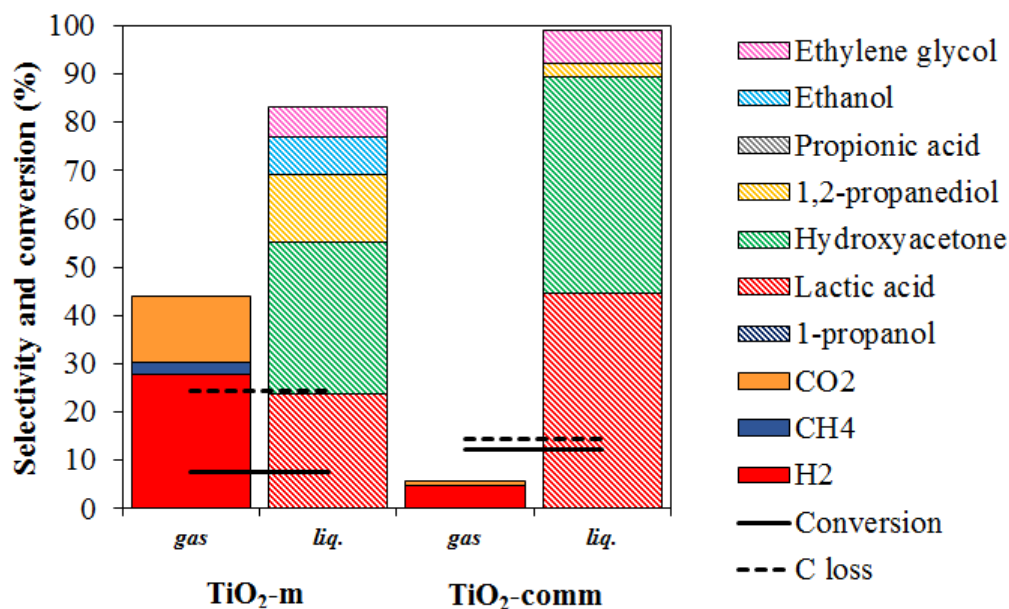

Figure 45: Comparison of tests with the same conversion value. Metal loading 3% temperature 225°C, glycerol feed 6%. Pt/TiO$_2$-m test performed for 0h, Pt/TiO$_2$-comm for 1.5h.

The differences within the supports were highlighted by characterization and are due to surface area, pore distribution, crystallite dimension and density of acid sites. As

reported in literature for alcohols, the adsorbed species can undergo dehydration over TiO_2, while it can give decarbonylation or dehydrogenation over the metal site[175]. Nevertheless, even if the support activity was demonstrated higher for the microemulsion titania, in presence of Pt it is not enough to explain the enhancement in activity. In fact, the interactions within metal and support play a major role for this class of catalysts. The stronger interactions within Pt and TiO_2 observed for the microemulsion support by chemisorption analyses compared the commercial permits to formulate the hypothesis of an improved exchange of adsorbed intermediates within the metal and the support. This assumption, coupled with the better surface properties of the microemulsion sample explains the higher activity of this catalyst, even considering the similar Pt dispersion on the surface of the two titania.

5.1.7   Recycle tests

Pt/TiO_2-m catalyst stability was tested at 225°C for 3h cycles. The catalyst was separated from the reaction mixture, washed, dried and reused as is in the sequent reaction. Results are presented in Figure 46 with normalized carbon yield. After the first loss catalyst remains stable for all the tests. Conversion decreases from 66 to 56-54%, lactic acid and hydroxyacetone increase slightly, while propionic acid, propanol, CH_4 and CO_2 selectivity decrease probably due to a reduction of catalyst activity that favours primary products compared to secondary. Propylene glycol, ethylene glycol and ethanol instead remain mainly constant with small fluctuations attributable to error. Furthermore, H_2 selectivity decreases from 27 to 16%. Considering that H_2-consuming reactions do not change within the recycles, it means that the capacity of producing hydrogen of the catalyst is reduced, probably due to the equilibration of the Pt in the first stage of the reaction (sintering) or coverage of some metal particles by heavy carbon containing molecules. An analysis over 1st cycle spent catalyst by TEM evidenced a slight increase in particle dimension together with the partial coverage of Pt particles by migration of oxide particles or carbon formation. In addition, a reduction of $20m^2/g$ in surface area was observed from fresh to spent catalyst. After the first stage loss of activity, conversion and selectivity values are maintained constant with the recycles, confirming the assumption of a stable catalyst with time.
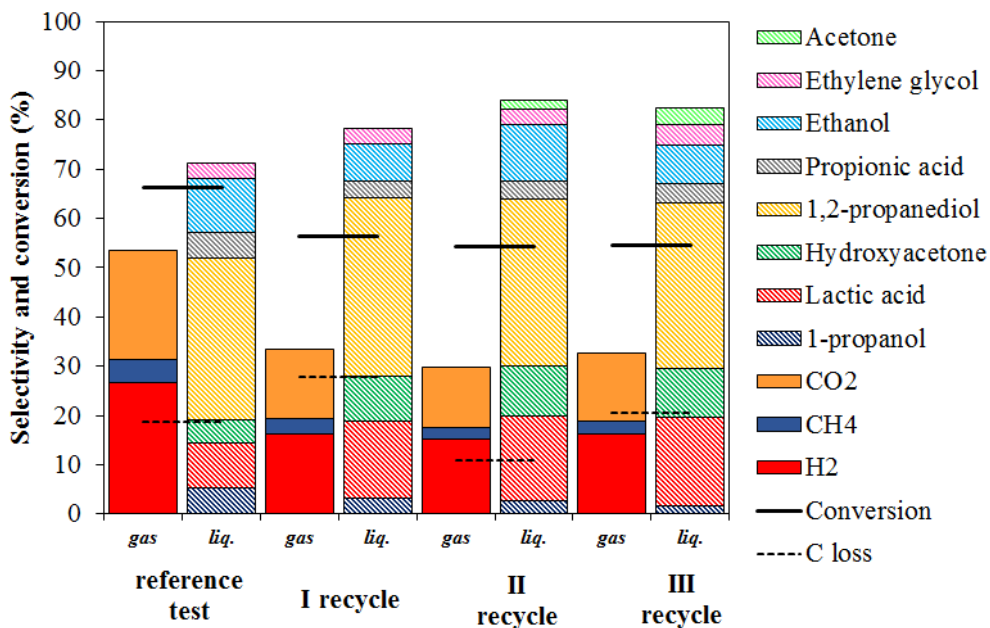
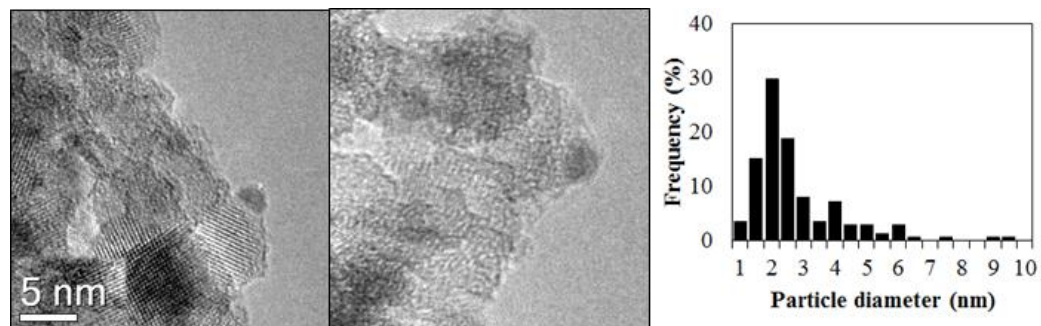*Figure 46: Recycle tests performed at 225°C for 3h with Pt/TiO₂-m 3%wt.Glycerol feed 6%.*

Figure 47: TEM images and metal particle distribution of Pt/TiO₂-m catalyst after 3h of reaction.

5.2   MgO and Mg/Al mixed oxides

Catalysts for Aqueous Phase Reforming reaction can be defined as bifunctional systems, since the support is participating in the reaction pathway in presence of an active metal. It is thus important to study the effect of the interactions within support active site properties and Pt. Within the most used oxides, MgO is the widely used basic support and it is reported having the highest results in hydrogen production via APR[176]. Starting from MgO studies it was developed an analysis over basic and acid sites with different Mg/Al ratios in a mixed oxide structure and a reference commercial γ-Al$_2$O$_3$ with acid properties with the aim of analyzing its effect in APR product distribution.

5.2.1   Preliminary tests over MgO

Precipitation technique from nitrate salt at constant pH allows the obtainment of high surface area MgO, up to 89m^2/g for a sample calcined at 650°C. The oxide, loaded with Pt 1%wt. was tested as is in the APR reaction at different temperatures. The results are shown in Figure 48. Compared to the previously reported data for TiO$_2$ (Figure 38), MgO shows a linear increase in conversion, but with lower values at high temperature reaching a 42% conversion compared to TiO$_2$ 58% at 250°C. Nevertheless, differently from the other support, the gas phase distribution favors hydrogen production than CO$_2$, and H$_2$ yield reaches 6% at 250°C. Also in liquid phase, MgO favors the production of lactic acid, in line with a higher dehydrogenation trend, disfavoring dehydration and decarboxylation pathways. A comparative test with only support showed the same trend of lactic acid and small quantities of hydrogen produces, but with negligible conversion lower than 2%.
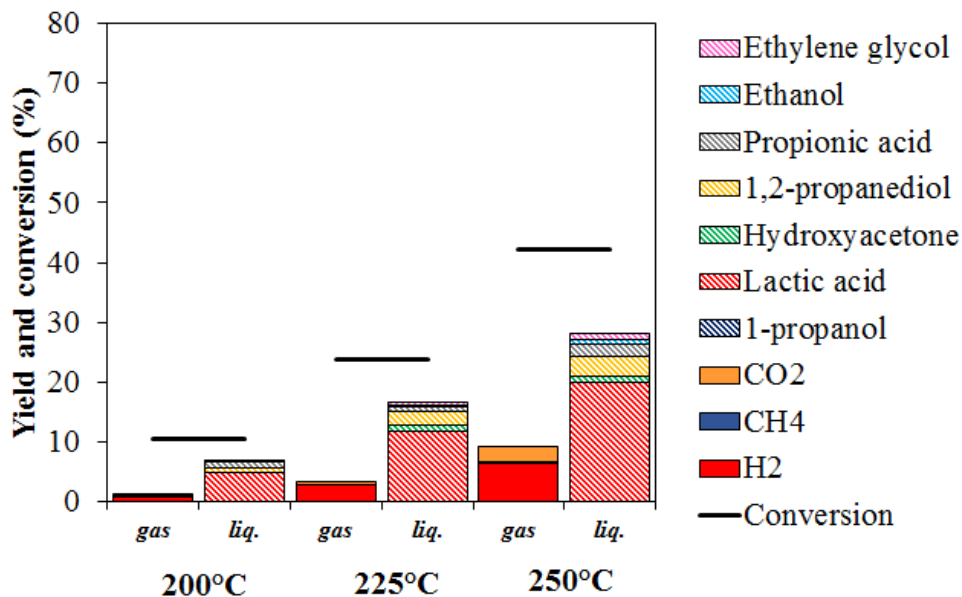
Figure 48: Gas and liquid yield and conversion for MgO 1%wt not reduced. Reactions performed for 3h; glycerol loading 17% wt.

Even if MgO shows an enhanced hydrogen yield compared to TiO_2, one of its main disadvantages as support is the instability in the reaction environment in terms of both crystalline phase and recovery. Preliminary tests showed a return of MgO periclase phase to brucite Mg(OH) after reaction, together with a significant loss of catalyst at high reaction temperature. The first is a widely known issue in water environment and depends on the hydration of surface periclase layers, as reported in literature[177,178]. The loss of catalyst is a combined effect of Mg(OH) formation and the final reaction pH, due to the presence of acids within the products. Reactions at 200-225°C showed a final pH value around 8-9, while at 250°C the pH was 4. Moreover, lactic acid itself (pK_a=3.86) can work as a ligand for the removal of Mg from the brucite layers[179]. Thus the combination of acid pH, with an increase of thickness of Mg(OH) superficial layer at high temperature and a larger quantity of lactic acid can cause the partial dissolution of MgO. Even if in principle the interaction with Mg^{2+} can affect the quantification of acids and in particular of lactic acid, in practice, the determination of the product was not affected since lactic acid will be restored by the excess of acid eluent in HPLC analysis. To limit the dissolution of MgO, the calcination temperature of the oxide was

increased up to 750°C. This temperature allows a higher crystallinity of the solid together with a limited loss in superficial area.

5.2.2   *Synthesis of MgO via microemulsion technique*

The interesting results obtained with titania microemulsion synthesis suggested the application of this method also to other oxides. Since in this case the precursor is a nitrate salt soluble in aqueous phase it was adapted a method reported in literature for Ce/Zr mixed oxides[131]. The oil solution was prepared maintaining the organic compound ratios of Ce/Zr preparation while it was adjusted an Mg/base ratio of 1:2.2 to maintain the excess for precipitation. DLS analysis of the cation-containing microemulsion showed a monomodal distribution centered at 38nm while the base microemulsion was opalescent due to pH interactions with the surfactant. The precipitation of the oxide was obtained both by sonication and reflux treatments, the second being more reproducible. Other parameters analyzed were the metal precursor concentration and the R_w factor, with the aim of increasing the solid yield per volume of solution, which was much lower compared to TiO_2 synthesis. The increase in R_w was done at constant total organic concentration within 14 and 56; unfortunately, the system was not stable towards the increase in amount of water solution. On a second test, the salt concentration was increased from 1 to 3M maintaining $R_w=14$ and the ratio within Mg and precipitating agent. The microemulsion system in this case was stable, while the amount of solid obtained per unit of volume was increased not proportionally to the cation increase.

The microemulsion-obtained solid was calcined at 650°C and characterized in comparison with the solid by precipitation. They both presented periclase phase with similar nanocrystal dimension around 10nm (Table 7). Even if the precipitation method was reported to produce a high-surface area solid, the porosimetry analyses show a higher value for the microemulsion sample, with monomodal pore distribution and higher pore volume. Moreover, as for the previously reported microemulsion titania, the hysteresis loop (Figure 49) is similar to progressive size and shape pores, while the commercial sample has porosity attributable to slit-shaped channels[180,181]. TEM images

of 1%wt. Pt supported catalysts (Figure 50) evidenced for both the supports a composition of lamellar and spherical structures confirming the dimension of the particles determined by Scherrer equation. The distribution of Pt particles on the surface is centered at 1-1.5nm for both the samples, but it shows a more wide distribution for the microemulsion sample for the presence of bigger aggregates. The MgO-p sample has a multimodal distribution showing also small pores, together with a sharper Pt particles distribution.
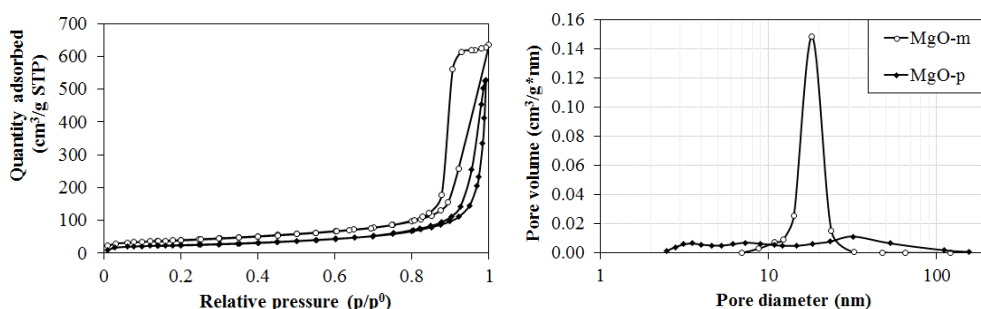
Figure 49: Adsorption/desorption isotherms and pore distribution of the MgO samples calcined at 650°C.

Table 7: Characterization of MgO-m compared to MgO-p sample calcined at 650°C. Particle size is calculated by Scherrer equation, surface characterization done by porosimetry.

	Crystal phase	Particle size (nm)	S_{BET} (m²/g)	V_{pore} (cm³/g)	Pore average diameter (nm)
MgO-p	periclase	10.8	89	0.64	3.5-7.3-31.8
MgO-m	periclase	9.8	143	0.98	18.2
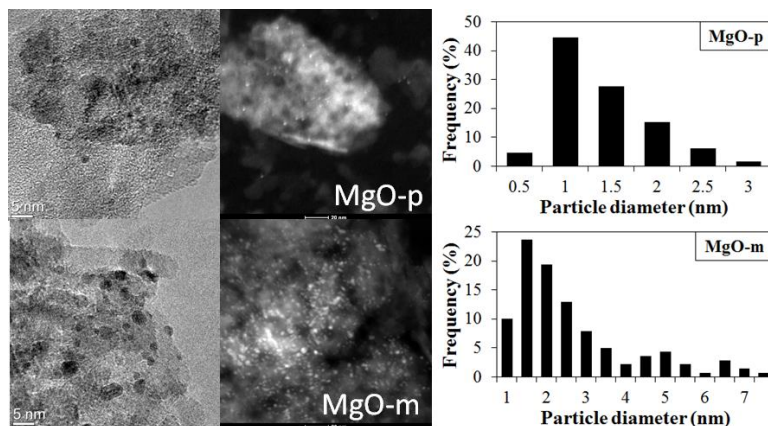
Figure 50: TEM images of Pt/MgO catalysts obtained by precipitation and microemulsion techniques and Pt particles distribution for 1% wt. loading.

The two catalysts were then tested in APR reaction of glycerol at 250°C, to boost the product formation (Figure 51). MgO-m sample shows higher conversion up to 57% than the precipitated sample. Gas products selectivity does not present a significant difference, while in liquid phase the MgO-p presents a selectivity 7% higher in lactic acid and 2% lower in propylene glycol.
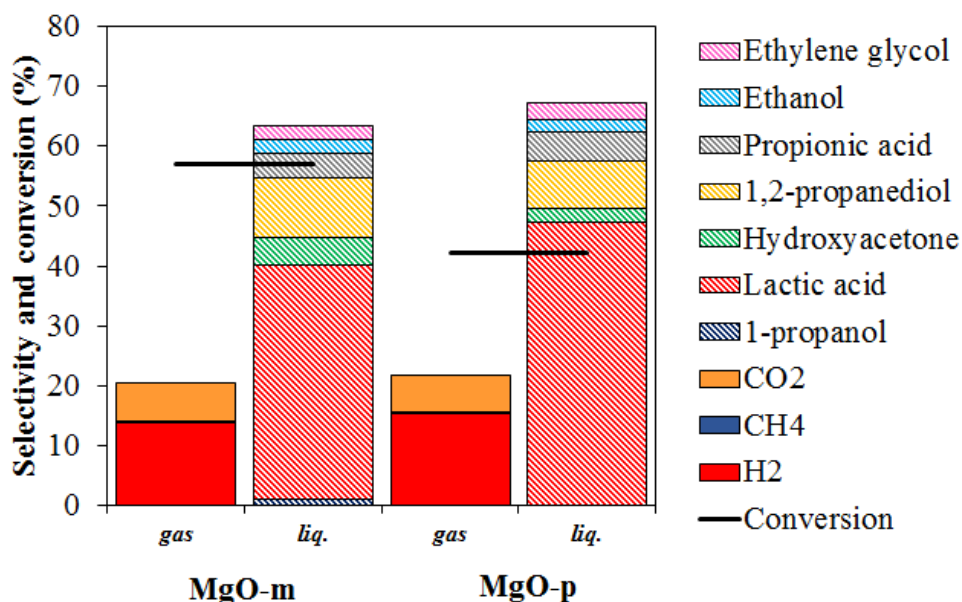
Figure 51: Comparison within gas and liquid selectivity and conversion for MgO 1%wt. not reduced catalysts with different preparation methods. Reactions performed for 3h; glycerol loading 17% wt.

This is consistent with the lower conversion being lactic acid a primary product and propylene glycol a consecutive. The microemulsion method applied to MgO synthesis allowed the obtainment of a higher surface area solid but worsening the distribution of the active phase by impregnation technique. Those differences do not reflect significantly over APR reaction giving a higher activity in dehydration pathway for the MgO-p sample and in dehydrogenation for the microemulsion. For those reasons, together with the lower yield of solid obtained for MgO-m synthesis compared to TiO$_2$-m, the application in APR of this oxide was limited and not further explored.

5.2.3   *Basic and acid sites effect with Mg/Al mixed oxides*

The instability of MgO in the reaction environment, coupled with the significant reactivity difference found in comparison with acid TiO$_2$ support, led to the possibility of studying the effect of acid and basic support sites over APR reaction. Al$_2$O$_3$ is the most studied catalyst in APR[41,162,182–184], while MgO presents interesting properties in terms of H$_2$ and lactic acid selectivity. Mg and Al can be combined in the thermodynamically stable spinel structure MgAl$_2$O$_4$, or coupled in a statistic ordered distribution in the same oxide structure, via hydrotalcite precursor. Mg/Al mixed oxides were thus synthesized via co-precipitation technique and calcined at 750°C to improve oxide stability. The M^{2+}/M^{3+} ratios 2:1 and 3:1 were selected to maintain the solid in the mixed oxide framework, avoiding segregation of spinel or alumina phases, as further confirmed by XRD analyses and literature[185]. MgAl$_2$O$_4$ was synthesized with the same technique with a M^{2+}/M^{3+} ratio of 1:2 but calcined at 900°C to favor the formation of the spinel phase and reduce the contribution of mixed oxide framework. MgO considered for comparison was obtained by precipitation and calcined at the same mixed oxide temperature. Moreover, for a more complete comparison, a commercial Al$_2$O$_3$ was inserted in the analysis set.

XRD patterns are reported in Figure 52; they show a gamma phase for Al$_2$O$_3$, and a periclase phase for MgO, without any residual brucite. MgAl$_2$O$_4$ sample has the characteristic peaks of the spinel, together with a residual periclase structure, probably due to the not complete formation of the spinel even at high calcination temperature.

The Mg/Al samples present a pattern attributable to mixed oxide structure, with two main reflects at 43 and 62°2θ and no segregation of spinel structure. As reported in literature[186,187], Mg/Al containing samples, with a cation ratio lower than 3.5, show a periclase-like structure poorly crystalline with the trivalent cation uniformly dispersed in the MgO lattice, mainly in octahedral cavities. The progressive increase in Al content corresponds to a small shift towards higher °2θ values, by decrease of the volume of the MgO cell with insertion of smaller Al^{3+} cations[188]. The intensity of the two main reflects for the two samples is linked to the decrease in Mg content; in fact the 3:1 ratio sample shows higher intensity due to the lowest substitution of Al in the periclase matrix. This sample presents also small reflects at 11 and 23°2θ, for the presence of negligible quantities of brucite Mg(OH) phase, probably due to moisture hydration of the surface. A further increase in Al content was not studied because it led to the formation of a separate $MgAl_2O_4$ phase together with the mixed oxide structure, and at high Al content, to an Al_2O_3 matrix with spinel regions[189]. As for surface analyses, reported in Table 8, there is a significant change in surface area within the samples that can be attributable in part to the different phases stabilized during calcination, leading to differences in sample crystallinity. This confirms the similarity within the surface characteristics in the 2:1 and 3:1 mixed oxides. Adsorption and desorption measurements are typical of mesoporous materials with H1 hysteresis loop and a bimodal pore dispersion for all the samples.
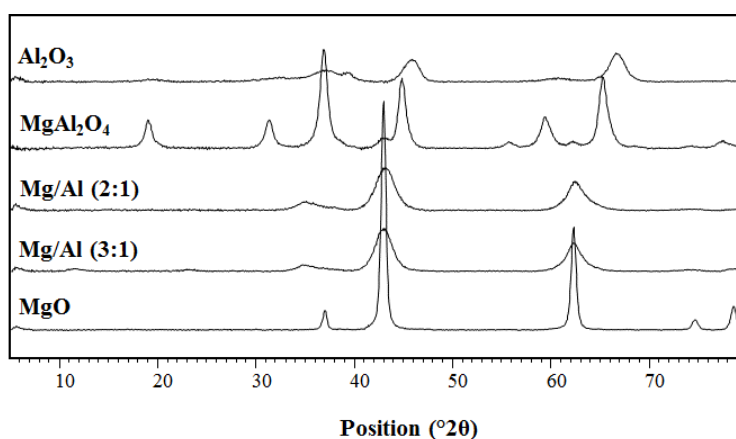

Figure 52: XRD analyses of the prepared sample and commercial Al$_2$O$_3$.

Table 8: Prepared catalysts at different Mg/Al content and surface characterization. The synthesized catalysts were calcined at 750°C for 5h, while MgAl₂O₄ was calcined at 900°C and Al₂O₃ analyzed as purchased.

Catalyst	Metal cation molar ratio (%)		X $M^{3+}/(M^{3+}+M^{2+})$	S.A. (m^2/g)	Pore volume (cm^3/g)	Pore dimension (nm)
	Mg	Al				
γ-Al₂O₃	0	100	1	196	0.71	7.1-11.7
MgAl₂O₄	33	66	0.66	90	0.50	3.7-18.5
Mg/Al (2:1)	66	33	0.33	192	0.62	3.5-10.8
Mg/Al (3:1)	75	25	0.25	184	0.59	3.5-12.4
MgO-p	100	0	0	58	0.37	3.3-49.9

Since the aim of this part of the study was the synthesis of intermediate basic and acid supports, TPD analyses were performed both with basic and acid probe gases (Figure 53 and Figure 54 respectively). The reported graphs are obtained with TCD detector, but mass analyses were performed to discriminate the contributions. It was in fact discovered that around 350°C there is a loss of CO_2 in NH_3 desorption analysis, and above 500°C a release of water probably from the crystalline structure and not from adsorbed molecules, because the samples were pretreated in-situ before the analysis. Thus in Figure 53 was considered for all the samples the contribution of the first peak, as only NH_3 release. The water release above 300°C was observed also in CO_2 TPD, and the contribution was higher because in this case it was not possible to insert an absorber before the detector due to interactions with CO_2 probe molecule. In this case it was again analyzed only the contribution of the first peak. Quantitative uptakes are reported in Table 9. MgO shows, as expected, the highest contribution in CO_2 adsorption and the lowest in NH_3, the opposite of the commercial Al_2O_3. From the CO_2 TPD graph is possible to assign to MgO support medium and strong basic sites with desorption curve within 200 and 500°C similar to the overlapping of two peaks. Two types of CO_2 adsorption are reported: bidentate is desorbed around 190°C while unidentate is removed at 280°C. The first bidentate one can be associated in case of Mg rich samples over both ions of an acid-base pairs (Mg^{2+}-O^{2-}), while the latter is formed on low coordination oxygen atoms (O^{2-}) as strong basic sites[190]. For what concerns NH_3 adsorption over MgO, the small curve at 200-300°C can be due to synthesis impurities.

The acid strength of Al_2O_3 is also medium-strong with a tailed desorption within 200 and 450°C explained by an overlapping of higher amount of medium force sites and a lower contribution of strong sites. As for alumina CO_2 adsorption measurements, the peak at temperature below 200°C is assigned to bicarbonate species formed over Brönsted OH groups, due to the amphoteric character of Al^{3+} cations. The two Mg/Al samples instead show similar behavior with comparable gas uptake. The NH_3 TPD curves are similar to Al_2O_3 medium-force contribution, without the presence of the second peak due to strong acid sites and the area is proportional to the Al quantity in the sample. As for CO_2 uptake of Mg/Al samples, the peak can be the result of three contributions: the first at lower temperature is similar to bicarbonate Al_2O_3 formation due to weak basic OH[190], instead the last at higher temperature is water release. The intermediate one, around 250-300°C, presents lower intensity and it is centered in the same position of medium-strength MgO contribution. To confirm this assignation, the peak is more evident for Mg/Al sample with higher Mg content. The total evolved CO_2 is increased in parallel with the amount of Mg in the sample[186,187]. $MgAl_2O_4$ sample instead seems to present an unconventional trend in NH_3 TPD. By mass analysis, it was detected for this sample the presence of CO_2 and H_2O under the same NH_3 peak, with a percentage of area respectively of 30 and 3% explaining thus the excessive uptake determined by TCD detector. As for CO_2 measurements, the sample shows the expected intermediate behavior within Mg/Al 2:1 and Al_2O_3 samples.

Table 9: Prepared catalysts at different Mg/Al content and surface chemisorption data by TPD measurements with TCD detector. The synthesized catalysts were calcined at 750°C for 5h, while Al_2O_3 was analyzed as purchased.

Catalyst	X $M^{3+}/(M^{3+}+M^{2+})$	NH_3 uptake $(cm^3/g$ STP$)$	NH_3 uptake normalized S.A. $(cm^3/g)/(m^2/g)$	CO_2 uptake $(cm^3/g$ STP$)$	CO_2 uptake normalized S.A. $(cm^3/g)/(m^2/g)$
γ-Al_2O_3	1	6.57	0.034	1.49	0.010
$MgAl_2O_4$	0.66	11.65	0.129	1.98	0.022
Mg/Al (2:1)	0.33	4.19	0.022	2.26	0.012
Mg/Al (3:1)	0.25	3.57	0.019	3.75	0.020
MgO-p	0	0.16	0.003	7.75	0.134
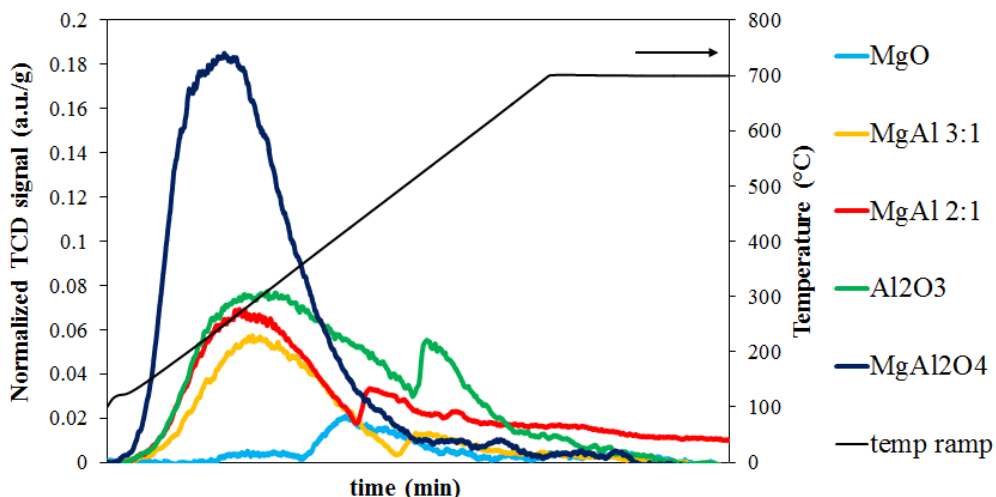
Figure 53: Temperature programmed desorption analysis of NH₃.
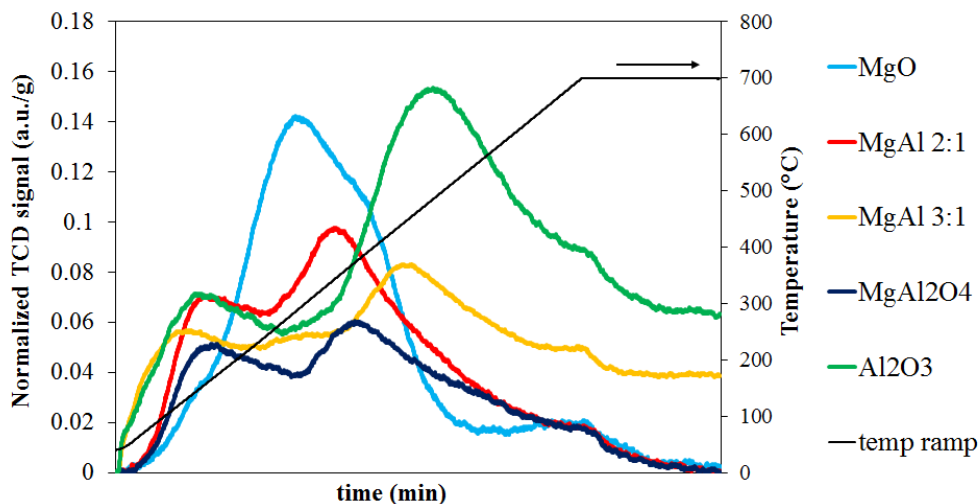
Figure 54: Temperature programmed desorption analysis of CO₂.

The reactivity of the Pt loaded catalysts was analyzed in APR reaction to evaluate the differences of basic and acid sites (Figure 55). Literature reports[152] that presence of acid and basic sites on the catalyst can differently favor the absorption of the reagent. In particular, the interactions of glycerol with acid and basic sites can give rise to different intermediates. For Lewis acid sites, two possible adsorptions of the primary alcoholic groups of glycerol are reported: a dissociative monodentate one and a not dissociative bidentate in bulk water. Basic oxygen or hydroxyl groups can instead interact by hydrogen bond with the secondary alcohol of glycerol. These sites are most reactive

when nearby Lewis sites allow a coordinative adsorption of glycerol. Free Lewis sites instead they are easily poisonable by water or CO_2 molecules. For these reasons, the reactivity of glycerol is strongly dependent on the acid/base features of the support, giving rise to different product ratio. Glycerol conversion varies from 30 to 50% and in Mg/Al samples raises in parallel with the increase in Mg content. The maximum value is given by Mg/Al 3:1 followed by 2:1. The trend is not clearly linkable to surface area values but can be a combination of superficial features and metal dispersion. Gas selectivity shows an increase in H_2 with a maximum of 51% for $MgAl_2O_4$ support, together with an increase in CO_2 up to 30%. Nevertheless, the highest yield value is obtained with Mg/Al 3:1 thanks to the highest conversion. CH_4 selectivity follows the hydrogen trend. Regarding liquid phase selectivity, lactic acid is increases steeply from 3 to 55% with increasing Mg content, while 1,2-propanediol, hydroxyacetone and ethanol are higher for alumina sample. A part from a difference in 1,2-propanediol the two Mg/Al supports show similar selectivity values and intermediate within MgO and alumina samples.
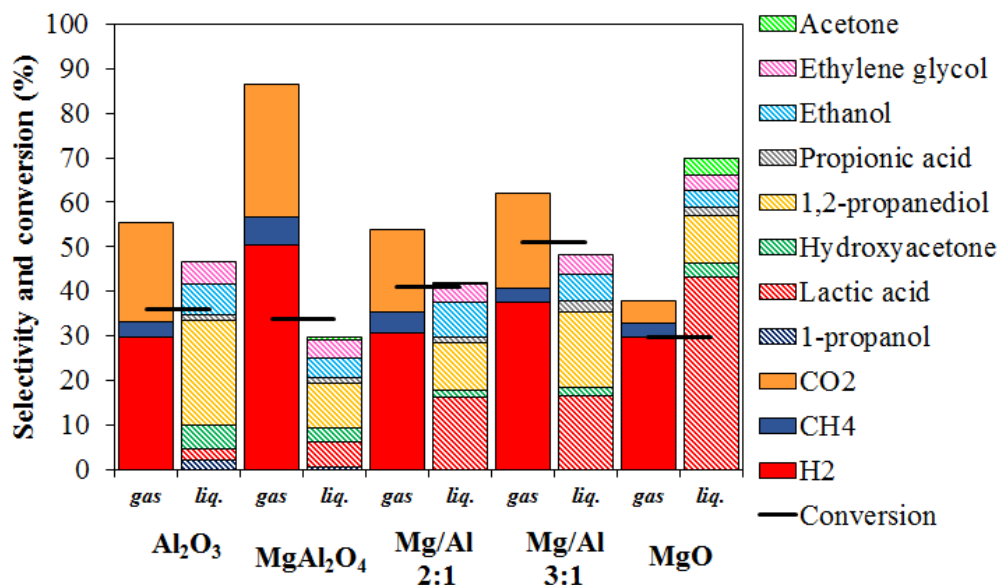

Figure 55: Comparison within normalized gas and liquid selectivity and conversion for MgO, Mg/Al and Al₂O₃ supports with Pt loading 3% wt.. Reactions performed for 3h; glycerol loading 6% wt.

Due to the complexity of the trends based on the study of single reaction products, with except of lactic acid, a new method of analysis has been developed. The idea was to start from the mechanism reported in Figure 42 for Pt/TiO_2 and it is based on lump sum method. It consisted in the sum of the specific steps that lead from glycerol to the desired product, such as dehydration, dehydrogenation, hydrogenation and decarboxylation. By this way, it permits to analyze the mechanism and preferential catalyst pathways.

Figure 56 reports the lump sum data for Mg/Al samples. It shows that dehydrogenation sum of products increases with the Mg content. This effect can be directly linked to the basicity of the system that stabilizes lactic acid formation (lactate salt is in some cases present) after metal dehydrogenation to glyceraldehyde. On the other hand, dehydration products globally decrease from Al_2O_3 to MgO, with similar behavior for all the Mg-containing supports. The activity of Al_2O_3 in dehydration mechanism is confirmed by literature[191]. Furthermore, the global ratio within dehydrogenation and dehydration products is coherent with the basic/acid sites ratio over the support detected by TPD analyses. Decarboxylation products are approximately constant in presence of Al, while decrease in presence of Mg. This may be due to the need of acid sites neighboring Pt particles to act as decarboxylation agent, and it is not affected by the total density of acid sites on the surface.
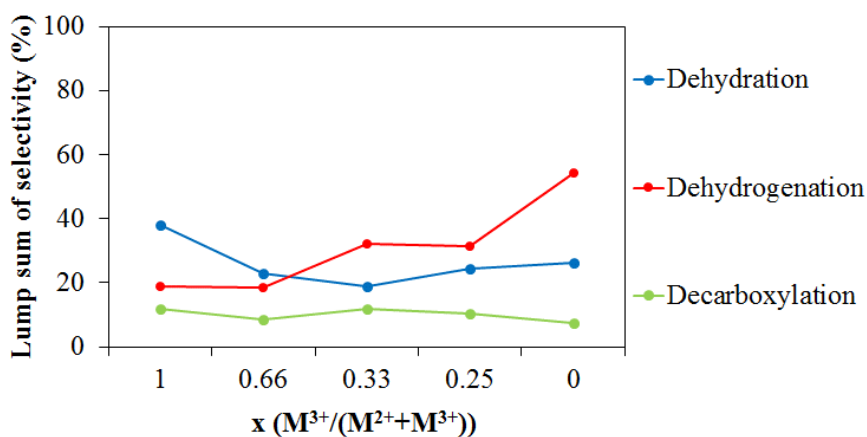

Figure 56: Lump sum of selectivity in different pathways for Pt supported MgO, Al_2O_3 and Mg/Al catalysts.

5.2.4   *Synthesis of Mg/Al via microemulsion technique*

The microemulsion preparation of the oxide was also tested for the preparation of Mg/Al. An analysis of literature microemulsion preparations for hydrotalcite compounds showed that some methods allowed a procedure similar to co-precipitation technique but with microemulsion solutions[192,193]. It was thus set up a method starting from co-precipitation technique for the synthesis of Mg/Al mixed oxides. Three solutions were prepared with R_w=21: a cationic one (containing Mg and Al precursors in the 3:1 molar ratio), another with soda and a third with carbonate anions. As co-precipitation method, the cation microemulsion was dropped into the anion one and the pH maintained with base microemulsion. Several stability tests were performed: an analysis of surfactants with Triton X-100, Marlophen NP5, CTABr and sodium dodecyl sulphate together with a variation of base and carbonate concentration to work with stable microemulsion solutions. Optimal values were found at 0.15M for the carbonate solution with R_w=11.5 and 0.5M for the NaOH at R_w=21. The amount of solid obtained was limited by the dilution of the system. The filtration has been carried out with hot solutions to avoid the reformation of the microemulsion and collect the solid.

The final oxide has been obtained by calcination at 750°C and showed a periclase-like structure, typical of well dispersed mixed oxides[194], the same observed for the co-precipitated sample. Surface characterization is reported in Figure 57 and Table 10. The as-synthesised hydrotalcite shows a crystallite dimension of 9nm compared to the co-precipitated at 14nm. However, after calcination, the crystallite diameter becomes similar for both the structures. This is an indication that microemulsion synthesis works differently in the formation of the precursor, but the difference is not maintained after calcination. The lower properties of the Mg/Al-m oxide are also a lower surface area, together with bigger pores with monomodal distribution and higher pore volume. The hysteresis loop is typical of slit shaped channels[180,181]. On the other hand, the co-precipitated sample presents a bimodal distribution of pore diameter with a broad peak centered at 12nm. Similar synthetic methods reported in literature[192,193] show comparable characterization results in terms of crystalline phase and dimension of

oxides particles, thus the smoothing of differences can be a result of the peculiar collapse of hydrotalcite precursor to form the mixed oxide phase.
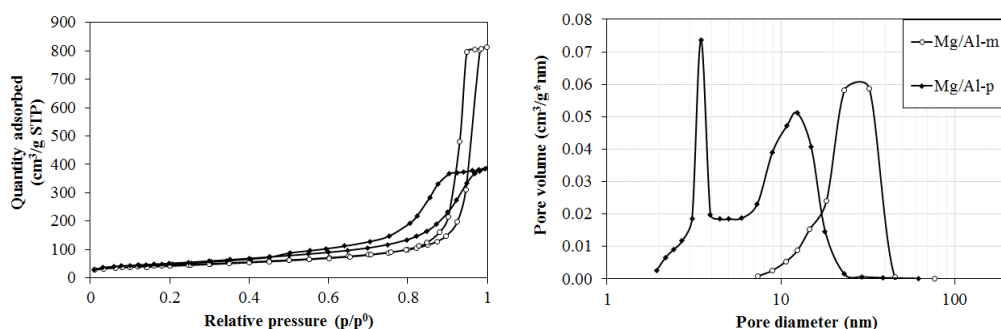
Figure 57: Adsorption/desorption isotherms and pore distribution of the Mg/Al samples calcined at 750°C.

Table 10: Characterization of Mg/Al-m compared to Mg/Al-p sample calcined at 750°C. Particle size is calculated by Scherrer equation (main peak at 44°2θ for oxide and 11.4°2θ for the hydrotalcite precursor), surface characterization done by porosimetry.

	Crystal phase	Particle size oxide (nm)	Particle size hydrotalcite (nm)	S_{BET} (m^2/g)	V_{pore} (cm^3/g)	Pore average diameter (nm)
Mg/Al-p	Periclase-like	4.4	13	184	0.59	3.5-12.4
Mg/Al-m	Periclase-like	6.0	9	153	1.3	25.3

APR tests of the two oxides, loaded with Pt 3% and reduced are reported in Figure 58. The Mg/Al-m catalyst shows a glycerol conversion 10% higher than the co-precipitate. Gas phase selectivity are 2% higher for the latter, with a 4% increase in lactic acid, and smaller differences in ethanol and acetone. On the other hand, H_2 and lactic acid yields are higher for Mg/Al-m catalyst. This represents that the microemulsion support is slightly more active, but there are not preferential pathways that differentiate one synthesis from the other. To confirm this hypothesis the two supports were tested without Pt loading. They reached the same low conversion value (2%), but the microemulsion shows a small production of gas and liquid phase compounds, while only traces of H_2 and lactic acid and hydroxyacetone were obtained by the co-precipitated.

Reactivity results demonstrate that microemulsion synthesis in the case of Mg/Al mixed oxides does not allow a significant improvement in the oxide features, thus it does not justify further work on Mg/Al-m oxide.
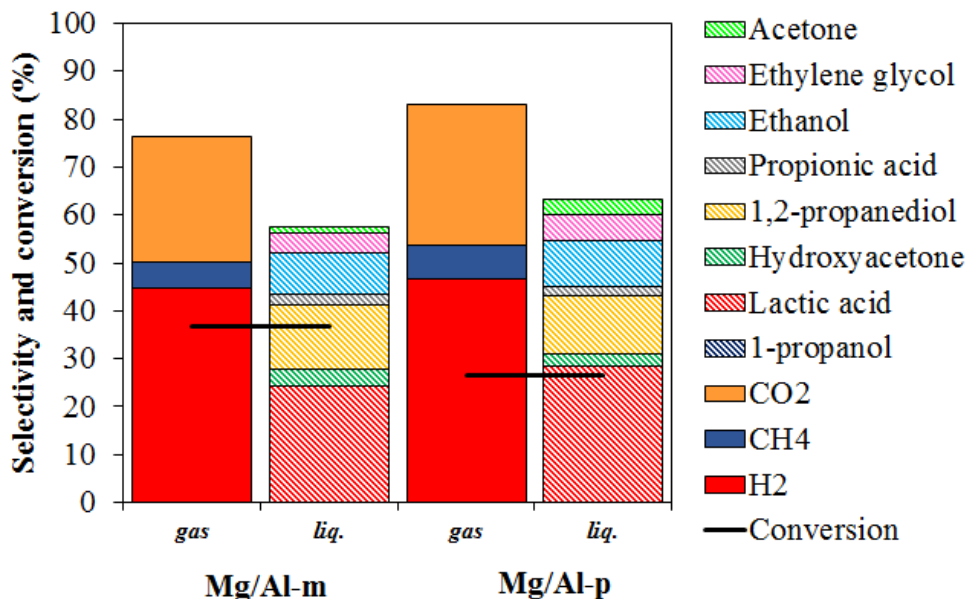
Figure 58: Comparison within gas and liquid selectivity and conversion for Mg/Al 3%wt. catalysts with different preparation methods. Reactions performed for 3h; glycerol loading 6% wt.

5.3 Redox metal inserted in the support

The presence of acid or basic sites in the support was demonstrated to favor the selectivity towards a specific pathway. However, glycerol conversion remains around 40%, with 30-40% H_2 selectivity. Within the variety of metals applied in APR reaction, nickel appears in literature to have significant activity and properties similar to platinum: it is a good catalyst for hydrogenolysis, C-C cleavage, and WGS reactions and presents intermediate activity in coupling and methanation processes[195–198]. Moreover, nickel-containing catalysts are widely applied in steam reforming reactions[199]. For those reasons, nickel is also used in APR reaction both as single metal and in combination with other noble metals. The supporting technique most used is impregnation[184,200–205] and only few works deal with the preparation of the oxide by sol-

gel techniques[206,207]. Nevertheless, nickel is a well-known catalyst with possible problems related to leaching and sintering issues. The layered double hydroxide precursor used to prepare mixed oxides allow the insertion of several metals in their structure maintaining the uniform distribution of cations in the lattice, without significantly changing their crystalline structure[69]. It was thus decided to embed Ni inside the mixed oxide structure and combine its catalytic activity with the presence of Mg and Al. Beside the use of a well-known reforming catalyst such as Ni, Fe was studied in the layered double hydroxide as trivalent cation. Iron is widely applied in organic cross-coupling reactions, as oxidation catalyst or hydrogenation[208,209]. Even if its use is not common in APR, it appears as an interesting metal with non-toxicity and low cost advantages.

5.3.1   *Nickel effect in Mg/Al supports*

The first test was done comparing supports prepared with co-precipitation technique with the same Ni loading but different M^{2+}/M^{3+} ratio (Table 11). The aim was analyzing the catalytic behavior with acid and basic sites combined with the activity of Ni. For this reason the parameter adopted was called X* and, differently from the X value, takes into account only the Mg/Al ratio. Three samples were prepared: two with only Ni and Mg or Al cations, and a third with similar quantities of Mg and Al. The crystalline structures of the calcined samples is shown in Figure 59 show different phases. There is the presence of $NiAl_2O_4$ spinel and γ-Al_2O_3 for the Ni/Al sample and a highly crystalline (Ni/Mg)O phase, representing a solid solution of both NiO and MgO that have the similar structure. Ni/Mg/Al support shows characteristic reflects of the mixed oxide structure are at 37, 43 and 62°2θ. These can be attributable analogously to the (Ni/Mg)O phase with Al^{3+} in the octahedral sites, together with the presence of empty octahedral cavities every two Al^{3+} cations to balance the charge. Surface area values are higher for the Ni/Al structure with small pores, that maintains high porosity also at high calcination temperatures[210]. As for the $Ni_{16}Mg$ sample, surface area is low and pore dimension is high due to the high crystalline structure, as reported for MgO sample. Ni/Mg and Ni/Al hysteresis loops are similar to slit shaped channels, while Ni/Mg/Al presents progressive size and shape pores, all of them with a bimodal distribution.
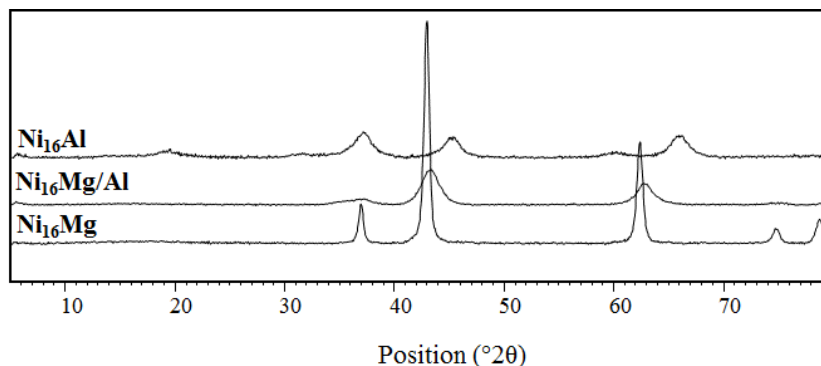
Figure 59: XRD analyses of the prepared Ni/Mg/Al samples.

Table 11: Surface characterization of prepared catalysts at different Ni/Mg/Al ratio and calcined at 750°C for 5h.

Catalyst	Metal cation molar ratio (%)			X $M^{3+}/(M^{3+}+M^{2+})$	X* $Al^{3+}/(Al^{3+}+Mg^{2+})$	S.A. (m^2/g)	pore volume (cm^3/g)	pore dimension (nm)
	Ni	Mg	Al					
$Ni_{16}Al$	16	0	84	0.84	1	235	0.8	3.2-8.9
$Ni_{16}Mg/Al$	16	59	25	0.25	0.30	189	0.46	6.2-10.9
$Ni_{16}Mg$	16	84	0	0	0	67	0.55	3.5-23.2

The reducibility of Ni inside the crystalline structure was analyzed by TPR at 900°C (Figure 60). The samples were tested in presence of Pt, which favors the reducibility of the oxide. All the oxides present three reduction peaks with different intensity. Ni/Mg/Al sample has the highest uptake (as reported in Table 12) that can be attributable to the higher mobility of Ni typical of hydrotalcite-deriving oxides that has some empty octahedral cavities, if compared to periclase-like structure. The lowest value is given by Ni/Mg sample both because the reduction at 900°C is still incomplete but also due to the high-stabilized crystalline structure. An evaluation of the reducibility of the samples was calculated taking into account the theoretical percentage of NiO in the oxide. Pt contribution was neglected since the hydrogen consumed should be the same for all the samples. The calculations confirm the higher reduction for the Ni/Mg/Al sample and lower for the Ni/Mg. In terms of the peak attribution, the first is in the range 230-350°C and cannot be clearly attributed to Pt reduction because it

should have the same intensity for all the samples and should occur at lower temperature than 350°C, as reported in literature[211,212]. A possible hypothesis on the nature of this peak could be the early reduction, together with Pt, of Ni atoms that surround the Pt particle for spillover effect. This could explain why the intensity in Ni/Mg/Al sample is higher than the other two samples. The second peak located at around 480-550°C can be due to the reduction of the surface and free NiO. The higher temperature peak starting from 860°C is assignable to bulk Ni inside the Mg and/or Al oxide matrix. The Ni/Al support shows peaks at lower temperature demonstrating a more easy reduction than the other solids, while the mixed oxide presents high intensity due to the better degree of reducibility related to the higher mobility of cations in the oxide. It is worth to underline that the latter has also two negative peaks at 220 and 420°C, assigned as water release by mass analysis, which can reduce the total uptake detected by overlapping of positive and negative signals. Mass detection of simulated TPR analyses with no H_2 flux have confirmed the release of water at 250°C and water and CO_2 around 350°C probably linked to surface adsorption of atmospheric gases over the sample.
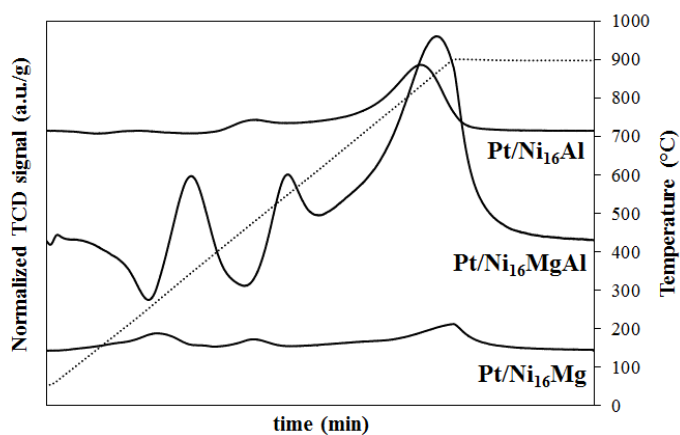

Figure 60: TPR profiles of Pt 3% wt. over Ni/Mg/Al supports with equal Ni content.

Table 12: Probe gas uptake for catalysts at different Mg/Al ratio but equal Ni content.

Catalyst	X^* $Al^{3+}/(Al^{3+}+Mg^{2+})$	Total H_2 uptake (cm^3/g)	Ni reduction (%)	CO_2 uptake (cm^3/g)	CO_2 uptake normalized S.A. $(cm^3/g)/(m^2/g)$
$Ni_{16}Al$	1	41	63	2.09	0.009
$Ni_{16}Mg/Al$	0.30	61	82	3.00	0.016
$Ni_{16}Mg$	0	28	36	7.03	0.105

The analysis of acid and basic sites was carried out by CO_2 TPD and results are reported in Table 12 and Figure 61). The Ni/Mg curve is similar to MgO sample with a convolution of medium and high strength basic sites and a total uptake slightly lower than MgO due to the presence of Ni. Ni/Mg/Al sample is comparable to Mg/Al 3:1 with low strength basic sites and a small contribution of medium one. Considering the CO_2 uptake, Ni/Mg/Al sample is intermediate between Mg/Al 3:1 and 2:1 samples. Finally, Ni/Al has a normalized uptake comparable to Al_2O_3, while the total one is higher to a small extent due to the higher surface area. This can be attributed to the defects in the structure created by Al^{3+} cations in order to compensate the total charge, which leaves coordinately unsaturated oxygen atoms and can increase the total basicity[186,187]. It can thus be concluded that the presence of Ni is not affecting the aim of the study, which is the analysis of basicity coupled with Ni activity.
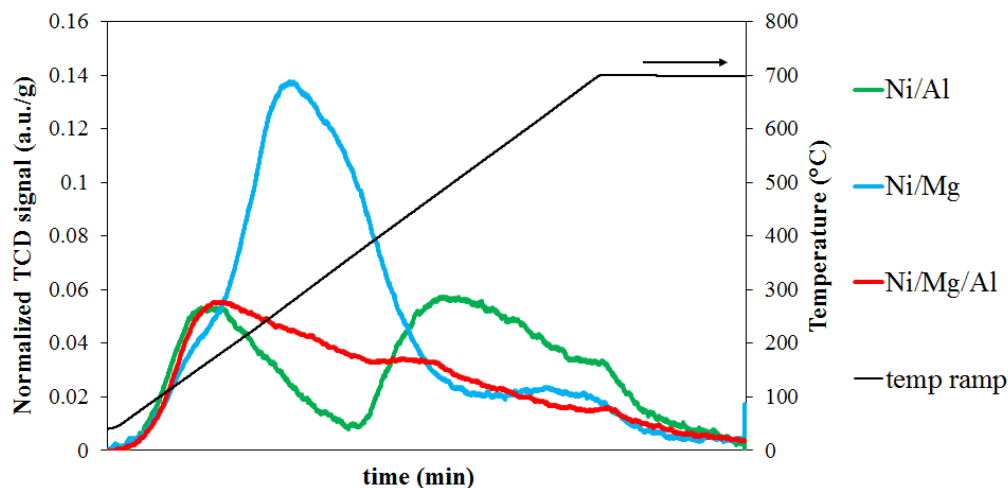
Figure 61: Temperature programmed desorption analysis of CO_2 for different Ni/Mg/Al supports at equal Ni content.

APR tests can be read both in term of product selectivity (Figure 62) and in lump sum for selected reaction pathways (Figure 63). Conversion values are significantly increased compared to Mg/Al samples but, as for the previous samples, the combination of Mg and Al cations gives better results up to 82%. The same trend is followed by CO_2 and H_2 selectivity with maxima respectively at 24 and 39% for the Ni/Mg/Al support. A more clear trend is present in liquid phase with a decrease in 1,2-propanediol and the simultaneous raise in lactic acid selectivity together with the increase in basicity of the sample. Even lump sum method reports trends in line with the basicity of the catalysts. Dehydrogenation linearly increases with the basicity together with a decrease in dehydration; on the other hand, decarboxylation is maintained constant due to the presence of an equal Ni content in the samples. Figure 63 reports also the trends and productivity values in hydrogenation and total H_2, calculated as sum of hydrogen-consuming and detected H_2 selectivity. The Ni/Al sample shows the highest hydrogenation tendency, while the Ni/Mg one has the lowest values, probably due to the low reduction degree and low surface area. Intermediate selectivity, together with the highest productivity value are obtained in presence of both Mg and Al cations.

A comparison within the Ni containing supports and Mg/Al ones evidences a lower H_2 selectivity, due to the hydrogenation reaction at high conversion; contrarily dehydrogenation reaction is globally increased. The total hydrogen produced by the

reaction is 10% higher for the Ni/Al compared to Al$_2$O$_3$ and slightly lower for Ni/Mg/Al and Ni/Mg samples. Nevertheless, if productivity values are considered, the values increase from 5-9 for the Mg/Al samples to 21-24 for Ni-containing supports. The data confirm that even if Ni does not favor hydrogen selectivity, the quantity produced (and consumed) in the reaction environment is significantly higher for the Ni samples. Moreover dehydration mechanism is strongly enhanced, for the higher selectivity in 1,2-propanediol but the ratio within dehydration and dehydrogenation mechanisms is maintained as previously reported samples.
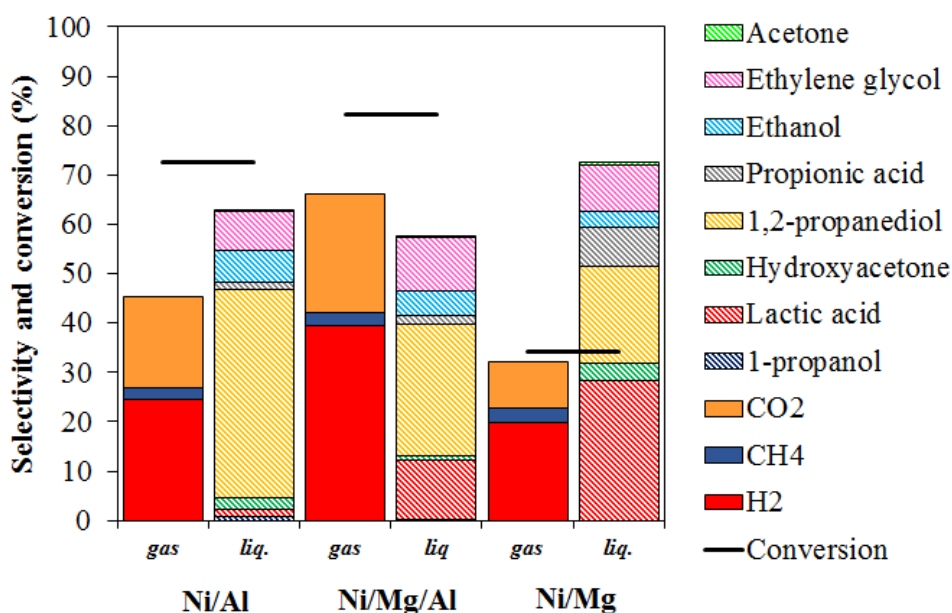

Figure 62: Comparison within Ni/Mg/Al samples with Pt 3% wt. Reactions performed at 225°C for 3h; glycerol loading 6%.
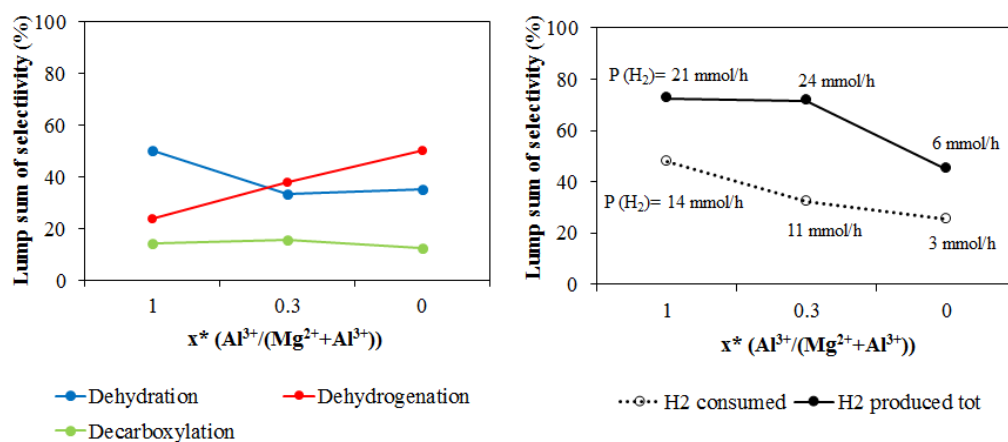
Figure 63: Lump sum of selectivity in different pathways for Pt supported Ni/Mg/Al catalysts with equal Ni loading and different X* ratio. On the left are reported the H_2 consumed and totally produced (H_2 consumed + H_2 selectivity) expressed as selectivity and productivity values.

It can be concluded that the peculiar activity of Ni in reforming and methanation reactions is not directly reported in APR, because it is necessary the coupling with Pt activity to obtain significant yield and conversion values. This is confirmed also by literature values[184,201,204,206] that report a preferential distribution of Pt particles over Ni surface as main cause of this improvement. Nevertheless, the possibility of enhancing reaction yield is demonstrated to be associable with acid and or basic sites with positive effect, maintaining the control over products distribution and reaction pathways over a redox metal embedded in the support and not traditionally impregnated on the surface.

5.3.2   *Study of Nickel quantity*

Once determined the positive effect of Ni presence in the support, the aim was the optimization of its loading in the mixed oxide structure. Table 13 reports the synthesized supports. To avoid significant variations in superficial areas and crystalline structures, the bivalent/trivalent cation ratio (X) was maintained to 0.25 for all the samples but varying the relative Ni/Mg content and compared with the previously analyzed Mg/Al 3:1 sample. Figure 64 presents the XRD patterns with characteristic reflects of the mixed oxide structure for all the samples. The most significant differences are the shift in the 37°2θ reflect and the ratio within the reciprocal intensity of the 37 and 43°2θ reflects. The first shift is attributable to the substitution of Mg^{2+}

larger cations[213] with Ni^{2+} that changes the unit cell of the lattice. The second instead is an indicator of the Ni content in the sample, since Ni has a higher number of electrons and higher structure factor in X-ray diffraction. This affects the relative intensity of the tetrahedral (containing Ni and Mg) and octahedral (mainly containing Al) reflects. Moreover, no $NiAl_2O_4$ crystalline spinel phase was detected in the sample, thus remaining in the mixed oxide range. Surface area values show a decreasing surface area by diminishing the Mg content, with smaller pore volume and a bimodal distribution with Ni/Al being the only having a monomodal distribution.

Table 13: Prepared catalysts at different Ni content, calcined at 750°C for 5h.

Catalyst	Metal cation molar ratio (%)			X $M^{3+}/(M^{3+}+M^{2+})$	X* $Al^{3+}/(Al^{3+}+Mg^{2+})$	S.A. (m^2/g)	pore volume (cm^3/g)	pore dimension (nm)
	Ni	Mg	Al					
Mg/Al (3:1)	0	75	25	0.25	0.25	184	0.59	3.5-12.4
Ni₁₆Mg/Al	16	59	25	0.25	0.30	189	0.46	6.2-10.9
Ni₄₀Mg/Al	40	35	25	0.25	0.42	170	0.34	3.6-6.2
Ni₇₅Al	75	0	25	0.25	1	148	0.27	6.1

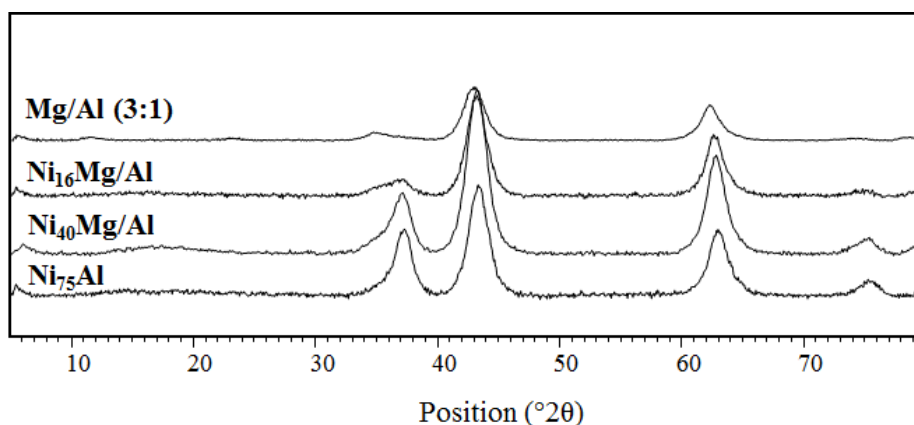Figure 64: XRD analyses of the prepared Ni containing samples.

TPR profiles in Figure 65 are reported for bare and Pt loaded supports. From the comparison within the two graphs, it is clear how the Pt on the surface enhances the reducibility of the sample, especially at lower Ni loading. The Pt loaded curves report the same three peaks as indicated above. The reduction temperatures are similar for Ni₁₆

and Ni_{40} mixed oxides with a small shift towards lower temperatures of about 50°C, while the peaks are centered at significant lower temperatures (250 and 600°C) for the Ni_{75} loading. Considering H_2 uptake reported in Table 14, it increases with the loading, but not enough to maintain the Ni reduction percentages. Thus, the different behavior of $Ni_{75}Al$ oxide can be a consequence of the higher availability of Ni on the surface and no NiO free but, due to the more packed structure the reducibility degree is decreased of more than 10% compared to the others support. Figure 66 and Table 14 present the basic site strength of the supports, since it is important to underline that Ni loading increases despite Mg one. CO_2 TPD profiles are similar to the Mg/Al sample. All the support show the formation of bicarbonate adsorption, typical of Al containing samples, in the range 150-200°C. The medium force peak centered at 250-350°C instead is evident only for Mg/Al and $Ni_{16}Mg/Al$ supports, while may be present as a tail of the first peak for $Ni_{40}Mg/Al$, in line with the decrease in Mg content of the sample[214]. The reported CO_2 uptake decrease, as expected reaching a value for the $Ni_{75}Al$ lower than $Ni_{16}Al$ and Al_2O_3 supports. The Al^{3+} cation is smaller than Ni^{2+} [213], and should have an higher acidity due to the total charge. Nevertheless, the presence Ni in the structure may change the total acidity with an effect related to its quantity by the formation of Ni-O-Al bond that enhance the bicarbonate adsorption on the surface[214].
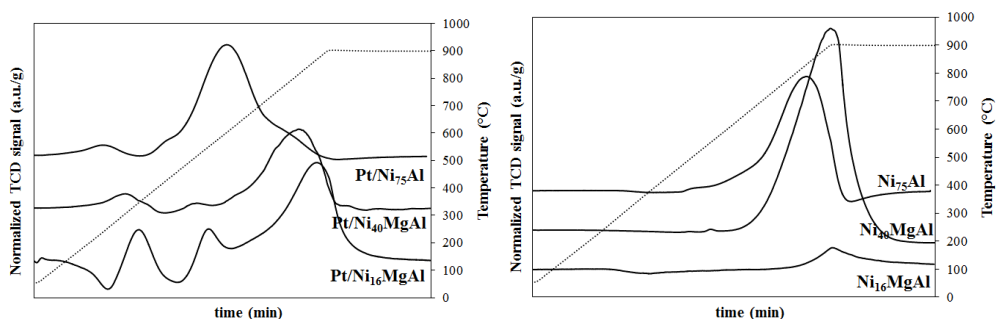
Figure 65: TPR profiles of Pt 3% wt. over supports with different Ni and Mg content.

Table 14: Probe gas uptake for catalysts at different Ni and Mg content. Ni reduction calculated for Pt loaded sample.

Catalyst	Ni content (% mol)	Total H_2 uptake (cm^3/g)	Ni reduction (%)	CO_2 uptake (cm^3/g)	CO_2 uptake normalized S.A. (cm^3/g)/(m^2/g)
Mg/Al (3:1)	0	6	-	3.75	0.020
Ni$_{16}$Mg/Al	16	61	82	3.00	0.016
Ni$_{40}$Mg/Al	40	124	78	2.59	0.013
Ni$_{75}$Al	75	167	68	1.01	0.007
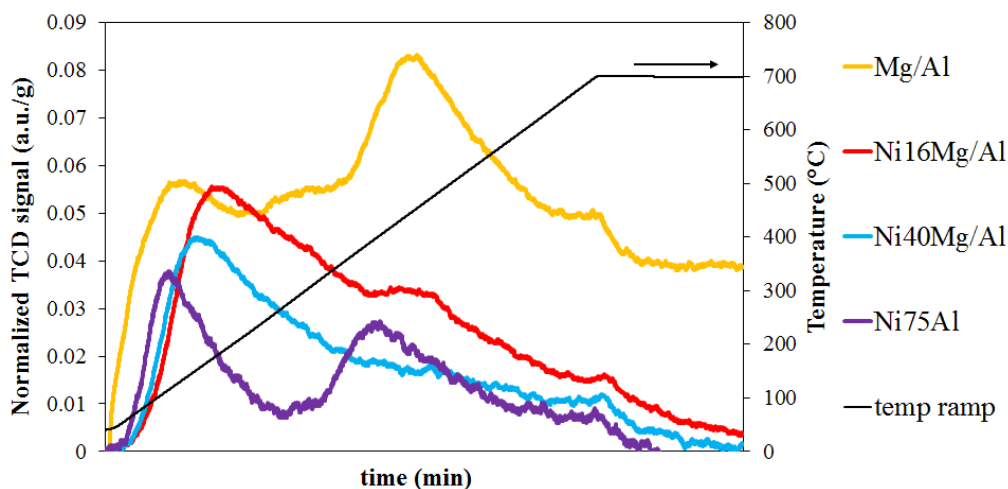
Figure 66: Temperature programmed desorption analysis of CO_2 for samples with different Ni and Mg content.

A confirm of the effective distribution of Ni, Mg and Al cations in the structure was obtained by EDS spectra in TEM microscopy. The mean Ni:Mg:Al percentage of metal calculated were 17:59:23 for the Ni$_{16}$ oxide, 39:36:25 for Ni$_{40}$ and 41:0:28 for Ni$_{75}$. All of them were near to the theoretical ratios reported in Table 13. Moreover, by TEM images it was possible to detect the lamellar and spherical composition of the oxides, with particles around 5-10nm (Figure 67). STEM images make evidence both of the small distribution of Pt particles centered at 1-1.5nm and of the absence of Ni agglomerates on the surface, confirming the effectiveness of the mixed oxide structure.
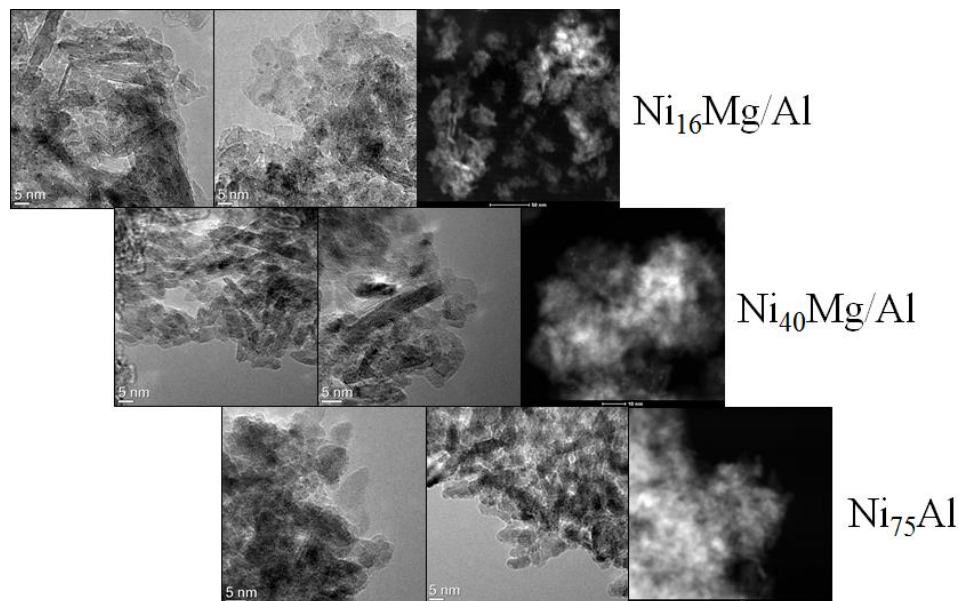
Figure 67: TEM and STEM-HAADF images of Pt loaded Ni/Mg/Al supports. Samples reduced at 350°C.

Figure 68 shows the catalytic trend starting from Mg/Al 3:1 sample and increasing the Ni ratio through Ni/Mg/Al supports with up to a $Ni_{75}Al$ support. Glycerol conversion presents a maximum at 82% with 16% of Ni, slightly decreasing to 75% when no Mg was contained in the support and dropping to 27% in absence of Ni. H_2 selectivity is apparently decreasing, but this is due to the increase in Ni content that favors hydrogenating reactions, as reported in Figure 69. This explains also the progressive increase in CO_2/H_2 ratio together with Ni content. CH_4 quantity is usually dependent on H_2 quantity with a CH_4/H_2 ratio range of 0.1-0.2. As for liquid phase products, mainly lactic acid and 1,2-propanediol generate a trend in dehydrogenation and dehydration products similar to basic and acid properties. This is due to two parallel factors: since the Al content in the samples is the same for all the oxides, the decrease in Mg quantity causes a diminution of basic properties and an enhancement of acid sites, as reported by TPD measurements; moreover, as shown before, Ni enhances dehydration activity. Dehydrogenation values are not as low as expected in absence of Mg because it comes significant the contribution of ethylene glycol and ethanol, which are contemporarily products of decarboxylation and dehydrogenation. As for decarboxylation, surprisingly, it is not increasing with the Ni content, but remains approximately constant apart from

the last point. This can be linked to the fact that Mg/Al sample favors the formation of ethanol from ethylene glycol, while in presence of Ni ethanol yield is lower compared to ethylene glycol. It can be supposed that ethanol comes preferably from decarboxylation of lactic acid and thus linked to the amount of this product, but at high Ni content, the dehydration/hydrogenation pathways are favored, thus enhancing its production from ethylene glycol, respect to lactic acid. This may explain why the sum of these products gives the unexpected trend.
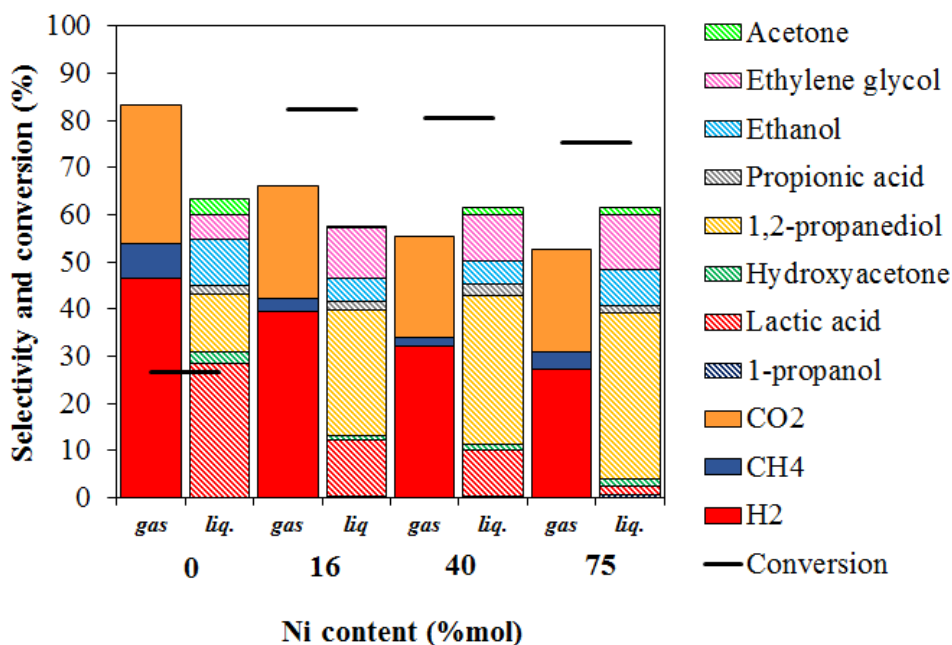
Figure 68: Comparison within samples with Pt 3% wt. and different Ni and Mg content. Reactions performed at 225°C for 3h; glycerol loading 6%.

In Figure 69 are reported also the H_2 values produced and consumed by the different catalysts. While the hydrogenating activity increases with the Ni content, the total selectivity in H_2 remains approximately constant for all the supports. Since the conversion of glycerol is significantly different, the productivity in total H_2 is notably higher in presence of Ni. The best data, also in this case are given by the $Ni_{16}Mg/Al$ and $Ni_{40}Mg/Al$ supports that show similar results in term of productivity and selectivity due to the peculiar mixed oxide features.
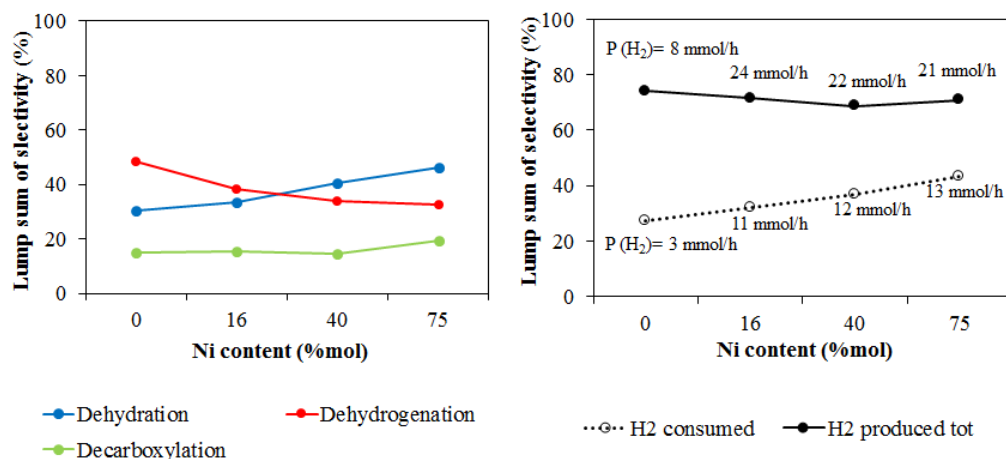
Figure 69: Lump sum of selectivity in different pathways for Pt supported Ni/Mg/Al catalysts at different Ni and Mg loading. On the left are reported the H$_2$ consumed and totally produced (H$_2$ consumed + H$_2$ selectivity) expressed as selectivity and productivity values.

5.3.3 Analysis of synthesis parameters with Ni/Mg/Al catalyst

Previous paragraphs have shown the positive effect in APR reaction of Ni presence. Nevertheless, the catalyst is subject to several thermal pretreatments during its synthesis. A more in-depth analysis of these parameters was performed over the intermediate Ni containing catalyst Ni$_{40}$Mg/Al catalyst. It shows, in fact, good conversion and selectivity in the main products (1,2propanediol, lactic acid and ethylene glycol). Moreover, it presents a good balance within dehydrogenating and dehydrating properties due to the similar ratios within the three metals. Thermal treatments lead to a modification of the catalyst structure and surface, thus the calcinations and reduction temperature were studied. The first one was changed with the aim of analyzing the effect in the reaction of crystalline phase and surface properties, the latter to modify the degree of reduced Ni. For the first test were selected layered double hydroxide structure with no thermal treatment before impregnation, a second sample was calcined at 400°C, that allows the formation of a low crystalline mixed oxide and the latter was calcined at 750°C with a high crystallinity structure. No higher temperatures were selected to avoid a steep decrease in surface area and segregation of atoms with the formation of spinel phase.

As reported in Table 15, hydrotalcite sample is significantly different because it has a layered structure, with low surface area and pore volume. After the formation of the mixed oxide, further increase in temperature leads, as expected, to a decrease in surface area with pore dimension substantially unaffected and pore volume increasing due to the collapsing of the structure. As for XRD patterns (Figure 70), the first sample corresponds to the hydrotalcite phase[215], while increasing the calcination temperature the transformation to mixed oxide and the increase in phase crystallinity is registered. The reducibility of the reported samples was also tested in Figure 71. Increasing the calcination temperature changes the ratio within the different Ni species on the sample increasing meanwhile the reduction temperature of the catalysts in presence of Pt. It is worth to note that the HT and 400°C samples does not have a significant difference in the position of the peaks because both the samples were subjected to thermal treatment during Pt deposition. Moreover, the reducibility increases by reducing the temperature of the thermal treatment due to the better mobility of the cations inside the structure. Nevertheless, the HT show the last peak of much lower intensity demonstrating that most of the Ni is already reduced before the mixed oxide crystalline structure increases.

A second post-synthesis parameter analyzed was the reduction temperature and time, since the systems used were different but with the same H_2/N_2 ratio and flow. Characterization data are presented in Table 15 and Figure 70. As for surface area measurements, the reduction performed at 350°C does not change significantly the value from reference sample, except a pore collapsing from a bimodal to a monomodal distribution; higher temperatures led to a decrease in surface area and an enlargement of pores. As for XRD data, the sample reduced at 350°C presents the above discussed mixed oxide phase (periclase-like) with intensity proportional to the reference sample. Thus, the reduction at lower temperature does not affect the mixed oxide structure and porosity. The sample reduced at higher temperature and time shows a mix of phases due to the presence of the mixed oxide and Ni^0 particles (reflects at 44 and 52°2θ). Moreover there is a small presence of the thermodynamic stable spinel $MgAl_2O_4$ phase (59 and 65°2θ) due the removal of Ni form the matrix that increases the tendency of spine formation. The detection by XRD of Ni^0 crystals is also an indication of sintering, since XRD measurement depends on mean value of crystal size. Scherrer measurements

confirm the presence of Ni^0 crystals with mean dimension of 8-13nm. The TPR comparison in Figure 71 analyzes the effectiveness of reduction treatments. Data confirm that at 350°C only Pt particles with a small amount of neighboring Ni atoms have been reduced without a significant change in the curve and reduction percentage compared to the calcined oxide. At 750°C however, the reduction is not complete, but the shift of the peak from 800 to 450°C indicates a high difference in Ni mobility in the structure, due to the extraction of part of the metal during the reduction treatment and thus the formation of vacancies. The amount of Ni reduced during the 750°C pretreatment can be approximated around 30%, calculated as the difference within TPR data at 750°C and standard sample.

Table 15: Comparison of superficial values within different preparation procedures and post treatments in the $Ni_{40}Mg/Al$ sample.

Catalyst	Calcination T (°C)	Reduction T (°C)	Reduction time (h)	S.A. (m^2/g)	Pore volume (cm^3/g)	Pore dimension (nm)	Total H_2 uptake (cm^3/g)	Ni reduction (%)
$Ni_{40}Mg/Al$-HT	-	-	-	52	0.1	3.4-5.9	124	79
$Ni_{40}Mg/Al$-400	400	-	-	223	0.27	3.9-6.5	166	97
$Ni_{40}Mg/Al$-750	750	-	-	170	0.34	3.6-6.2	124	78
$Ni_{40}Mg/Al$-R350	750	350	3	162	0.32	5.1	105	67
$Ni_{40}Mg/Al$-R750	750	750	12	105	0.32	8.8	72	46
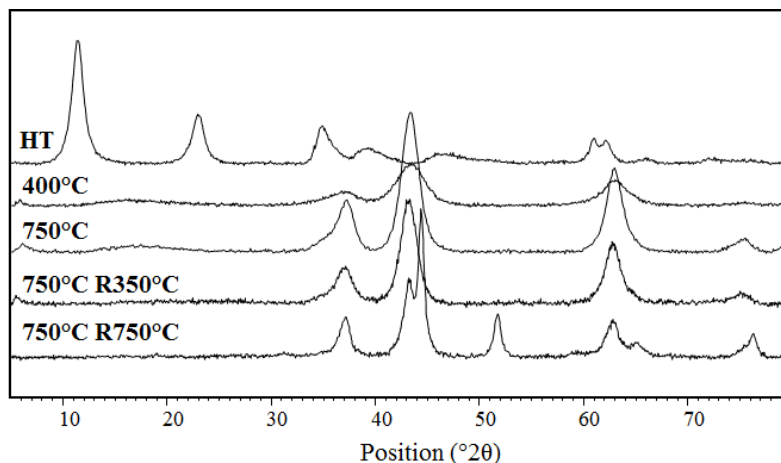
Figure 70: XRD analyses of the prepared Ni₄₀Mg/Al containing samples at different post-treatments.
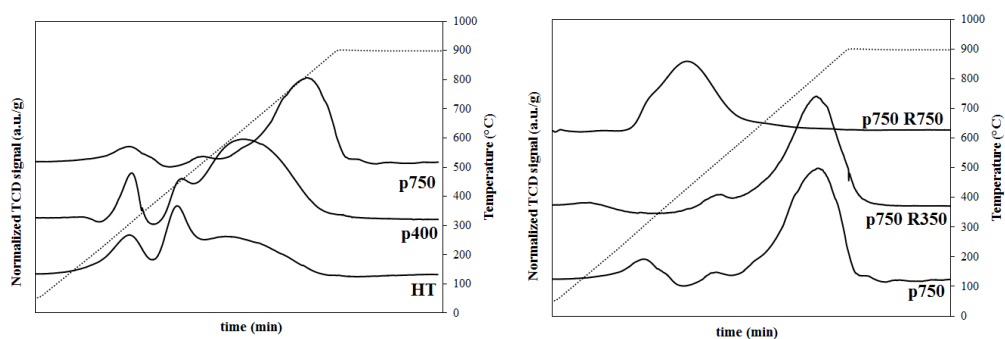
Figure 71: TPR profiles of Pt 3% wt. over Ni₄₀Mg/Al supports at different reduction and calcination temperature.

TEM analysis were performed over the Pt loaded samples to check the morphology of the catalyst and the distribution of the cations in the matrix. Figure 72 reports Pt/Ni₄₀Mg/Al samples at different reduction temperature. The two samples show the same combination of spherical and flat crystals. In the case of R750 sample, the dimension of the crystals is increased, due to the modification of the composition of the structure. EDS analyses evidenced a mean Ni:Mg:Al ratio of 39:27:34, slightly different than the 39:36:25 reported for the R350 sample. At higher temperature, Ni-rich areas of the sample were detected together with parts containing mainly Mg and Al, confirming the reduction of the metal from the structure. Moreover, analyses over the single particle determined the presence of both Pt and Ni in the same particle suggesting the formation of core-shell or alloy of reduced metals.
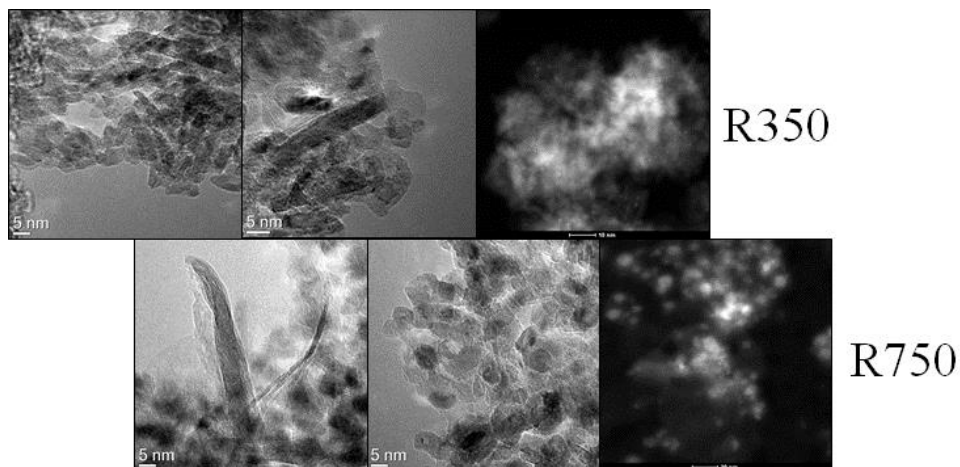
Figure 72: TEM and STEM-HAADF images of Pt loaded $Ni_{40}Mg/Al$ supports. Samples reduced at 350°C and 750°C.

From catalytic tests are reported in Figure 73 at different calcination temperatures no differences were highlighted within the hydrotalcite and 400°C calcined support. That is because, to allow the reduction of Pt, both the samples were treated at 350°C for 3h in a H_2/N_2 mixture, and this caused a change in the HT structure leading to partial mixed oxide phase and to the same results in term of selectivity and conversion. A further increase in calcination temperature gives a small decrease in conversion and gas yield, and an increase in liquid selectivity. The results can be justified in terms of reducibility of Ni and increase in the formation of hydrogen and reforming reaction.

Analyzing the differences in reduction temperature (Figure 74), can be seen the effect of the reduction of Ni particles, together with sintering effect. Products selectivity show a decrease in all the values except ethanol, according to the increase in Ni activity due to the higher degree of reduction. Even though, the reduction differences detected by XRD analyses do not produce a significant variation in the reactivity of the sample. It can be assumed that the higher reduction of Ni leads to the partial extraction of the metal from the mixed oxide structure with the formation of bigger particles, which are not highly reactive in APR compared to the reduction of Ni on the surface of the sample with the treatment at 350°C.

Figure 73: Comparison within Ni₄₀Mg/Al samples with Pt 3% wt. at different calcination temperature. Reactions performed at 225°C for 3h; glycerol loading 6%.

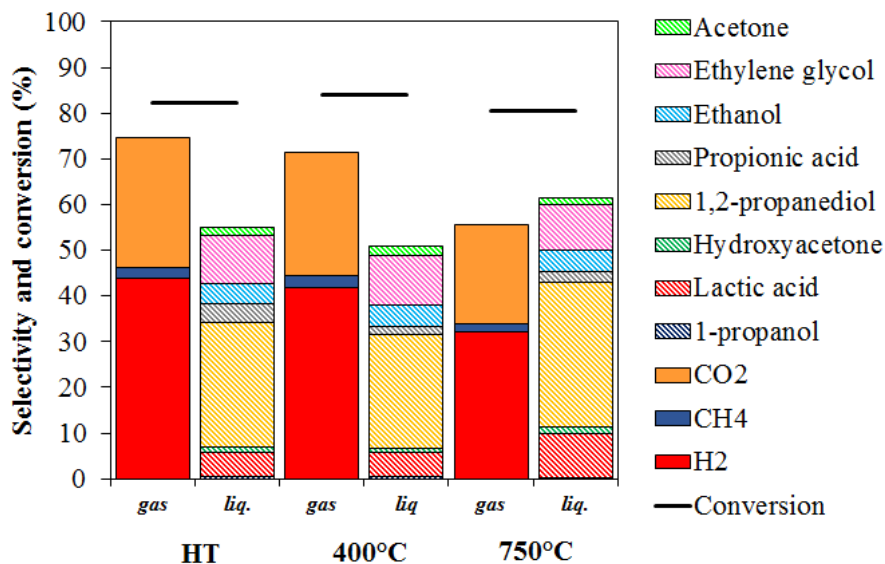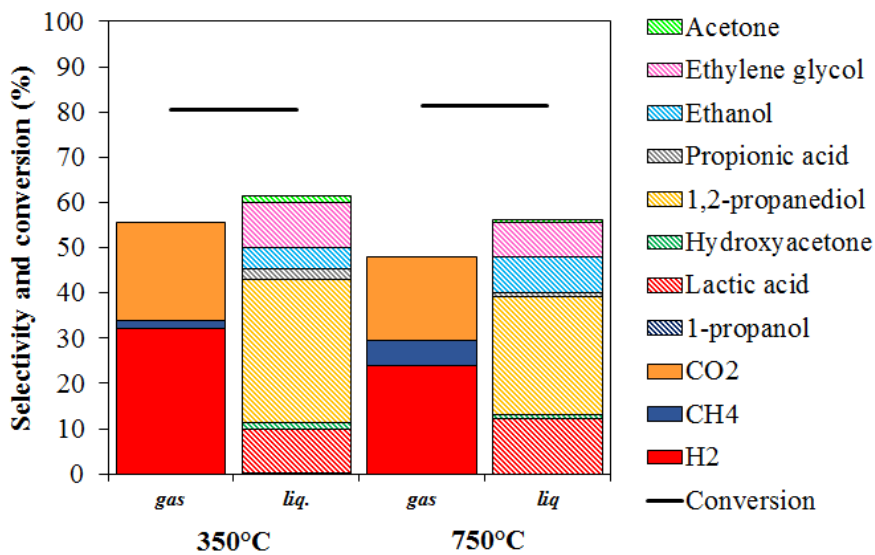*Figure 74: Comparison within Ni₄₀Mg/Al samples with Pt 3% wt. at different reduction temperature. Reactions performed at 225°C for 3h; glycerol loading 6%.*

In conclusion, a small variation in the reaction conditions does not lead to significant changes in the product distribution. The best way to drive the reaction with a change in

selectivity toward the production of specific molecules is to act over the support and active metal type and characteristics.

5.3.4   Addition of iron in the support

Iron is not a largely studied metal for APR reaction. A screening test performed by Huber et al.[216] have reported that it Pd/Fe_2O_3 presents higher activity than Pd/Al_2O_3 due to the WGS promotion of the support; moreover, the alloy of Pt with Ni, Co or Fe has positive effect compared to the traditional Pt/Al_2O_3 catalyst. Except screening tests, few works have been developed over iron in APR reaction[217,218]. It was thus found interesting to add to support and Ni study the effect of iron if embedded in the oxide, and comparing its catalytic activity with magnetite and hematite supports. The sample was prepare substituting Al^{3+} with Fe^{3+} cation in the mixed oxide structure, maintaining the previously determined ratio of 3:1. Table 16 reports the features of the synthesized support in comparison with Mg/Al and MgO. Surface area and pore dimension values are more comparable to MgO sample, while CO_2 uptake is lower compared the other samples, due to the higher acidity of iron cation compared to aluminum. TPD curves, reported in Figure 75, show a broad distribution of basic sites with the contribution of Mg-deriving strong sites and low temperature bicarbonate formation.

XRD analyses of the Mg/Fe in Figure 76 showed magnetite characteristic peaks at 30, 35, 57 and 62°2θ, while MgO periclase structure is evident at 43 and 62°2θ. The comparison with Mg/Al support apparently indicates that no mixed oxide phase is formed, evidenced also by the correspondence in relative height of magnetite and periclase reflects. As a comparison, two commercial iron oxides were impregnated with Pt and analyzed by XRD to determine a possible phase change with posttreatments. The graph reports also the maintenance of pure hematite (Fe_2O_3) and pure magnetite (Fe_3O_4) phases.

Table 16: Comparison within Mg containing catalysts and surface characterization. Samples calcined at 750°C for 5h.

Catalyst	X $M^{3+}/(M^{3+}+M^{2+})$	S.A. (m^2/g)	pore volume (cm^3/g)	pore dimension (nm)	CO_2 uptake $(cm^3/g$ STP)	CO_2 uptake normalized S.A. $(cm^3/g)/(m^2/g)$
Mg/Fe (3:1)	0.25	51	0.48	2.8-30.6	1.16	0.023
Mg/Al (3:1)	0.25	184	0.59	3.5-12.4	3.75	0.020
MgO-p	0	58	0.37	3.3-49.9	7.75	0.134
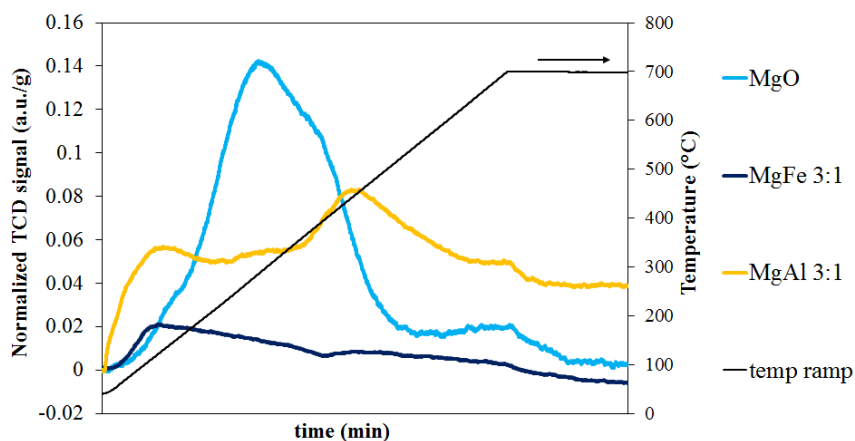
Figure 75: Temperature programmed desorption analysis of CO_2.
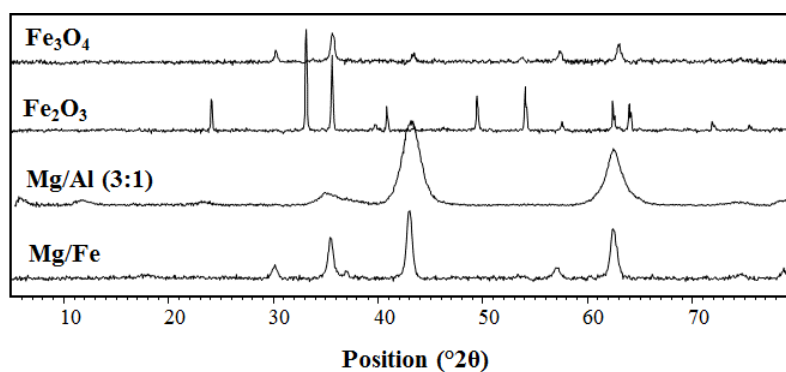
Figure 76: XRD analyses of the prepared Mg/Fe, hematite and magnetite supports after Pt loading.

An analysis of the reported samples in glycerol APR shows the data in Figure 77. Iron-containing supports present a very low gas phase selectivity (lower than 5%). Mg/Fe and hematite samples have similar behavior with hematite oxide showing the highest

conversion values and liquid phase selectivity. In particular a 1,2-propanediol selectivity of 32% and 28% in lactic acid. Regarding the effect on the catalyzed reaction (Figure 78), it is possible to underline two different contributions for the Mg/Fe supports. A dehydrogenating one with a value comparable with Mg/Al support and a dehydrating with a substantial effect of iron oxide, higher than Al_2O_3. Moreover, the hydrogen detected at the end of the reaction is low and the hydrogenation products are notably high for the Mg/Fe support. Decarboxylation instead is lower than 2% for all the iron-containing supports, probably due to the absence of strong acid sites. Comparing hematite and magnetite contributions, even at different conversion values, it is confirmed the dehydrating contribution of iron, combined with a high use of hydrogen in solution to form liquid products.
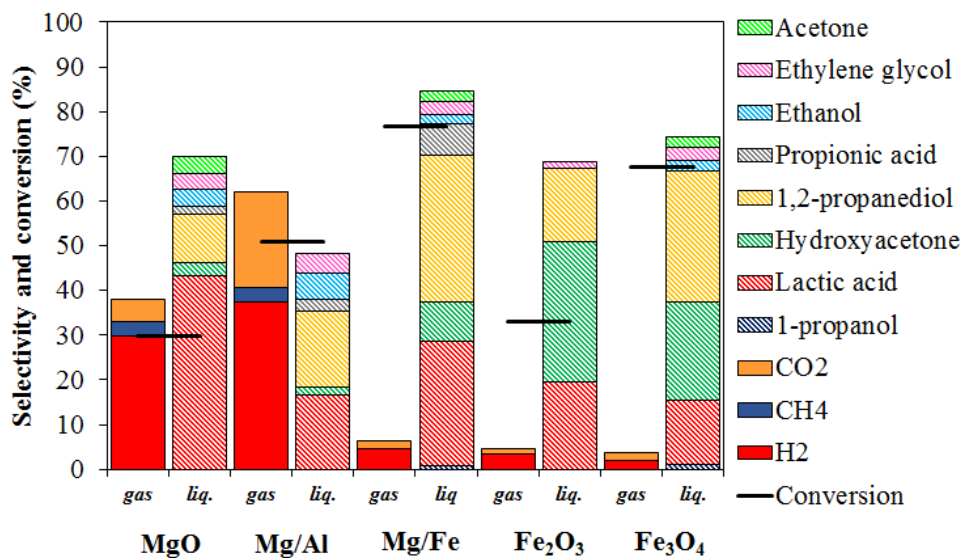
Figure 77: Comparison within Mg/Fe mixed oxide and reference Fe, Mg/Al and Mg supports with Pt 3% wt. Reactions performed at 225°C for 3h; glycerol loading 6%.
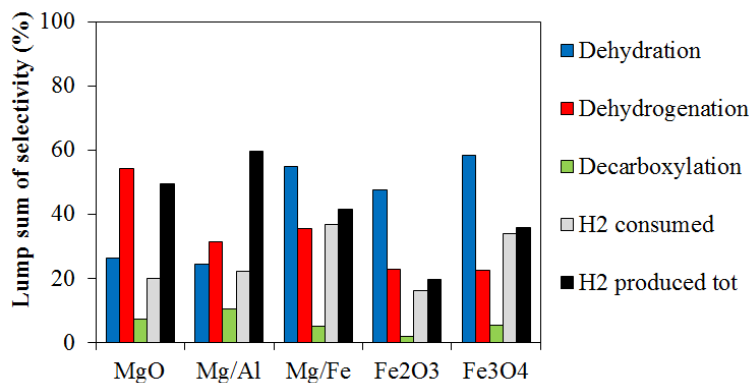
Figure 78: Lump sum of selectivity in different pathways for Pt supported over different oxides.

In conclusion, the catalytic activity of Pt using iron in the support does not lead to the increase in hydrogen production but has specific activity that can be included in the picture of tuning reaction products via changes in the support acid, basic and redox properties. However, differently from the reported literature which indicates an increase in WGS activity or global promoting effect[216,218], it is underlined a specific activity in dehydration mechanism of Fe acid cations in APR reaction of glycerol.

5.4   Study of bimetallic active phase over TiO$_2$

Previous studies have analyzed the effect of redox metals inserted in the support, and the study of the activity in combination with Pt as active phase. In this part, some efforts were also devoted to the study of different VIII group metals with the aim of verifying the activity of systems less studied in the literature either studying the activity of the single metal itself or in combination with Pt[216]. The first example is Ruthenium, which is widely applied in catalysis for hydrogenation and other organic reactions. Its activity can be interesting in APR of glycerol for its opposite intrinsic activity compared to Pt. Another study derives form a collaboration with professors L. Prati and A. Villa from the chemistry department of the "Università degli studi di Milano". The collaboration deals with the possibility of supporting over TiO$_2$ peculiar NiO nanoparticles. These have the possibility to be reduced at lower temperature thus

permitting to avoid sintering phenomena occurring at high reduction temperature in the studied Ni-containing hydrotalcite precursor.

5.4.1   *Ruthenium as active phase*

Ruthenium nitrosyl nitrate [$Ru(NO)(NO_3)_x(OH)_y$, x+y=3] was impregnated 3%wt. over titania synthesized by microemulsion technique and tested in APR reaction (Figure 79). It shows a significantly lower conversion compared to Pt loaded catalyst, with main selectivity in primary liquid reaction products and a 12% selectivity in H_2. Its expected activity in hydrogenation reaction was not significant, giving a higher value in dehydrogenation and dehydration compared to Pt (Figure 80). The two metals were than combined to study the possible sum of their effect in the reaction. The precursors were dissolved in the same solution and impregnated over titania with a total loading of 3 and 6%. From catalytic tests, the 1.5-1.5 catalyst shows a positive trend, with a conversion of 49% and similar selectivity in lactic acid, hydroxyacetone and 1,2-propanediol. Only gas phase selectivity is lowered compared to previous tests. The use of higher loadings of both metals instead did not give the expected results maintaining a lower conversion than Pt3 catalyst and without modification of ratios within preferred pathways compared to 1.5-1.5.
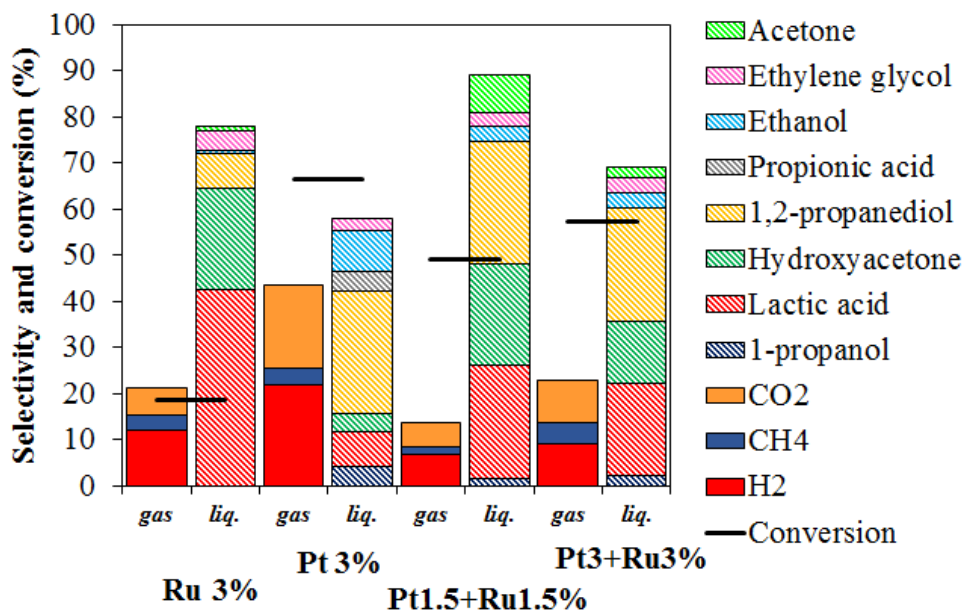
Figure 79: Comparison within TiO₂-m support with different metal loadings of Pt and Ru. Reactions performed at 225°C for 3h; glycerol loading 6%.
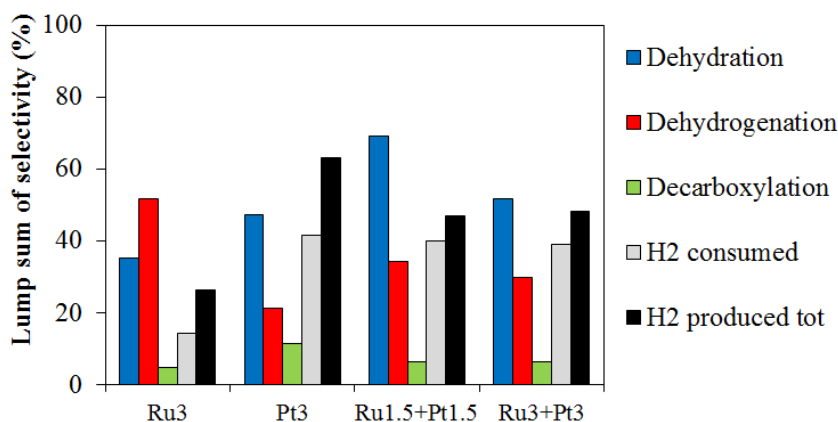
Figure 80: Lump sum of selectivity in different pathways for TiO₂-m support with different metal loadings of Pt and Ru.

In conclusion, the preliminary tests using Ru in APR did not give significant results requiring to be deeply examined, especially if compared to a highly active catalyst as Pt. Nevertheless, the combination of the two metals at low loading allowed the possibility of reducing Pt content together with the maintenance of a good activity.

5.4.2   *Immobilization of NiO nanoparticles*

The significant activity of Ni in APR suggests the possibility of testing the same metal as immobilized phase not via traditional impregnation method, but loading NiO nanoparticles. The method was developed by Prati et al. [132,133], and consisted in the preparation of 3-5nm NiO nanoparticles via urea reduction and their deposition over commercial titania (Degussa P25). It was thus interesting to study the effect of those materials in APR reaction to analyze the differences with previously reported bulk systems. Moreover, the loaded samples were prepared also over microemulsion titania and it was compared with P25 support.

Preliminary tests were done with different loadings of NiO over P25 TiO_2 (25 and 50% wt.). The samples were characterized, loaded with 3%wt. of Pt and reduced at 350°C, since previous results have demonstrated the better activity in APR of the combination of the two metals. As a comparison, the NiO loaded samples in absence of Pt were reduced at 750°C and tested. XRD characterization in Figure 81 reports the supports and the two reduction steps. NiO reflects are present at 37, 43 and 63°2θ, while Ni^0 is present at 44 and 51°2θ. After the reduction step at 350°C it is evident the formation of metallic Ni particles and the absence of NiO reflects probably due to the reduction of Ni atoms for spillover effect of Pt particles. The reduction at higher temperature instead causes the presence of larger Ni crystals, for the increase in sharpness of the peak. Moreover, there is also the disappearance of anatase phase and the formation of rutile crystals together with other not stoichiometric phases of titanium oxide in lower quantity. TPR analysis of the Pt loaded catalysts were performed but not reported since the curves were not significantly different. Two peaks were detected at 130 and 320-340°C, the first attributable to the reduction of Pt and the second to Ni particles. Nevertheless, the reducibility of 25%wt. sample was complete, while 50%wt. was reduced only up to 71%, maybe due to the presence of bigger particles as indicated by the broadening of NiO reflect in XRD.
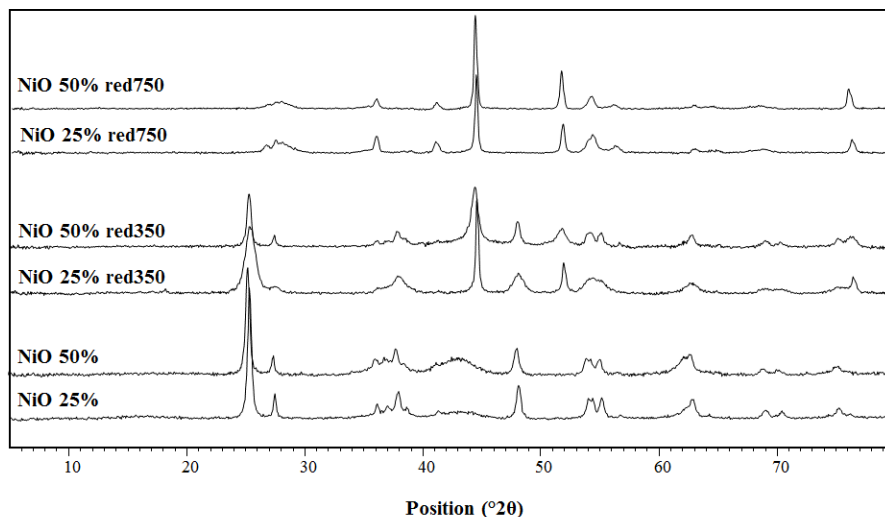
Figure 81: XRD analyses of different NiO loading over TiO$_2$ P25 before and after reduction treatment at 350 and 750°C.

The catalysts were tested in APR of glycerol, but conversion lower than 10% were obtained for unreduced and unloaded NiO/TiO$_2$ catalysts. Figure 82 reports the reactivity data for Pt loaded samples reduced at 350°C and NiO/TiO$_2$ catalysts reduced at 750°C. The first test on the left shows no significant differences within the two NiO loadings. Conversion values, larger than what obtained with other catalysts, are 95 and 92% respectively, with 20% selectivity in hydrogen and CO$_2$ and 10% in methane. In this case the main liquid phase products are 1,2-propanediol and ethanol, indicating a significant activity in C-C cleavage and hydrogenation for those systems. The negligible difference within the two loadings can be due to a mechanism involving Pt sites in combination or in cascade with Ni. Thus, even if the reactivity becomes dependent only over Pt quantity, a more specific comparison within the two loadings can be done analyzing the tests reported on the right of Figure 82. The samples were reduced at 750°C to assure the complete reduction of Ni particles. The decrease in conversion can be due to the absence of Pt as activating metal thus the obtained 16 and 27% values are dependent on Ni content. Primary products are favored, as lactic acid and hydroxyacetone with gas phase yields lower than 10%. Moreover, 50% NiO/TiO$_2$ test presents a significant carbon loss, maybe due to the formation of condensed molecules not detectable via HPLC. Nevertheless, as already observed during tests with

Ni/Mg/Al, it was defined that high NiO loading is not necessary to improve activity in APR especially in presence of Pt.
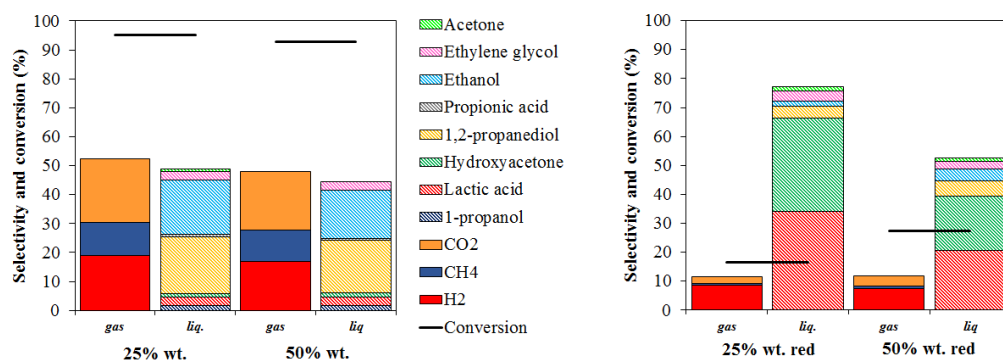
Figure 82: Comparison within TiO₂ P25 support with different metal loadings of NiO. On the left catalyst loaded with 3%wt. Pt; on the right catalyst reduced at 750°C. Reactions performed at 225°C for 3h; glycerol loading 6%.

Previous data have reported the higher activity of microemulsion synthesized titania compared to a commercial anatase. Thanks to the collaboration, we were able to obtain NiO nanoparticles loaded over TiO₂-m with a 25%wt., subsequently added with Pt 3%. The two NiO/TiO₂ supports were characterized via porosimetry, TPR and TEM, to analyze the different interactions within the nickel oxide and titania support. Mean particle size dimension, calculated over anatase peak by Scherrer equation in Table 17, show smaller particles, as analysed previously, compared to the commercial sample. The analysis of the reducibility of NiO over the two supports was done in absence of Pt, to avoid the flattening of the results by spillover effect (Figure 83). The P25 sample shows four reduction peaks, linkable to surface and bulk reduction of the particles but possibly due to convolution of more peaks. The microemulsion-supported instead shows four maxima maybe attributable to bigger particles or less accessible, due to lower dimension of the pores. The first two peaks are present at similar temperatures within the two samples and can thus be due to similar type of particles. Table 17 reports the reducibility of the two samples that is again slightly different, suggesting a dissimilar distribution of NiO particles over the two titania. Surface characterization was done on the two Pt loaded samples, to detect the possible pore blocking by NiO particles (Figure 84 and Table 17). NiO/TiO₂-m sample shows slightly lower surface

area compared to the microemulsion titania analyzed in the previous paragraphs, and a reduction of pore average diameter, probably due to partial pore blocking due to the presence of NiO particles. The commercial loaded sample instead shows comparable surface area values and a sharp decrease in pore volume and average diameter. The adsorption curves for the P25 samples reported in Figure 84 are significantly different, suggesting a change in crystallinity of the support due to Ni loading treatment.

Table 17: Characterization of NiO loaded over TiO₂-m and commercial P25 TiO₂. Particle size is calculated by Scherrer equation, surface characterization done by porosimetry of Pt loaded samples and hydrogen uptake by TPR analysis.

	Particle size (nm)	S_{BET} (m²/g)	V_{pore} (cm³/g)	Pore average diameter (nm)	H₂ uptake (cm³/g STP)	Ni reduction (%)
NiO/TiO₂-m	8	144	0.21	3.5	65.4	87
NiO/TiO₂ P25	28	78	0.19	7.4	75	100
TiO₂-m	8	152	0.15	5.9	-	-
TiO₂ P25	27	79	0.34	30.1	-	-
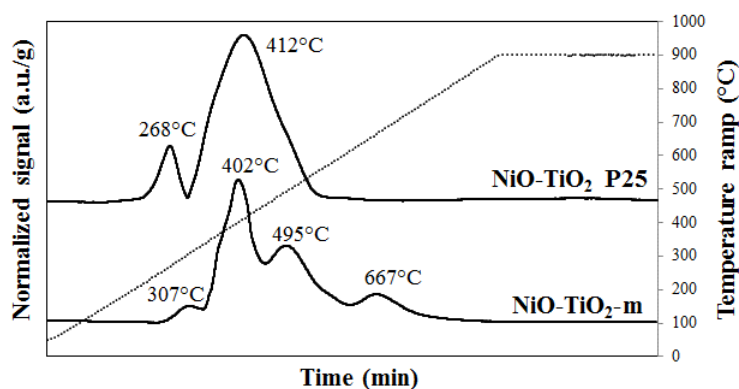
Figure 83: TPR profiles of untreated 25%wt. NiO supported on TiO₂-m and P25.
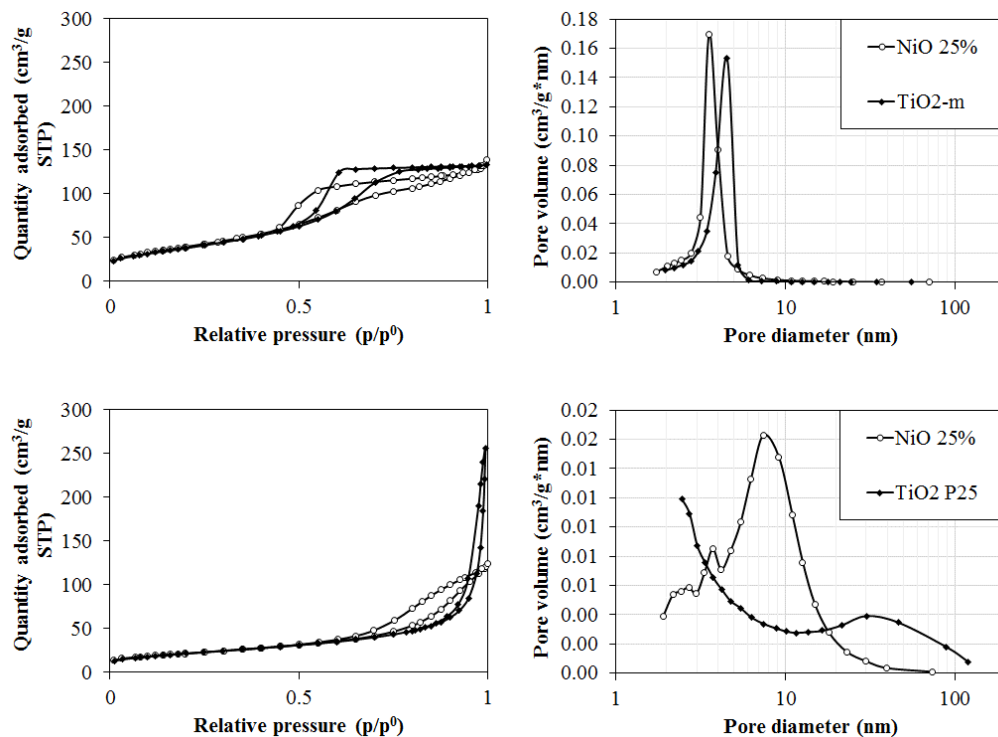
Figure 84: Adsorption/desorption isotherms and pore distribution of pure TiO₂ supports and loaded with 25%wt. NiO.

The most interesting comparison was done by TEM microscopy, evidencing, as reported in Figure 85, a different dispersion of the NiO nanoparticles over TiO₂. In particular it was detected a better contact within flat NiO crystals and TiO₂ spherical particles for the P25 sample, while the microemulsion support shows areas with predominant presence of NiO or TiO₂. A possible explanation of this behavior can be given by the smaller dimension of titania particles that act less as support and work more as dispersant increasing the interactions with nickel oxide. Punctual and area EDS spectra were analyzed to confirm the assumption, and evidenced for the microemulsion sample a lamellar area with excess of Ni and a spherical one with prevalence of Ti and small Ni content; generally the amount of Ni detected in Ti-rich areas was around 1-3% atomic. This evidenced a partial deposition of NiO nanoparticles over TiO₂ surface, with small spherical crystals not clearly detectable from the support, while the lamellar part remains separated from the support. As for P25 sample, EDS spectra evidenced a not complete homogeneity of the sample, even so higher than the microemulsion one,

with areas at high Ni or Ti content (with Ni presence 1-5% atomic) and others at comparable amount of the two oxides confirming a better interaction. TEM analyses were also performed over Pt loaded samples reduced at 350°C. As hypothesized the microemulsion sample shows small Pt particles and bigger Ni ones with a diameter up to 40-60nm. EDS profile of the particles determined the smaller composed only by Pt and the bigger with both the metals but a higher Ni contribution. The P25 instead shows smaller Ni particles up to 6-15nm. These analyses confirm on a side the preferential Pt deposition over Ni particles that favors an enhanced reactivity of the support. On the other, underline a not homogeneous mixture within NiO and TiO_2 microemulsion sample.
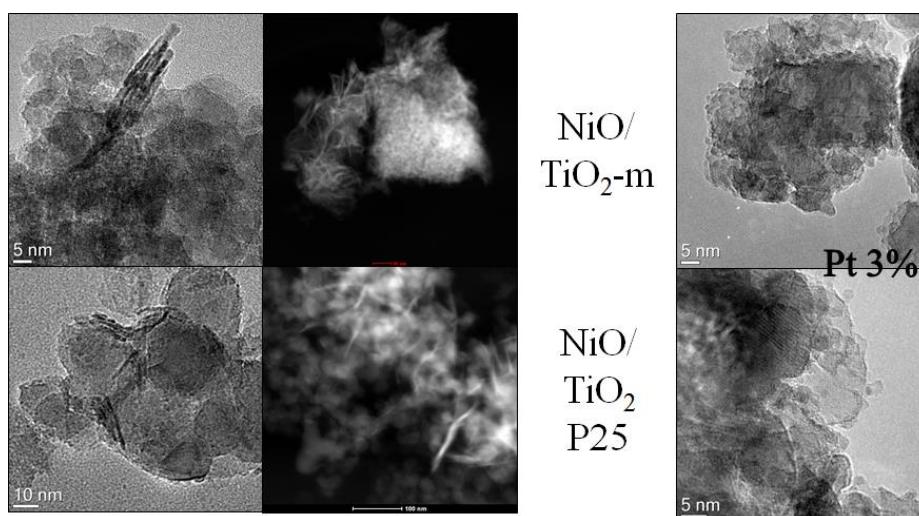
Figure 85: TEM and STEM-HAADF images of bare (left) and Pt loaded (right) NiO/TiO₂ microemulsion and P25 supports. Samples reduced at 350°C.

APR reactivity of the two samples showed at similar conversion values (91 and 95%) and significantly lower gas phase selectivity for the microemulsion support. Liquid phase products using microemulsion support show high selectivity for 1,2-propanediol and ethanol, 42 and 8% respectively while the P25 presents for the two compounds the same selectivity (19%). Lump sum method reports a 60% selectivity in total hydrogen produced for both the samples, but the H_2 consumed by reaction products accounts for 50% for TiO_2-m, while only 42% for P25. This indicates that the first support has a lower tendency in dehydrogenation reaction together with a high hydrogenation to 1,2-propanediol and dehydration processes. For what concerns decarboxylation, the highest

(10%) is obtained using P25 support. The dehydration process is typical of the support, thus is linked to different particle dimension and availability of acid sites. Hydrogenation and dehydrogenation depend primarily from Pt and in part from Ni, while decarboxylation is enhanced by Ni, in particular by smaller and more active particles. The latter can be easily linked to a better Ni dispersion for the P25 sample. As for H_2 production and consumption, it may be dependent on the combination of activity of Pt and Ni. It is suggested that in the case of small Pt particles over big Ni clusters the hydrogen produced tends to remain over the metal particles and further react in liquid phase. Oppositely, when the Ni particle is smaller there is a higher activity in dehydrogenation and a high quantity of the produced hydrogen evolved as molecular H_2 in the gas phase.

Figure 86: Comparison within TiO$_2$-m and P25 supports with 25%wt. loading of NiO and 3%wt. Pt. Reactions performed at 225°C for 3h; glycerol loading 6%.

In conclusion, the NiO supported catalyst was compared with the single metal impregnated over TiO$_2$-m and to the Ni$_{16}$Mg/Al oxide corresponding to the same Ni loading (Figure 87). The NiO/TiO$_2$ support allows a higher conversion up to 91%, compared with the 82% of the mixed oxide and 66% of the Pt loaded. The ratio within H_2 and CO_2 or CH_4 is more similar to Pt/TiO$_2$, while the mixed oxide shows a higher

hydrogen selectivity, due to the Mg presence. Liquid products distribution is again similar to Pt/TiO_2, but also not very different to the mixed oxide, taking into account the presence of Mg, which favors lactic acid production. Lump sum method (Figure 88) confirmed the reactivity of $Pt/NiO/TiO_2$ catalyst more similar to Pt/TiO_2 with a higher amount of hydrogen-consuming reactions and equal decarboxylation. The explanation may be similar to the comparison within P25 and microemulsion support, and it is related to the change in the dimension of the Ni particles. Nevertheless, the presence of Ni in the support enhances the selectivity in products maintaining a similar ratio within the reaction pathways. Bigger differences instead are present with the mixed oxide. A part from the presence of Mg, the selectivity of the latter is higher in gas phase products because Ni is distributed in the framework and thus it favors reforming mechanism to CO_2 and hydrogen, differently from NiO nanoparticles that participate to liquid phase reactions. Finally, as a comparison, Ni was loaded with standard impregnation method over titania with a 25% wt. Beside practical problems of impregnation of high quantity of solution, the catalyst is significantly less active with a 12% conversion and opposite selectivity compared to the other products, also due to the absence of Pt on the catalyst. Leaching tests by XRF have also reported a value around 0.1% of Ni for this catalyst, compared to zero value for the other catalysts, confirming this method as not suitable for Ni loading on the support.

The immobilization of NiO nanoparticles over titania surface has been demonstrated an interesting method for enhancing conversion and yield maintaining the selectivity of Pt/TiO_2 catalysts. On the other hand, this kind of catalyst does not show the peculiar reforming and C-C cleavage processes of Ni catalysts in mixed oxide. Nevertheless, more studies have to be performed to improve the distribution and the interactions of NiO nanoparticles over the support, in particular if synthesized by microemulsion technique.
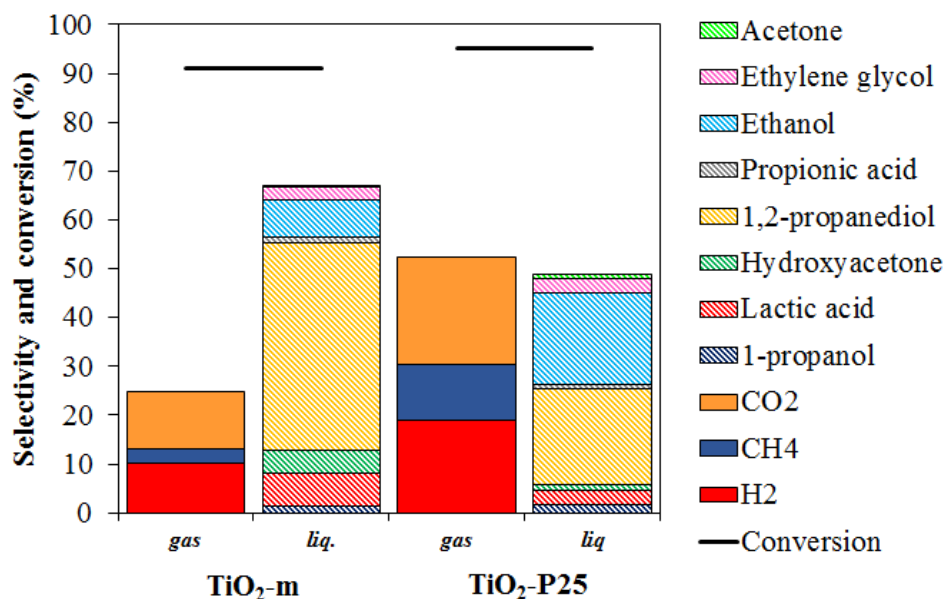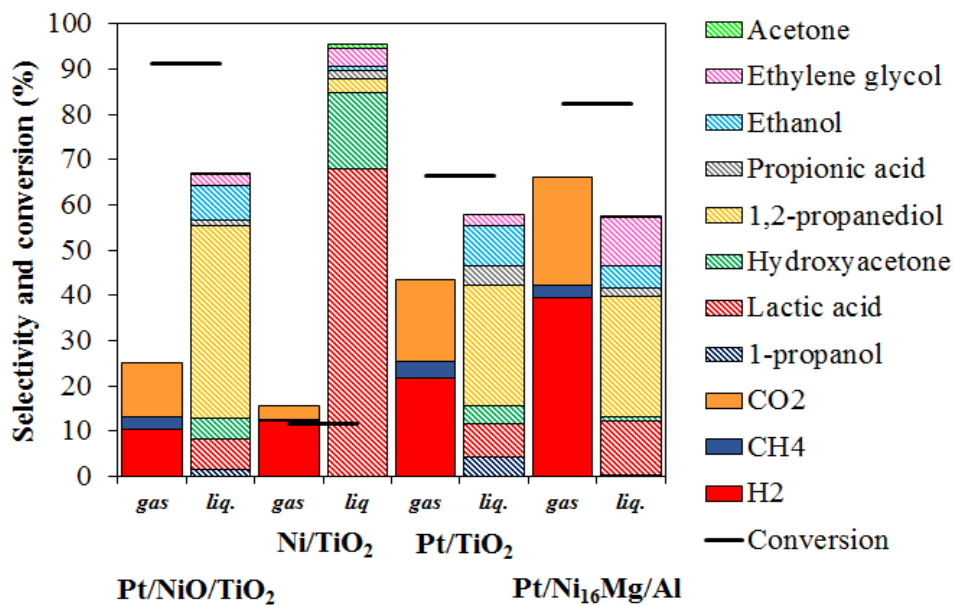
Figure 87: Comparison within different catalysts with 25%wt. loading of NiO and/or 3%wt. Pt. Reactions performed at 225°C for 3h; glycerol loading 6%.
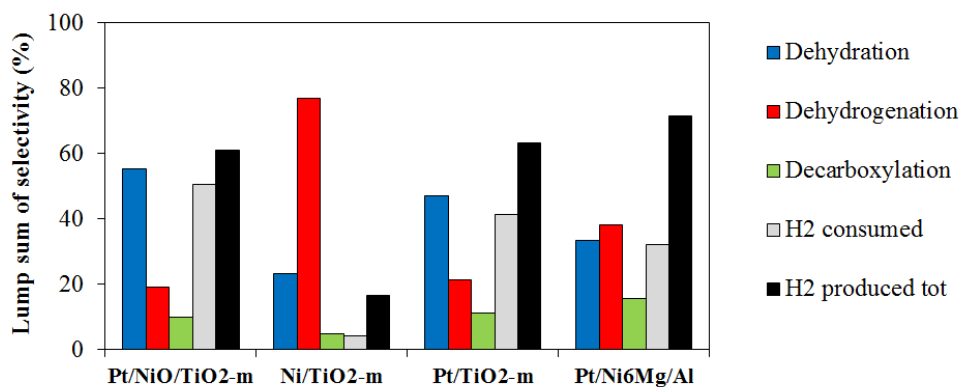
Figure 88: Lump sum of selectivity in different pathways for Pt, NiO and Ni supported over different oxides.

6. In-situ mechanism determination via ATR-IR

The previous paragraphs have reported the effect in glycerol conversion of several metal/support combinations. A deep study on reaction mechanism was carried out only for titania, assuming for the other catalysts the lump sum method as an indication of the reaction pathways and thus avoiding the complete study for each support. Nevertheless, it is still hard the complete understand of the mechanism of APR because batch system does not allow the detection of reactive intermediates, especially aldehydes. Moreover, several mechanisms are reported in literature, with intermediates having different roles increasing the difficulty in clarifying the detailed pathways. For this reason, the possibility of using an in-situ high temperature technique as attenuated total reflectance (ATR) IR spectroscopy opens several perspectives in the understanding of the intermediates and processes behind theoretical mechanisms.

6.1 Identification and analysis of intermediates

The first step was the setting of an optimal analysis method after several trials. The sample holder is constituted of a 7cm wide and 1cm long ZnSe crystal mounted in a heated trough plate electronically controlled. There is the possibility of analyzing liquid solutions in temperature or depositing a thin layer of catalyst within the crystal and the liquid. It was found that the optimal way to deposit the catalyst was to sonicate a suspension of catalyst powder and a volatile alcohol (methanol was selected) and deposit few drops of the mixture to fully cover the crystal. The alcohol is then removed by mild heating and the reactant solution is added on the cooled catalyst. Tests can be done with a controlled heating ramp with an acquisition each 5°C or rapidly heating to the desired temperature for isothermal analyses with 1spectrum/min. The major issue of the reported system is the evaporation, since there is no way to apply an overpressure to contrast the solution vapor pressure. The application of an aluminum cap over the plate permitted to extend the time range of the analysis but did not resolve completely the problem. Therefore, some high temperature analysis were maintained only for short time due to the rapid evaporation of the solution. Moreover, high temperature ones were

done with pure glycerol instead of a solution of the reagent to increase the boiling point up to 290°C and thus decrease the vaporization. The more significant analysis were performed with 1%wt. glycerol solution, to simulate the dilution of the ATR system, even with a different water/catalyst ratio. IR band assignment was done comparing the obtained results with typical vibrational regions reported in literature[219–223] or with IR spectra of compounds from database[224–226]. Background spectra were done before each set of analysis with simple crystal or catalyst deposited without solution, depending on the scope of the test. Nevertheless, CO_2 band changes ($2300cm^{-1}$)[226] during the analysis were not taken into account because atmospherically changes could influence the not sealed analysis system.

6.1.1   *Preliminary tests*

Pt/TiO$_2$-m 3%wt. was selected as starting catalyst because it was widely studied and characterized in APR batch system. Preliminary tests were done to check the adsorption of the catalyst in ramp and the shift of water bands due to the temperature. As for the first one, no adsorption was detected apart from moisture and CO_2 passivation of the surface. Thus, the catalyst was defined as transparent to IR radiation up to $800cm^{-1}$. Water presents three adsorption peaks in the analyzed range at 25°C: $1644cm^{-1}$ OH bending, $2126cm^{-1}$ (lower intensity) angle deformation plus bending and $3404cm^{-1}$ symmetric and asymmetric stretching plus overtone of bending band[227]. The shift of water IR bands in ramp up to 100°C was significant for the $3400cm^{-1}$ band and showed an increase of around $70cm^{-1}$ while other bands showed less relevant shift. Water and catalyst system in ramp was also tested but no particular evidence of peak shift was observed during the temperature ramp.

The assignation of glycerol peaks at room temperature analysis is done as reported in Figure 89. The broad band centered at $3600cm^{-1}$ is the combination of symmetrical and asymmetrical OH stretching (respectively centered at 3756 and $3652cm^{-1}$). The twin peaks at 2936 and $2882cm^{-1}$ are assigned to asymmetrical and symmetrical CH stretch of saturated bonds. Other particular bands are the CH$_2$ bending at $1416cm^{-1}$, the C-C stretching convoluted band at $1226-1219cm^{-1}$ and the C-O stretching of primary and

secondary alcohols respectively at 1043 and 1110cm^{-1} [225,226]. Several CH bending bands are present in the 1350-1480cm^{-1} range and other bands in the fingerprint region below 1000cm^{-1}. As for the temperature shift of glycerol bands, only the OH stretching is influenced, giving an increase of around 130cm^{-1} up to 200°C. The eventual degradation of glycerol due to the increase in temperature was also checked maintaining pure glycerol and 1% aqueous solution at 50, 70 and 150°C for 100min or until evaporation. The formation of only one peak at 1637cm^{-1} was observed at 70°C, probably because the evaporation at higher temperature was significant. The band falls in an intermediate region beside ketone carbonyl adsorption (1705-1725cm^{-1}) and C=C stretch (1640-1670cm^{-1}) but cannot be assigned to any specific specie. It is reported in literature the possible combination of C=C and C=O bands in the range 1600-1580cm^{-1} by keto-enol equilibrium[228], possibly obtained by dehydration of secondary OH group of glycerol.
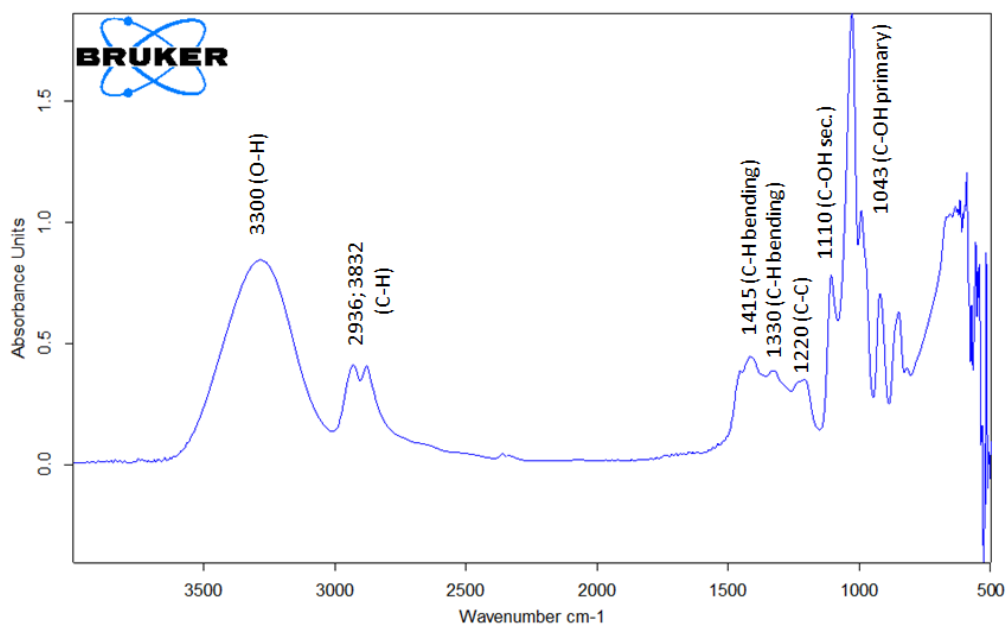

Figure 89: ATR-IR spectrum of glycerol at room temperature.

6.1.2 *Ramp and isothermal analyses*

As reported in materials and methods section, two type of analyses were performed: a controlled ramp with a 5°C steps and isothermal tests both of them until evaporation of

the solution starts. The first tests gave less significant data, probably because the time in temperature was not enough to obtain significant glycerol conversions (it was possible to perform the test up to 80°C due to evaporation). The subtraction of catalyst plus water ramp analysis from the 1% glycerol and catalyst one gave as result adsorbed glycerol peaks and products ones, as reported in Figure 90. Assignable to glycerol are the two CH stretching around 2800-2900cm^{-1} and the two C-O stretching bands around 1100cm^{-1}. A broad band is present in the OH region but it can be due to several contributions as water, alcohols or acids. Moreover, a peak is present at 1640cm^{-1}, probably assignable to keto-enolic equilibrium as reported previously. Another signal is present at 2000cm^{-1}. As the previous peak (1640 cm^{-1}) , no IR vibrational mode are generally assigned to a specific bond in this particular region, but the proximity to C=C and C≡C signals respectively at lower and higher frequencies, can indicate the presence of a multiple bond, slightly shifted due to surface adsorption and resulting from dehydration or dehydrogenation processes. Moreover, this peak could be assigned to surface catalyst hydration, as reported for alumina to bohemite transition in a similar region and it is present also in further tests[229]. Since this peak cannot be clearly assigned, it will not be taken into account in further tests. The same analysis but with the subtraction of 1% solution ramp gave as result the product's peaks. The most significant signals were the OH ones, shifted to lower wavelength and thus linkable to sp^2 or sp^3 carbon ibridization and the previously reported peak at 1640cm^{-1}, not significantly increasing or decreasing with temperature. Other signals of minor intensity were the 2000cm^{-1} one and some peaks in the CH bending and CO alcoholic regions. A ramp tests with pure glycerol solution permitted to reach 120°C. Results are reported in Figure 91, after subtraction of pure glycerol ramp test. In addition to the previously reported peaks, there are strong CH bands at 2860 and 2920cm^{-1} and more evident signals in the CH bending region (1260-1480cm^{-1}) and CO alcoholic stretching (1100 and 1040cm^{-1}). These signals can be due both to the formation of new molecules but also to the shift of glycerol bands (in particular CO ones) for interaction with Pt active phase. Moreover, the band at 1640cm^{-1} shifts with temperature to 1670cm^{-1} giving confirm of the hypothesis of a forming C=O bond previously adsorbed on the surface. Even if those analyses give an indication over the functional groups of forming

products, no significant trend of formation was observed with the increase in temperature, thus isothermal tests were performed to follow the formation of intermediates.
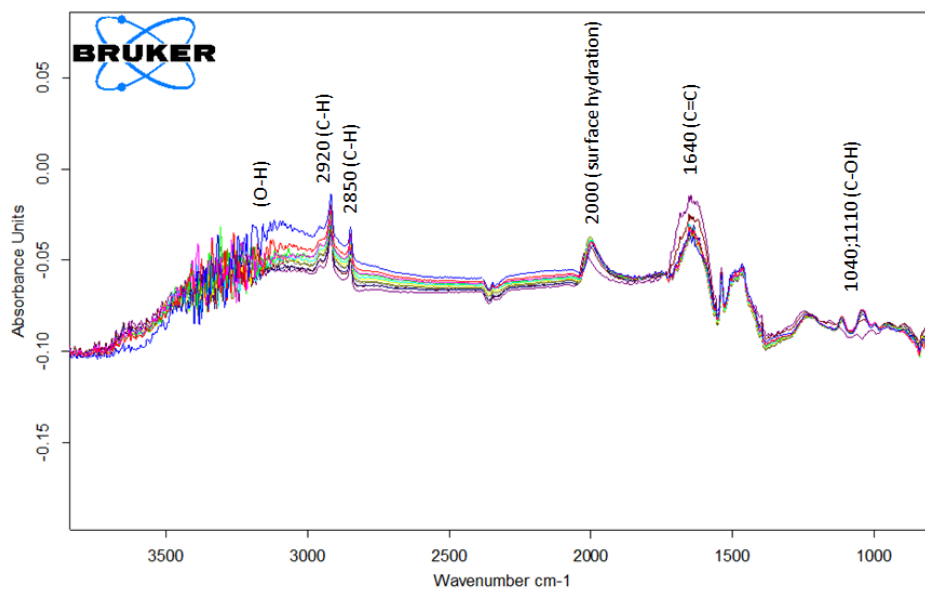

Figure 90: ATR-IR difference spectrum of adsorbed glycerol and products over catalyst in ramp up to 80°C.
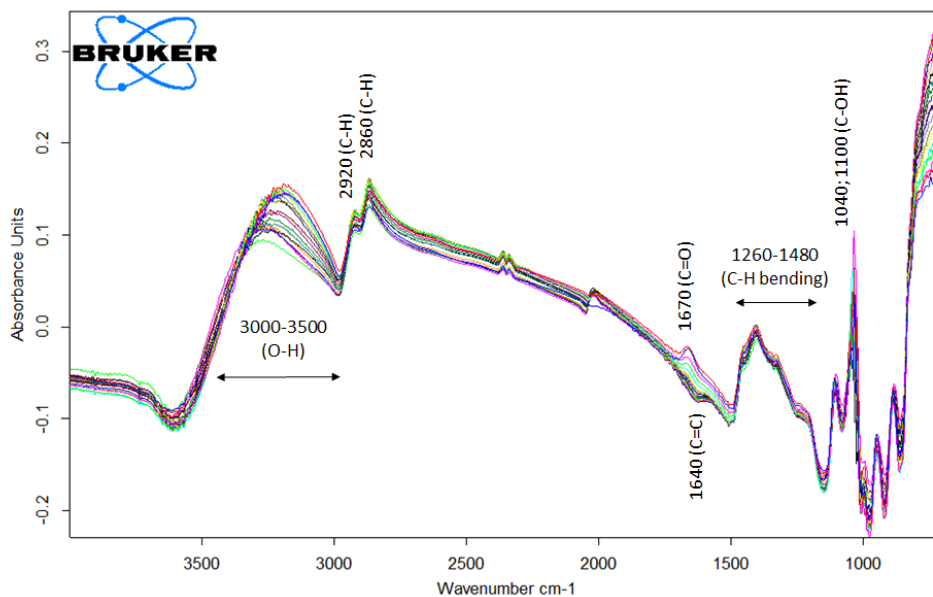
Figure 91: ATR-IR difference spectrum of pure glycerol and catalyst in ramp up to 120°C.

Lower temperature isothermal tests were performed with 1% glycerol solution at 50, 70 and 90°C; the higher temperature series at 70, 100, 130, 150 and 180°C used pure glycerol to limit evaporation. Nevertheless, evaporation was predominant for the last run of each series. Figure 92 and Figure 93 show the difference spectra obtained by subtraction of the first analysis, assumed as starting point at 50 and 70°C. In complex, it is clear that at lower temperature the product formation is significantly lower than 70°C. 50°C analysis show the formation of convoluted peaks around 1100, 1300-1400, 1600, 2024 and 2900cm^{-1}. At 50°C, is not possible to identify the single peaks, due to the low intensities, but it is confirmed that the intensity increases with time of analysis, apart from the band at 2024cm^{-1}.

A more clear analysis is possible with the spectra run at 70°C in Figure 93. In the OH and CH stretching region (>2400cm^{-1}), there is the formation of a broad band with two maxima at 2941 and 2889cm^{-1}. Those peaks are slightly shifted to higher wavelength compared to glycerol ones and do not present the same intensity. Beside the possible explanation of OH adsorbed on catalyst surface that shifts the maximum, several products present similar CH bands in that region, especially the ones with the same carbon involved in C-O bonds. The analyzed intermediates that present two peaks in this region are ethylene glycol, glycerol, glyceraldehyde and 1,2-propanediol with two twin bands of comparable height, while pyruvic acid, pyruvaldehyde, dihydroxyacetone and lactic acid present two bands with different intensities and shifted higher wavelength. Clearly, the difference within the two groups of products is due to the presence of carbonylic functionalities bonded to the carbon atom that shift the vibration of C-H group. Comparing those molecules with the difference spectra obtained at 70°C it is more evident the presence of C-OH groups for the twin peak at the same intensity, but a more precise assignation only on this base is not possible. Moreover, in the region around 2900-3100cm^{-1} are present also vinyl C=CH adsorptions that are possible as reaction intermediate. OH bands are more difficult to be assigned due to the broadening of the band and to the subtraction of water and glycerol that give a signal around 3200-3500cm^{-1}. The presence of carboxylic OH signal is suggested for the presence of a band around 3500cm^{-1} and a broad signal at 2500-3100cm^{-1} under the CH stretching band typical of carboxylic acids. Finally, taking into account the broad OH signal and the CH

stretching, a shoulder is present in the 2700-2800cm^{-1} region assignable to CH aldehyde stretching. The identification of specific intermediates of reaction is not possible using only this part of the spectrum; nevertheless, more significant signals are present in the carbonylic region (1500-1800cm^{-1}), due to the absence of glycerol and water bands. Experimental results present three strong and well-defined peaks at 1620, 1695 and 1723 cm^{-1}. The latter and stronger signal is surely attributable to C=O stretching of aldehyde or carboxylic acid, even if it is not possible to discriminate within the two for adsorption shifts[230]. This peak is present in pyruvic acid, pyruvic aldehyde, glyceraldehyde and lactic acid products even if the first one presents two more bands at higher wavelength that are not shown in the reaction spectra while the pyruvic aldehyde one is more broadened. The second signal at 1695cm^{-1} is in the ketones region, halfway within acyclic and αβ-unsaturated molecules. It could be assigned to hydroxyacetone, considering a shift in its adsorption due to catalyst presence[45]. The last signal at 1620cm^{-1} is also in a peculiar region and it is typical of C=C bonds. In particular it can be assigned to conjugated C=O dienes, it is the same signal detected in the spectra during temperature ramp analyses with glycerol and catalyst. More difficult to be analyzed is the fingerprint spectra region lower than <1500cm^{-1}: two widely overlapped groups are present within 1500-1170 and 1150-950cm^{-1}. The last and most significant signals to be identified in this region are the C-O ones. 1044 and 1067cm^{-1} signals can be assigned to primary alcoholic groups, while the more intense 1117cm^{-1} signal is a secondary one; no tertiary are detected. 1280cm^{-1} peak instead is relatable to C-O stretching of carboxylic acid. Other two intense signal at 1237 and 1400cm^{-1} are instead similar to alkyl CH bending bands; while the lower around 1000cm^{-1} can be assigned to vinyl CH.

Considering the evolution of the spectra with time, up to 15 minutes only the C=C signal is present in agreement with the ramp analysis findings evidencing a trend of formation of a double bond by dehydration before the starting of dehydrogenation mechanism to ketones and acids. Than after 30min also the C=O bands are appearing with lower intensity together with C-O and C-H bending and stretching. Around 60min it becomes significant the OH contribution and the C=O signal becomes higher compared to C=C one, it appears also the C-O signal at 1269cm^{-1}. After that time, no

further bands are appearing and the reciprocal intensity remains constant with a raise in all bands suggesting an increase in concentration of all products. The timing suggests a first dehydration over glycerol molecule, later followed to the formation of aldehydes and ketone intermediates. The formation of carboxylic acids occurring later, since the signal of the OH broad band is not present before 30min.

The analysis performed at 90°C with glycerol solution did not give appreciable results due to quick evaporation. The isothermal tests with pure glycerol and catalyst at 100°C is similar to Figure 91, with low intensity signals, probably because the adsorption of glycerol on the catalyst is predominant with respect to the limited activity of catalyst in forming intermediates and products at this temperature. Stronger signals in 130 and 150°C tests, even if lower than solution tests, are present in the C=O and C-O regions but shifted to lower wavelength around 1500cm^{-1}. This suggests a lower reactivity of the system even with the formation of similar intermediates, due to the appearance of signals in the same order in the double bond region, when the catalyst is saturated by glycerol molecules.
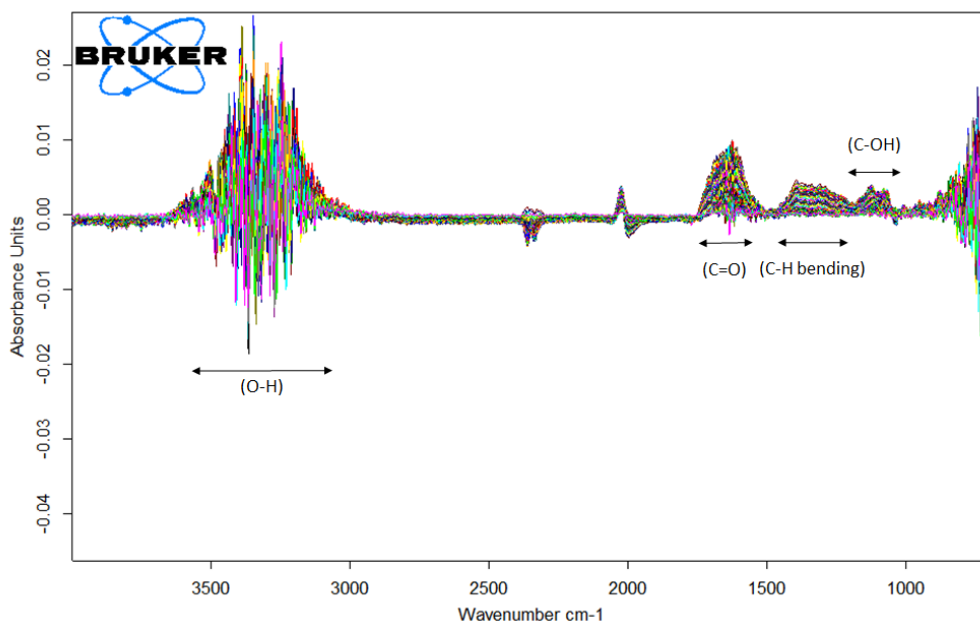
Figure 92: ATR-IR difference spectrum of glycerol 1%wt. solution and catalyst in isothermal analysis at 50°C.
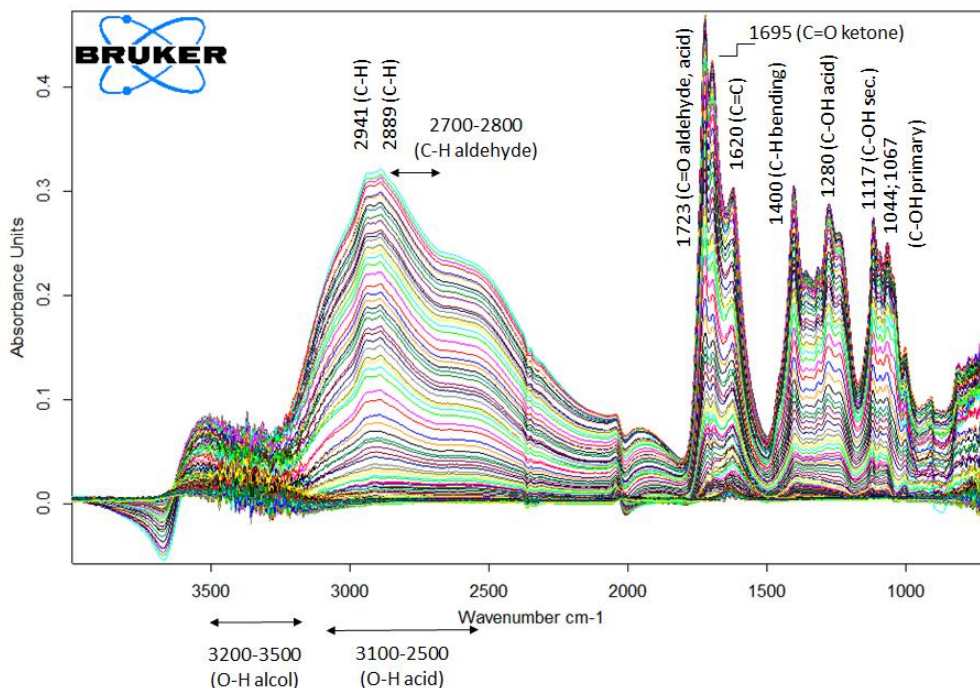
Figure 93: ATR-IR difference spectrum of glycerol 1%wt. solution and catalyst in isothermal analysis at 70°C.

The strong overlapping of bands and the shift due to the adsorption over catalyst surface makes impossible to assign specific products with reliability. Nevertheless, specific signals, as the ones in the C=O region allow forming hypothesis to support the reaction mechanism taking into account even the lower working temperature of those tests compared to batch system. A starting point is the formation of a C=C conjugated signal since the early stages of reaction, supposed coming from dehydration of glycerol. After that the system evolves towards the formation of C=O bands assigned to glyceraldehyde from dehydrogenation and hydroxyacetone from keto-enolic equilibrium. As a following stage acids are formed with an enhancement in the C=O band together with the presence of the broad OH and C-OH typical signals. This is the case of pyruvic and lactic acid, whose signals are corresponding to the ones in the test. On the other hand, the assignment of C-OH alcoholic and C-H stretching signals is more complicated due to the presence of those bonds in all the products suggested by the mechanism. In conclusion, obtained data go in parallel with the mechanism hypothesis, at least for the first stages of the two pathways. Further tests have still to be

performed with simpler molecules to analyze the reactivity and the product assignment to specific pathways.

6.1.3 Tests with intermediates

As performed with mechanism identification, some intermediates were tested in ATR-IR over Pt/TiO$_2$-m 3%wt. catalyst. Isothermal analysis at 50 and 70°C were selected because were the most significant of previous analyses. The intermediates tested were glyceraldehyde, hydroxyacetone and pyruvic aldehyde with concentration varied from 0.2 to 1%wt. in water; lactic and pyruvic acid were not tested due to pH limits of the instrument.

The first test was done with glyceraldehyde 0.5%wt. solution to evidence the presence of this key intermediate in the reaction pathway. The spectrum of the intermediate analyzed at room temperature did not show the characteristic C=O adsorption at 1700cm^{-1} not for the solid reagent neither for its aqueous solution at room temperature. This is because the reagent condensates into a cyclic hemiacetal molecule with a low dissociation constant at room temperature, depending also on solvent type and concentration[231–233]. For this reason, a low concentration 0.2% wt. solution was prepared. Ramp tests did not give significant signals a part from the 1620cm^{-1} peak assigned to keto-enolic equilibrium. Isothermal test at 50°C show at the beginning the same peak shifted at 1630cm^{-1} later becoming an overlap of signals within 1560-1717cm^{-1} plus a small signal at 1409cm^{-1}. This change could be due or to the formation of reaction products, explained by the presence of the CH bending signal halfway within saturated and unsaturated C-C bond, or by hydrolysis of glyceraldehyde dimer and formation of the C=O signal that should be around 1700cm^{-1}. 70°C isothermal test is reported in Figure 94. As for glycerol solution, it shows the formation of several peaks the most interesting ones in the carbonyl region. The signal at 1730cm^{-1} is comparable with glycerol 70°C analysis and increases with the reaction time. It can be assigned to lactic acid since glyceraldehyde should be removed by first spectrum subtraction. A 1640cm^{-1} peak is present since the beginning of the reaction, while a signal at 1593cm^{-1} starts around 15min increasing with time. If the first signal is

attributable to C=C conjugated bond, the second one can be assigned to ketone, since acetone and acetic acid are present in batch reaction tests as products. Lactic acid presence can be sustained also by the OH broad peak around 3000cm^{-1}.
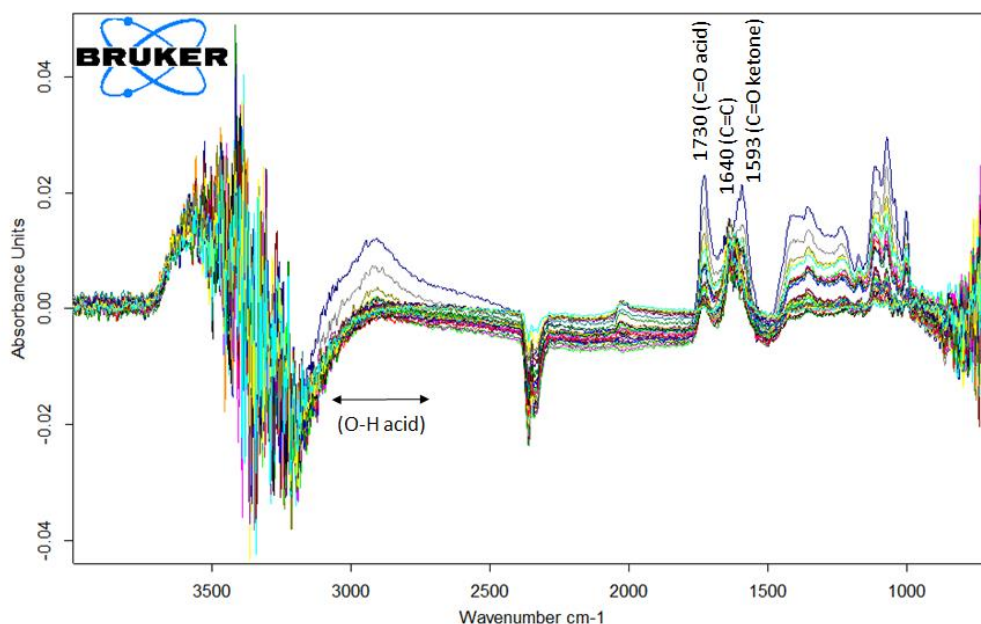
Figure 94: ATR-IR difference spectrum of glyceraldehyde 0.5%wt. solution and Pt/TiO$_2$-m catalyst in isothermal analysis at 70°C.

Pyruvaldehyde was also tested in the same conditions as glyceraldehyde. In this case, the characteristic aldehyde and double bond peaks at 1638-1719cm^{-1} are present even in the starting solution. 50°C isothermal test showed the formation of the 1620cm^{-1}peak and a broad band in the CH bending and CO stretching region. As for the 70°C test, reported in Figure 95, there is the formation of a first peak at 1620cm^{-1}, that increases with time subsequently neighbored by a 1718cm^{-1} signal. The first can be the C=C shifted by adsorption over the catalyst, while the second can be the formation of a carboxylic group for example from lactic or pyruvic acids. The analysis of the maxima at 1380 and 1104cm^{-1} are more similar to lactic than pyruvic acid and can be assigned respectively to OH groups (more similar to secondary one) and C-O carboxylic stretching.
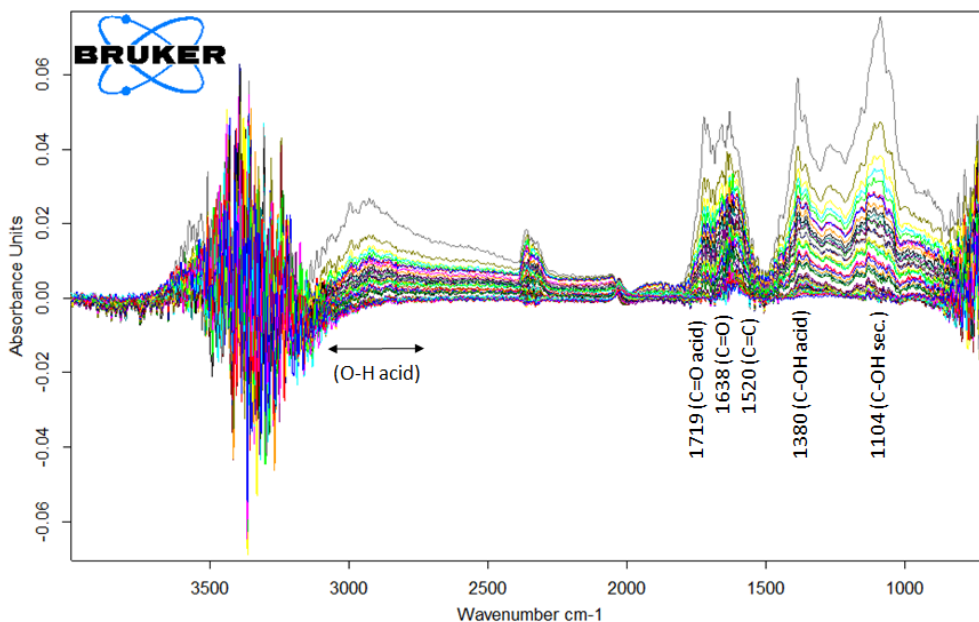
Figure 95: ATR-IR difference spectrum of pyruvaldehyde 0.2%wt. solution and Pt/TiO$_2$-m catalyst in isothermal analysis at 70°C.

In addition, hydroxyacetone was tested as intermediate of dehydration mechanism. Its characteristic peaks are 1719cm^{-1} C=O and 1078cm^{-1} the primary OH. 50°C test showed again the formation of 1620cm^{-1} peak, and a small formation of bands in the CH and CO range. 70°C test presents too the same peak as stronger one, as reported in Figure 96, due to the strong keto-enolic equilibrium. After 20 minutes there is the formation of a second peak around 1720cm^{-1}, possibly the shift of C=O ketone bond for adsorption or the formation of acetone. The 1043cm^{-1} signal is not more similar to the broad OH band of hydroxyacetone but is in the same position of 1,2-propanediol bands with two smaller shoulders on each side.
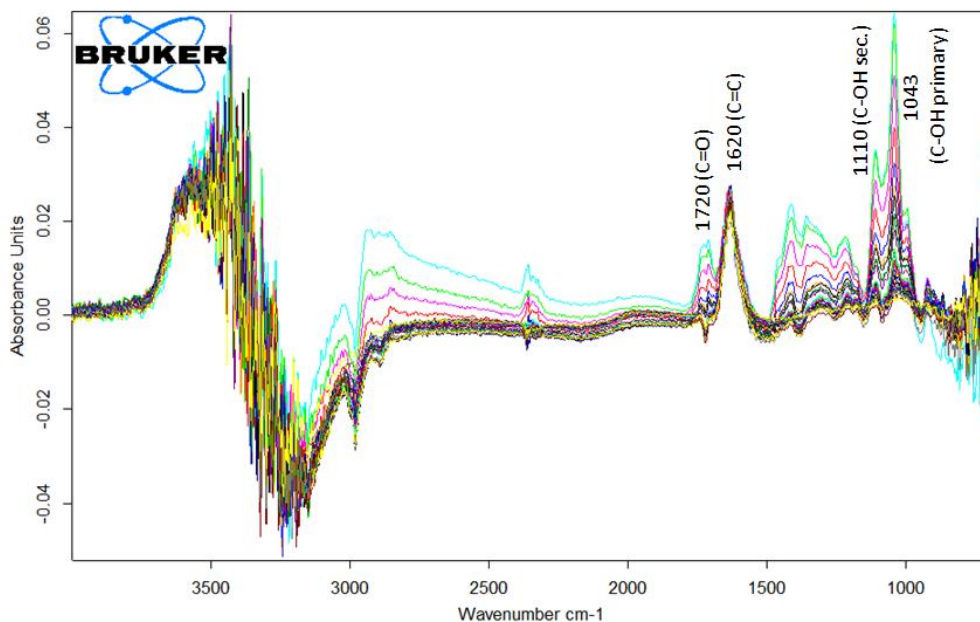
Figure 96: ATR-IR difference spectrum of hydroxyacetone 1%wt. solution and Pt/TiO₂-m catalyst in isothermal analysis at 70°C.

Even if the analysis of intermediates was complex due to the high number of functional groups present in the molecules, some confirms were obtained. In particular it was determined the possible formation of 1,2-propanediol from hydroxyacetone, together with a carbonylic containing molecule as acetone, unlikely an acid. On the other hand, both glyceraldehyde and pyruvic aldehyde show the formation of a C=O and acid OH stretching bands, coming after the C=C conjugated one suggesting those molecules as precursor for an acid formation via dehydration pathway.

6.2 Comparison within Pt/TiO₂ catalysts

Previously reported reactivity comparison within commercial and microemulsion-synthesized support can be applied to ATR-IR technique to define if the difference is due only to a lower activity or to a change in reaction intermediates. Preliminary tests with water and only catalyst were done for the commercial and no adsorption was obtained neither in this case. The most meaningful analysis is reported in Figure 97 as a comparison within the two Pt supported catalysts. At a first examination, the same

peaks are present but with different reciprocal intensity. In the OH region, the bands assigned to vinyl and aldehyde CH stretching around $3100cm^{-1}$ are reduced for the commercial sample. In the carbonylic region instead the C=O acid stretching remains the highest signal but the C=C one at $1620cm^{-1}$ is significantly reduced for the commercial. Moreover, the ketone signal at $1695cm^{-1}$ is present only in the microemulsion sample. Also the CH bending signal at $1400cm^{-1}$ and the C-O carboxylic are reduced compared to the microemulsion support while the other CH bending signal at $1236cm^{-1}$ and primary and secondary C-O alcoholic signals are increased (with a higher intensity for primary ones compared to secondary).

Figure 97: ATR-IR difference spectrum of glycerol 1%wt. solution and catalyst in isothermal analysis at 70°C. Comparison within microemulsion and commercial catalysts with Pt 3%wt. loading. Spectra acquired every 10min are presented even if data were collected with a 1spectrum/min frequency.

Reactivity data in batch system have shown a preponderance of primary products (as hydroxyacetone and lactic acid) for the commercial support compared to the microemulsion one. On the other hand, ATR-IR system does not allow the identification of single products due to the complexity of signals and the reaction conditions are different from batch ones. A strict comparison within the products formed in autoclave and over the crystal is thus not possible, but some hypothesis are

possible. The higher intensity of C-OH signals, in particular primary ones, compared to the absence of ketone and lower C=C double bond, suggest a minor presence of unsaturated intermediates over the catalyst. It is in particular significant the ratio within primary and secondary OH groups over the surface with a predominance of secondary for the microemulsion support. This is in fact linkable to the presence of hydroxyacetone, suggested also by the 1695cm^{-1} carboxylic signal. Oppositely, the minor presence of reactive intermediates (unsaturated CO and CC bonds) can mean also a lower tendency to convert glycerol, as evidenced by isoconversion reactivity tests. Moreover, comparing spectra at the same time of reaction it is evidenced a late increase in products concentration for the commercial sample compared to the microemulsion. The latter shows in fact within 50 and 80min of reaction a higher intensity of signals and becomes comparable with the commercial only near the end of reaction. Thus the commercial catalysts seems more active in the product saturation to alcohol or acid form, but with a lower intermediates concentration, maybe due to a decrease in glycerol adsorption or activation.

The analysis of reactivity in ATR cell of the supports was analyzed also in absence of Pt. In Figure 98 for the analysis at 70°C is evident the higher evaporation in the commercial test and the latter and not gradual formation of products, as evidenced in the previous analysis. Neither of the two supports show the formation of carbonylic bands at 1700cm^{-1}, acid OH stretching of C-O acid stretching at 1270cm^{-1}. This indicates that those products are result of dehydrogenation pathway promoted from the metal. The most significant signals are CH stretching at 2941 and 2889cm^{-1} and the C-O alcoholic stretching with a predominance of primary compared to secondary together with CH bending signals indicating the predominance of dehydration pathway to alcohols. A part from the differences within support and Pt-containing catalyst, the two support present a similar reactivity, but the microemulsion support shows a higher amount of products indicating a higher reactivity.

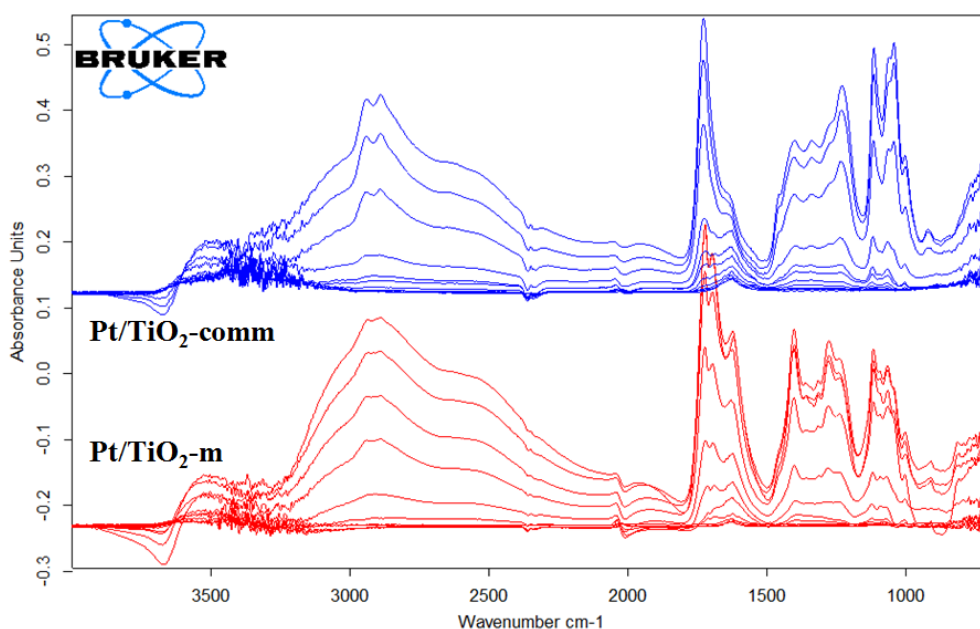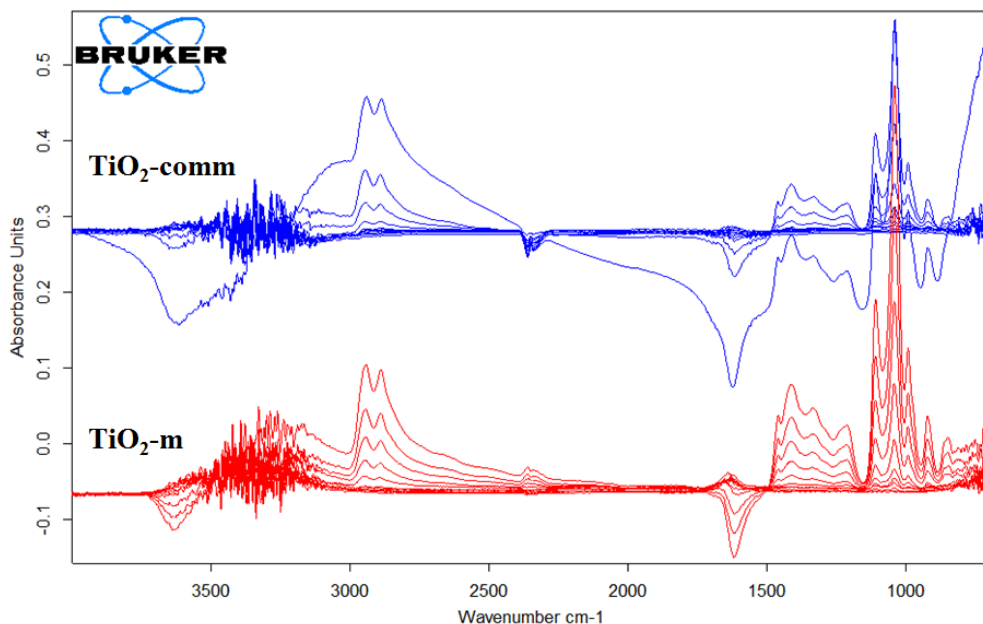*Figure 98: ATR-IR difference spectrum of glycerol 1%wt. solution and catalyst in isothermal analysis at 70°C. Comparison within microemulsion and commercial supports.*

6.3   Comparison with other catalysts

After Pt/TiO_2 tests, other catalyst that have shown a significant activity in glycerol APR were tested. MgO, Mg/Al 3:1, $Ni_{40}Mg/Al$ and NiO/TiO_2-m were selected as support for 3%wt. Pt and tested in isothermal conditions at 70°C with glycerol 1%wt. solution. Pt/MgO test is reported in Figure 99. In comparison with Pt/TiO_2, it shows only a small shoulder in the carboxylic range at $1670cm^{-1}$ with a two peaks not present in titania sample at 1590 and $1517cm^{-1}$. The assignation in this range is not easy since it could still be a C=O or C=C bond shifted by strong adsorption over the catalyst surface. Due to the low intensity of acid OH stretching and the absence of $1270cm^{-1}$ C-O acid stretching, it is more probable the assignation to adsorbed C=C bond. 1416 and $1372cm^{-1}$ peaks instead are similar to titania CH bending signals, together with CH stretching signals at $2800-2900cm^{-1}$. In addition, C-O alcoholic region presents the same signals, but with an intensity more similar to hydroxyacetone over titania support tests and a preponderance of primary groups compared to secondary. There is also the

presence of vinyl signal around 920cm^{-1}; also, the sharp peak at 3700cm^{-1} can be a result of OH shift. This indicates that only some intermediates of MgO reactivity are similar to titania ones. Since MgO was demonstrated as a dehydrogenation catalyst the presence of saturated C-OH bonds instead of C=O can suggest that the hydrogen remains over the surface of the catalyst giving a saturated intermediate instead of stabilizing double bond ant the temperature tests. On the other hand, there is still a contribution of dehydration mechanism due to the presence of unsaturated C=C signals together with CH ones.

Figure 99: ATR-IR difference spectrum of glycerol 1%wt. solution over Pt/MgO-p750 3%wt. catalyst in isothermal analysis at 70°C.

The second support tested was Mg/Al with a 3:1 ratio. Figure 100 presents a high evaporation rate for this test, but the signals are still detectable. This is because the hydration degree of this support is higher than the others are, and gives an exothermic contribution to the evaporation. As for MgO, there is only the presence of C=O signals with a stronger one at 1590cm^{-1}. The CH bending signals are in the same position but with higher intensity for the 1359cm^{-1} one. The C-OH region too is very similar to the previous test. Reactivity tests have shown for Mg/Al 3:1 catalyst a similar reactivity compared to MgO, with a lower dehydrogenation pathway and a similar dehydration

one. The only difference detected by ATR tests is in the C=C and CH bending region indicating the same groups but with different relative concentration. This suggests, as reported by APR tests, the same reactivity slightly changed by the presence of Al cation in the sample.
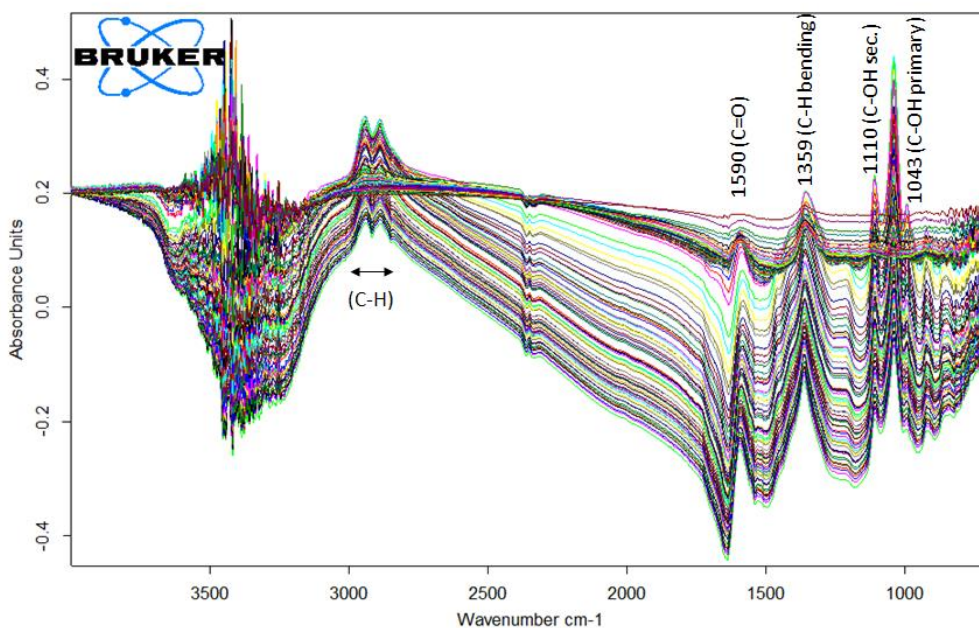
Figure 100: ATR-IR difference spectrum of glycerol 1%wt. solution over Mg/Al-p750 3:1 with Pt 3%wt. catalyst in isothermal analysis at 70°C.

Quite different is the graph of Ni containing sample with the same M^{2+}/M^{3+} ratio in Figure 101. The first dissimilarity is the intensity of the peaks, lower compared to all the previous reported samples and with the low intensity of CH stretching band at 2900cm^{-1}. The double bond stretching shifts from 1627 to 1584cm^{-1} during the test while CH bending at 1400 and 1357cm^{-1} are increasing with time, together with the C-OH signals. In complex, all the signals correspond to the reactivity of Mg/Al sample. The lower intensity can be due to the higher activation energy necessaire for the catalyst due to the presence of Ni embedded in the support, which affects only gas phase reactions leaving unaffected the liquid reactivity at this temperature. Similar results are obtained with Pt/NiO/TiO$_2$-m catalyst with NiO loading 25%wt. in Figure 102. Even in this case the intensity of the peaks is low and the only two detectable peaks are the C-OH stretching at 1109 and 1040cm^{-1} with similar intensity as for titania

sample. Since NiO particles are superficial ones for this catalyst, the presence of only C-OH groups, with a more significant noise in the OH region may be due to direct reforming of glycerol to lower alcohols in small amount, together with a low activation of the catalyst at the tested temperature.
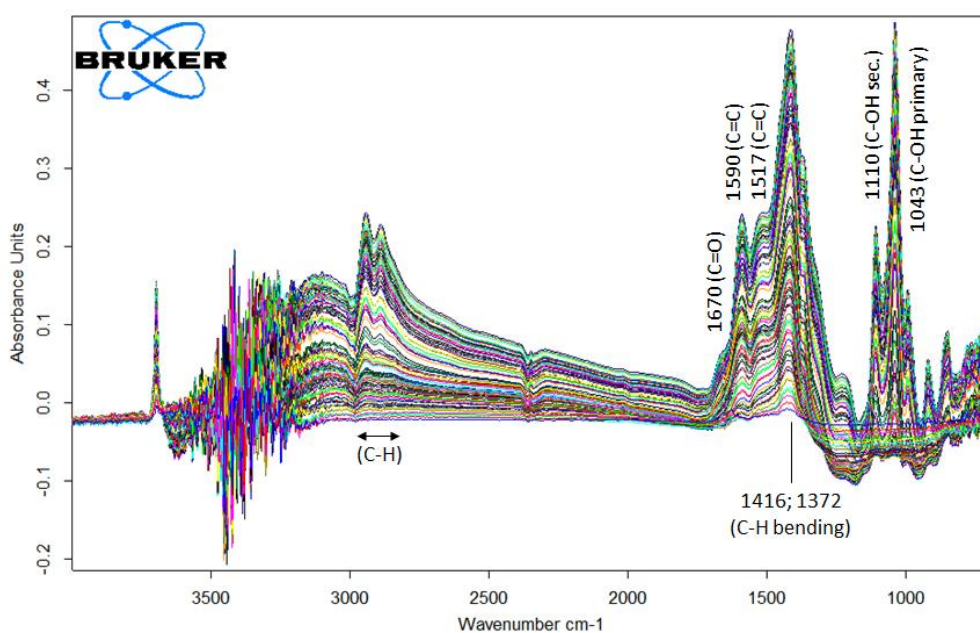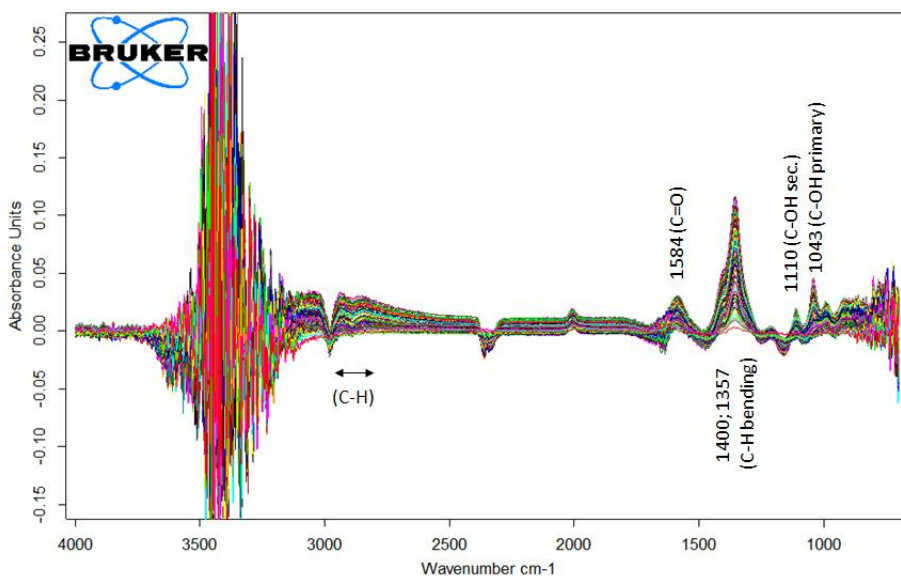

Figure 101: ATR-IR difference spectrum of glycerol 1%wt. solution over $Pt/Ni_{40}Mg/Al$-p750 3%wt. catalyst in isothermal analysis at 70°C.
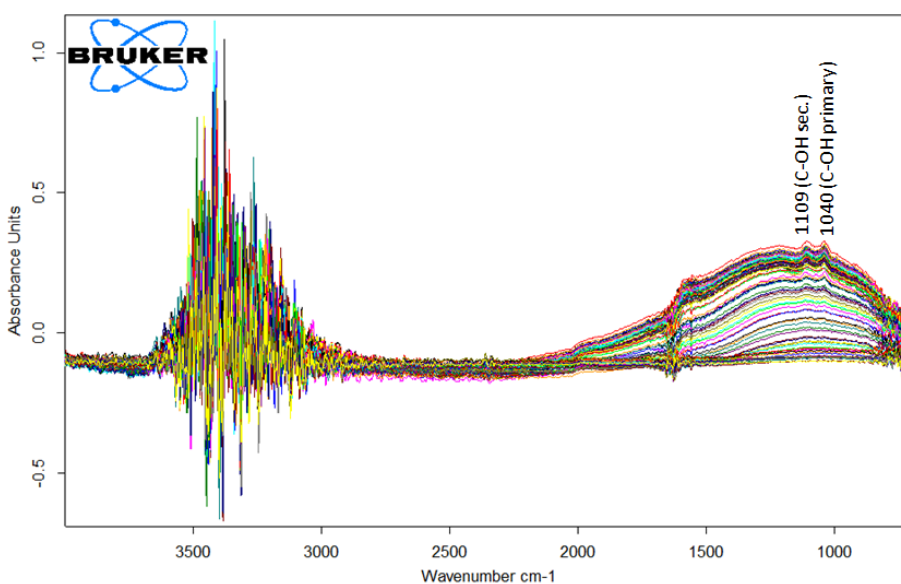
Figure 102: ATR-IR difference spectrum of glycerol 1%wt. solution over NiO/TiO_2 m 25% with Pt 3%wt. catalyst in isothermal analysis at 70°C.

6.4   Conclusions on ATR-IR

To sum up, the presence of functional groups assignable to the hypothesized reaction intermediates was found in presence of Pt/TiO_2-m catalyst. The hypothesis were compared also with tests with theoretical intermediates giving a good agreement with the assumptions. Moreover, the technique allowed also the comparison within activity of commercial and microemulsion-synthesized TiO_2. Beside, not noteworthy results were obtained by changing the catalyst at constant conditions, a part from the individuation of different reactivity due to the presence of shifted peaks and activation of the active metals. Nevertheless, ATR-IR technique remains a powerful method to analyze liquid phase reactions in presence of a catalyst, but a more in-depth consideration should be given to the assigned bands, maybe coupled with model simulation spectra or the use of molecules with simpler functional groups to differentiate the contributions.

7. Conversion of glucose

Glucose is the most abundant polyol in the world[234] because, besides the presence of sugars and amid, it can come from depolymerization of cellulose natural polymer. For this reason, its employment in fuels and chemical valorization has attracted increasing attention[235–238]. APR reaction is thus an interesting method to convert glucose and other sugars (mainly xylitol, sorbitol and fructose) into gas or liquid phase molecules, as a second step of biomass treatment after hydrolysis reaction[239–246]. Together with the reported advantages of APR process, it can be added the possibility of using biomass wastes from industry without pretreatment (i.e. paper liquors, food processing…) because they are already depolymerized and in water solution at low concentration. Nevertheless, these polyols present more reactivity problems compared to glycerol. First of all, their productivity to gas phase is lower than simpler ones and it is paired with a self-degradation to insoluble condensation products at high temperatures both in acid and basic catalysis[247,248]. For these reasons, part of this thesis research was devoted to the study of glucose reactivity in APR, being a more interesting and difficult challenge after the knowledge obtained on simpler polyols.

As a first step Pt/TiO_2-m catalyst was tested, with the aim of optimizing the reaction conditions and identify the obtained products. After that, similar catalysts studied in APR of glycerol were analyzed by changing active phase and support sites to correlate the activity with the product distribution. Finally, the catalyst was optimized trying to sum the analyzed parameters.

7.1   Study of the reactivity in APR

7.1.1 Identification of reaction products

Glucose reactivity was found to be more complex than glycerol one starting from the identification of reaction products in liquid phase. HPLC tests with ROA column at 30 and 60°C showed a complex mixture of products with frequent overlapping of the peaks. These analyses gave a good separation for C_2 and C_3 molecules, leaving the monosaccharides retention time in the range 10-12min with bad separation. Several

operating parameters were changed as eluent flow, pH and column temperature to try the optimization of separation but no better results were obtained compared to the analyses optimized for glycerol reaction. The same mixture was injected also in different HPLC systems as Hi-Plex monosaccharides column and two ROA column in series. The first method permitted a good separation of the monosaccharides part, but it was not good enough for the C_2-C_3 products, which overlapped with monosaccharides. The latter instead showed good separation of the peaks, together with a slight enlargement, nevertheless the main disadvantage of this analysis was the time of analysis that lasted more than 2h for the complete elution of all the products thus it was used only for few reactions. It was decided to maintain the same analysis method with two injection at different temperature because the overlapping was limited to a peak within 11.8 and 13minutes under which several C_4 and C_5 products were individuated.

The product identification was mainly done by retention time comparison in HPLC, checking the hypothesis with mass analyses. GC-MS and ESI-MS tests were done over reaction mixtures and standard solutions. The first method detected the C_3 products plus some traces of furanic compounds and unsaturated C_5 cycles but did not allow seeing lighter molecules due to overlapping with eluent peak. Moreover the technique was not able to detect sugars, thus it was not useful for the clarification of the overlapped HPLC peak. ESI-MS showed also some problems in product detection because of fragmentation of bigger molecules and coupling with cation impurities of the solvent (Na^+ for positive ions and Cl^- for negative ones). ESI^+ analysis was able to detect furfuryl alcohol, HMF and levulinic acid, while ESI^- lactic acid (or glyceraldehyde because it has the same molecular weight), furfural, glucose/fructose, ethylene glycol and levulinic acid. The analysis of standard mixtures anyway confirmed also this method as not optimal for sugars, since not all of the starting compounds were detected. In conclusion, the identification of the overlapped peak was done by HPLC analysis with double ROA column, which individuated two partially overlapped peaks. The most certain candidates is arabinose for the first one, while the second peak could be ribose, erythrose or xylitol, all C_5 and C_4 compounds. In conclusion, the overlapped peak was named as C_{4-5} and quantified with arabinose calibration factor in HPLC, since neighboring molecules with similar structure generally present similar response factors.

Compared to glucose, the amount of products in liquid phase is significant, accounting 15 calibrated over more than 40 possible molecules individuated in HPLC. For this reason, reactivity comparison is notably more difficult than previous reactions. Lump sum method was used as well in this part of the work with the aim of better analyzing the differences within the catalysts. It was considered the direct reaction from glucose to the product and the yield was multiplied by its stoichiometry factor considering dehydration, dehydrogenation, hydrogenation, isomerization and C-C cleavage pathways (as reported in materials and methods section). Since it is not possible to assign correctly the C_{4-5} peak this was considered as mean value within the reactivity of the four hypothesized molecules.

7.1.2 Degradation of the reagent

The first parameter that has to be studied in glucose APR is the degradation of the reagent in water at the reaction temperature in absence of catalyst. Cellulose and hemicellulose can undergo auto-hydrolysis in hydrothermal conditions at mild temperature (150-200°C), this step is then widely applied in combination with acid and basic catalysis to obtain one-pot production of chemicals[249–252]. The same auto-hydrolysis conditions can have an effect also over glucose degradation[253], it is thus important to define the auto-conversion of glycerol in blank tests, performed only with reagent and water. As it was reported in the previous chapter, the high amount of products calibrated causes difficulties in a graphic representation of the reactivity. Thus detected yield for blank reactions are reported in Table 18, while lump sum results are summarized in Figure 103 and Figure 104 at different time of reaction. The first test was done in a wide range of temperatures within 150 and 250°C for a short time of reaction. It can be seen that the conversion is significant even at low temperatures and becomes approximately complete from 225°C. Gas phase products are really low, while the only significant in liquid phase are sugars (fructose and C_{4-5}) and HMF. The latter is the expected dehydration product from glucose and its yield decreases during reaction due to the transformation to levulinic acid[234,254]. The stoichiometric amount of acetic acid was not detected probably because it undergoes decarboxylation at high temperature conditions. Lump sum method shows in Figure 103 the predominant effect

in dehydration. Isomerization contribution is higher at low temperature because the working conditions are too high to favor fructose formation and this reaction is favored by acid catalysis[255–257]. Finally, there is a dehydrogenation and cleavage contribution above 225°C, i.e. decarboxylation for the formation of CO_2 and other small molecules. Nevertheless, the most interesting parameters represented in the graph are carbon balance and yield sum. The latter calculates the amount of C-containing products detected by HPLC and GC, while the first accounts also the moles of reagent still present at the end of the reaction. It can be seen that the carbon balance (white square) decreases steeply with the increase in temperature, opposite to the conversion. The yield sum (black square) shows instead a maximum at 200°C, then becoming, as predictable, similar to carbon balance at conversion near to 100%. Total hydrogen values instead are not significant because depends on hydrogenation reactions since small amount of hydrogen were detected at the end of reaction. Blank reactivity was analyzed also for longer time of reaction giving similar results in terms of product yield but higher conversion, almost complete up to 200°C. The carbon balance is complete up to 175°C but decreases at lower than 50% at 200°C while the yield sum is comparable with reactions at 30min.

Table 18: Yields and parameters for blank APR reactions performed at different time and temperature, glucose concentration 3%wt.

Reaction		Gas phase yields			Glucose conversion	Liquid phase yields														
Temperature (°C)	time (h)	H_2	CH_4	CO_2		Fructose	Sorbitol	C_{4-5}	Lactic acid	Acetic acid	Levulinic acid	Propionic acid	Methanol	Ethanol	HMF	Glycerol	Formic acid	Hydroxyacetone	Ethylene glycol	1,2-propanediol
150	0.5				0	3		1							1					
175	0.5				19	4		1	3						6					
200	0.5				46	4		4			1				28					
225	0.5	1		2	96	1		2	1	1	1				20		1	1		
250	0.5	1		2	100			2	1	1	4				3		1			
150	3				4	3		2												
175	3				28	3		3							16					
200	3				91	1		3	1		2			1	28					

Figure 103: Lump sum of yield in reaction pathways and product sum for blank tests at different temperatures Reactions performed for 30min, glucose 3% wt.
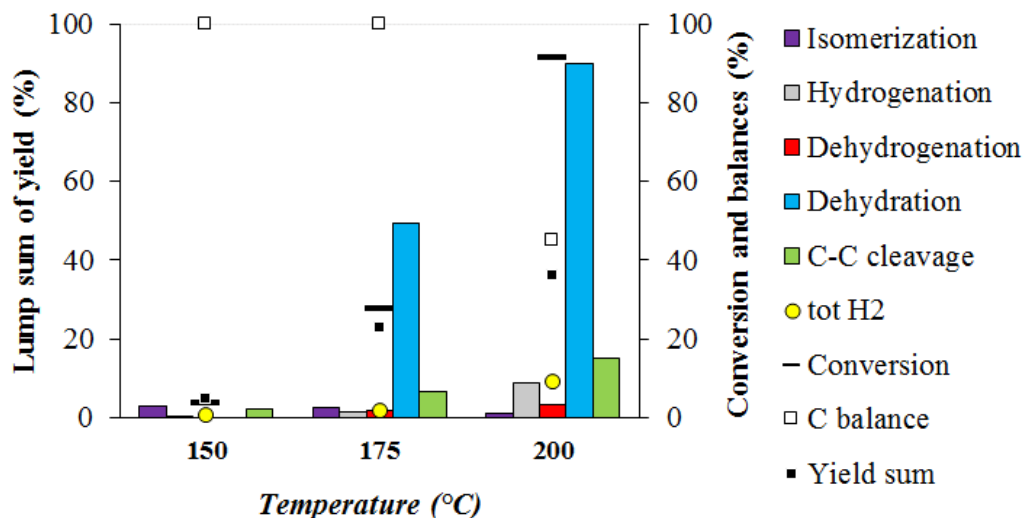
Figure 104: Lump sum of yield in reaction pathways and product sum for blank tests at different temperatures Reactions performed for 3h, glucose 3% wt.

The reported data evidenced high conversion and carbon loss at temperature above 200°C even in absence of catalyst. This underlines one of the major drawbacks of working with sugars due to the formation with temperature and time of soluble and insoluble heavy compounds. Generally are named humins if coming from acid catalyzed hydrolysis process of different types of sugars, and are based on furan rings with several oxygenated functional groups and aliphatic substituents on furan rings. They can come from both glucose, HMF and other reaction products (fructose, xylose, and other sugars) and present different functionalities depending on the reagent[247,248,258]. Due to the high molecular weight they usually deposit on the wall of the reactor or can block the catalyst active sites; if instead their formation is lower they remain suspended in the final solution but even so cannot be detected by HPLC analysis method resulting in a low carbon balance. Also basic reaction conditions are reported to give condensation products, probably via aldol condensation mechanism, and identified by a darkening of reaction mixture with time due to the presence of unsaturated bonds[259]. Due to humins formation and non-catalytic water dehydration, glucose APR tests were done in the range 150-200°C, differently from glycerol ones in the 225-250°C range. The temperature choice at this stage allows the study the specific catalyst activity, which is necessary for the obtainment of products different from HMF before the

condensation to humins. Despite the positive results obtained in liquid phase, the temperature range selected was not suitable for hydrogen production even in previous glycerol tests.

Table 19 and Figure 105 show the comparison of blank test with TiO_2-m support and the Pt/TiO_2-m used with glycerol. Even at low reaction time, the support and catalyst conversions are higher and there is the formation of a wider selection of products, with the inhibition of HMF formation and in general of dehydration pathway. The presence of Pt moreover enhances cleavage, dehydrogenation and dehydration pathways compared to the support itself. Nevertheless, even if product variety is increased, the yield sum is maintained at the same value causing a decrease in carbon balance values together with the increase in conversion. This is due to the presence of titania acid sites that favor the formation of humins with similar values in presence or absence of active metal. It is thus necessary to find optimal conditions and catalyst to enhance products formation despite glucose reactivity in water.

Table 19: Yields and parameters for APR blank reaction compared to support and Pt/TiO_2-m tests, conditions: 200°C, 30min, glucose concentration 3%wt. and Pt loading 3% wt.

Reaction / Catalyst	Gas phase yields (%)			Glucose conversion (%)	Liquid phase yields (%)														
	H_2	CH_4	CO_2		Fructose	Sorbitol	C_{4-5}	Lactic acid	Acetic acid	Levulinic acid	Propionic acid	Methanol	Ethanol	HMF	Glycerol	Formic acid	Hydroxyacetone	Ethylene glycol	1,2-propanediol
blank				46	4		4			1				28					
TiO_2-m			1	85	1	1	9	4	1	4				13					
Pt/TiO_2-m	1		2	94	2	1	10	4	1	2		2		10					

Figure 105: Lump sum of yield in reaction pathways and product sum for blank, support and Pt/TiO$_2$-m tests. Reactions performed for 30min at 200°C, glucose 3% wt., Pt loading 3% wt.

7.1.3 Optimization of reaction conditions

It is necessary to optimize reaction parameters to reduce humins formation and enhance the production of chemicals before glucose degradation. Pt/TiO$_2$-m catalyst was chosen since it was well characterized and demonstrated good activity in APR of glycerol. Even if the support shows reactivity itself, it was selected to operate in presence of Pt to try to favor H$_2$ production.

One of the most important parameters in this kind of reaction is temperature, for its contribution in blank glucose tests. Reaction data in presence of catalyst are reported in Figure 106 and Table 20 for 30min tests within 150 and 250°C. The trend of carbon balances, conversion and yield sum are the same as reported in blank tests, with an enhancement in conversion values. The best balance is obtained within 175-200°C with respectively 66 and 44% balances and 62 and 94% conversions. The main product at low temperature is fructose, due to acid catalyzed isomerization reaction. Than C$_{4-5}$, and HMF show a volcano trend with maximum at 200°C, while levulinic and lactic acid increase and remain constant with temperature. Gas phase products are again quite low, but H$_2$ production is consumed by sorbitol and other hydrogenation reactions. Lump sum method in fact shows a continuous increase in hydrogenation reactions, while dehydrogenation end cleavage trends present a maximum at 225°C. This can be due to

the more rapid formation of humins at higher temperatures that reduces the activity of the catalyst for occlusion of the pores and coverage of active metal sites.

Table 20: Yields and parameters for APR reactions performed at different reaction temperature for Pt/TiO₂-m tests. Glucose 3% wt., Pt loading 3% wt.

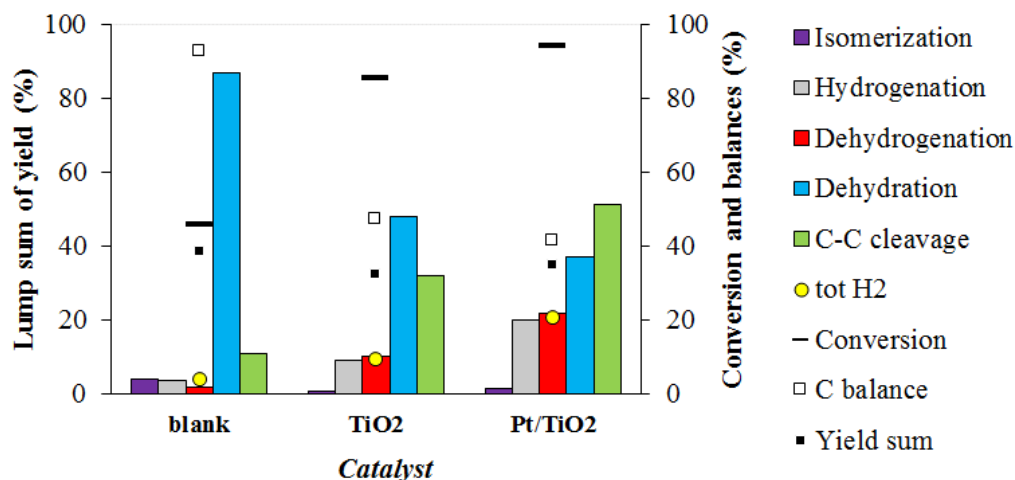| Reaction		Gas phase yields (%)			Glucose conversion (%)	Liquid phase yields (%)														
Temperature (°C)	time (min)	H_2	CH_4	CO_2		Fructose	Sorbitol	C_{4-5}	Lactic acid	Acetic acid	Levulinic acid	Propionic acid	Methanol	Ethanol	HMF	Glycerol	Formic acid	Hydroxyacetone	Ethylene glycol	1,2-propanediol
150	30				26	12	1	4							1			1		
175	30			1	62	7		6	2		1				9			1	1	
200	30	1		2	94	2	1	10	4	1	2			2	10					
225	30	1		6	98			8	4	1	4	1	1	1	2			1		
250	30	1		4	100			6	4		4	1		2	1			2	1	

Figure 106: Lump sum of yield in reaction pathways and product sum for Pt/TiO₂-m tests. Reactions performed for 30min at different temperatures, glucose 3% wt., Pt loading 3% wt.

An interesting comparison is reported in Figure 107 given by the differences in lump sum within Pt/TiO₂ tests and blank ones at the same temperature. First, dehydration mechanism is catalyst-enhanced only at low temperature, becoming predominant in blank tests above 200°C for the higher production of HMF, while at 250°C HMF starts

to degrade in blank tests. On the other hand, all the other mechanisms of reaction are enhanced by the presence of catalyst and no significant improvement and trends are evidenced above 200°C, probably due to the competition of non-catalyzed reactions. The reported data thus suggests thus to work at maximum 200°C temperature, even if the yields are not maximized in particular in gas phase, to allow the catalyst working before the full consumption of the reagent in parallel degradation pathways.
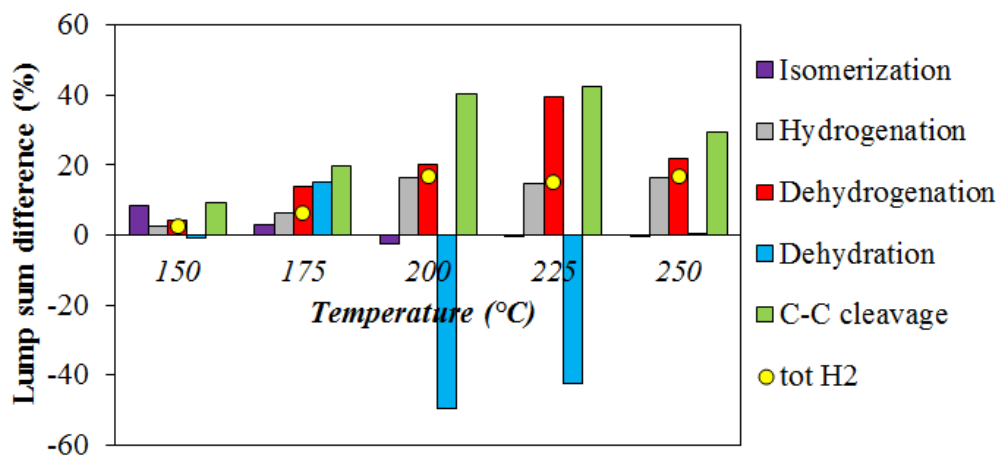
Figure 107: Difference in lump sum within Pt/TiO$_2$-m and blank tests. Reactions performed for 30min at different temperatures, glucose 3% wt., Pt loading 3% wt.

The second parameter analyzed was the time of reaction at a set temperature 200°C to maximize the differences even at low time (Figure 108 and Table 21). The zero point was chosen as the moment in which the system reaches the desired temperature and suddenly cooled. As expected conversion increases with time together with CO_2, C_{4-5} and lactic acid yields. HMF, levulinic acid instead present maxima around 1.5h. Lump sums decrease in dehydration production together with a global increase in C-C cleavage and dehydrogenation. Hydrogenation trend, together with total H$_2$ produced show an oscillating trend not significantly different within 15min and 3h reaction. As for C balance, it decreases with time but not as significantly with temperature indicating that the formation of humins is quite controlled at 200°C, leaving time for catalyst reactivity up to 3h. Even yield sum oscillates within similar values (29-39%). A proposed explanation of the oscillation of some parameters can be due to the interchange within glucose and product reactivity. Since the conversion comes above

90% after 30min, the subsequent increase in product distribution can be assigned to the reactivity of the formed products, in particular for C_{4-5}, sorbitol, fructose, HMF and other high molecular weight products that give the same products as glucose reactivity. It was thus settled 3h as the most interesting time to reduce support reactivity (expressed by dehydration and isomerization) and maximize metal-support interactions, notwithstanding the reactivity of reagent or other produced sugars.

Table 21: Yields and parameters for APR reactions performed at different reaction time at 200°C for Pt/TiO₂-m tests. Glucose 3% wt., Pt loading 3% wt.

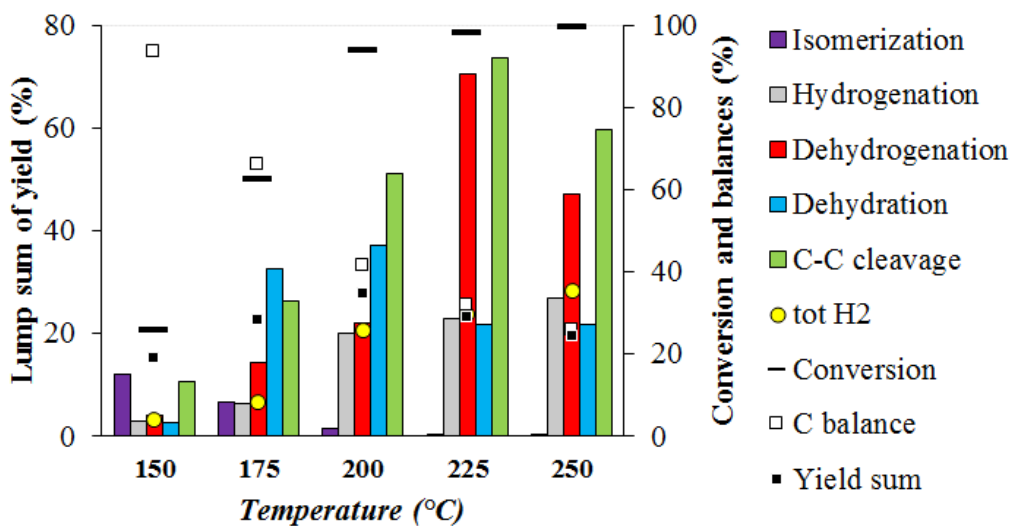| Temperature (°C)	time (h)	H₂	CH₄	CO₂	Glucose conversion (%)	Fructose	Sorbitol	C4-5	Lactic acid	Acetic acid	Levulinic acid	Propionic acid	Methanol	Ethanol	HMF	Glycerol	Formic acid	Hydroxyacetone	Ethylene glycol	1,2-propanediol
200	0			2	75	5		2	3		1		1	1	13			1		
200	0.25			3	85	3	1	9	3		2		2	1	12			1		
200	0.5	1		2	94	2	1	10	4	1	2		2		10					
200	1.5	1		4	94			9	4	1	5				3					
200	3	1		6	99		1	9	4	2	3		2	3	1					

Figure 108: Lump sum of yield in reaction pathways and product sum for Pt/TiO₂-m tests. Reactions performed for different time at 200°C, glucose 3% wt., Pt loading 3% wt.

The reagent concentration was also analyzed in Table 22 and Figure 109. From the second to the last test the concentration of glucose was increased from 0.5 to 3% wt. at constant catalyst loading in the reaction, 200°C and 3h. The aim was to investigate not only the effect of dilution over the system but also of catalyst/reagent ratio. As a comparison the first test (named 0.5* in the graph) is performed at lower time, lower concentration and maintaining the usual catalyst/reagent ratio. The three comparable tests show complete glucose conversion with increasing yield a part from HMF that show a maximum for lower concentrations. Interesting to note are gas phase yields with a maximum H_2 concentration at low glucose loading and high CO_2. This is probably due to the higher amount of catalyst with a glucose/metal molar ratio of 20, instead of the most used 120 ratio. Within lump sums, the three tests show similar ratios within the selected pathways with higher values for 1%wt. loading. On the other hand, the test at constant reagent/catalyst ratio but higher dilution shows lower yield compared to the 3%wt. test or compared to the previous reported test at 30min. That means that maintaining low both the catalyst and reagent was not a solution to increase selectivity in reaction products, but can reduce humins formation for the higher dilution of the system. The tests performed lowering only glucose concentration gave a significantly higher gas phase yield, in particular at 0.5 and 1%wt. Nevertheless, the catalyst/reagent ratio was maintained at 120 for further tests to be comparable with previously reported tests in this section.

Table 22: Yields and parameters for APR reactions performed at different glucose concentration and time at 200°C for Pt/TiO$_2$-m tests. Glucose 3% wt., Pt loading 3% wt.

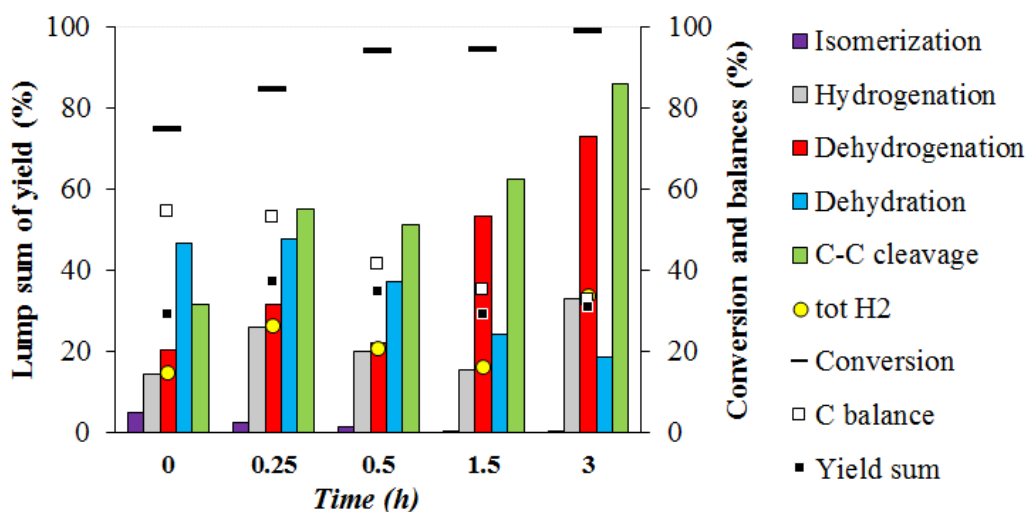| Reaction			Gas phase yields (%)			Glucose conversion (%)	Liquid phase yields (%)														
Glucose (%wt.)	Glu/cat ratio (mol)	time (h)	H$_2$	CH$_4$	CO$_2$		Fructose	Sorbitol	C$_{4-5}$	Lactic acid	Acetic acid	Levulinic acid	Propionic acid	Methanol	Ethanol	HMF	Glycerol	Formic acid	Hydroxyacetone	Ethylene glycol	1,2-propanediol
0.5	120	0.5	2		2	88	2		10	6	2	1	1			10		2			1
0.5	20	3	6		8	100			1	3	2	1	4		5						
1	40	3	3	1	14	100		1	8	6	1	2	2		6				1		
3	120	3	1		6	99		1	9	4	2	3		2	3	1					

Figure 109: Lump sum of yield in reaction pathways and product sum for Pt/TiO$_2$-m tests. Reactions performed for 3h at 200°C, glucose 3% wt., Pt loading 3% wt. (0.5* test performed for 0.5h with lower glucose/catalyst ratio)

Finally, the presence of inert or reducing atmosphere was tested: 7bar of H$_2$ or N$_2$ were loaded at the beginning of the reaction and the test was performed at 200°C for 3h to analyze the effect of pressure itself or reactive agent. Both of them are compared with the normal procedure i.e. the autoclave degassed with N$_2$. As expected the H$_2$ test showed a higher sorbitol yield, but comparing with the reference test the hydrogenation pathway, it is not significantly different and the presence of hydrogen in gas phase since

the beginning of reaction mainly inhibits the dehydrogenating pathway. The cleavage pathway is also reduced due to the higher C_2 and C_3 yield in the reference test from retro-aldol condensation mechanism. The use of hydrogen has thus bee discovered as not significant in this reaction system. As for the nitrogen pressure, yields are comparable with the reference test with a slightly higher H_2 production. Dehydrogenation is maintained with a loss in cleavage and hydrogenation. It is also interesting to note that carbon balances and yield sums are maintained for all the tests at similar values.

Table 23: Yields and parameters for APR reactions performed at different reaction pressure for Pt/TiO$_2$-m tests. Time 3h, temperature 200°C, glucose 3% wt., Pt loading 3% wt.

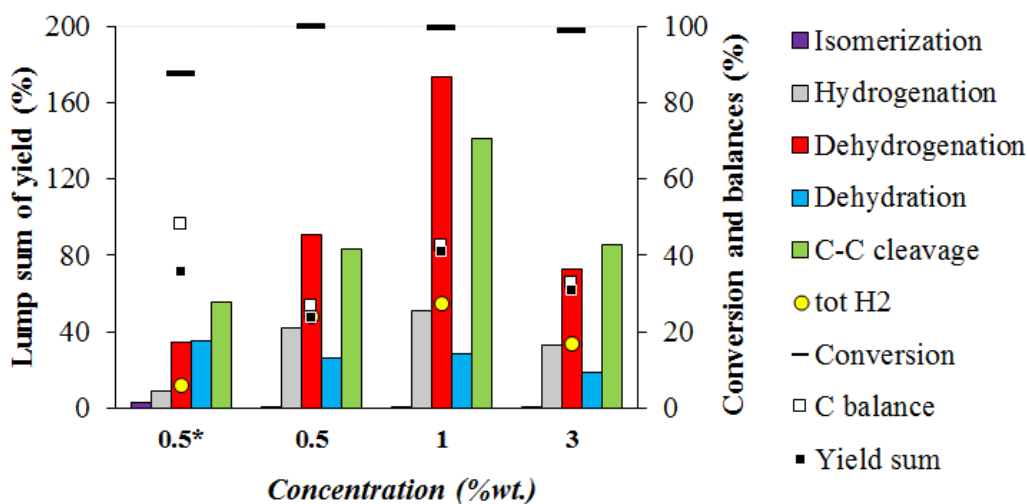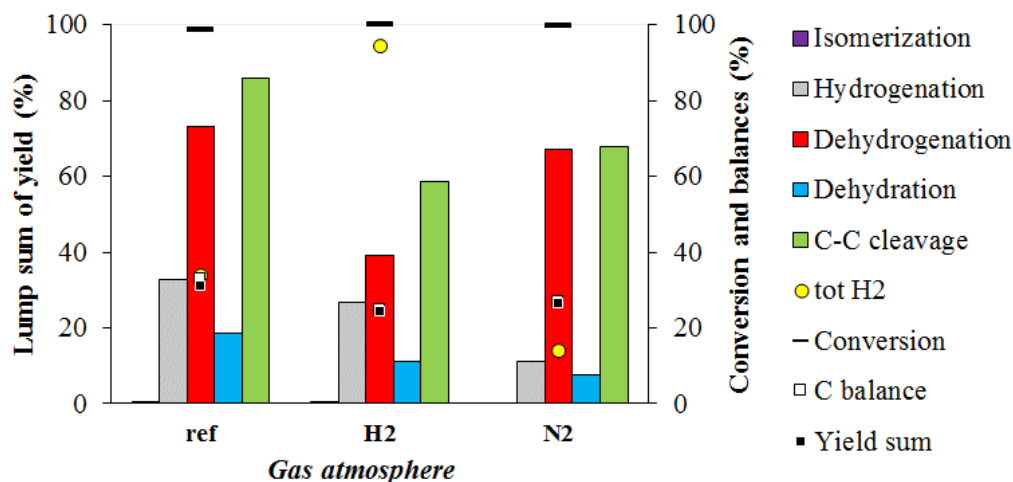| Reaction		Gas phase yields (%)			Glucose conversion (%)	Liquid phase yields (%)														
Type of gas	Over-pressure (bar)	H_2	CH_4	CO_2		Fructose	Sorbitol	C_{4-5}	Lactic acid	Acetic acid	Levulinic acid	Propionic acid	Methanol	Ethanol	HMF	Glycerol	Formic acid	Hydroxyacetone	Ethylene glycol	1,2-propanediol
N_2	0	1		6	99		1	9	4	2	3		2	3	1					
H_2	7	68		3	100		2	7	3	1		3	1				1			2
N_2	7	3		6	100			11	5	1	1	1		1						

Figure 110: Lump sum of yield in reaction pathways and product sum for Pt/TiO$_2$-m tests. Reactions performed for 3h at 200°C, glucose 3% wt., Pt loading 3% wt. Reference test is with no overpressure; for H$_2$ and N$_2$ tests 7bar of gas were loaded before heating the system.

7.1.4 Mechanism hypothesis

A first study was done analyzing the trends of the products during the time, for Pt/TiO$_2$-m tests reported in Table 21. Some products as hydroxyacetone, fructose and HMF are clearly decreasing with time, suggesting a role as primary ones, even if they may be produced from other intermediates during the increase in temperature. Sorbitol, glycerol, ethylene glycol, propionic and levulinic acid present a volcano trend in some cases more relevant (sorbitol and levulinic acid) with maxima at 0.5 and 1.5h respectively and at low concentration for the others. C$_{4-5}$, lactic acid and methanol increases to remain then constant, a behavior typical of not further reactive molecules or balanced within production and consumption. In addition, CO$_2$, acetic acid, ethanol, H$_2$, formic acid globally increase with time as complete degradation products of cleavage and reforming reactions. Nevertheless, it is hard to make a hypothesis over the reactivity of glucose due to the high number of products, possible pathways and their interconnections. It was further suggested by previous tests about reaction parameters the possibility of intermediates of reaction to present similar reactivity compared to glucose, in particular C$_6$ and C$_5$ sugars. Maintaining the reaction conditions, fructose, sorbitol and arabinose were thus testes, as reported in Table 24. Fructose show similar reactivity compared to glucose with small sorbitol production and higher levulinic acid

yield, probably assignable to further degradation of HMF, since the production from fructose is more probable compared to glucose[260]. On the other hand, sorbitol presents lower conversion, suggesting that it necessitates higher reaction temperatures to react completely. This may also explain the lower reactivity of the test under H_2 pressure. Arabinose was taken as representative of C_{4-5} peak because it was the only one certainly assigned. It shows nearly complete conversion but the only calibrated products were CO_2, ethanol and hydroxyacetone together with small amount of others. Thus, also arabinose was a reactive intermediate but showing slightly different reactivity compared to glucose and fructose. A further test was also done with HMF to confirm the hypotheses over levulinic acid formation and formic degradation. It was in fact found a relevant yield in levulinic acid, together with CO_2 and no formic acid confirming its reforming pathway in these conditions. Ethanol instead can be given by reforming of bigger molecules as levulinic acid or HMF. For all the conducted tests, other not individuated products were detected by HPLC but not further analyzed; moreover, carbon balances remained at low values as for glucose.

Table 24: Yields and parameters for APR reactions for different reagents and Pt/TiO₂-m catalyst. Time 3h, temperature 200°C, reagent/metal ratio 120mol/mol, Pt loading 3% wt.

Reaction / Reagent	Gas phase yields (%) H_2	CH_4	CO_2	Conversion (%)	Glucose	Fructose	Sorbitol	C_{4-5}	Lactic acid	Acetic acid	Levulinic acid	Propionic acid	Methanol	Ethanol	HMF	Glycerol	Formic acid	Hydroxyacetone	Ethylene glycol	1,2-propanediol	C balance (%)
Glucose	1		6	99	-		1	9	4	2	3		2	3	1						33
Fructose	1		7	100		-		7	1	1	8			1							27
Sorbitol	5		3	48			-	3						7							73
Arabinose	1		7	95		2		4		1	1	1		5				2			27
HMF	1		9	96							7			10	-						31

Due to the complexity of the system, literature analysis was used to support the indications given by the reactivity. As a first step, the possible isomers of glucose were studied, together with the formation of reduced sugars and C_5, as reported in Figure

111. Each aldose, as glucose, can undergo two transformation reactions towards molecules with equal weight. Glucose can be converted to the respective ketose sugar, fructose, by isomerization reaction; but can also undergo epimerization in C_2 position to another aldose, which is mannose. These reactions are favored by mild conditions and can be improved both by basic and acid catalysis[255,256,261,262]. The obtained sugars can be themselves reactive in APR, especially in the case of fructose for the dehydration to HMF and levulinic acid[235,254,260,263,264], as indicated in Figure 112. This reaction is reported being faster from fructose compared to glucose. Nevertheless, no mannose was detected in the reaction environment, probably due to the rapid conversion of glucose and fructose that shifts the equilibrium epimerization reaction. Neither acetic acid was obtained with the same ratio of levulinic one due to reforming process, as confirmed by reactions with intermediates. Another direct reaction from glucose is the hydrogenation to sorbitol. This sugar is reported being active both in APR[242–244,265] and in hydro deoxygenation reactions[241,246]. A wide variety of products coming from sorbitol reactivity was individuated by Murzin et al.[265] containing alcohols, ketones, acids, furanics and aromatics obtainable by retro-aldol condensation, C-C cleavage and dehydration reactions. Moreover it shows a wide range of gas phase alkanes especially at high temperature[265]. Being the sorbitol concentration not so relevant in reaction environment and its reactivity similar to other sugars, the possible products obtainable by sorbitol were not analyzed in depth. From C_6 sugars, C_5 are obtainable by cleavage of terminal group. The individuation of C_5 and further C_4 was previously discussed in this paragraph, thus Figure 111 reports only the supposed products of reaction without specification of the direct production pathway.
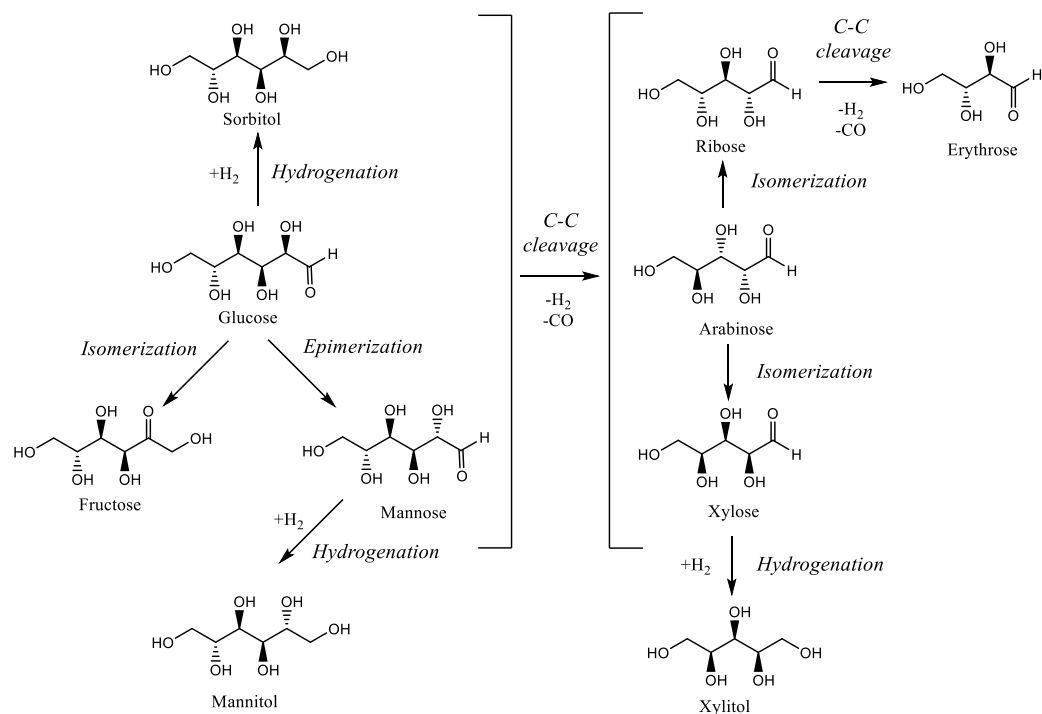
Figure 111: Ipothesis of formation of C₆, C₄ and C₅ sugars from glucose by isomerization and cleavage mechanisms.

More interesting from the APR point of view was the production of C_2 and C_3 molecules from glucose (Figure 112) but also assuming similar reactivity from other produced sugars. First of all the cleavage mechanism is supposed to happen as C=C scission or retro aldol condensation of intermediates of glucose-fructose isomerization following the Lobry de Bruyn-Alberda van Ekenstein theory[266]. More in detail glucose as open form can undergo reverse aldol condensation to form erythrose and glycolaldehyde; fructose ketone open form can give instead two glyceraldehyde molecules by the same reaction. The intermediate enediol hypothesized during the glucose-fructose transformation instead presents a double C=C bond between carbons 1 and 2, weakening the bond within 3 and 4 and giving two glyceraldehyde molecules. Moreover, the possible keto-enolic isomer of fructose can undergo the same reaction giving as possible products erythrose and glycolaldehyde[267,268]. The aldehyde intermediates can thus give glycols and polyols[244,245,269,270], glycerol[245], lactic acid[270–272] and other acids[270] similar to glycerol reactivity reported in glycerol chapter.
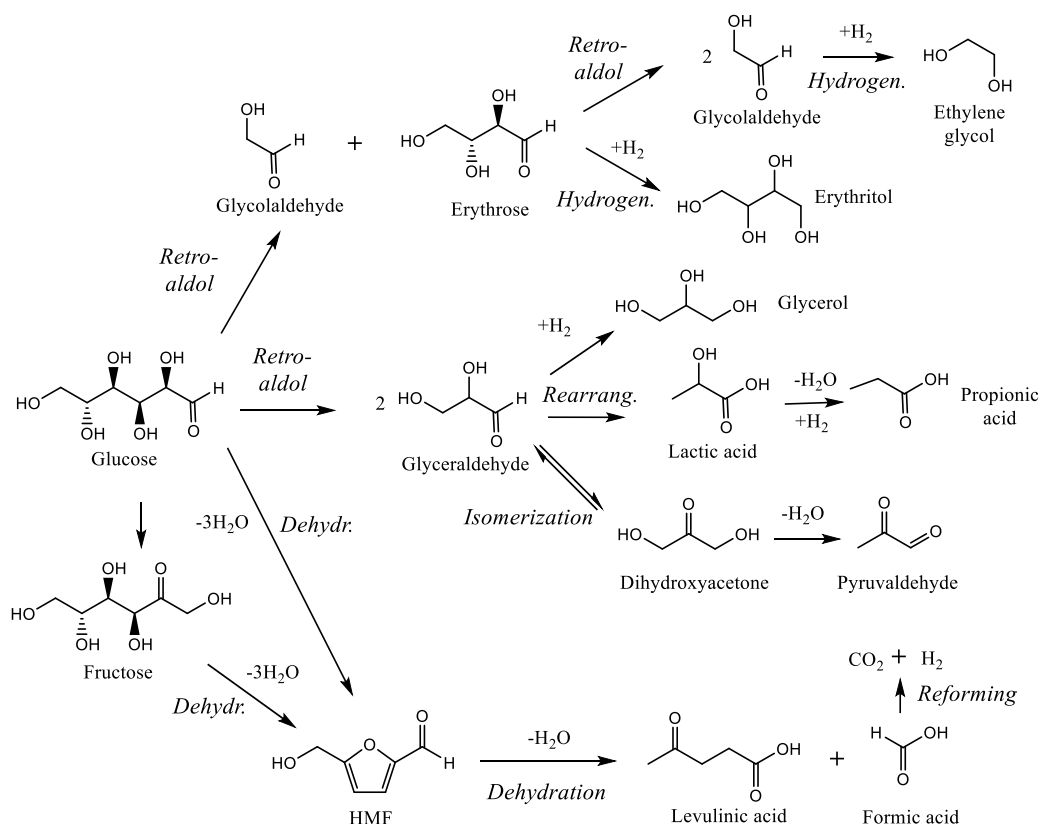
Figure 112: Ipothesis of formation of C_2 and C_3 sugars from glucose by dehydration, hydrogenation and retro-aldol condensation.

Nevertheless, Figure 111 and Figure 112 are hypothesis about the possible formation of products in glucose APR, more in depth studies are still necessary to completely elucidate the reported pathways and find a correspondence in batch reactivity.

7.2 Study of the support

After the optimization of reaction parameters, it was studied the possible effect of basic/acid support in APR over glucose. The same supports tested for glycerol were analyzed, in this case considering both the reactivity of the support itself and with 3%wt. Pt loading (Table 25). Complete conversion is obtained for all tests at 200°C for 3h, but gas phase yields are favored by the presence of Pt. Together with the increase in basicity is present a raise in C_{4-5}, lactic and acetic acid yields for the support reactivity.

While, a part from the increase in CO_2, these trends are not maintained in the Pt supported catalysts.

Table 25: Yields in APR reaction performed at 200°C for 3h over supports and Pt loaded supports at different basicity. Glucose 3% wt., Pt loading 3% wt.

Reaction Catalyst	Gas phase yields (%)			Glucose conversion (%)	Liquid phase yields (%)														
	H_2	CH_4	CO_2		Fructose	Sorbitol	C_{4-5}	Lactic acid	Acetic acid	Levulinic acid	Propionic acid	Methanol	Ethanol	HMF	Glycerol	Formic acid	Hydroxyacetone	Ethylene glycol	1,2-propanediol
Al$_2$O$_3$	1		2	100			4	12	2	6			1	2		2			
MgAl$_2$O$_4$	1		2	100			8	7	4		1		1	2	1		4		
Mg/Al 2:1	1		1	100			8	13	5		1					2	3		
Mg/Al 3:1	1		2	100			10	15	6		1				2	1	4		
MgO			2	99			9	18	9	1						3	2		
Pt/Al$_2$O$_3$	1		3	100			3	12	2	11	1	1	1						
Pt/MgAl$_2$O$_4$	1		8	100		2	7	4	3		1						5		
Pt/Mg/Al 2:1	7		8	100			2	10	5		2	1	2		1		2		1
Pt/Mg/Al 3:1	9		9	100			3	9	5		2	1	2				2		1
Pt/MgO	3		4	99	1		3	8	5		1		1		1		3		
Pt/Ni$_{40}$	3		5	100			3	7	4		1	1	2		1		2		
Pt/AC			3	96	1		2	1	1	1			2	6					

Lump sum method for the reported reactivity is presented in Figure 113 and Figure 114. In both the graphs, yield sum and carbon balance values are coincident due to the conversion near to 100% value. The first graph shows an interesting trend comparable with the one obtained in glycerol APR. Dehydration mechanism is favored by the acidity of the samples and shows a minimum for MgO; on the other hand, dehydrogenation is favored at high Mg content. C-C cleavage steeply increases with support basicity, due to the presence of more C_3 and C_2 molecules, for the activity in retro-aldol condensation of basic sites, balanced by reforming for acid catalysts. In parallel, also carbon balance raises from 30 to 43% for basic supports. Hydrogenation trend instead does not follow a clear line, as was for glycerol reactivity. Literature data support the trends individuated evidencing an acid-promoted dehydration to HMF and

further levulinic acid and base-promoted isomerization to other sugars (C$_{4-5}$) [273]. An elaborate study by Huber et al.[274] underlines the difference in dehydration over Lewis or Brönsted-type acid sites. They claimed that Brönsted sites favor dehydration, but both acids cause humins generation the first one by condensation and the second by degradation pathways. Nevertheless, they evidenced also the absence of correlation within total acid sites calculated by probe gas adsorption and liquid titration suggesting a negative effect of pore confinement for solid acids that causes degradation of products and reagent[274]. In our case, the tests are quite well linkable with total acidity/basicity of the supports probably due to the presence of both Lewis and Brönsted sites over acid supports.
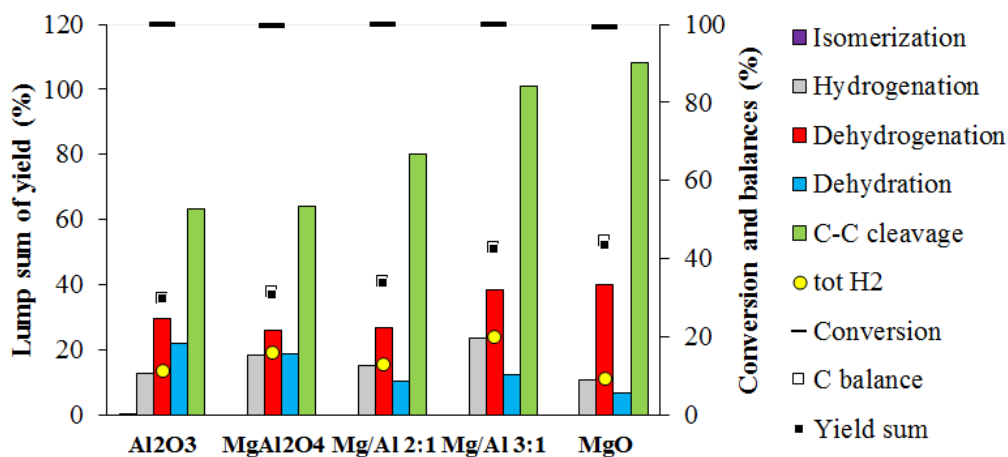

Figure 113: Lump sum of yield in reaction pathways and product sum for supports at different basicity. Reactions performed at 200°C for 3h, glucose 3% wt.

Literature reports the enhancement in hydrolysis and hydrogen production processes by the addition of Pt over acid catalyst[275], nevertheless, few literature studies are reported for the study of metal-support interactions for sugar APR reactivity. Beside metal-support interactions, even the size and distribution of Pt particles, due to support features, can significantly change the reactivity[276]. Comparing the support activity with Pt loaded catalyst in Figure 114, it is notable that the described trends are more complex, a part from dehydration mechanism which seems unaffected by the presence of metal. Dehydrogenation and cleavage instead seem favored by the presence of both Mg and Al cations in the structure with increasing trend together with the raise in

Mg/Al ratio from 1:2 to 3:1. Thus the not linear trend in activity can be a combination of several factors as Pt dimension and dispersion, interactions with Pt and acid or basic sites and support surface properties. For all the supports, dehydrogenation, hydrogenation and total hydrogen values are increased with respect to the support at comparable carbon balance values due to the presence of Pt, also C-C cleavage is increased of a little extent a part for MgO catalyst. Those differences are better exposed in Figure 115, where it is calculated the effect of the presence of metal subtracting the support reactivity. It can be summarized that dehydration depends principally on the support features while other reactions are metal dependent. The lower activity of MgO can be explained considering that it is the support with lower surface area, the combination of metal deposition and humins formation can cause a reduction in activity, which is not evidenced in the support reactivity due to the lower amount of products. Total hydrogen productivity seems dependent also on surface area of the support since $MgAl_2O_4$ and MgO show significant lower values compared to the others. In conclusion, Pt activity, in particular in dehydrogenation and cleavage, was found favored by the contemporaneous presence of intermediate strength acid and basic sites on the surface, while strong basic sites, as for MgO, do not show a significant increase.
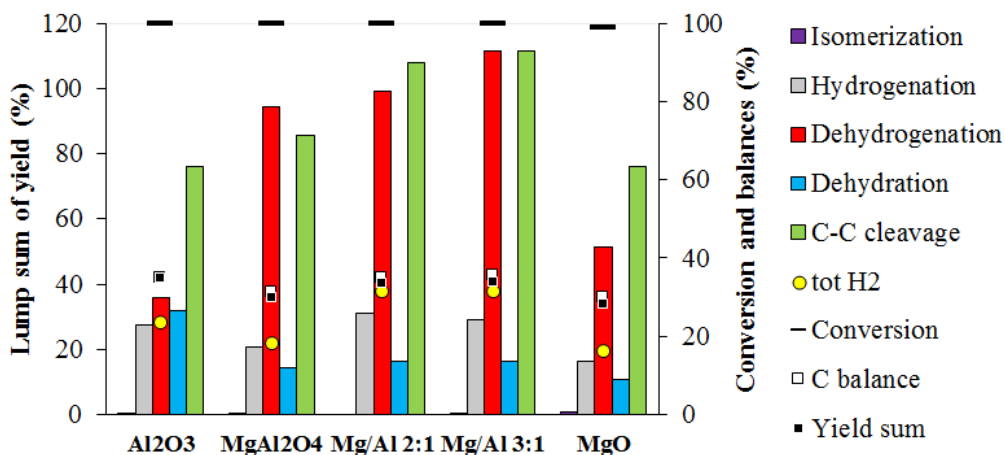

Figure 114: Lump sum of yield in reaction pathways and product sum for supports at different basicity with Pt loading 3% wt. Reactions performed at 200°C for 3h, glucose 3% wt.
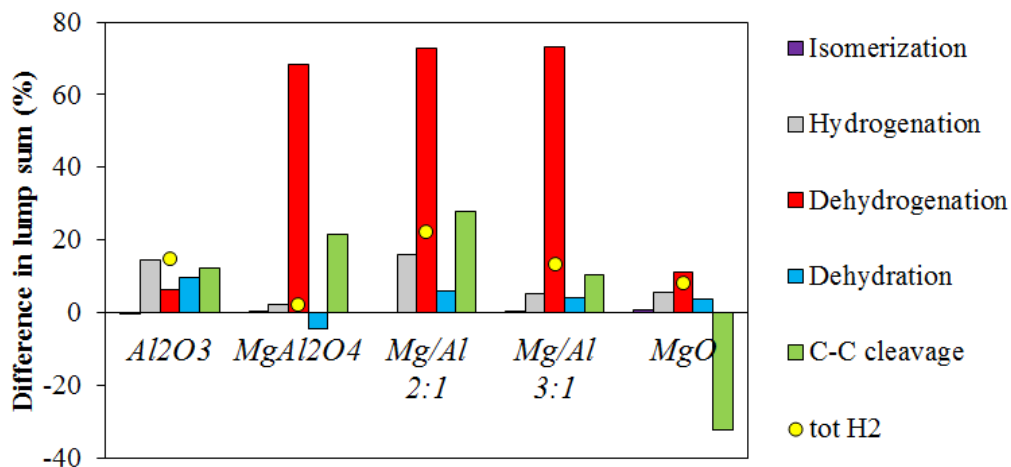
Figure 115: Differences in lump sum of yield in reaction pathways for supports at different basicity. Reactions performed at 200°C for 3h, glucose 3%wt, Pt loading 3% wt.

Even Pt/Ni$_{40}$Mg/Al-p750 catalyst reduced at 750°C and a commercial Pt/AC were tested in glucose APR. Results are reported in Figure 116 and Table 25. The reactivity of Ni/Mg/Al catalyst is lower compared to the corresponding Mg/Al 3:1 catalyst, thus small nickel effect was observed when embedded in the mixed oxide structure. On the other hand, the active carbon showed the lowest activity values with lump sum data similar to Al$_2$O$_3$ and lower C-C cleavage. In this case, the basic or acid sites present on the surface did not influence the reactivity similar to the previously reported data. In fact, the Ni/Mg/Al sample has an acidity comparable to Mg/Al samples, while the carbon has the lowest value. Thus, none of them is relatable with similar acidity samples.

Figure 116: Lump sum of yield in reaction pathways and product sum for catalysts with Pt loading 3% wt. Reactions performed at 200°C for 3h, glucose 3% wt.

7.3 Study of the active metal
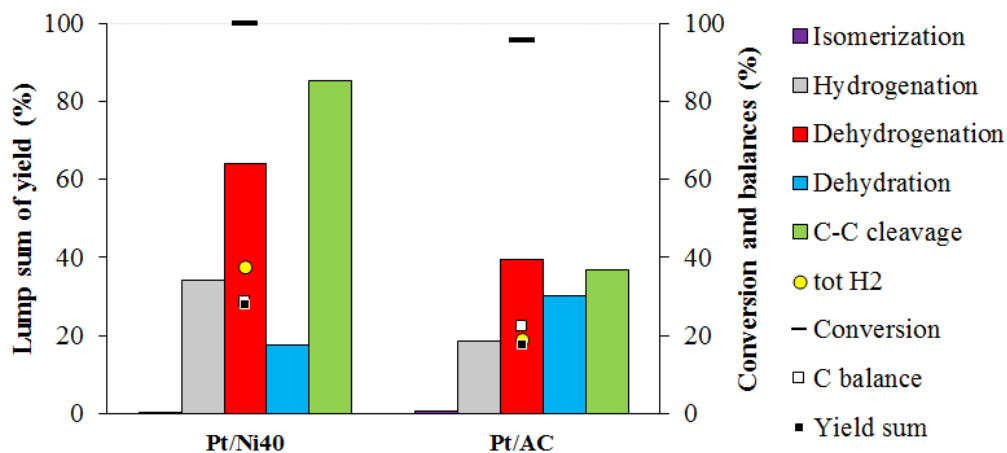
The study of Pt reactivity over different supports did not allow overcoming the main problem of the reaction as low carbon balance and complex products mixture. A different approach based on the metal screening was then developed. Taking into account the formation of humins and the difficult recovery of the catalyst due to the presence of humins, the analysis has also the goal to obtain a less expensive and more robust catalyst avoiding Pt supported on oxides that have been used so far as reference catalyst. The study of the effect of metal in the activity started with meal support, avoiding a strong metal support interaction. The reported approach first avoided the embedding of the active metal in the mixed oxide phase, due to the low results reported for Ni/Mg/Al mixed oxide. Moreover, it tried to maximize the catalyst activity with a higher availability of active phase, necessary for glucose reactivity, due to the presence of humins. One of the main starting problems was the choice of the support, since previous chapter has demonstrated the high reactivity of all the supports tested. Thus, the choice relapsed to an active support that presented both Mg and Al cations (to contemporarily favor acid and basic reactivity) and low surface area, to reduce humins formation by pore constraint, as $MgAl_2O_4$ spinel calcined at 900°C. After the metal preliminary screening tests, efforts were devoted to couple the reactivity of metals first

as supported active phases and then as bi or tri-metallic spinel-like bulk catalyst. The aim was again finding a robust catalyst without the need of supported phase, more subject to deactivation.

7.3.1 *Screening of the metal*

Within the active metals ruthenium, iron, copper, nickel and cobalt were selected because they are claimed to have catalytic activity in C-C cleavage reaction, interesting for APR applications[198]. Moreover, as reported in Table 26, they are currently sold at considerably lower prices compared to Pt, in line with the aim of finding cheaper active phases for APR reaction. Among the possible candidates, iridium, rhodium and palladium were not considered due to their price comparable to Pt[277]; ruthenium instead was analyzed because, even if a noble metal, the price was significantly lower.

Table 26: Prices of metals on the market in date 27/02/2017.

	Pt	**Ru**	**Fe (ore)**	**Cu**	**Ni**	**Co**
Price (US $/kg)	32'633	1'286	0.08	5.9	10.7	47.5
Reference	277,278	277	279	280	280	280

$MgAl_2O_4$ support was synthesized as previously reported by co-precipitation technique and calcined at 900°C to obtain the spinel phase with surface area of 90m^2/g. The metals were deposited by IWI technique with a loading of 3% wt. for Pt and Ru, since they are expensive noble metals, and 10% wt. for the other candidates. The catalysts were characterized by TPR and XRD before and after reduction at 350°C (Figure 117, Figure 118 and Figure 119). TPR profiles in Figure 117 underline that at the selected temperature the reduction process has started for all the catalysts, but completed for none of them. This indicated that the particles were at least partially reduced; moreover, in the catalyst reduction process with a hold in temperature of 3h the reduction degree will be higher. Percentage of reduction calculations were not significant for those samples since several types of oxides with different hydrogen uptake could be present for Fe, Co, Ru and Cu, as supported by the presence of two or three peaks for each metal indicating different phases on the surface. In addition, the presence of negative peaks was detected as water release by mass analyses. Nevertheless, the reduction

temperature was not further raised to avoid sintering phenomena. XRD analyses of the as synthesized catalysts in Figure 118 showed that the Pt is partially reduced even after drying process for the presence of a small reflect at 39°2θ. As for Ru and Cu, strong reflects are evidenced for CuO and RuO_2 phases suggesting the presence of big aggregates on the surface around 60-70nm for RuO_2 and 30nm for CuO by Scherrer calculations. As for Co, Ni and Fe it is not possible to identify the oxide phase by XRD because NiO, Co_3O_4 and Fe_3O_4 reflects are overlapped with $MgAl_2O_4$ signals. Even if this is an indication of the predominant crystal phase of the metal, XRD analysis is not enough to reject the presence of other oxide phases with smaller crystals.

XRD analysis of reduced phases (Figure 119) shows the clear presence of reduced metal for Pt and Cu with signals respectively at 39 and 43-50°2θ. The high intensity in the case of Cu confirms by Scherrer analysis particles around 20-30nm and lower than 5nm for Pt. As for Ru, Fe, Co and Ni, the metallic phase is identifiable as a broad peak around 44°2θ or as a shoulder of the $MgAl_2O_4$ reflect at 45°2θ. This confirms the effective surface reduction of the metals but do not gives further indications about their dispersion.
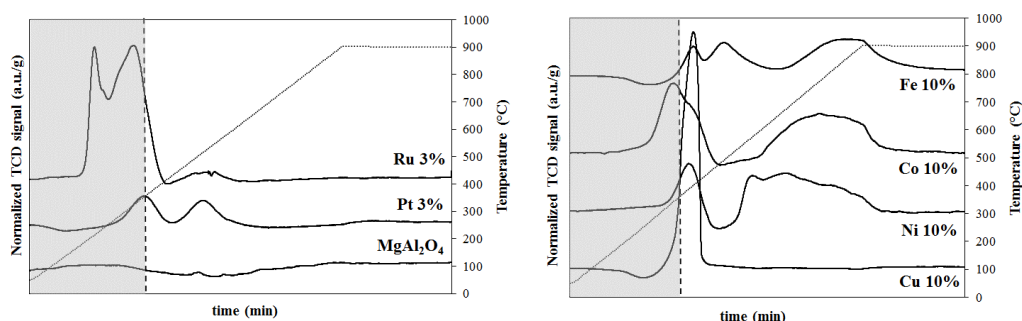
Figure 117: TPR profiles of catalysts loaded over MgAl₂O₄ support. Grey bar represents reduction temperature 350°C.
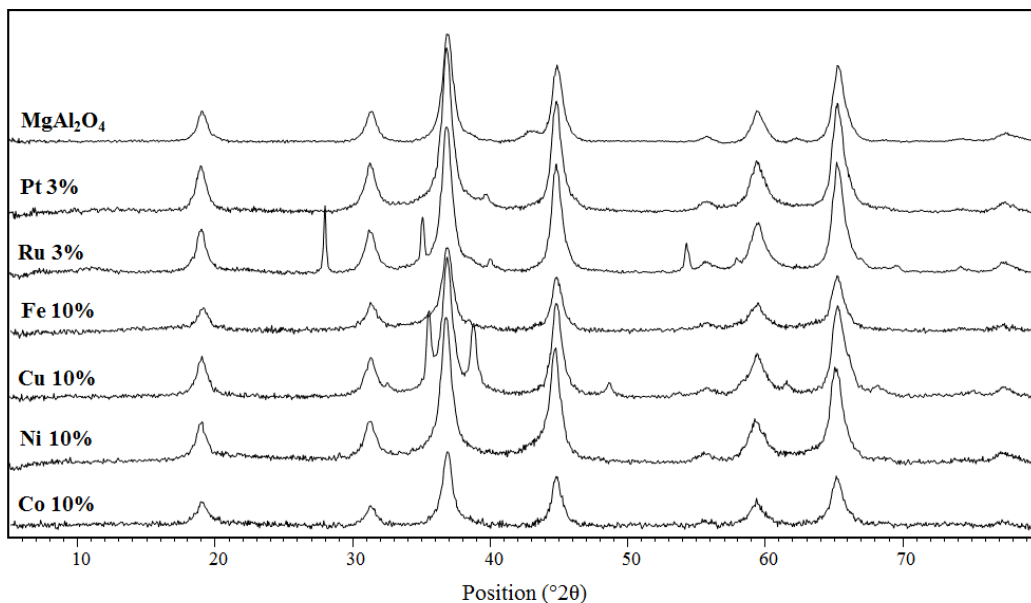
Figure 118: XRD analyses of the support and metal supported catalysts not reduced.
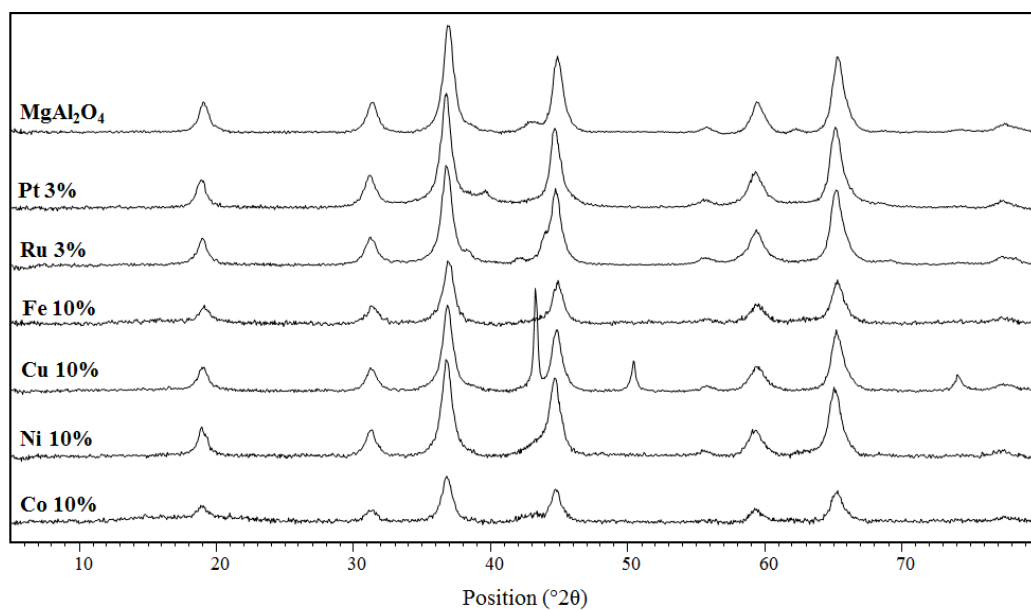
Figure 119: XRD analyses of the support and metal supported catalysts reduced at 350°C.

The catalysts were tested in APR reaction with the temperature lowered from 200 to 175°C to better analyze the differences within the metals. Results in comparison with the support are reported in Table 27 and Figure 120. All the tests reach almost complete conversion, even the temperature was lowered, with low gas phase yields. Pt sample

shows the highest number of products, while for the others the main ones are C_{4-5}, lactic acid, HMF and hydroxyacetone. Lump sum method in Figure 120 confirmed Pt as the most active metal in cleavage, hydrogenation and dehydrogenation pathways, and all the metal supported catalysts inhibit dehydration mechanism promoted by the support, probably because due to the coverage of the surface. Moreover all the tests show similar carbon balance values within 35 and 45%, while the total H_2 produced depends only from the dehydration reaction, being H_2 yield almost zero.

Table 27: Yields and parameters for APR reactions for metal screening tests at 175°C loaded over MgAl$_2$O$_4$. Glucose 3% wt., reaction time 3h.

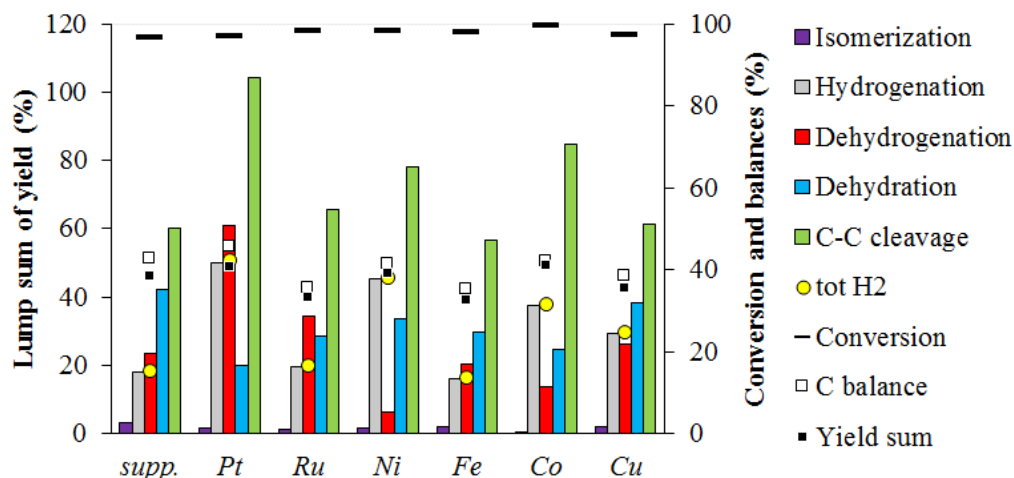| Reaction		Gas phase yields (%)			Glucose conversion (%)	Liquid phase yields (%)														
Metal	Loading (% wt.)	H$_2$	CH$_4$	CO$_2$		Fructose	Sorbitol	C$_{4-5}$	Lactic acid	Acetic acid	Levulinic acid	Propionic acid	Methanol	Ethanol	HMF	Glycerol	Formic acid	Hydroxyacetone	Ethylene glycol	1,2-propanediol
MgAl$_2$O$_4$				2	96	3		8	6	3			1		12		1	3		
Pt	3	1		4	97	2	4	10	4	3		1	3	1	0		2	7	1	
Ru	3			3	98	1		8	5	4			1		6		0	5		
Ni	10				98	2		9	6	3			5		8	1	1	3		
Fe	10			1	98	2		8	5	3			1		7		2	3		
Co	10	1			99			9	9	3			2		5	5	1	4		
Cu	10	1		2	97	2	1	8	5	3			1	3	8			3		

Figure 120: Lump sum of yield in reaction pathways and product sum for metal loaded over MgAl₂O₄. Reactions performed at 175°C for 3h, glucose 3% wt.

A more interesting comparison is reported in Figure 121 by calculating the differences in lump sums within the metal supported catalysts and the support evidencing the specific activity of the metal. Beside Pt activity, which was assumed as reference catalyst, all the metals except Fe present specific reactivity. Ni and Co are the most active catalysts, with specific activity in hydrogenation and cleavage mechanisms, principally in C_{4-5} and lactic acid. Cu shows activity only in hydrogenation mechanism while Ru in dehydrogenation and small in cleavage. The trends reported are not in line with the metal reactivity in APR suggested by Dumesic et al.[198] The reason can be twofold: on one side, the literature proposed reactivity is done on the behalf of model small molecules. On the other hand, the reactivity of a high molecular weight reagent with several functionalities as glucose can depend not only on the intrinsic reactivity of the metal but also on its dispersion, availability on the surface and interactions with the support. Having thus demonstrated by XRD the presence of big crystals for some of the analyzed metals, this parameter surely has an influence over the reactivity.
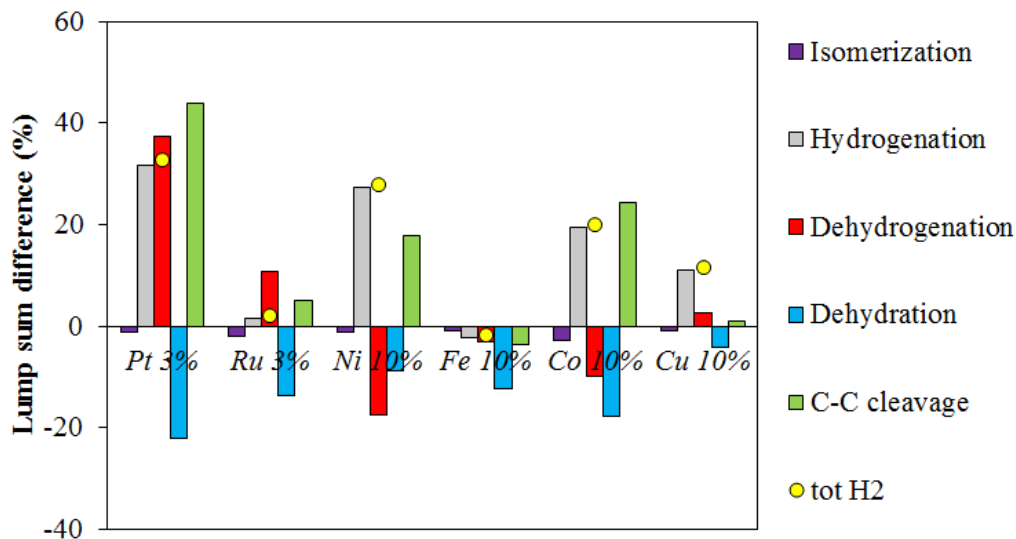
Figure 121: Differences in lump sum of yield in reaction pathways for metal loaded over MgAl$_2$O$_4$. Reactions performed at 175°C for 3h, glucose 3% wt.

The same catalysts were tested also at 150°C to verify the possibility of maintaining the metal activity. Yields and lump sum values are reported in Table 28 and Figure 122. As expected, lowering the temperature in presence of a support with acid functionalities fructose yield is favored up to 20%. In addition, conversion values are lowered, showing an enhanced C balance over 70% for Ni, Fe, Co and Cu with the lowest 56% value for the support. Main products are again, beside fructose, C$_{4-5}$ and lactic acid with nearly absent gas products. Lump sum data are maintained but lowered of around 20% respect to the previous test due to the temperature decrease.

Differences in lump sum are reported in Figure 123. It is significant to underline the higher activity of Pt compared to the other metals and the lower difference in dehydration compared to the support. Moreover, the support shows higher conversion compared to all the metals, due to the intrinsic reactivity of acid and basic tests and to the higher surface area in absence of metal coverage. All the metals except Pt evidenced an activity in isomerization, especially significant for higher loadings and well-known acid catalysts as Ni and Fe. The comparison within the reactivity of each metal at 175 and 150°C is difficult, due to the contemporaneous presence of metal and support, whose activity changes with temperature. The only parameters maintained are the C-C

cleavage of Ni and Co, together with a positive increase in Cu and Fe specific reactivity, which were the lowest in the previous test. No changes, a part from a small decrease in crystallinity was detected by XRD analyses before and after catalytic tests.

Table 28: Yields and parameters for APR reactions for metal screening tests at 150°C loaded over MgAl₂O₄. Glucose 3% wt., reaction time 3h.

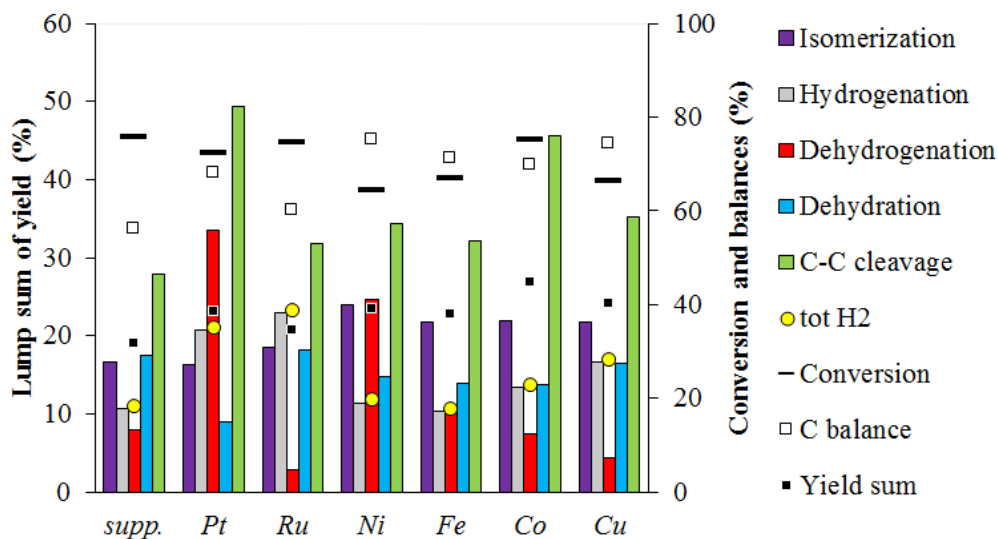| Reaction		Gas phase yields (%)			Glucose conversion (%)	Liquid phase yields (%)														
Metal	Loading (% wt.)	H₂	CH₄	CO₂		Fructose	Sorbitol	C₄₋₅	Lactic acid	Acetic acid	Levulinic acid	Propionic acid	Methanol	Ethanol	HMF	Glycerol	Formic acid	Hydroxyacetone	Ethylene glycol	1,2-propanediol
MgAl₂O₄					76	17		3	2	2					4		1	2		1
Pt	3			2	72	16	5	6	1	1							2	4	1	
Ru	3				75	19		4	2	2				2	2			2		
Ni	10			2	64	24		4	2	1			1		4			1		
Fe	10				67	22		6	2	1			1		3		1	2		
Co	10				75	22		8	6	2			1		3		1	2		
Cu	10				66	22		6	2	2			1		4		1	2		

Figure 122: Lump sum of yield in reaction pathways and product sum for metal loaded over MgAl₂O₄. Reactions performed at 150°C for 3h, glucose 3% wt.
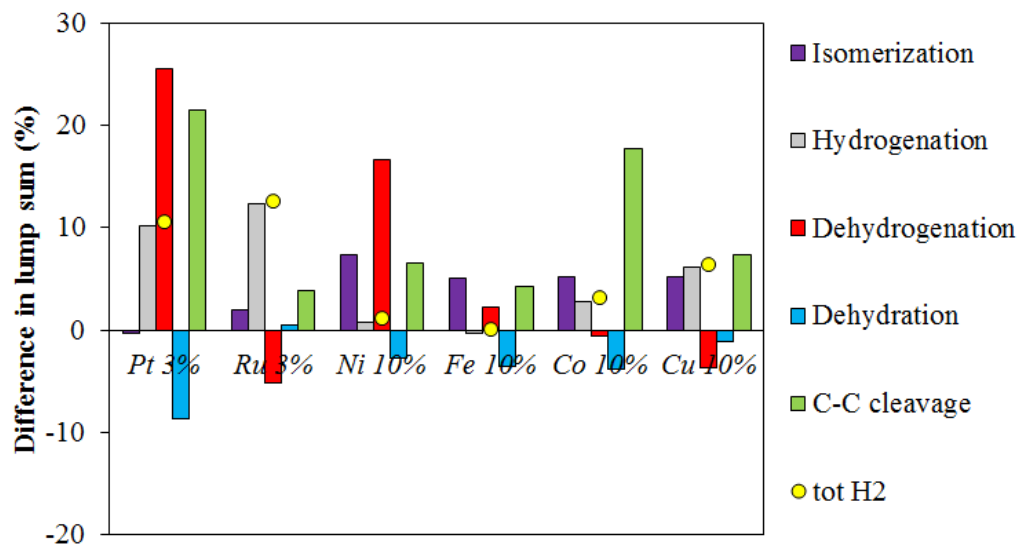
Figure 123: Differences in lump sum of yield in reaction pathways for metal loaded over MgAl$_2$O$_4$. Reactions performed at 150°C for 3h, glucose 3% wt.

The most interesting metals appeared to be Ni and Co, in particular for their C-C cleavage activity, followed by Ru and Cu, less interesting because they show the stronger change in reaction products depending on the temperature. Finally, even if iron did not show activity significantly different from the support, was not discarded in further studies being the cheapest within the metals.

7.3.2. *Coupling of metal reactivity*

With the aim of enhancing the catalyst reactivity, some attempts were done to impregnate two or three metal precursors over MgAl$_2$O$_4$ and compare their reactivity with the monometallic samples. The metal selected were a combination of Ni, Co and Fe for the reasons previously reported maintaining the total loading at 10% wt. with a 5%wt. amount each metal for the bimetallic and 3.3% for the trimetallic ones. TPR profiles are reported in Figure 124, while XRD are not presented because no significant peaks are evident a part from support structure. In this case, the reduction temperature was increased up to 500°C because the obtained profiles were shifted at higher temperatures compared to the monometallic ones. As for NiFe and CoFe samples, the Ni, Fe and Co lower temperature reduction peaks are present in the bimetallic sample

while the larger one, probably due to water release, is shifted at lower temperature. The trimetallic sample instead is shifted more at lower temperature compared the bimetallic. This may indicate a strong interaction within the metals that favor the reduction of the active phase. Moreover, due to the presence of several oxides phases the peaks are not strictly assignable to a specific metal or oxide.
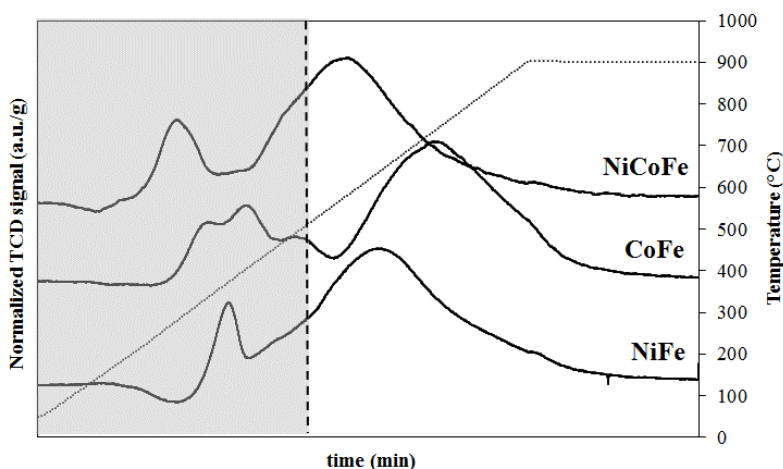

Figure 124: TPR profiles of bimetallic and trimetallic catalysts loaded over MgAl$_2$O$_4$ support.

Glucose APR results are reported in Figure 125 and Table 29. Due to the low temperatures, the conversion is around 70% for all the samples with main yield in sugars (fructose and C$_{4-5}$). The tests are highly similar one to each other, and present mean values within Ni, Co and Fe single metal reactivity results. Respect to previous tests, they obtain slightly higher carbon balances and total yield. As for lump sum values, considering the effective amount of loading for each metal, CoFe and NiFe shows similar values compared to the monometallic reactivity with slightly lower values in dehydration and hydrogenation for the NiFe, probably due to the lower reducibility of the sample compared to the others. As for the NiCoFe sample, the values are again comparable with the sum of one third of the reactivity of the composing metals. In particular, there is a slight increase in hydrogenation, dehydration and cleavage and a small decrease in dehydrogenation.

Table 29: Yields and parameters for APR reactions for bimetallic and trimetallic catalysts at 150°C loaded over MgAl₂O₄. Glucose 3% wt., reaction time 3h, total metal loading 10%wt.

Metals	Loading each metal (% wt.)	Gas phase yields (%)			Glucose conversion (%)	Liquid phase yields (%)														
		H_2	CH_4	CO_2		Fructose	Sorbitol	C_{4-5}	Lactic acid	Acetic acid	Levulinic acid	Propionic acid	Methanol	Ethanol	HMF	Glycerol	Formic acid	Hydroxyacetone	Ethylene glycol	1,2-propanediol
CoFe	5				69	23		7	3	1				1	3		1	2		
NiFe	5				69	25		7	4	2					3		1	2		
NiCoFe	3.3				71	24		7	4	1				1	3		1	2		

Figure 125: Lump sum of yield in reaction pathways and product sum for bimetallic and trimetallic catalysts loaded over MgAl₂O₄. Reactions performed at 150°C for 3h, glucose 3% wt, and total metal lading 10% wt.

Figure 126 reports the difference in lump sum once subtracted the support reactivity. As for isomerization mechanism, it is lowered than the single metals, and only in the NiCoFe catalyst, the dehydrogenation activity typical of Ni is expressed together with a significant C-C cleavage contribution assignable to cobalt.

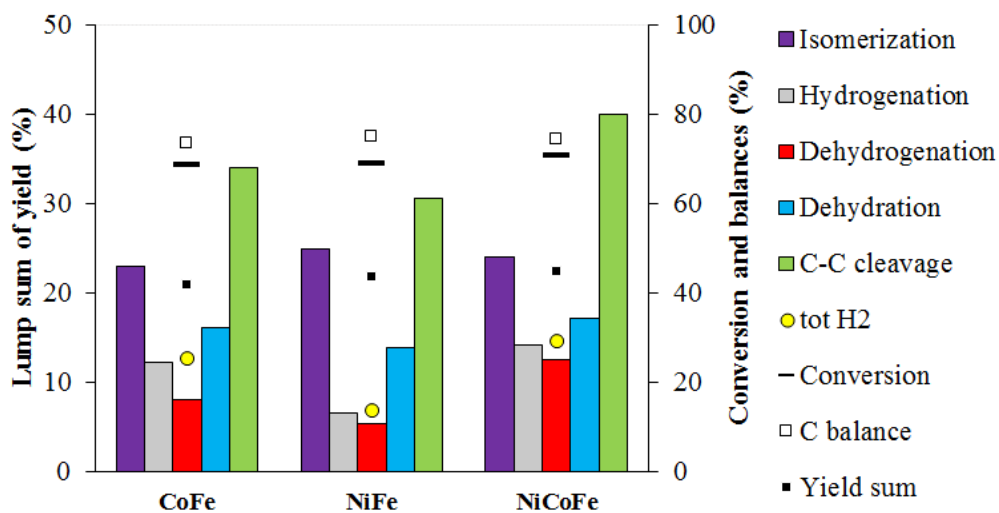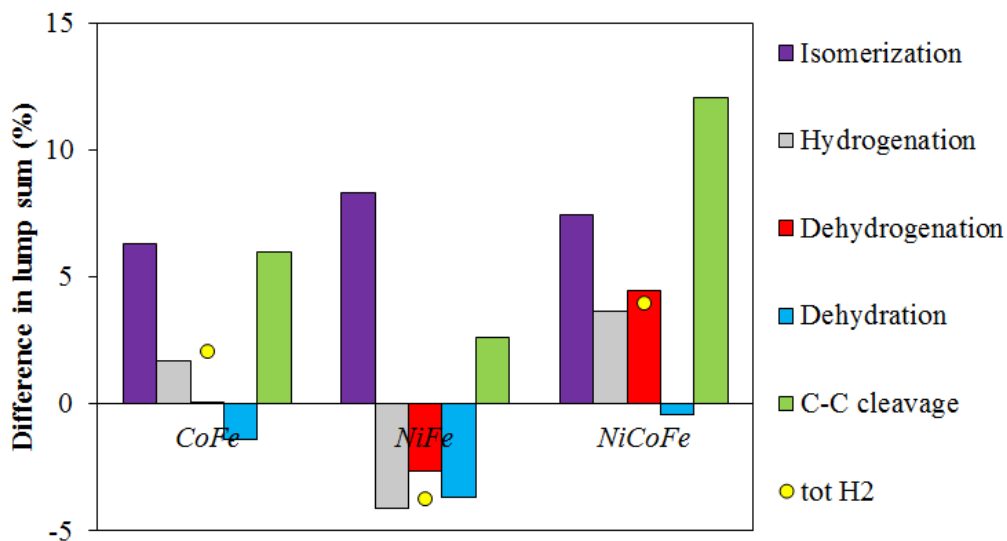*Figure 126: Differences in lump sum of yield in reaction pathways for bimetallic and trimetallic catalysts loaded over MgAl₂O₄. Reactions performed at 150°C for 3h, glucose 3% wt. and total metal lading 10% wt.*

In conclusion, it is demonstrated possible to couple the metal activity by adding several active phases, even if more characterization studies have to be performed to determine the formation of an alloy or separate deposition. Within the combinations selected, the use of three metals has given the most interesting results.

7.3.3 Bulk catalysts

One of the main problems of glucose APR deals with the formation of humins that on one side cause the reagent consumption in not valuable products and on the other deactivates the catalyst for blockage of active sites. The first drawback can be partially reduced by working at lower temperatures while for the second a more robust catalyst is necessary. The synthesis of bi- and tri-metallic bulk catalysts appeared to be interesting from this point of view for the possibility of having a high density of active sites combined with the presence of several interspersed metals on the surface. Differently from glycerol APR tests, in this case a spinel crystalline phase was selected because it is less sensitive to phase changes even in hydrothermal conditions and shows a lower surface area compared to mixed oxides. Moreover, no active Pt phase was deposited on the surface, in line with the aim of substituting noble metals with cheaper elements.

As a comparison with previous bi and tri-impregnated catalysts, $NiFe_2O_4$, $CoFe_2O_4$ and $NiCoFe_2O_4$ were synthesized. In the case of the tri-metallic one, the M^{2+} amount was equally divided within Ni and Co, maintaining constant in the tree samples the M^{3+} quantity. Table 11 presents the characterization data of the synthesized samples after calcination at 600°C. With respect to $MgAl_2O_4$ spinel calcined at 900°C, they have significantly lower surface area, pore volume, due to the lower crystal size and favored direct spinel formation. Moreover, the obtained particles around 30-40nm are significantly bigger compared the $MgAl_2O_4$ structure, presenting 11nm dimension. Figure 127 reports the XRD analyses of the oxides before and after reduction at 500°C. All the samples present a similar pattern slightly shifted to lower °2θ values for the $CoFe_2O_4$ but even so corresponding to database cubic spinel phase. As for the analysis of reduced patterns, the NiFe sample shows the presence of a NiFe 1:1 metal alloy with main reflects at 43, 50 and 76°2θ and a second reflect with lower intensity compared to the previous. The second peak at 45°2θ is more probably assignable to Fe^0 compared to Ni^0, due to the presence of a second lower signal at 65°2θ, not existent in the Ni^0 pattern. The CoFe sample instead shows a single main signal at 45°2θ typical of CoFe 1:1 alloy with no evidence of Co^0 phase. Lastly, the NiCoFe catalyst shows a broadened peak around 44°2θ that could be the sum of NiFe alloy and Co^0 phases respectively centered at 43.7 and 43.9°2θ with a second signal at 45°2θ assignable to CoFe alloy or Fe^0 metal, both supported by the presence of the second reflect at 65°2θ. Moreover, this last sample, together with NiFe, shows a residual presence of spinel phase. No samples evidence the presence of iron oxides. The reported phases are in accordance with metal redox potentials that show the best reducibility for cobalt, shortly followed by nickel and at later by iron. TPR profiles (Figure 128) confirm the necessity of reduction at 500°C for those samples, because the reducibility, as expected, is significantly lower compared to impregnated samples. Moreover, it can be seen that the nickel-containing oxides start to reduce around 350°C, while cobalt necessitates a higher temperature maybe due to the bigger dimension of crystals of the metal. Mass analyses have detected for all the samples a significant release of water above 500°C, justifying the high temperature peaks. Further analyses by TEM over bulk samples will better clarify surface properties and crystal distribution.

Table 30: Surface characterization of prepared spinel-like catalysts calcined at 600°C for 5h. Particle size is determined by Scherrer equation.

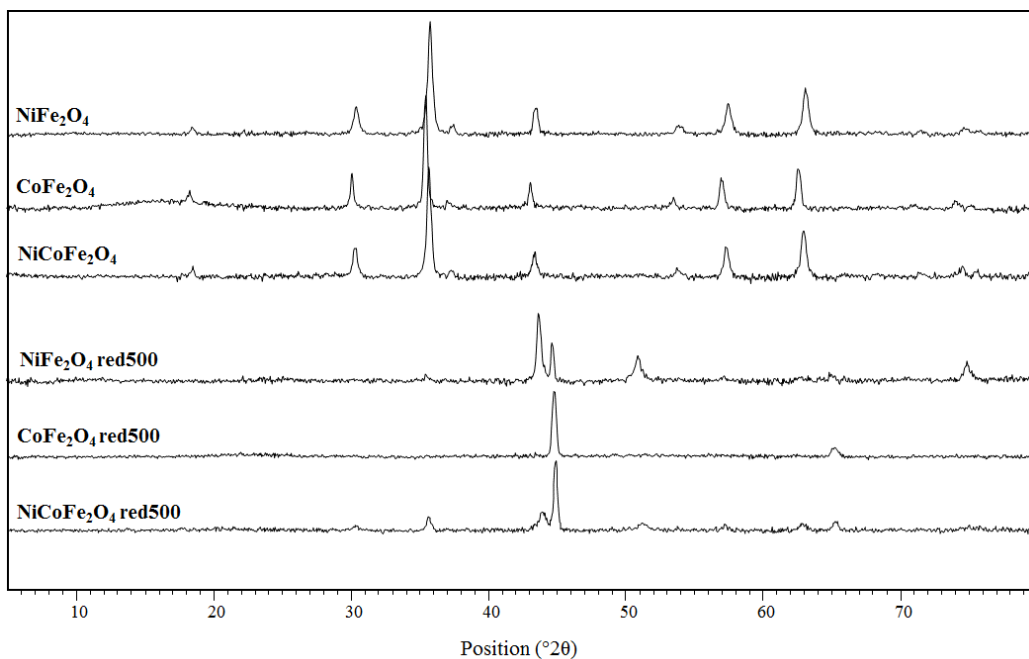| Catalyst	Metal stoichiometry ratio			Particle size (nm)	S.A. (m²/g)	pore volume (cm³/g)	pore dimension (nm)
	Ni	Co	Fe				
NiFe₂O₄	1	0	2	30.7	23	0.10	12.2
CoFe₂O₄	0	1	2	45.3	17	0.09	18.6
NiCoFe₂O₄	0.5	0.5	2	33.1	28	0.13	14.3

Figure 127: XRD analyses of the spinel-like catalysts calcined and reduced at 500°C.
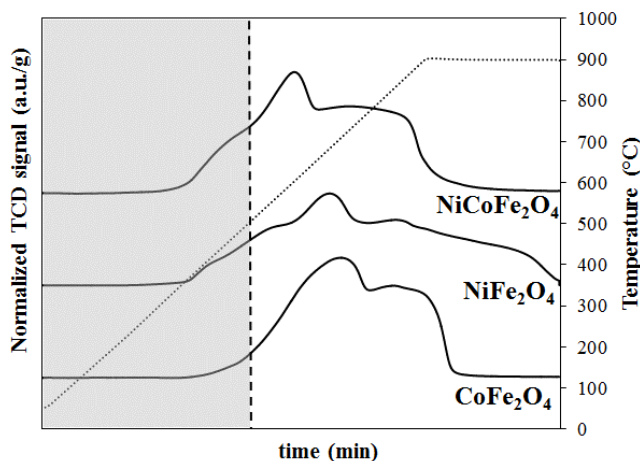
Figure 128: TPR profiles of bulk catalysts.

Glucose APR tests are reported in Table 31 and Figure 129. Conversion is increased of more than 10% compared to the impregnated samples at the same reaction conditions. Gas phase yield are absent, while in liquid phase main products are fructose, C_{4-5}, lactic acid and hydroxyacetone. Fructose yield is lowered due to the absence of strong acid aluminum sites, while the formation of other low carbon number sugars is favored. In addition, scission to C_3 molecules is higher for bulk samples. Comparing the studied catalysts, the $NiFe_2O_4$ presents the lowest activity, while the $CoFe_2O_4$ one the highest. The trimetallic one has intermediate values within the two bimetallic, confirming the possibility of metal combination. Carbon balance values are around 10% less compared to the impregnated samples, and are higher in presence of Ni in the sample, probably due to the lower conversion. The comparison by lump sum method in Figure 129 underlines higher cleavage and dehydrogenation for all the samples. The dehydrogenation is higher only in presence of Ni in the spinel catalyst, and the same happens for dehydration in presence of Co.

Table 31: Yields and parameters for APR reactions for bimetallic and trimetallic spinel-like catalysts at 150°C. Glucose 3% wt., reaction time 3h.

Reaction	Gas phase yields (%)			Glucose conversion (%)	Liquid phase yields (%)														
Catalyst	H_2	CH_4	CO_2		Fructose	Sorbitol	C_{4-5}	Lactic acid	Acetic acid	Levulinic acid	Propionic acid	Methanol	Ethanol	HMF	Glycerol	Formic acid	Hydroxyacetone	Ethylene glycol	1,2-propanediol
$CoFe_2O_4$	1			89	11		10	8	2		1		1	1			7		
$NiFe_2O_4$				79	26		8	5	2							1	4		
$NiCoFe_2O_4$				82	22		9	6	2		1			1		1	5		
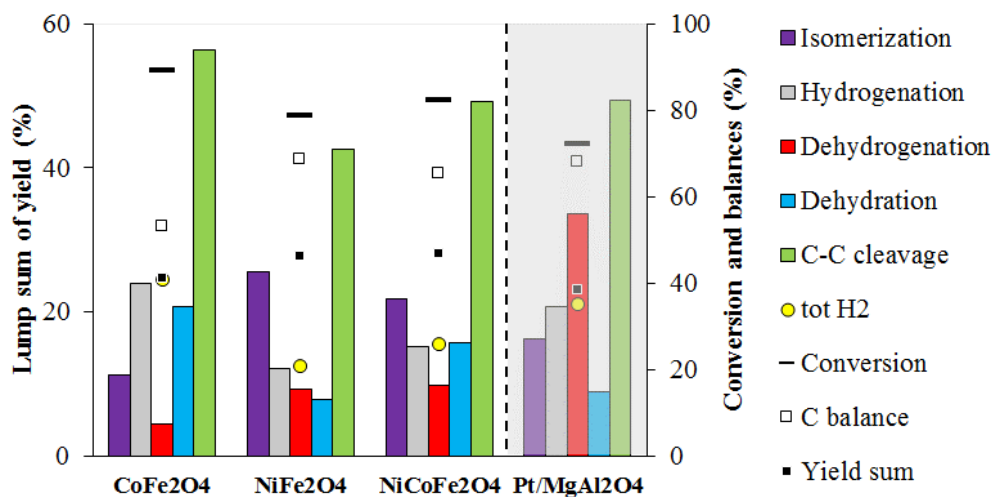
Figure 129: Lump sum of yield in reaction pathways and product sum for bimetallic and trimetallic spinel-like catalysts, in comparison with Pt reference catalyst. Reactions performed at 150°C for 3h, glucose 3% wt.

The stability of the phase was confirmed by post-reaction XRD with the presence of the same phases with a small reduction in crystallinity and absence of leaching confirmed by XRF analyses. In conclusion, bulk catalyst have demonstrated to be comparable within themselves depending on the type of metal inserted, and show higher activity than impregnated tests of the same metal. Figure 129 reports the activity in the same reaction conditions of the reference Pt/MgAl$_2$O$_4$ 3%wt. catalyst. Bulk catalyst conversion is higher compared to the reference, with similar carbon balances. C-C

cleavage and hydrogenation yields were obtained higher for the $CoFe_2O_4$ catalyst and comparable for the trimetallic one using cheaper metals in a more robust catalyst; while dehydrogenation activity is still low. Moreover, dehydration activity is still higher for bulk system due to different acidity of Fe^{3+} cation compared to Al^{3+}. These preliminary results evidence some interesting systems for APR reaction of glucose with results comparable with noble metal supported catalysts together with the possibility of a wide range for improvement and optimization.

7.3.4 Bulk catalysts by microemulsion technique

The good results obtained for bulk catalysts suggested driving some efforts towards the synthesis of oxides via microemulsion technique. Since the co-precipitation method used involved the formation of the oxide in strong basic conditions, it was chosen to adapt a method reported for Ce/Zr mixed oxides[131] with excess of TMAH as a basic precipitating agent. $NiFe_2O_4$ was selected to be synthesized because, being the less active spinel catalyst, it had interesting margins of improvement.

Surface characterization data are reported in Table 32 and Figure 130. The microemulsion-synthesized sample, named $NiFe_2O_4$-m, showed similar distribution associable to H1 hysteresis loop typical of aggregation of spherical particles[149]. Surface area is slightly higher compared to the co-precipitated due to the smaller particle size but with the same dimension of pores. The main dissimilarity was evidenced by XRD test in Figure 131. Even the two supports have reflects in the same position, the reciprocal intensity of the peaks is different, in particular the ones at 37, 43 and 63°2θ are more intense in the microemulsion sample. It was thus hypothesized the formation of a second phase with reflect in those positions, as NiO. Approximate Rietveld calculation suggested a 24% of NiO beside the $NiFe_2O_4$ phase. A possible explanation is the phase separation with lower Ni amount in the spinel structure or the loss of some iron nitrate in the precipitation solution.

Table 32: Surface characterization of prepared catalysts pore distribution of the NiFe₂O₄ samples calcined at 600°C. Particle size calculated by Scherrer equation.

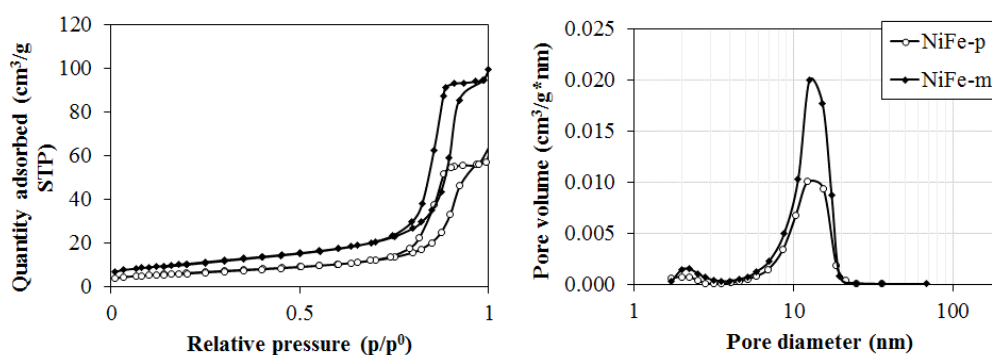| Catalyst	Particle size (nm)	S.A. (m²/g)	pore volume (cm³/g)	pore dimension (nm)
NiFe₂O₄-p	30.7	23	0.099	12.21
NiFe₂O₄-m	20.4	38	0.154	12.54

Figure 130: Adsorption/desorption isotherms and pore distribution of the NiFe₂O₄ samples calcined at 600°C.
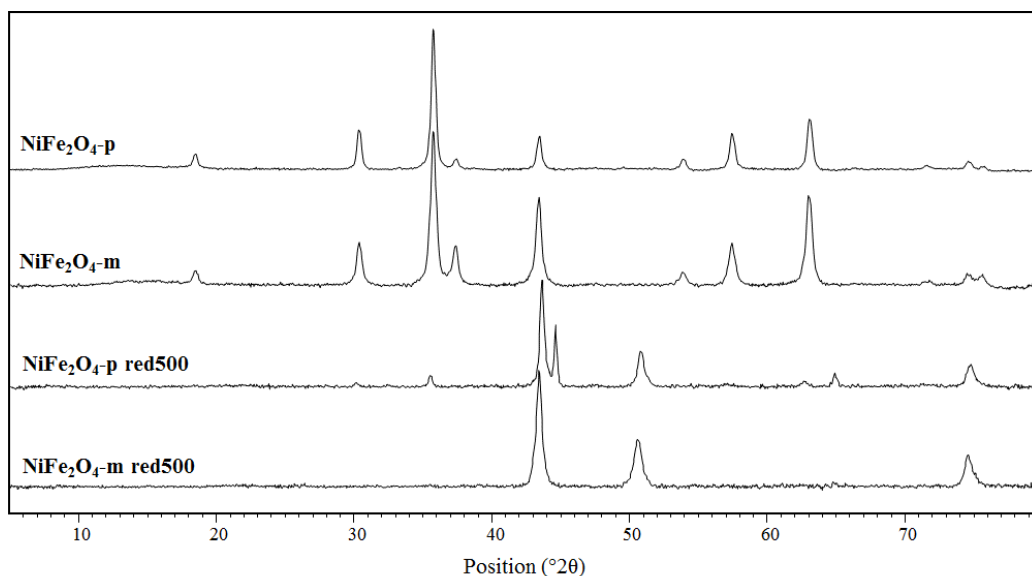

Figure 131: XRD analyses of the support synthesized by microemulsion and co-precipitation technique.

TPR profile (Figure 132) shows for the two samples reduction in the same temperature range but with different maxima, due to the dimension of the crystals. As confirmed by XRD analyses, the two samples report a change in surface crystallinity. Differently from the previously discussed $NiFe_2O_4$-p sample, the microemulsion showed the presence of only one peak, shifted in comparison to the NiFe alloy and attributed by database to a Fe^0 gamma phase.

The synthetic differences within the two supports was analysed by TEM microscopy as reported in Figure 133. The co-precipitated sample showed a uniform distribution of crystals around 20-30nm and a Ni:Fe molar ratio of 36:64, similar to the stoichiometry one. Neither hematite phase was detected by SAED in the crystals, while NiO phase was not distinguishable from spinel for the presence of the same reflects[281]. As for the microemulsion sample, it can be clearly seen in the images the lower homogeneity of the crystals within 5 and 30nm. EDS spectra in different part of the sample have confirmed Ni percentage in the range 30-70% with a mean molar ratio Ni:Fe of 45:54, with an excess of Ni in the structure compared to spinel phase, more similar to 1:1 ratio. Moreover, SAED measurements present a complexity of d spacing detected, which are not relatable neither to spinel nor to NiO or magnetite phases[281]. It can be concluded, as previously hypothesized by XRD diffractograms the presence of $NiFe_2O_4$ and NiO phases with a loss in Fe cation, which probably remains inside the micelles not precipitated.
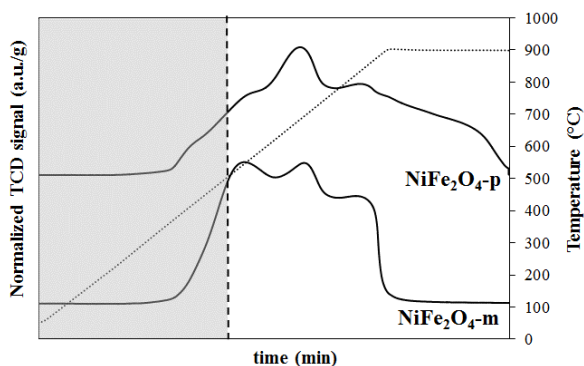
Figure 132: TPR profiles of bulk catalysts synthesized with different technique.
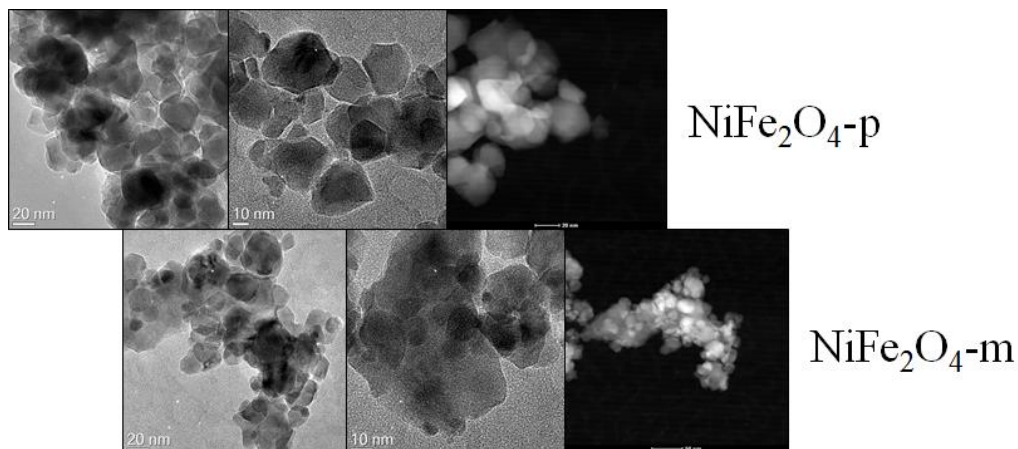
Figure 133: TEM and STEM-HAADF images of NiFe$_2$O$_4$ catalysts synthesized by different technique. Samples not reduced.

Characterization data report, together with an improvement in surface area and smaller crystals, a difference in crystal formation and precipitation. This may be due to pH changes in presence of micelles, which causes a not complete precipitation of Fe. Further studies are thus ongoing to improve the microemulsion synthesis to make it comparable with co-precipitation one maintaining the positive effects described. Nevertheless, the microemulsion catalysts was tested in APR reaction of glucose and compared with the co-precipitated (Table 33 and Figure 134). Glucose and yield values do not show significant differences indicating that the system is not sensitive to small variations in the catalyst features, or the two oxides present in the microemulsion sample (NiFe$_2$O$_4$ and NiO) work in similar directions in glucose APR, as demonstrated by lump sum diagram.

Table 33: Yields and parameters for APR reactions for bimetallic NiFe2O4 catalysts synthesized by different technique. Glucose 3% wt., reaction time 3h.

Reaction / Catalyst	Gas phase yields (%)			Glucose conversion (%)	Liquid phase yields (%)														
	H_2	CH_4	CO_2		Fructose	Sorbitol	C_{4-5}	Lactic acid	Acetic acid	Levulinic acid	Propionic acid	Methanol	Ethanol	HMF	Glycerol	Formic acid	Hydroxyacetone	Ethylene glycol	1,2-propanediol
$NiFe_2O_4$-m				74	29		7	4	1			1				1	3		
$NiFe_2O_4$-p				74	26		6	3	1					2			3		
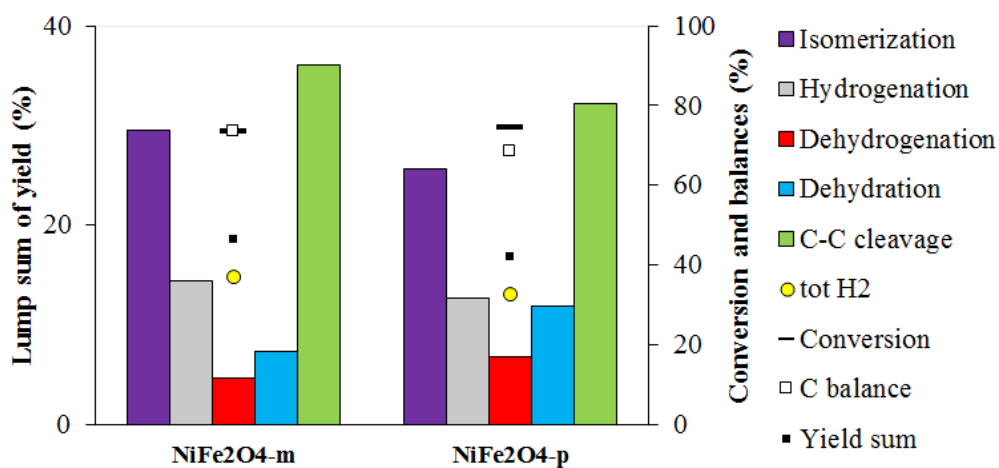
Figure 134: Lump sum of yield in reaction pathways and product sum for bimetallic spinel-like catalysts synthesized with different technique. Reactions performed at 150°C for 3h, glucose 3% wt.

In conclusion, microemulsion synthesis did not give the expected results neither in the synthesis of the oxide nor in reactivity, due to a multiplicity of phases and giving similar results compared to the co-precipitated sample. Further studies are still ongoing to improve the synthesis to justify by improved catalytic results a bigger synthetic effort.

Conclusions

In the wide scenario of wastes and biomass upgrading, the aqueous phase reforming (APR) reaction offers an interesting method to obtain hydrogen and platform chemicals from raw materials of low cost. The present study started from the upgrade of glycerol, as main waste from biodiesel plants, via APR process passing through the optimization of catalyst features, and then shifting to a more complex polyol as glucose, as most abundant monosaccharide from biomass.

The first step was the synthesis of titanium oxide by optimizing a microemulsion technique[120]. The ratio within oil, surfactants, water and acid was studied and the formation of the oxide was followed by SEM and DLS measurements to find the best reaction parameters to obtain anatase phase instead of rutile, which is more active in heterogeneous catalysis. The solid, named TiO_2-m was found to have crystals with average diameter of 5nm, smaller compared to a reference commercial anatase (TiO_2-comm), higher surface area and density of acid sites. The solids were loaded with Pt 3%wt. and tested in APR reaction of glycerol. Results underlined a higher glycerol conversion for the Pt/TiO_2-m catalyst, at the same reaction conditions against Pt/TiO_2-comm catalyst. Moreover, a comparison within reactions performed at different conditions but with similar conversion values, showed for the Pt/TiO_2-m catalyst elevated selectivity towards gas phase products and secondary reaction products, thus a higher catalyst activity compared to the commercial.

Pt/TiO_2-m catalyst was used to determine the APR mechanism of glycerol. Tests at different reaction time and temperature were analysed joint with reaction with supposed intermediates and literature study[45,46]. Beside the characterization and reactivity work, implementation of the reaction mechanism for commercial and microemulsion titania was done via in-situ Attenuated Total Reflectance (ATR) IR technique with multiple reflection on ZnSe crystal. Tests were performed in ramp up to 200°C or in isothermal conditions with pure glycerol or solution to simulate the reaction environment. Both supports were tested also in presence of Pt depositing a thin layer of catalyst over the

crystal and covering with reagent solution. Significant results were obtained for reaction at 70°C and showed the formation of several bands, after subtraction from water and glycerol spectra. In particular it was individuated the presence of a C=O stretch at $1697cm^{-1}$, that in combination with the broad acid OH stretch at $2900cm^{-1}$, can confirm the presence of lactic acid in the reaction mixture. This peak appears from the early stages of reaction but becomes predominant only after 1h. Earlier interesting signals found in the carbonyl region was at $1620cm^{-1}$, this is similar to pyruvic aldehyde C=O stretch, but can fit also to a C=C stretch of supposed dehydration intermediates or coming from keto-enol equilibrium. Another signal that rises with acid stretching is at $1723cm^{-1}$ and can be assigned to C=O stretch of glyceraldehyde, followed by another carbonyl signal at $1695cm^{-1}$ assigned to lactic acid or hydroxyacetone. Several other signals were present, in particular the C-H alkyl stretch coupled with aldehyde one in the range $2200-3200cm^{-1}$, CH_2 bending around $1170-1500cm^{-1}$ and C-O alcoholic stretch at $950-1170cm^{-1}$. By comparison results within the two TiO_2 catalysts, it was confirmed the hypothesis of the same reactivity within the two supports. Nevertheless, with this powerful technique it was possible to highlight some differences, in particular in the carbonyl region the microemulsion catalyst shows three signals with high intensity, while the commercial presents only glyceraldehyde one with a small shoulder indicating a lower amount of dehydration keto-enol products. Moreover, the ratio within acid and OH group signals is different giving a higher yield in OH-containing molecules for the commercial support, as detected products.

The possibility of tuning the reaction with conditions and catalyst was than studied. Several combination of time, temperature, metal loading and type and reduction of metal were analysed but the most interesting results were obtained with changes in the support. The first parameter examined was the effect of acid and basic sites on the reaction. A simplification in the calculations was done considering the selectivity sum in specific pathways from glycerol to the analysed product, considering only the total exchanged molecules. The mechanisms considered were dehydration, dehydrogenation and decarboxylation; hydration reactions permitted to calculate the H_2 consumed and the total H_2 produced was valued as sum of consumed and produced. Reactivity results were evaluated with TPD analyses of acid and basic sites over Pt supported on Al_2O_3,

MgO and Mg/Al oxides with different ratio. The effect was the steep increase in dehydrogenation activity together with the basicity of the system, dehydration meanwhile was mainly favoured only in presence of acid sites, as further confirmed by literature reported mechanisms over glycerol[152]. A further step was done adding in the support blend Ni, a well-known dehydrogenating catalyst with high activity in reforming reaction. The synthesis was performed via co-precipitation, permitting a statistic distribution of the cations in the matrix and a variability within bivalent and trivalent cations in the structure[130]. Ni was loaded first with a constant amount but changing the Mg/Al ratio to study the effect of basicity with the enhancement in activity. Experimental data confirmed the same trend evidenced in earlier studies, but with glycerol conversion up to 80%. Moreover, decarboxylation mechanism was increased at the same Ni loading. The effect over the reaction of the change in Ni/Mg ratio is decreasing with the rise in Ni loading, giving the expected ratio within dehydration and dehydrogenation reactions. It was interestingly noted a decarboxylation ratio independent by Ni loading and the total H_2 produced by the reaction, even if hydrogenation reactions are favoured by high amount of Ni. Thus, it was confirmed the possibility of tuning reaction products by changing support and active metal features. The activity of Ni in APR was also tested as peculiar NiO nanoparticles loaded over TiO_2 commercial and microemulsion, synthesized in collaboration with Milan catalysis group[132]. $Pt/NiO/TiO_2$ sample showed a similar reactivity compared to Pt/TiO_2, but with enhanced dehydration and liquid phase selectivity. Moreover, the conversion values obtained with those systems are the highest reached in glycerol reactivity.

Further studies were developed with glucose as reagent for APR. The first approach was to transfer the knowledge obtained over simpler polyols to a molecule that could undergo degradation in acid or basic conditions at the working temperature, it was in fact necessary to lower the reaction temperature to avoid the formation of humins even if that reduced significantly gas phase yields. All the catalysts tested with glycerol were examined in the new conditions. The first set of analysis studied the effect of the support at Pt loading 3%wt. The complexity of the liquid mixture was higher compared to glycerol tests, with C_6 to C_2 products, and it was thus impossible to determine the

correct mechanism of reaction. Lump sums of selectivity were again analysed to study the effect of support, considering isomerization, hydrogenation, dehydrogenation, dehydration and C-C cleavage reactions. Results showed a significant difference in product distribution at total conversion in presence and absence of Pt for different supports. In specific, high results in dehydrogenation, C-C cleavage and hydrogen production were obtained for Mg/Al supports and TiO_2, while MgO and Ni/Mg/Al supports were the most active in presence of Pt. Besides the support analysis, which did not give the same clear trends as glycerol, the metal activity was also evaluated to study its influence over the reaction products. $MgAl_2O_4$ was selected as a support because it presents both acid and basic sites with low strength. Pt, Ru, Ni, Fe, Co and Cu were tested in APR and it was analysed the subtraction within the metal/support reactivity and the support itself. As expected platinum is the most active catalyst towards hydrogenation/dehydrogenation and C-C cleavage reactions, moreover it strongly inhibits dehydration, which is favoured by acid sites on the support. Nickel and cobalt are active instead in hydrogenation, C-C cleavage disfavouring the dehydrogenation pathway, copper hydrogenates only, and ruthenium and iron are the less active catalysts. Metal activities were than coupled both by production of bi-impregnated support together with the synthesis of mixed oxides with two or three metals by co-precipitation and microemulsion technique. Ni/Fe, Co/Fe and Ni/Co/Fe combinations were characterized and studied obtaining good results in joint reactivity. In particular the Co containing bulk catalyst showed higher conversion and C-C cleavage compared to Pt impregnated reference catalyst.

In conclusion, the work demonstrates the possibility of enhancing the activity and tuning the reaction mechanism in APR reaction of different polyols by acting on the catalyst features, in particular over support's properties and type of metal. Moreover, the observations over simpler polyols can be transferred to molecules that are more complex as glucose with a different intrinsic degradation. All the reactivity tests were joined with synthesis of catalysts both by co-precipitation and innovative microemulsion technique and with in-depth characterization to correlate the results with surface properties. Mechanism analyses were also done in autoclave system and in-situ measurements for the analysis of forming intermediates.

Bibliography

(1) Buekens, A. G. *Commercial and Marketing Aspects of Gasifiers-Introduction*; Office for Official Publications of the European Communities, 1990.

(2) Beenackers, A. *Renew. Energy* **1999**, *16* (1), 1180–1186.

(3) Higman, C.; Burgt, M. van der. *Gasification*; Gulf Professional Publishing, 2011.

(4) Stahl, K.; Neergaard, M. *Biomass Bioenergy* **1998**, *15* (3), 205–211.

(5) Kitzler, H.; Pfeifer, C.; Hofbauer, H. *Fuel Process. Technol.* **2011**, *92* (5), 908–914.

(6) Albertazzi, S.; Basile, F.; Brandin, J.; Einvall, J.; Hulteberg, C.; Fornasari, G.; Rosetti, V.; Sanati, M.; Trifirò, F.; Vaccari, A. *Catal. Today* **2005**, *106* (1), 297–300.

(7) Fornasiero, P.; Graziani, M.; Basile, F.; Trifirò, F. *Biomass gasification for second-generation fuel production*; CRC Press, 2011.

(8) Wang, L.; Chen, J.; Watanabe, H.; Xu, Y.; Tamura, M.; Nakagawa, Y.; Tomishige, K. *Appl. Catal. B Environ.* **2014**, *160*, 701–715.

(9) Wilhelm, D. J.; Simbeck, D. R.; Karp, A. D.; Dickenson, R. L. *Fuel Process. Technol.* **2001**, *71* (1), 139–148.

(10) Gerhartz, W.; Ullmann, F. *Ullmann's encyclopedia of industrial chemistry, 5th edition*; A12; VCH, 1987.

(11) Twigg, M. V. *Catalyst Handbook, 2nd ed.*; Manson Pub., 1989.

(12) Solbakken, \AAge. *Stud. Surf. Sci. Catal.* **1991**, *61*, 447–455.

(13) Mafessanti, R. Catalysts and processes for next-generation H2 production. Tesi di dottorato, Alma Mater Studiorum-Università di Bologna, Dipartimento di Chimica Industriale, 2014.

(14) Holladay, J. D.; Hu, J.; King, D. L.; Wang, Y. *Catal. Today* **2009**, *139* (4), 244–260.

(15) Albertazzi, S.; Basile, F.; Trifirò, F.; Vaccari, A. *Gasification of Biomass to Produce Hydrogen in "Renewable Resources and Renewable Energy: A Global Challenge";* Fornasiero, P., Graziani, M., Eds.; Taylor&Francis, 2013.

(16) Al Arni, S.; Bosio, B.; Arato, E. *Renew. Energy* **2010**, *35* (1), 29–35.

(17) Ni, M.; Leung, D. Y.; Leung, M. K.; Sumathy, K. *Fuel Process. Technol.* **2006**, *87* (5), 461–472.

(18) Lin, Y.-C. *Int. J. Hydrog. Energy* **2013**, *38* (6), 2678–2700.

(19) Li, J.; Dai, J.; Liu, G.; Zhang, H.; Gao, Z.; Fu, J.; He, Y.; Huang, Y. *Biomass Bioenergy* **2016**, *94*, 228–244.

(20) Lee, H.; Kim, Y.-M.; Lee, I.-G.; Jeon, J.-K.; Jung, S.-C.; Chung, J. D.; Choi, W. G.; Park, Y.-K. *Korean J. Chem. Eng.* **2016**, *33* (12), 3299–3315.

(21) Garcıa, L.; Salvador, M. L.; Arauzo, J.; Bilbao, R. *J. Anal. Appl. Pyrolysis* **2001**, *58*, 491–501.

(22) Alonso, D. M.; Wettstein, S. G.; Dumesic, J. A. *Chem. Soc. Rev.* **2012**, *41* (24), 8075–8098.

(23) Esposito, D.; Antonietti, M. *Chem. Soc. Rev.* **2015**, *44* (16), 5821–5835.

(24) Biomass to Renewable Energy Processes https://www.crcpress.com/Biomass-to-Renewable-Energy-Processes/Cheng-Cheng/p/book/9781420095173 (accessed Jan 16, 2017).

(25) Dhepe, P. L.; Fukuoka, A. *ChemSusChem* **2008**, *1* (12), 969–975.

(26) Van de Vyver, S.; Geboers, J.; Jacobs, P. A.; Sels, B. F. *ChemCatChem* **2011**, *3* (1), 82–94.

(27) Zakzeski, J.; Bruijnincx, P. C.; Jongerius, A. L.; Weckhuysen, B. M. *Chem. Rev.* **2010**, *110* (6), 3552–3599.

(28) Zhou, C.-H.; Xia, X.; Lin, C.-X.; Tong, D.-S.; Beltramini, J. *Chem. Soc. Rev.* **2011**, *40* (11), 5588–5617.

(29) Liu, X.; Wang, X.; Yao, S.; Jiang, Y.; Guan, J.; Mu, X. *Rsc Adv.* **2014**, *4* (90), 49501–49520.

(30) Dumesic, J. A.; Gurbuz, E. I.; Braden, D. J. *Aqueous Phase catalytic processing in biomass valorization to H2 and liquid fuels in "Renewable Resources and Renewable Energy: A Global Challenge", Second Edition*; Fornasiero, P., Graziani, M., Eds.; CRC Press, 2011.

(31) Li, H.; Bhadury, P. S.; Riisager, A.; Yang, S. *ResearchGate* **2014**, *46* (4).

(32) Corma, A.; Iborra, S.; Velty, A. *Chem. Rev.* **2007**, *107* (6), 2411–2502.

(33) Davda, R. R.; Shabaker, J. W.; Huber, G. W.; Cortright, R. D.; Dumesic, J. A. *Appl. Catal. B Environ.* **2005**, *56* (1–2), 171–186.

(34) Gao, J.; Wang, Y.; Ping, Y.; Hu, D.; Xu, G.; Gu, F.; Su, F. *RSC Adv.* **2012**, *2* (6), 2358.

(35) Cortright, R. D.; Davda, R. R.; Dumesic, J. A. *Nature* **2002**, *418* (6901), 964–967.

(36) Dumesic, J. A.; Gurbuz, E. I. *Catalytic Strategies and Chemistries Involved in the Conversion of Sugars to Liquid Transportation Fuels in "Catalysis for the Conversion of Biomass and Its Derivatives"*; Behrens, M., Datye, A. K., Eds.; Max Planck Research Library for the History and Development of Knowledge, epubli, 2013; Vol. Chapter 10.

(37) Sinfelt, J. H.; Yates, D. J. *J. Catal.* **1967**, *8* (1), 82–90.

(38) Grenoble, D. C.; Estadt, M. M.; Ollis, D. F. *J. Catal.* **1981**, *67* (1), 90–102.

(39) Vannice, M. A. *J. Catal.* **1977**, *50* (2), 228–236.

(40) Menezes, A. O.; Rodrigues, M. T.; Zimmaro, A.; Borges, L. E. P.; Fraga, M. A. *Renew. Energy* **2011**, *36* (2), 595–599.

(41) Shabaker, J. W.; Huber, G. W.; Davda, R. R.; Cortright, R. D.; Dumesic, J. A. *Catal. Lett.* **2003**, *88* (1–2), 1–8.

(42) Shabaker, J. W.; Dumesic, J. A. *Ind. Eng. Chem. Res.* **2004**, *43* (12), 3105–3112.

(43) Eggleston, G.; Vercellotti, J. R. **2000**.

(44) Lehnert, K.; Claus, P. *Catal. Commun.* **2008**, *9* (15), 2543–2546.

(45) Wawrzetz, A.; Peng, B.; Hrabar, A.; Jentys, A.; Lemonidou, A. A.;

Lercher, J. A. *J. Catal.* **2010**, *269* (2), 411–420.

(46) King, D. L.; Zhang, L.; Xia, G.; Karim, A. M.; Heldebrant, D. J.; Wang, X.; Peterson, T.; Wang, Y. *Appl. Catal. B Environ.* **2010**, *99* (1–2), 206–213.

(47) Jiang, T.; Wang, T.; Ma, L.; Li, Y.; Zhang, Q.; Zhang, X. *Appl. Energy* **2012**, *90* (1), 51–57.

(48) Irmak, S.; Kurtuluş, M.; Hasanoğlu (Hesenov), A.; Erbatur, O. *Biomass Bioenergy* **2013**, *49*, 102–108.

(49) Wen, G.; Xu, Y.; Xu, Z.; Tian, Z. *Catal. Commun.* **2010**, *11* (6), 522–526.

(50) Chang, A. C.-C.; Lee, Y.-S.; Lin, K.-H. *Int. J. Hydrog. Energy* **2012**, *37* (20), 15691–15695.

(51) Zakzeski, J.; Weckhuysen, B. M. *ChemSusChem* **2011**, *4* (3), 369–378.

(52) Cortright, R. D.; Virent Energy System Inc. "Hydrogen generation from biomass-derived carbohydrates vie the Aqueous phase reforming (APR) process", award number: DE-FG36-05G15046 - (2005-2008)DOE Hydrogen and Fuel Cells Program: 2005 Annual Progress Report https://www.hydrogen.energy.gov /annual_progress05_production.ht ml.

(53) Cortright, R. D.; Virent Energy System Inc. "Hydrogen Generation from Biomass-Derived Carbohydrates via the Aqueous-Phase Reforming (APR) Process" - DOE Hydrogen and Fuel Cells Program: 2008 Annual Progress Report - Hydrogen Production https://www.hydrogen.energy.gov /annual_progress08_production.ht ml.

(54) Virent BioForming Technology http://www.virent.com/technolog y/bioforming/.

(55) Emerson, S. C.; Vanderspurt, T. H.; United Technology Research Center. "A Novel Slurry-Based Biomass Reforming Process" - DOE Hydrogen and Fuel Cells Program: 2005 Annual Progress Report - Production https://www.hydrogen.energy.gov /annual_progress05_production.ht ml.

(56) Monnier, J.; Zhang, Y.; Mcfarlan, A. Production of Hydrogen from Oxygenated Hydrocarbons. WO/2009/129622, October 30, 2009.

(57) Monnier, J.; Zhang, Y.; Mcfarlan, A. Production of Hydrogen from Oxygenated Hydrocarbons. US2011027169 (A1), February 3, 2011.

(58) Cortright, R.; Dumesic, J. Low-Temperature Hydrocarbon Production from Oxygenated Hydrocarbons. WO2004039918 (A2), May 13, 2004.

(59) Cortright, R.; Dumesic, J. Low-Temperature Hydrogen Production from Oxygenated Hydrocarbons. EP1458645 (A2) Abstract of corresponding document: WO03045841 (A1), September 22, 2004.

(60) Cortright, R. D. Methods and Systems for Generating Polyols. US2013289302 (A1), October 31, 2013.

(61) Cortright, R. D. Methods and Systems for Generating Polyols. CA2651770 (A1), June 12, 2008.

(62) Powell, J. B.; Chheda, J. N. Process to Produce Biofuels from

Biomass. CA2822109 (A1), June 28, 2012.

(63) Chheda, J. N.; Powell, J. B. Process to Produce Biofuels from Biomass. US2014161689 (A1), June 12, 2014.

(64) Ma, L.; Wang, T.; Yuan, Z.; Zhang, X.; Zhuang, X.; Wu, C.; Jiang, T.; Zhang, Q. Process for Hydrolysed Reforming of Liquous Cellulose Biomass to Produce Bio-Gasoline. US2012216451 (A1), August 30, 2012.

(65) Vilcocq, L.; Cabiac, A.; Especel, C.; Guillon, E.; Duprez, D. *Oil Gas Sci. Technol. D'IFP Energ. Nouv.* **2013**, *68* (5), 841–860.

(66) Huber, G. W. *Science* **2005**, *308* (5727), 1446–1450.

(67) IUPAC Gold Book https://goldbook.iupac.org/.

(68) Fechete, I.; Wang, Y.; Védrine, J. C. *Catal. Today* **2012**, *189* (1), 2–27.

(69) Cavani, F.; Trifirò, F.; Vaccari, A. *Catal. Today* **1991**, *11* (2), 173–301.

(70) Meynen, V.; Cool, P.; Vansant, E. F. *Microporous Mesoporous Mater.* **2009**, *125* (3), 170–223.

(71) Perego, C.; Villa, P. *Catal. Today* **1997**, *34* (3), 281–305.

(72) Schulman, J. H.; Friend, J. A. *J. Colloid Sci.* **1949**, *4* (5), 497–509.

(73) Corolleur, C.; Tomanova, D.; Gault, F. G. *J. Catal.* **1972**, *24* (3), 401–416.

(74) Boutonnet, M.; Kizling, J.; Stenius, P.; Maire, G. *Colloids Surf.* **1982**, *5* (3), 209–225.

(75) Negro, E.; Latsuzbaia, R.; Koper, G. J. *Langmuir* **2014**, *30* (28), 8300–8307.

(76) López-Quintela, M. A.; Tojo, C.; Blanco, M. C.; García Rio, L.; Leis, J. R. *Curr. Opin. Colloid Interface Sci.* **2004**, *9* (3–4), 264–278.

(77) Eriksson, S.; Nylén, U.; Rojas, S.; Boutonnet, M. *Appl. Catal. Gen.* **2004**, *265* (2), 207–219.

(78) Winsor, P. A. *Trans. Faraday Soc.* **1948**, *44*, 376–398.

(79) Bourrel, M.; Schechter, R. S. *Microemulsions and Related Systems: Formulation, Solvency, and Physical Properties*; Editions TECHNIP, 2010.

(80) Schwarze, M.; Pogrzeba, T.; Volovych, I.; Schomäcker, R. *Catal. Sci. Technol.* **2014**, *5* (1), 24–33.

(81) Stubenrauch, C. *Microemulsions: Background, New Concepts, Applications, Perspectives*; Wiley, 2008.

(82) Sun, Y.-P.; Atorngitjawat, P.; Meziani, M. J. *Langmuir* **2001**, *17* (19), 5707–5710.

(83) Bonini, M.; Bardi, U.; Berti, D.; Neto, C.; Baglioni, P. *J. Phys. Chem. B* **2002**, *106* (24), 6178–6183.

(84) Higgins, R. J. *Propos. NSF Program Solicitation* **1996**, No. 96–67.

(85) Eastoe, J.; Warne, B. *Curr. Opin. Colloid Interface Sci.* **1996**, *1* (6), 800–805.

(86) Lopez-Quintela, M. A. *Curr. Opin. Colloid Interface Sci.* **2003**, *8* (2), 137–144.

(87) Qiu, S.; Dong, J.; Chen, G. *J. Colloid Interface Sci.* **1999**, *216* (2), 230–234.

(88) Tai, C. Y.; Lee, M.-H.; Wu, Y.-C. *Chem. Eng. Sci.* **2001**, *56* (7), 2389–2398.

(89) Chen, D.-H.; Wu, S.-H. *Chem. Mater.* **2000**, *12* (5), 1354–1360.

(90) Wang, C.-C.; Chen, D.-H.; Huang, T.-C. *Colloids Surf. Physicochem. Eng. Asp.* **2001**, *189* (1), 145–154.

(91) Moulik, S. P.; De, G. C.; Panda, A. K.; Bhowmik, B. B.; Das, A. R. *Langmuir* **1999**, *15* (24), 8361–8367.

(92) Curri, M. L.; Agostiano, A.; Manna, L.; Monica, M. D.; Catalano, M.; Chiavarone, L.; Spagnolo, V.; Lugarà, M. *J. Phys. Chem. B* **2000**, *104* (35), 8391–8397.

(93) Panda, A. K.; Moulik, S. P.; Bhowmik, B. B.; Das, A. R. *J. Colloid Interface Sci.* **2001**, *235* (2), 218–226.

(94) Hanaoka, T.; Hatsuta, T.; Tago, T.; Kishida, M.; Wakabayashi, K. *Appl. Catal. Gen.* **2000**, *190* (1), 291–296.

(95) Ingelsten, H. H.; Bagwe, R.; Palmqvist, A.; Skoglundh, M.; Svanberg, C.; Holmberg, K.; Shah, D. O. *J. Colloid Interface Sci.* **2001**, *241* (1), 104–111.

(96) Schwuger, M.-J.; Stickdorn, K.; Schomaecker, R. *Chem. Rev.* **1995**, *95* (4), 849–864.

(97) Holmberg, K. *Eur. J. Org. Chem.* **2007**, *2007* (5), 731–742.

(98) Pera-Titus, M.; Leclercq, L.; Clacens, J.-M.; De Campo, F.; Nardello-Rataj, V. *Angew. Chem. Int. Ed.* **2015**, *54* (7), 2006–2021.

(99) Wu, D.-Y.; Zhang, L.-P.; Wu, L.-Z.; Wang, B.; Tung, C.-H. *Tetrahedron Lett.* **2002**, *43* (7), 1281–1283.

(100) Antonietti, M.; Basten, R.; Lohmann, S. *Macromol. Chem. Phys.* **1995**, *196* (2), 441–466.

(101) Wang, J.; Shah, Z. H.; Zhang, S.; Lu, R. *Nanoscale* **2014**, *6* (9), 4418–4437.

(102) Hyde, E. D. E. R.; Seyfaee, A.; Neville, F.; Moreno-Atanasio, R. *Ind. Eng. Chem. Res.* **2016**, *55* (33), 8891–8913.

(103) Hsueh, H.-Y.; Yao, C.-T.; Ho, R.-M. *Chem. Soc. Rev.* **2015**, *44* (7), 1974–2018.

(104) Buceta, D.; Pineiro, Y.; Vazquez-Vazquez, C.; Rivas, J.; Arturo Lopez-Quintela, M. *Catalysts* **2014**, *4* (4), 356–374.

(105) Jones, B. H.; Lodge, T. P. *Polym. J.* **2012**, *44* (2), 131–146.

(106) De Rogatis, L.; Cargnello, M.; Gombac, V.; Lorenzut, B.; Montini, T.; Fornasiero, P. *Chemsuschem* **2010**, *3* (1), 24–42.

(107) Boutonnet, M.; Logdberg, S.; Svensson, E. E. *Curr. Opin. Colloid Interface Sci.* **2008**, *13* (4), 270–286.

(108) Andersson, P. F.; Pirjamali, M.; Jär\a as, S. G.; Boutonnet-Kizling, M. *Catal. Today* **1999**, *53* (4), 565–573.

(109) Boutonett, M.; Kizling, J.; Touroude, R.; Maire, G.; Stenius, P. *Appl. Catal.* **1986**, *20* (1–2), 163–177.

(110) Touroude, R.; Girard, P.; Maire, G.; Kizling, J.; Boutonnet-Kizling, M.; Stenius, P. *Colloids Surf.* **1992**, *67*, 9–19.

(111) Martınez-Arias, A.; Fernández-Garcıa, M.; Iglesias-Juez, A.; Hungrıa, A. B.; Anderson, J. A.; Conesa, J. C.; Soria, J. *Appl. Catal. B Environ.* **2001**, *31* (1), 51–60.

(112) Masui, T.; Fujiwara, K.; Machida, K.; Adachi, G.; Sakata, T.; Mori, H. *Chem. Mater.* **1997**, *9* (10), 2197–2204.

(113) Kim, W.-Y.; Hayashi, H.; Kishida, M.; Nagata, H.;

Wakabayashi, K. *Appl. Catal. Gen.* **1998**, *169* (1), 157–164.

(114) Agrell, J.; Birgersson, H.; Boutonnet, M.; Melián-Cabrera, I.; Navarro, R. M.; Fierro, J. G. *J. Catal.* **2003**, *219* (2), 389–403.

(115) Escudero, M. J.; Hontanon, E.; Schwartz, S.; Boutonnet, M.; Daza, L. *J. Power Sources* **2002**, *106* (1), 206–214.

(116) Liu, Z.; Lee, J. Y.; Han, M.; Chen, W.; Gan, L. M. *J. Mater. Chem.* **2002**, *12* (8), 2453–2458.

(117) Kim, W.-Y.; Hanaoka, T.; Kishida, M.; Wakabayashi, K. *Appl. Catal. Gen.* **1997**, *155* (2), 283–289.

(118) Hanaoka, T.; Won-Young, K. I. M.; Kishida, M.; Nagata, H.; Wakabayashi, K. *Chem. Lett.* **1997**, *1997* (7), 645–646.

(119) Kishida, M.; Umakoshi, K.; Ishiyama, J.; Nagata, H.; Wakabayashi, K. *Catal. Today* **1996**, *29* (1), 355–359.

(120) Andersson, M.; Österlund, L.; Ljungström, S.; Palmqvist, A. *J. Phys. Chem. B* **2002**, *106* (41), 10674–10679.

(121) Fuerte, A.; Hernández-Alonso, M. D.; Maira, A. J.; Martınez-Arias, A.; Fernández-Garcıa, M.; Conesa, J. C.; Soria, J.; Munuera, G. *J. Catal.* **2002**, *212* (1), 1–9.

(122) Spiro, M.; de Jesus, D. M. *Langmuir* **2000**, *16* (6), 2464–2468.

(123) Haumann, M.; Koch, H.; Schomäcker, R. *Catal. Today* **2003**, *79*, 43–49.

(124) Fanti, M.; Mancin, F.; Tecilla, P.; Tonellato, U. *Langmuir* **2000**, *16* (26), 10115–10122.

(125) Toebes, M. L.; van Dillen, J. A.; de Jong, K. P. *J. Mol. Catal. Chem.* **2001**, *173* (1–2), 75–98.

(126) Augustine, R. L. *Heterogeneous Catalysis for the Synthetic Chemist*; CRC Press, 1995.

(127) Mäki-Arvela, P.; Murzin, D. Y. *Appl. Catal. Gen.* **2013**, *451*, 251–281.

(128) Cansell, F.; Aymonier, C. *J. Supercrit. Fluids* **2009**, *47* (3), 508–516.

(129) Andersson, M.; Kiselev, A.; Österlund, L.; Palmqvist, A. E. C. *J. Phys. Chem. C* **2007**, *111* (18), 6789–6797.

(130) Cavani, F.; Trifirò, F.; Vaccari, A. *Catal. Today* **1991**, *11* (2), 173–301.

(131) Menad, S.; Ferreira-Aparicio, P.; Cherifi, O.; Guerrero-Ruiz, A.; Rodriguez-Ramos, I. *Catal. Lett.* **2003**, *89* (1–2), 63–67.

(132) Villa, A.; Chan-Thaw, C. E.; Veith, G. M.; More, K. L.; Ferri, D.; Prati, L. *ChemCatChem* **2011**, *3* (10), 1612–1618.

(133) Villa, A.; Veith, G. M.; Ferri, D.; Weidenkaff, A.; Perry, K. A.; Campisi, S.; Prati, L. *Catal. Sci. Technol.* **2013**, *3* (2), 394–399.

(134) Liu, Z.; Jian, Z.; Fang, J.; Xu, X.; Zhu, X.; Wu, S. *Int. J. Photoenergy* **2012**, *2012*, 1–8.

(135) Shen, X.; Zhang, J.; Tian, B. *J. Hazard. Mater.* **2011**, *192* (2), 651–657.

(136) Xu, H.; Li, M.; Jun, Z. *Mater. Res. Bull.* **2013**, *48* (9), 3144–3148.

(137) Hara, M. *Bull. Chem. Soc. Jpn.* **2014**, *87* (9), 931–941.

(138) Leung, D. Y.; Fu, X.; Wang, C.; Ni, M.; Leung, M. K.; Wang, X.; Fu, X. *ChemSusChem* **2010**, *3* (6), 681–694.

(139) Keswani, R. K.; Ghodke, H.; Sarkar, D.; Khilar, K. C.;

Srinivasa, R. S. *Colloids Surf. Physicochem. Eng. Asp.* **2010**, *369* (1–3), 75–81.

(140) Zielińska, A.; Kowalska, E.; Sobczak, J. W.; Łącka, I.; Gazda, M.; Ohtani, B.; Hupka, J.; Zaleska, A. *Sep. Purif. Technol.* **2010**, *72* (3), 309–318.

(141) Zubieta, C. E.; Soltero - Martínez, J. F. A.; Luengo, C. V.; Schulz, P. C. *Powder Technol.* **2011**, *212* (3), 410–417.

(142) Jian, Z.; Fang, J.; Peng, F. *J. Chem. Technol. Biotechnol.* **2010**, *85* (6), 860–865.

(143) Zhu, K.-R.; Zhang, M.-S.; Hong, J.-M.; Yin, Z. *Mater. Sci. Eng. A* **2005**, *403* (1–2), 87–93.

(144) Wu, M.; Long, J.; Huang, A.; Luo, Y.; Feng, S.; Xu, R. *Langmuir* **1999**, *15* (26), 8822–8825.

(145) Messina, P. V.; Verdinelli, V.; Pieroni, O.; Ruso, J. M. *Colloid Polym. Sci.* **2013**, *291* (4), 835–844.

(146) Nilsson, E.; Sakamoto, Y.; Palmqvist, A. E. C. *Chem. Mater.* **2011**, *23* (11), 2781–2785.

(147) Jones, R. N.; Thorn, G. D. *ResearchGate* **2011**, *27B* (6), 580–603.

(148) Diebold, U. *Surf. Sci. Rep.* **2003**, *48* (5–8), 53–229.

(149) Horikawa, T.; Do, D. D.; Nicholson, D. *Adv. Colloid Interface Sci.* **2011**, *169* (1), 40–58.

(150) Sing, K. S. *Pure Appl. Chem.* **1985**, *57* (4), 603–619.

(151) Das, D.; Shivhare, A.; Saha, S.; Ganguli, A. K. *Mater. Res. Bull.* **2012**, *47* (11), 3780–3785.

(152) Copeland, J. R.; Santillan, I. A.; Schimming, S. M.; Ewbank, J. L.; Sievers, C. *J. Phys. Chem. C* **2013**, *117* (41), 21413–21425.

(153) Ekou, T.; Ekou, L.; Vicente, A.; Lafaye, G.; Pronier, S.; Especel, C.; Marécot, P. *J. Mol. Catal. Chem.* **2011**, *337* (1–2), 82–88.

(154) Liang, H.; Zhang, Y.; Liu, Y. *J. Nat. Gas Chem.* **2008**, *17* (4), 403–408.

(155) Jabłońska, M. *Catal. Commun.* **2015**, *70*, 66–71.

(156) Panagiotopoulou, P.; Christodoulakis, A.; Kondarides, D. I.; Boghosian, S. *J. Catal.* **2006**, *240* (2), 114–125.

(157) Tsubaki, N.; Fujimoto, K. *Top. Catal.* **2003**, *22* (3–4), 325–335.

(158) Haller, G. L.; Resasco, D. E. *MyScienceWork* **2016**.

(159) Tauster, S. J.; Fung, S. C.; Garten, R. L. *J. Am. Chem. Soc.* **1978**, *100* (1), 170–175.

(160) Panagiotopoulou, P.; Kondarides, D. I. *J. Catal.* **2004**, *225* (2), 327–336.

(161) Kirilin, A. V.; Tokarev, A. V.; Kustov, L. M.; Salmi, T.; Mikkola, J.-P.; Murzin, D. Y. *Appl. Catal. Gen.* **2012**, *435–436*, 172–180.

(162) Barbelli, M. L.; Pompeo, F.; Santori, G. F.; Nichio, N. N. *Catal. Today* **2013**, *213*, 58–64.

(163) Roy, D.; Subramaniam, B.; Chaudhari, R. V. *Catal. Today* **2010**, *156* (1–2), 31–37.

(164) Lahr, D.; Shanks, B. *J. Catal.* **2005**, *232* (2), 386–394.

(165) Maris, E.; Davis, R. *J. Catal.* **2007**, *249* (2), 328–337.

(166) Zhang, L.; Karim, A. M.; Engelhard, M. H.; Wei, Z.; King, D. L.; Wang, Y. *J. Catal.* **2012**, *287*, 37–43.

(167) Wang, J.; Masui, Y.; Onaka, M. *Appl. Catal. B Environ.* **2011**, *107* (1–2), 135–139.

(168) Pescarmona, P. P.; Janssen, K. P. F.; Delaet, C.; Stroobants, C.; Houthoofd, K.; Philippaerts, A.; De Jonghe, C.; Paul, J. S.; Jacobs, P. A.; Sels, B. F. *Green Chem.* **2010**, *12* (6), 1083–1089.

(169) Taarning, E.; Saravanamurugan, S.; Holm, M. S.; Xiong, J.; West, R. M.; Christensen, C. H. *Chemsuschem* **2009**, *2* (7), 625–627.

(170) West, R. M.; Holm, M. S.; Saravanamurugan, S.; Xiong, J.; Beversdorf, Z.; Taarning, E.; Christensen, C. H. *J. Catal.* **2010**, *269* (1), 122–130.

(171) Miyazawa, T.; Kusunoki, Y.; Kunimori, K.; Tomishige, K. *J. Catal.* **2006**, *240* (2), 213–221.

(172) Bolado, S.; Treviño, R. E.; García-Cubero, M. T.; González-Benito, G. *Catal. Commun.* **2010**, *12* (2), 122–126.

(173) Dietrich, P. J.; Lobo-Lapidus, R. J.; Wu, T.; Sumer, A.; Akatay, M. C.; Fingland, B. R.; Guo, N.; Dumesic, J. A.; Marshall, C. L.; Stach, E.; Jellinek, J.; Delgass, W. N.; Ribeiro, F. H.; Miller, J. T. *Top. Catal.* **2012**, *55* (1–2), 53–69.

(174) Maris, E.; Davis, R. *J. Catal.* **2007**, *249* (2), 328–337.

(175) Bahruji, H.; Bowker, M.; Brookes, C.; Davies, P. R.; Wawata, I. *Appl. Catal. Gen.* **2013**, *454*, 66–73.

(176) Menezes, A. O.; Rodrigues, M. T.; Zimmaro, A.; Borges, L. E. P.; Fraga, M. A. *Renew. Energy* **2011**, *36* (2), 595–599.

(177) Kuleci, H.; Schmidt, C.; Rybacki, E.; Petrishcheva, E.; Abart, R. *Mineral. Petrol.* **2016**, *110* (1), 1–10.

(178) Amaral, L. F.; Oliveira, I. R.; Salomao, R.; Frollini, E.; Pandolfelli, V. C. *Ceram. Int.* **2010**, *36* (3), 1047–1054.

(179) Pokrovsky, O. S.; Schott, J.; Castillo, A. *Geochim. Cosmochim. Acta* **2005**, *69* (4), 905–918.

(180) Horikawa, T.; Do, D. D.; Nicholson, D. *Adv. Colloid Interface Sci.* **2011**, *169* (1), 40–58.

(181) Sing, K. S. *Pure Appl. Chem.* **1985**, *57* (4), 603–619.

(182) Chheda, J. N.; Huber, G. W.; Dumesic, J. A. *Angew. Chem. Int. Ed.* **2007**, *46* (38), 7164–7183.

(183) Iriondo, A.; Barrio, V. L.; Cambra, J. F.; Arias, P. L.; Güemez, M. B.; Navarro, R. M.; Sánchez-Sánchez, M. C.; Fierro, J. L. G. *Top. Catal.* **2008**, *49* (1–2), 46–58.

(184) El Doukkali, M.; Iriondo, A.; Arias, P. L.; Requies, J.; Gandarías, I.; Jalowiecki-Duhamel, L.; Dumeignil, F. *Appl. Catal. B Environ.* **2012**, *125*, 516–529.

(185) Fornasari, G.; Gazzano, M.; Matteuzzi, D.; Trifirò, F.; Vaccari, A. *Appl. Clay Sci.* **1995**, *1–2* (10), 69–82.

(186) Di Cosimo, J. I.; Apesteguıa, C. R.; Ginés, M. J. L.; Iglesia, E. *J. Catal.* **2000**, *190* (2), 261–275.

(187) Bolognini, M.; Cavani, F.; Scagliarini, D.; Flego, C.; Perego, C.; Saba, M. *Catal. Today* **2002**, *75* (1), 103–111.

(188) Corma, A.; Fornes, V.; Rey, F. *J. Catal.* **1994**, *148* (1), 205–212.

(189) Díez, V. K.; Apesteguía, C. R.; Di Cosimo, J. I. *J. Catal.* **2003**, *215* (2), 220–233.

(190) Díez, V. K.; Apesteguía, C. R.; Di Cosimo, J. I. *J. Catal.* **2003**, *215* (2), 220–233.

(191) Ciftci, A.; Peng, B.; Jentys, A.; Lercher, J. A.; Hensen, E. J. M. *Appl. Catal. Gen.* **2012**, *431–432*, 113–119.

(192) Liu, S.; Chen, D.; Zhang, K.; Li, J.; Zhao, N. *Int. J. Hydrog. Energy* **2008**, *33* (14), 3736–3747.

(193) Aguilera, D.; Perez, A.; Molina, R.; Moreno, S. *Stud. Surf. Sci. Catal.* **2010**, *175*, 513–516.

(194) Bolognini, M.; Cavani, F.; Scagliarini, D.; Flego, C.; Perego, C.; Saba, M. *Catal. Today* **2002**, *75* (1), 103–111.

(195) Vannice, M. A. *J. Catal.* **1977**, *50* (2), 228–236.

(196) Grenoble, D. C.; Estadt, M. M.; Ollis, D. F. *J. Catal.* **1981**, *67* (1), 90–102.

(197) Sinfelt, J. H.; Yates, D. J. *J. Catal.* **1967**, *8* (1), 82–90.

(198) Davda, R. R.; Shabaker, J. W.; Huber, G. W.; Cortright, R. D.; Dumesic, J. A. *Appl. Catal. B Environ.* **2005**, *56* (1–2), 171–186.

(199) Li, S.; Gong, J. *Chem. Soc. Rev.* **2014**, *43* (21), 7245–7256.

(200) Chakinala, A. G.; van Swaaij, W. P. M.; Kersten, S. R. A.; de Vlieger, D.; Seshan, K.; Brilman, D. W. F. (Wim). *Ind. Eng. Chem. Res.* **2013**, *52* (15), 5302–5312.

(201) Rahman, M. M.; Church, T. L.; Variava, M. F.; Harris, A. T.; Minett, A. I. *RSC Adv.* **2014**, *4* (36), 18951.

(202) Lee, H.-J.; Shin, G. S.; Kim, Y.-C. *Korean J. Chem. Eng.* **2015**, *32* (7), 1267–1272.

(203) Miranda, B. C.; Chimentão, R. J.; Santos, J. B. O.; Gispert-Guirado, F.; Llorca, J.; Medina, F.; Bonillo, F. L.; Sueiras, J. E. *Appl. Catal. B Environ.* **2014**, *147*, 464–480.

(204) He, C.; Zheng, J.; Wang, K.; Lin, H.; Wang, J.-Y.; Yang, Y. *Appl. Catal. B Environ.* **2015**, *162*, 401–411.

(205) Tupy, S. A.; Chen, J. G.; Vlachos, D. G. *Top. Catal.* **2013**, *56* (18–20), 1644–1650.

(206) El Doukkali, M.; Iriondo, A.; Cambra, J. F.; Arias, P. L. *Top. Catal.* **2014**, *57* (10–13), 1066–1077.

(207) Yun, Y. S.; Park, D. S.; Yi, J. *Catal. Sci. Technol.* **2014**, *4* (9), 3191.

(208) Bauer, E. *Iron Catalysis II*; Springer, 2015.

(209) Plietker, B. *Iron Catalysis: Fundamentals and Applications*; Springer Science & Business Media, 2011.

(210) Hasan, M.; Drazin, J.; Dey, S.; Castro, R. H. R. *Am. Mineral.* **2015**, *100* (2–3), 652–657.

(211) Pawelec, B.; Damyanova, S.; Arishtirova, K.; Fierro, J. L. G.; Petrov, L. *Appl. Catal. Gen.* **2007**, *323*, 188–201.

(212) Iriondo, A.; Cambra, J. F.; Barrio, V. L.; Guemez, M. B.; Arias, P. L.; Sanchez-Sanchez, M. C.; Navarro, R. M.; Fierro, J. L. G. *Appl. Catal. B Environ.* **2011**, *106*, 86–93.

(213) Radii of atoms and ions https://www.webelements.com/.

(214) Coleman, L. J. I.; Epling, W.; Hudgins, R. R.; Croiset, E. *Appl.*

Catal. -Gen. **2009**, *363* (1–2), 52–63.

(215) Cavani, F.; Trifirò, F.; Vaccari, A. *Catal. Today* **1991**, *11* (2), 173–301.

(216) Huber, G. W.; Shabaker, J. W.; Evans, S. T.; Dumesic, J. A. *Appl. Catal. B Environ.* **2006**, *62* (3–4), 226–235.

(217) Liu, X.; Shen, K.; Wang, Y.; Wang, Y.; Guo, Y.; Guo, Y.; Yong, Z.; Lu, G. *Catal. Commun.* **2008**, *9* (14), 2316–2318.

(218) Kim, M.-C.; Kim, T.-W.; Kim, H. J.; Kim, C.-U.; Bae, J. W. *Renew. Energy* **2016**, *95*, 396–403.

(219) Silverstein, R. M.; Webster, F. X.; Kiemle, D. J.; Bryce, D. L. *Spectrometric Identification of Organic Compounds*; John Wiley & Sons, 2014.

(220) Nakanishi, K.; Solomon, P. H. *Infrared absorption spectroscopy*, 2d ed.; Holden-Day: San Francisco, 1977.

(221) Stuart, B. H. *Infrared Spectroscopy: Fundamentals and Applications*; John Wiley & Sons, 2004.

(222) Alpert, N. L.; Keiser, W. E.; Szymanski, H. A. *IR: theory and practice of infrared spectroscopy*; Plenum Pub. Corp., 1973.

(223) Günzler, H.; Gremlich, H.-U. *IR Spectroscopy: An Introduction*; Wiley, 2002.

(224) Company, A. C. *The Aldrich library of infrared spectra*; Aldrich Chemical Co., 1981.

(225) AIST:Spectral Database for Organic Compounds,SDBS http://sdbs.db.aist.go.jp/sdbs/cgi-bin/direct_frame_top.cgi (accessed Feb 6, 2017).

(226) NIST | National Institute of Standards and Technology http://webbook.nist.gov/ https://www.nist.gov/national-institute-standards-and-technology.

(227) Max, J.-J.; Chapados, C. *J. Chem. Phys.* **2009**, *131* (18), 184505.

(228) Dolati, F.; Tayyari, S. F.; Vakili, M. *J. Mol. Struct.* **2015**, *1094*, 264–273.

(229) de Vlieger, D. J. M.; Mojet, B. L.; Lefferts, L.; Seshan, K. *J. Catal.* **2012**, *292*, 239–245.

(230) Profeta, L. T. M.; Sams, R. L.; Johnson, T. J.; Williams, S. D. *J. Phys. Chem. A* **2011**, *115* (35), 9886–9900.

(231) Yaylayan, V. A.; Harty-Majors, S.; Ismail, A. A. *Carbohydr. Res.* **1999**, *318* (1), 20–25.

(232) Kobayashi, Y.; Igarashi, T.; Takahashi, H.; Higasi, K. *J. Mol. Struct.* **1976**, *35* (1), 85–99.

(233) García-Jiménez, F.; Collera Zúñiga, O.; Castells García, Y.; Cárdenas, J.; Cuevas, G. *J. Braz. Chem. Soc.* **2005**, *16* (3A), 467–476.

(234) Climent, M. J.; Corma, A.; Iborra, S. *Green Chem.* **2011**, *13* (3), 520.

(235) Karinen, R.; Vilonen, K.; Niemelä, M. *ChemSusChem* **2011**, *4* (8), 1002–1016.

(236) Yan, Y.; Jiang, G. *J. Biobased Mater. Bioenergy* **2014**, *8* (6), 553–569.

(237) Sheldon, R. A. *Green Chem* **2014**, *16* (3), 950–963.

(238) Deng, W.; Zhang, H.; Xue, L.; Zhang, Q.; Wang, Y. *Chin. J. Catal.* **2015**, *36* (9), 1440–1460.

(239) Koklin, A. E.; Klimenko, T. A.; Kondratyuk, A. V.; Lunin, V. V.;

Bogdan, V. I. *Kinet. Catal.* **2015**, *56* (1), 84–88.

(240) Meryemoglu, B.; Hesenov, A.; Irmak, S.; Atanur, O. M.; Erbatur, O. *Int. J. Hydrog. Energy* **2010**, *35* (22), 12580–12587.

(241) Li, N.; Huber, G. W. *J. Catal.* **2010**, *270* (1), 48–59.

(242) Zhang, Q.; Wang, T.; Li, B.; Jiang, T.; Ma, L.; Zhang, X.; Liu, Q. *Appl. Energy* **2012**, *97*, 509–513.

(243) Kirilin, A. V.; Tokarev, A. V.; Kustov, L. M.; Salmi, T.; Mikkola, J.-P.; Murzin, D. Y. *Appl. Catal. Gen.* **2012**, *435–436*, 172–180.

(244) Godina, L. I.; Kirilin, A. V.; Tokarev, A. V.; Murzin, D. Y. *ACS Catal.* **2015**, *5* (5), 2989–3005.

(245) Ooms, R.; Dusselier, M.; Geboers, J. A.; Op de Beeck, B.; Verhaeven, R.; Gobechiya, E.; Martens, J. A.; Redl, A.; Sels, B. F. *Green Chem* **2014**, *16* (2), 695–707.

(246) Tronci, S.; Pittau, B. *RSC Adv* **2015**, *5* (29), 23086–23093.

(247) Tsilomelekis, G.; Orella, M. J.; Lin, Z.; Cheng, Z.; Zheng, W.; Nikolakis, V.; Vlachos, D. G. *Green Chem* **2016**, *18* (7), 1983–1993.

(248) Wang, S.; Lin, H.; Zhao, Y.; Chen, J.; Zhou, J. *J. Anal. Appl. Pyrolysis* **2016**, *118*, 259–266.

(249) Goncalves, F. A.; Ruiz, H. A.; dos Santos, E. S.; Teixeira, J. A.; de Macedo, G. R. *Ind. Crops Prod.* **2015**, *77*, 1–12.

(250) Imman, S.; Arnthong, J.; Burapatana, V.; Laosiripojana, N.; Champreda, V. *Appl. Biochem. Biotechnol.* **2013**, *170* (8), 1982–1995.

(251) Liu, L.; Liu, W.; Hou, Q.; Chen, J.; Xu, N. *Bioresour. Technol.* **2015**, *196*, 662–667.

(252) Sarip, H.; Hossain, M. S.; Azemi, M. M. N.; Allaf, K. *Bioresources* **2016**, *11* (4), 10625–10653.

(253) Myronyuk, I. F.; Mandzyuk, V. I.; Sachko, V. M.; Gun'ko, V. M. *Nanoscale Res. Lett.* **2016**, *11* (1), 508.

(254) Girisuta, B.; Janssen, L.; Heeres, H. J. *Chem. Eng. Res. Des.* **2006**, *84* (A5), 339–349.

(255) Marianou, A. A.; Michailof, C. M.; Pineda, A.; Iliopoulou, E. F.; Triantafyllidis, K. S.; Lappas, A. A. *ChemCatChem* **2016**, *8* (6), 1100–1110.

(256) *Asian J. Chem.* **2014**, *26* (15).

(257) Saravanamurugan, S.; Paniagua, M.; Melero, J. A.; Riisager, A. *J. Am. Chem. Soc.* **2013**, *135* (14), 5246–5249.

(258) van Zandvoort, I.; Wang, Y.; Rasrendra, C. B.; van Eck, E. R.; Bruijnincx, P. C.; Heeres, H. J.; Weckhuysen, B. M. *ChemSusChem* **2013**, *6* (9), 1745–1758.

(259) Albonetti, S.; Lolli, A.; Morandi, V.; Migliori, A.; Lucarelli, C.; Cavani, F. *Appl. Catal. B Environ.* **2015**, *163*, 520–530.

(260) Yang, G.; Pidko, E. A.; Hensen, E. J. M. *J. Catal.* **2012**, *295*, 122–132.

(261) Delidovich, I.; Palkovits, R. *ChemSusChem* **2016**, *9* (6), 547–561.

(262) Choudhary, V.; Pinar, A. B.; Lobo, R. F.; Vlachos, D. G.; Sandler, S. I. *ChemSusChem* **2013**, *6* (12), 2369–2376.

(263) Rackemann, D. W.; Doherty, W. O. *Biofuels Bioprod. Biorefining* **2011**, *5* (2), 198–214.

(264) Rasmussen, H.; Sørensen, H. R.; Meyer, A. S. *Carbohydr. Res.* **2014**, *385*, 45–57.

(265) Kirilin, A. V.; Tokarev, A. V.; Murzina, E. V.; Kustov, L. M.; Mikkola, J.-P.; Murzin, D. Y. *ChemSusChem* **2010**, *3* (6), 708–718.

(266) Speck, J. C. *Adv. Carbohydr. Chem.* **1958**, *13*, 63–103.

(267) Kabyemela, B. M.; Adschiri, T.; Malaluan, R. M.; Arai, K. *Ind. Eng. Chem. Res.* **1999**, *38* (8), 2888–2895.

(268) Watanabe, M.; Aizawa, Y.; Iida, T.; Nishimura, R.; Inomata, H. *Appl. Catal. Gen.* **2005**, *295* (2), 150–156.

(269) Maris, E.; Davis, R. *J. Catal.* **2007**, *249* (2), 328–337.

(270) Deng, W.; Zhang, Q.; Wang, Y. *J. Energy Chem.* **2015**, *24* (5), 595–607.

(271) Onda, A.; Ochi, T.; Kajiyoshi, K.; Yanagisawa, K. *Catal. Commun.* **2008**, *9* (6), 1050–1053.

(272) Holm, M. S.; Saravanamurugan, S.; Taarning, E. *Science* **2010**, *328* (5978), 602–605.

(273) Watanabe, M.; Aizawa, Y.; Iida, T.; Aida, T. M.; Levy, C.; Sue, K.; Inomata, H. *Carbohydr. Res.* **2005**, *340* (12), 1925–1930.

(274) Weingarten, R.; Tompsett, G. A.; Conner, W. C.; Huber, G. W. *J. Catal.* **2011**, *279* (1), 174–182.

(275) Valenzuela, M. B.; Jones, C. W.; Agrawal, P. K. *Energy Fuels* **2006**, *20* (4), 1744–1752.

(276) Meryemoglu, B.; Irmak, S.; Hasanoglu, A.; Erbatur, O.; Kaya, B. *Fuel* **2014**, *134*, 354–357.

(277) Johnson Matthey - Precious Metals Management http://www.platinum.matthey.com/ (accessed Feb 27, 2017).

(278) LBMA: the Competent Authority for the world's Bullion Market http://www.lbma.org.uk/pricing-and-statistics (accessed Feb 27, 2017).

(279) TRADING ECONOMICS http://www.tradingeconomics.com/ (accessed Feb 27, 2017).

(280) London Metal Exchange http://www.lme.com/en-gb/metals/ (accessed Feb 27, 2017).

(281) American Mineralogist Crystal Structure Database http://rruff.geo.arizona.edu/AMS/amcsd.php.

Appendix

Wiley reprint license

JOHN WILEY AND SONS LICENSE
TERMS AND CONDITIONS

Jan 02, 2017

This Agreement between Erica Lombardi ("You") and John Wiley and Sons ("John Wiley and Sons") consists of your license details and the terms and conditions provided by John Wiley and Sons and Copyright Clearance Center.

License Number	4020720240145
License date	Jan 02, 2017
Licensed Content Publisher	John Wiley and Sons
Licensed Content Publication	Wiley oBooks
Licensed Content Title	Biosyngas and Derived Products from Gasification and Aqueous Phase Reforming
Licensed Content Author	Francesco Basile,Stefania Albonetti,Fabrizio Cavani,Erica Lombardi,Rodolfo Mafessanti
Licensed Content Date	Feb 19, 2016
Licensed Content Pages	32
Type of use	Dissertation/Thesis
Requestor type	Author of this Wiley chapter
Format	Print and electronic
Portion	Full chapter
Will you be translating?	No
Title of your thesis / dissertation	Catalytic Aqueous Phase conversion of polyols to hydrogen and chemicals
Expected completion date	Mar 2017
Expected size (number of pages)	150
Requestor Location	Erica Lombardi Via del Risorgimento n.4 Bologna, 40136 Italy Attn: Erica Lombardi
Publisher Tax ID	EU826007151
Customer VAT ID	ITLMBRCE89B51D704A
Billing Type	Invoice
Billing Address	Erica Lombardi Via del Risorgimento n.4 Bologna, Italy 40136 Attn: Erica Lombardi
Total	0.00 EUR

More information on:

https://authorservices.wiley.com/author-resources/Journal-Authors/licensing-and-open-access/licensing/licensing-info-faqs.html

Acknowledgements